



UNIVERSITY OF  
LIVERPOOL

School of Engineering

# **Electrochemical Properties of Porous Metals Manufactured by Lost Carbonate Sintering**

Thesis submitted in accordance with the requirements of the  
University of Liverpool for the degree of Doctor of Philosophy

By

**Zejun Wang**

January 2023

## **Abstract**

Open-cell porous metals have received many attentions in both academia and industry because of their superior properties, including high surface area, great catalytic activity, low weight to volume ratio, and excellent mechanical properties. They are expected to find many applications in electrochemical fields. In particular, porous metals manufactured by the Lost Carbonate Sintering (LCS) process are potentially an excellent candidate to be used as a porous substrate material for electrochemical applications because they are low-cost and easy to be fabricated and have high surface areas and controllable pore size and porosity.

The main aim of this research is to increase the real and electroactive surface areas of the LCS porous Ni without changing its porous structure, with a focus on applications in electrochemical detections. Firstly, the effects of manufacturing parameters, including pore size, porosity, fine powder ratio, compaction pressure and sintering temperature, on the real and electroactive surface areas of the LCS porous Ni were investigated. Secondly, a new hierarchical porous Ni structure was manufactured by combining the LCS and the Dynamic Hydrogen Bubble Template (DHBT) processes to increase the surface areas. The effects of DHBT process parameters, including type and concentration of Ni salt, the concentration of H<sup>+</sup> source and deposition potential

and time, on the morphology and surface areas of the LCS/DHBT porous Ni were investigated.

The surface area of porous metals is normally measured by the BET gas absorption method, which is often not appropriate in electrochemical applications, because not all surfaces take part in the electrochemical reaction. In this thesis, the cyclic voltammetry method, which is a typical in-situ method, was employed to measure the electroactive (i.e., electrochemically effective) and real surface areas of the LCS porous Ni samples. The specific real and electroactive surface areas of the LCS porous Ni samples are 500-1600  $\text{cm}^{-1}$  and 200-650  $\text{cm}^2/\text{g}$ , and 80-115  $\text{cm}^{-1}$  and 30-55  $\text{cm}^2/\text{g}$ , respectively. The intermediate amount of fine Ni powder results in the highest real surface area, approximately 70% higher than the samples produced with coarse Ni powder. Samples produced with fine Ni powder can increase the electroactive surface area by up to 100%. Electroactive surface area is highly sensitive to scan rate, which controls the diffusion layer thickness.

The mass transfer performance of electrodes reflects the rate of electrochemical reactions of reactors and is one of the most important parameters for electrochemical applications. It depends on the mass transfer coefficient and the surface area of electrodes. While the LCS porous Ni has a good mass transfer coefficient, its effective surface area is relatively low. In this

thesis, the effective surface area of the LCS porous Ni was increased by deposit a high surface area DHBT coating on the LCS porous Ni substrate. The mass transfer performances of the LCS and LCS/DBHT porous Ni samples were measured by the limiting current method. The overall mass transfer performance of the LCS/DHBT porous Ni is in the range of 0.004 to 0.038 cm<sup>3</sup>/s, which is increased by up to 207% compared to the LCS porous Ni. The mass transfer performance of the LCS porous Ni was also increased when a suitable fine Ni powder ratio was used in the manufacture, because of an increase in the effective surface area.

A novel electrochemical sensor was developed for determination of glucose concentration using the LCS/DHBT porous Ni as a working electrode. It has many advantages, such as no enzyme, high sensitivity and large limit of detection range, compared to the other glucose sensors. The relationship between the current and glucose concentration of the Ni electrode was measured by the cyclic voltammetry peak current method. The nominal current density for the LCS/DHBT porous Ni increases by 750% and 250% comparing to the Ni plate and the LCS porous Ni electrode. The current density decreases with increasing the NH<sub>4</sub>Cl concentration during manufacturing and increases with increasing deposition potential and scan rate. It is decreased by 41% when the NH<sub>4</sub>Cl concentration is increased from 0.5 M to 1.5 M, and increased by 58% when the deposition potential is increased from -1.35 V to - 1.7 V. The current

density and the glucose concentration have linear relations in several segments. The slope of the current density - glucose concentration curves decreases, and the intercept increases, with increasing glucose concentration. The sensitivity values of the plate, LCS and LCS/DHBT Ni electrodes are 1724, 2651 and 5775  $\mu\text{A}/\text{cm}^2\text{mM}$ , respectively.

## **Declaration**

I hereby certify that the content of this thesis entitled “Electrochemical Properties of Porous Metals Manufactured by Lost Carbonate Sintering”, submitted for the degree of Doctor in Philosophy in the Faculty of Science and Engineering at the University of Liverpool, is my own work under the supervision of Prof. Yuyuan Zhao of the School of Engineering, University of Liverpool, and this work has not been used as the basis for the award of any other degree/diploma. The appropriate acknowledgement has been given.

Zejun Wang

January 2023

## Acknowledgements

I would like to express my deepest gratitude to my supervisor, Prof. Yuyuan Zhao, who is a fountain of knowledge and wisdom. I appreciated his supervision and patient guidance in my PhD programme.

I am very grateful to Dr Liping Zhang for her support and encouragement in my study and life. I would also like to thank Dr Richard Potter, my second supervisor, who gave me a lot of suggestions in this study journey. I would like to thank Mr Dave Atkinson for his professional technical support in metallography and machine operations. I thank him for the time to accompany me and talk to me about a lot of stories when I was in the laboratory alone.

A warm thank you to Dr Pengcheng Zhu for his endless help in my research and life. I would also like to acknowledge all my friends in our research group, Dr Zhining Wu, Dr Xianke Lu, Dr Yue Zhang, Dr Chen Liang and Dr Mehta, who let me feel that I was not alone in the world of academic research. Special thank goes to Yi Li for her time and patient help for years.

Last but not least, I dedicate my most personal thank you to my mother Xia Wang, my father Quanshan Wang and my elder sister Yixiao Wang, for their unconditional love, trust and support.

## List of Publications

1. Wang, Z. and Zhao, Y., 2023. Porous nickel electrode for highly sensitive non-enzyme electrochemical glucose detection. *Coatings*, 13, 290.
2. Wang, Z. and Zhao, Y., 2023. Effects of processing conditions and fine powder loading on real and electroactive surface areas of porous nickel manufactured by lost carbonate sintering. *Powder Metallurgy*, 1-11.



## List of Symbols

$A$	surface area	$m^2$
$a$	constant associated with the structural properties of the electrode	
$b$	constant associated with the mass transport condition	
$b'$	slope of the signal/concentration functional relationship	
$C$	capacitance	F
$C'$	reference capacitance per unit area	F/m <sup>2</sup>
$\Delta C$	differential capacitance	F
$c$	concentration of the reactive species in the bulk solution	M
$D$	diffusion coefficient of the electrolyte	m <sup>2</sup> /s
$d_e$	equivalent diameter of pores	m
$E$	potential applied on the electrode	V
$F$	Faraday constant	C/mol
$I$	charging current	A
$I_L$	limiting current	A
$i_p$	peak current	A
$J_0$	flux of the species	A/m <sup>2</sup>
$k$	mass transfer coefficient	m <sup>3</sup> /s
$k'$	expansion factor	
$m_{K_2CO_3}$	mass of K <sub>2</sub> CO <sub>3</sub>	kg
$m_{Ni}$	mass of Ni	kg

$n$	number of atom/electron	
$Q$	charge stored on the electrode	C
$Q_H$	charge of hydrogen adsorption	C
$Q_H^*$	charge of a monolayer of hydrogen adsorption per unit area	C/m <sup>2</sup>
$Q_M$	charge consumed in the range of voltammetric stripping	C
$Q_M^*$	charge corresponding to a monolayer of deposited metal per unit area	C/m <sup>2</sup>
$R$	gas constant	J/mol•K
$R'$	ohmic resistance between the electrodes	Ω
$Re$	Reynolds number	
$Sc$	Schmidt number	
$Sh$	Sherwood number	
$T$	temperature	K
$u$	kinematic viscosity of the electrolyte	m•s <sup>2</sup>
$V$	volume of the porous Ni	m <sup>3</sup>
$\Delta V$	potential shift	V
$v$	electrolyte flow velocity	m/s
$v'$	potential sweep rate	V/s
$x$	distance away the electrode surface	m

### Greek symbols

$\alpha$	constant associated with the geometrical structure of the electrode	
$\beta$	constant depending on the hydrodynamic regime	
$d$	diffusion layer thickness	m

$\varepsilon$	porosity	
$\rho_{K_2CO_3}$	densities of $K_2CO_3$	kg/m <sup>3</sup>
$\rho_{Ni}$	densities of Ni	kg/m <sup>3</sup>
$\sigma$	population standard deviation of the blank signals	
$\varphi_{anode}$	potentials at anodic peak	V
$\varphi_{cathode}$	potentials at cathodic peak	V

# List of Tables

## Chapter 2

Table 2. 1 Characteristics of different fabrication methods for porous metals (Banhart 2001).....	11
Table 2. 2 Major fuel cell types: proton exchange membrane fuel cell (PEMFC), phosphoric acid fuel cell (PAFC), alkaline fuel cell (AFC), molten carbonate fuel cell (MCFC) and solid oxide fuel cell (SOFC) (O'Hayre et al. 2016).	62

## Chapter 3

Table 3. 1 L16 orthogonal array design of experiments. ....	71
Table 3. 2 Bath compositions and deposition parameters in Ni(CH <sub>3</sub> COO) <sub>2</sub> electrolyte. ....	74
Table 3. 3 Bath compositions and deposition parameters in Ni(SO <sub>3</sub> NH <sub>2</sub> ) <sub>2</sub> electrolyte with 1.5 M NH <sub>4</sub> Cl. ....	75
Table 3. 4 Deposition potential and time for manufacturing the LCS/DHBT porous Ni samples for mass transfer study. ....	76
Table 3. 5 NH <sub>4</sub> Cl concentration and deposition potential for manufacturing the LCS/DHBT porous Ni samples for glucose detection study. ....	77
Table 3. 6 Uncertainty of physical parameters in this study .....	77

## Chapter 4

Table 4. 1 Nominal mean Ni particle size, range of scan rate and corresponding diffusion layer thickness of the transition region for samples with different fine Ni powder ratios .....	112
--	-----

## Chapter 6

Table 6. 1 Values of constants <i>a</i> and <i>b</i> for different fine Ni powder ratios, obtained by fitting the data to equation 6.1. ....	152
Table 6. 2 Values of constants <i>a</i> and <i>b</i> for different deposition potentials and deposition times, obtained by fitting the data to equation 6.1. ....	155

## Chapter 7

Table 7. 1 Electroactive surface areas of the LCS and composite LCS/DHBT porous Ni electrodes.....	160
Table 7. 2 Anodic current density and potential for plate, LCS and LCS/DHBT Ni electrodes at different scan rates. ....	166

Table 7. 3 Comparison of electrochemical properties of plate, LCS and LCS/DHBT Ni electrodes for glucose measurement.....	182
Table 7. 4 Comparison of electrochemical properties of Ni-based electrodes for electrochemical non-enzymatic glucose measurement .....	183

# List of Figures

## Chapter 2

Fig. 2. 1: Schematic of the direct foaming device (Luthardt et al. 2015). .....	13
Fig. 2. 2: A typical directly foamed open-cell structure with big pores (Luthardt et al. 2015).....	14
Fig. 2. 3: A typical process of space holder casting methods (Banhart 2001). .....	15
Fig. 2. 4: Cellular aluminium manufactured by a space holder process (Banhart 2001). .....	16
Fig. 2. 5: A schematic process of the investment casting (Banhart 2001). .....	17
Fig. 2. 6: Micrograph of an aluminium foam produced by the investment casting method (Harte et al.1999).....	18
Fig. 2. 7: Schematic of pores generated in the spray foaming process (Barnhart 2001). .....	19
Fig. 2. 8: Basic steps of the PM process (Upadhyaya 1997). .....	21
Fig. 2. 9: Loose powder sintered porous bronze (Eisenmann 1998).....	22
Fig. 2. 10: Schematic diagram of a typical CVD reactor (Park et al. 2001). ...	24
Fig. 2. 11: SEM micrograph of Inco Ni foam (Paserin et al. 2004). .....	25
Fig. 2. 12: Various PVD processes: a) vacuum evaporation, b-c) sputter deposition, d-e) arc vapour deposition and f-i) ion plating (Mattox 1999).	27
Fig. 2. 13: Schematic diagram of a typical arc PVD reactor (Yen et al. 1995). .....	28
Fig. 2. 14: Fundamental steps of electrodeposition at an electrode surface, where 1 refers to the hydrated ions, 2 refers to the diffusion of ions to activated sites and 3 refers to the growth of the deposit (Schwarzacher 2006). .....	31
Fig. 2. 15: SEM macrograph of a dealloyed porous metal (Chen et al. 2013). .....	33
Fig. 2. 16: Schematic of the LCS process (Zhao et al. 2005).....	34
Fig. 2. 17: Porous copper produced by LCS method (Diao et al. 2015).....	35
Fig. 2. 18: Schematic of DHBT for porous membrane production (Shin et al. 2003). .....	36
Fig. 2. 19: Schematic diagram of Helmholtz layer and the inner and outer plane (Bard 2002).....	40
Fig. 2. 20: (a) Typical current-potential plots obtained by the double layer capacitance method and (b) the corresponding dependence of current on scan rate (Cherevko et al. 2010). .....	41
Fig. 2. 21: Various reactions under different potential ranges at Pt electrode in 0.5 M H <sub>2</sub> SO <sub>4</sub> (Lukaszewski et al. 2016).....	42
Fig. 2. 22: A typical current-potential plot of the oxidation of ferrocyanide on the surface of an LCS porous Ni sample (Zhu and Zhao 2019).....	47
Fig. 2. 23: Schematic diagram of electrode reaction pathway (Bard 2002)....	51

Fig. 2. 24: Typical voltammogram for the reduction of 1 mM $K_3Fe(CN)_6$ in 1 M $Na_2CO_3$ (Recio et al. 2013). .....	53
Fig. 2. 25: Schematic diagram of a simple hydrogen-oxygen fuel cell (O'Hayre et al. 2016).....	61
Fig. 2. 26: Schematic diagram of the diffusion layer that develops at the anode of an operating hydrogen-oxygen fuel cell configuration (O'Hayre et al. 2016). .....	63
Fig. 2. 27: Contrast of resistance in Nyquist plots of the composite electrode and bare lithium metal (Li et al. 2017).....	64

### Chapter 3

Fig. 3. 1: The schematic diagram of the LCS process (Zhao et al.2005). .....	67
Fig. 3. 2: Schematic diagram of the compaction process for manufacturing the preforms (Diao et al. 2015). .....	69
Fig. 3. 3: Temperature profile of the sintering process (Zhu and Zhao 2017). 70	
Fig. 3. 4: Schematic diagram of the three-electrode electrochemical cell used for the CV measurement (Zhu and Zhao 2017). .....	78
Fig. 3. 5: A typical current-potential plot of redox reaction of ferrocyanide (Zhu and Zhao 2019). .....	79
Fig. 3. 6: Schematic of the electrochemical configuration for the mass transfer measurement. 1 is electrolyte reservoir, 2 is the solution input pipe, 3 is waste solution tank, 4 is a peristaltic pump, 5 is working electrode, 6 is SCE reference electrode, 7 is Pt coil counter electrode, 8 is the glass vial, 9 is conducting wire, 10 is potentiostat, 11 is computer monitor, 12 is an acrylic tube, 13 is water barrier film, 14 is porous working electrode, 15 is conducting wire and 16 is mirror-polished Ni plate (Zhu and Zhao 2017). .....	82
Fig. 3. 7: Typical current vs potential plot for the reduction of $Fe(CN)_6^{3-}$ in $10^{-4}$ M $K_3Fe(CN)_6$ + $10^{-3}$ M $K_4Fe(CN)_6$ + 1 M $Na_2CO_3$ at a porous Ni electrode with a scan rate of 0.005 V/s (Recio et al. 2013). .....	83
Fig. 3. 8: Current versus potential profiles as glucose concentration increases from 0 to 10 mM. ....	84

### Chapter 4

Fig. 4. 1: SEM micrographs of LCS porous Ni samples with benchmark processing parameters (pore size 425 – 710 $\mu m$ , porosity 60%, coarse Ni powder only, compaction pressure 200 MP and sintering temperature 850°C) or with one parameter different from the benchmark condition: a) benchmark, low magnification; b) benchmark, higher magnification, c) sintering temperature 850 °C, d) fine Ni content 60%, e) fine Ni content	
---	--

100%, f) no compaction and g) sintering temperature 700 °C. ....	91
Fig. 4. 2: Surface morphology of porous Ni sample treated with 20% diluted hydrochloric acid for 60 mins. ....	94
Fig. 4. 3: Surface morphology of porous Ni sample treated with concentrated sulfuric acid for 60 min, a) low magnification and b) high magnification. .	95
Fig. 4. 4: a) SEM micrograph and b) EDX spectrum of LCS porous Ni sample treated with concentrated sulfuric acid for 60 min and 20% diluted hydrochloric acid for 20 s. ....	96
Fig. 4. 5: Variations of (a) volumetric and (b) gravimetric real surface areas with level of parameter. ....	98
Fig. 4. 6: Variations of (a) volumetric and (b) gravimetric electroactive surface areas with a level of parameter. ....	101
Fig. 4. 7: Variations of a) volumetric and b) gravimetric real surface areas with fine Ni powder ratio at different porosities (see inset). Other parameters: pore size 425 – 710 μm, compaction pressure 200 MP and sintering temperature 850 °C. ....	105
Fig. 4. 8: Variations of a) volumetric and b) gravimetric electroactive surface areas with fine Ni powder ratio at selected scan rates (see inset, V/s). Other parameters: pore size 425 – 710 μm, porosity 60%, compaction pressure 200 MP and sintering temperature 850 °C. ....	107
Fig. 4. 9: Variations of peak current with scan rate (bottom abscissa) or diffusion layer thickness (top abscissa) for different fine Ni powder ratios (pore size 425 – 710 μm, porosity 60%, compaction pressure 200 MP and sintering temperature 850 °C). ....	109
Fig. 4. 10: Schematic diagram showing how scan rate affects diffusion layer and electroactive surface area. ....	111

## Chapter 5

Fig. 5. 1: Deposition nominal current density versus deposition time for different concentrations of a) Ni(CH <sub>3</sub> COO) <sub>2</sub> and b) Ni(NH <sub>2</sub> SO <sub>3</sub> ) <sub>2</sub> in the solution with 1.5 M NH <sub>4</sub> Cl, under a deposition potential of -1.5 V over 150 s. ....	116
Fig. 5. 2: Deposition nominal current density versus deposition time for different concentrations of NH <sub>4</sub> Cl in the solution with 0.2 M Ni(CH <sub>3</sub> COO) <sub>2</sub> under a deposition potential of -1.5 V over 150 s. ....	117
Fig. 5. 3: Deposition nominal current density versus deposition time for different applied deposition potentials in a) 0.2 M Ni(CH <sub>3</sub> COO) <sub>2</sub> and b) 0.2 M Ni(NH <sub>2</sub> SO <sub>3</sub> ) <sub>2</sub> solutions with 1.5 M NH <sub>4</sub> Cl over 150 s. ....	119
Fig. 5. 4: Deposition nominal current density versus deposition time for three samples with different lengths of deposition time in a) 0.2 M Ni(CH <sub>3</sub> COO) <sub>2</sub> and b) 0.2 M Ni(NH <sub>2</sub> SO <sub>3</sub> ) <sub>2</sub> solutions with 1.5 M NH <sub>4</sub> Cl under a deposition potential of -1.5 V over 60 - 300 s. ....	121
Fig. 5. 5: SEM micrographs of the deposits produced with benchmark process condition (0.2 M Ni(CH <sub>3</sub> COO) <sub>2</sub> , 1.5 M NH <sub>4</sub> Cl, -1.35 V, 150 s) or with one	



parameter different from the benchmark condition: A) benchmark, B) 0.1 M Ni(CH <sub>3</sub> COO) <sub>2</sub> , C) 0.4 M Ni(CH <sub>3</sub> COO) <sub>2</sub> , D) 0.5 M NH <sub>4</sub> Cl, E) 1.0 M NH <sub>4</sub> Cl, F) -1.5 V, G) -1.7 V, H) 60 s, I) 300 s. Suffixes 1, 2, 3 denote different magnifications.....	124
Fig. 5. 6: SEM micrographs of the deposits produced with benchmark process condition (0.2 M Ni(NH <sub>2</sub> SO <sub>3</sub> ) <sub>2</sub> , 1.5 M NH <sub>4</sub> Cl, -1.7 V, 150 s) or with one parameter different from the benchmark condition: A) benchmark, B) 0.1 M Ni(NH <sub>2</sub> SO <sub>3</sub> ) <sub>2</sub> , C) 0.4 M Ni(NH <sub>2</sub> SO <sub>3</sub> ) <sub>2</sub> , D) -1.9 V, E) -2.1 V, F) 100 s, G) 200 s. Suffixes 1, 2, 3 denote different magnifications.....	132
Fig. 5. 7: Variation of real surface area of the DHBT porous Ni with changing process parameters in the Ni(CH <sub>3</sub> COO) <sub>2</sub> solution. Levels 1, 2 and 3 correspond to 0.1, 0.2 and 0.4 M Ni(CH <sub>3</sub> COO) <sub>2</sub> ; 0.5, 1 and 1.5 M NH <sub>4</sub> Cl; -1.35, -1.5 and -1.7 V deposition potential; 60, 150 and 300 s deposition time. ....	137
Fig. 5. 8: Variation of real surface area of the DHBT porous Ni with changing process parameters in the Ni(SO <sub>3</sub> NH <sub>2</sub> ) <sub>2</sub> solution. Levels 1, 2 and 3 correspond to 0.1, 0.2 and 0.4 M Ni(SO <sub>3</sub> NH <sub>2</sub> ) <sub>2</sub> ; -1.7, -1.9 and -2.1 V deposition potential; 100, 150 and 200 s deposition time. ....	137

## Chapter 6

Fig. 6. 1: Mass transfer performance, <i>kA</i> of the LCS porous Ni as a function of fine Ni powder ratio at different electrolyte flow velocities.....	145
Fig. 6. 2: Mass transfer performance of the LCS/DHBT porous Ni as a function of deposition time under different deposition potentials of -1.35, -1.5 and -1.7 V and at different electrolyte flow velocities of (a) 1.32 cm/s, (b) 2.22 cm/s, (c) 4.38 cm/s and (d) 6.6 cm/s.....	149
Fig. 6. 3: Logarithmic plots of the mass transfer performance, <i>kA</i> , versus electrolyte flow velocity for the LCS porous Ni samples manufactured with different fine Ni contents. ....	151
Fig. 6. 4: Logarithmic plots of the mass transfer performance, <i>kA</i> , versus the electrolyte flow velocity for the LCS/DHBT porous Ni samples manufactured under different deposition potentials of (a) -1.35 V, (b) -1.5 V and (c) -1.7 V, at different deposition times.....	154

## Chapter 7

Fig. 7. 1: Cyclic voltammograms of the a) Ni plate electrode, b) the LCS porous Ni electrode (porosity: 80%, pore size: 710 - 1000 μm) and c) the LCS/DHBT porous Ni electrode (1.5 M NH <sub>4</sub> Cl and -1.7 V deposition potential) in 0.1 M KOH and 0.5 mM glucose solution at scan rates of 25 – 300 mV/s.....	163
--	-----

Fig. 7. 2: Relationship between anodic peak current density and potential shift for the plate, LCS and LCS/DHBT Ni electrodes. ....	165
Fig. 7. 3: Variations of current density with square root of scan rate for the three different Ni electrodes.....	168
Fig. 7. 4: Current density as a function of glucose concentration for LCS/DHBT electrodes manufactured with different NH <sub>4</sub> Cl concentrations of 0.5, 1 and 1.5 M in the electrolyte at a deposition potential of a) -1.35 V, b) -1.5V and c) -1.7 V. ....	172
Fig. 7. 5: Current density as a function of glucose concentration for LCS/DHBT electrodes manufactured with a) 0.5 M, b) 1 M and c) 1.5 M NH <sub>4</sub> Cl in the electrolyte at different deposition potentials of -1.35, -1.5 and -1.7 V. ...	176
Fig. 7. 6: Anodic peak current density as a function of glucose concentration for the plate, LCS and LCS/DHBT Ni electrodes. ....	179
Fig. 7. 7: Anodic peak current potential as a function of glucose concentration for the plate, LCS and LCS/DHBT Ni electrodes. ....	181

# Content

Abstract.....	i
Declaration.....	v
Acknowledgements.....	vi
List of Publications.....	vii
List of Symbols.....	viii
List of Tables.....	xi
List of Figures.....	xi
Chapter 1 Introduction.....	1
1.1 Background of Research.....	1
1.2 Project Aim and Objectives.....	4
1.3 Structure of Thesis.....	5
Chapter 2 Literature Review.....	8
2.1 Introduction to Porous Metals.....	8
2.2 Manufacturing Methods for Open-cell Porous Metals.....	9
2.2.1 Liquid State Process.....	11
2.2.1.1 Direct Foaming.....	12
2.2.1.2 Space Holder Casting.....	14
2.2.1.3 Investment Casting.....	17
2.2.1.4 Spray Forming.....	19
2.2.2 Solid State Process.....	19
2.2.2.1 Powder Metallurgy Process.....	20
2.2.2.2 Space Holder Process.....	23
2.2.3 Vapour State Process.....	23
2.2.3.1 Chemical Vapour Deposition (CVD).....	24
2.2.3.2 Physical Vapour Deposition (PVD).....	26
2.2.4 Ionic State Process.....	29
2.2.4.1 Electroless Plating Process.....	29
2.2.4.2 Electroplating Process.....	30
2.2.5 Other Methods.....	32
2.2.6 Lost Carbonate Sintering (LCS).....	33
2.2.7 Dynamic Hydrogen Bubble Template (DHBT).....	35
2.3 Properties of Porous Metals.....	37
2.3.1 Surface Area.....	37
2.3.1.1 Electrochemical Measurement Method.....	38
2.3.1.1.1 Double Layer Capacitance Method.....	39
2.3.1.1.2 Hydrogen Adsorption Method.....	41
2.3.1.1.3 Underpotential Deposition (UPD) Method.....	44
2.3.1.1.4 Peak Current Method.....	46
2.3.1.2 Effect of Structural and Processing Parameters on Surface Area.....	48
2.3.2 Mass Transfer Performance.....	51

2.4 Electrochemical Applications .....	56
2.4.1 Electrochemical Glucose Sensors .....	57
2.4.2 Electrochemical Batteries .....	59
2.5 Summary .....	65
Chapter 3 Experimental Methods.....	66
3.1 Introduction .....	66
3.2 Preparation of LCS Porous Ni .....	66
3.2.1 Raw Materials.....	67
3.2.2 Mixing and Compaction .....	68
3.2.3 Sintering and Dissolution.....	69
3.2.4 Taguchi Design in the Manufacture of LCS Porous Ni Samples .....	70
3.3 Preparation of DHBT and LCS/DHBT Porous Ni .....	72
3.3.1 Raw Materials.....	72
3.3.2 Electro-deposition.....	73
3.4 Measurement of Electroactive Surface Area.....	77
3.4.1 Experimental Apparatus .....	77
3.4.2 Procedure of Measurement.....	78
3.5 Measurement of Real Surface Area.....	80
3.6 Measurement of Mass Transfer Performance.....	81
3.6.1 Experimental Apparatus .....	81
3.6.2 Determination of Mass Transfer Performance .....	82
3.7 Correlation between Peak Current and Glucose Concentration .....	84
3.8 Error and Uncertainty .....	85
Chapter 4 Real and Electroactive Surface Areas of LCS Porous Ni .....	87
4.1 Introduction .....	87
4.2 Surface Morphology.....	87
4.3 Effect of Processing Parameters on Real Surface Area .....	97
4.4 Effect of Processing Parameters on Electroactive Surface Area .....	100
4.5 Effect of Fine Ni Powder ratio on Real Surface Area .....	103
4.6 Effect of Fine Ni Powder ratio on Electroactive Surface Area .....	105
4.7 Summary .....	112
Chapter 5 Real Surface Area of DHBT Porous Ni.....	114
5.1 Introduction .....	114
5.2 Effect of Deposition Condition on Current Density.....	114
5.3 Effect of Deposition Condition on Surface Morphology.....	122
5.3.1 Ni(CH <sub>3</sub> COO) <sub>2</sub> Solution.....	122
5.3.2 Ni(SO <sub>3</sub> NH <sub>2</sub> ) <sub>2</sub> Solution .....	130
5.4 Effects of Deposition Condition on Real Surface Area.....	135
5.4.1 Type of Ni Salt .....	136
5.4.2 Concentration of Ni Salt.....	138
5.4.3 Concentration of H <sup>+</sup> Source.....	139
5.4.4 Deposition Potential.....	140
5.4.5 Deposition Time.....	141

5.5 Summary .....	142
Chapter 6 Mass Transfer Performance of LCS and LCS/DHBT Porous Ni..	144
6.1 Introduction .....	144
6.2 Effect of Fine Ni Powder ratio in LCS .....	145
6.3 Effect of Deposition Potential and Time in LCS/DHBT .....	146
6.4 Effect of Flow Velocity .....	150
6.4.1 Fine Ni Powder ratio in LCS .....	150
6.4.2 Deposition Potential and Time in LCS/DHBT .....	153
6.5 Summary .....	156
Chapter 7 Relationship between Current and Glucose Concentration for LCS/DHBT Ni Electrodes .....	158
7.1 Introduction .....	158
7.2 Electroactive Surface Area .....	159
7.3 Effect of Scan Rate on Current-Potential Profile .....	161
7.4 Effects of Manufacturing Parameters on Current-Concentration Relationship .....	169
7.4.1 Effect of Concentration of $\text{NH}_4\text{Cl}$ .....	169
7.4.2 Effect of Deposition Potential .....	172
7.5 Comparison with Other Ni Electrodes .....	178
7.6 Summary .....	186
Chapter 8 Conclusions and Future Work .....	187
8.1 Conclusions .....	187
8.1.1 Surface Area of LCS Porous Ni .....	187
8.1.2 Surface Area of LCS/DHBT Porous Ni .....	188
8.1.3 Mass Transfer Performance of LCS and LCS/DHBT Porous Ni Electrodes .....	189
8.1.4 Relationship between Current and Glucose Concentration ....	189
8.2 Future Work .....	191
8.2.1 Surface Area of Porous Metals .....	191
8.2.2 Mass Transfer Performance .....	192
8.2.3 Electrochemical Sensors .....	193
References .....	194
Appendixes .....	214

## Chapter 1 Introduction

### 1.1 Background of Research

Open-cell porous metals have received considerable attention in electrochemical fields in recent years due to their high specific surface area, fast kinetics of catalytic activity, good mechanical properties, and mass transfer performance (Ashby 2000, Banhart 2001, Zhang et al. 2011). The open-cell porous metals provide a large number of active sites on the surface for reactions due to their high surface area and, therefore, a high energy generation and storage in the porous metal electrode. Such material electrodes increase the sensitivity and accuracy of electrochemical detection.

Lost Carbonate Sintering (LCS) is a space holder powder metallurgy technique developed by Zhao et al. (2005). The porous metals manufactured by the LCS method have the advantages of high surface area, controllable porous structure, high mass transfer coefficient and good mechanical strength (Zhu and Zhao 2017, Diao et al. 2015, Zhang et al. 2008). The manufacturing process of LCS includes four steps. 1) Metal powder and  $K_2CO_3$  powder are blended together with a ratio pre-calculated according to the intended porosity. 2) A hydraulic press applies a compaction pressure on the powder mixture to form a preform. 3) The compacted preform is transferred to a furnace and sintered at a temperature range of 850-950°C over a few hours. 4) The space holder  $K_2CO_3$  is removed by soaking the sintered sample in hot water. A considerable number

of studies on the LCS porous metals have been conducted. However, their surface areas are still limited and there is a large room for improvement in this aspect, especially in terms of mass transfer and electrochemical detection performance.

Dynamic Hydrogen Bubble Template (DHBT) is an electrodeposition method developed by Marozzi et al. (2000) for fabricating porous metals. The metal crystals and hydrogen bubbles precipitate together on the surface of the cathode at an overpotential. A metal deposit forms on the electrode substrate while the hydrogen bubbles form micropores in the deposit. This fabrication process is very simple and economic and the porous metals manufactured by this technique have a high surface area and excellent electrocatalytic activity (Herraiz-cardoona et al. 2012). However, the as-fabricated porous metals are hard to use without a substrate because of their poor mechanical strength. Moreover, the bubbles coalesce together with increasing deposition time to form larger pores. Hence, the size of the DHBT porous metal is a significant limitation.

In this study, a new composite LCS/DHBT porous Ni is fabricated by combining the LCS and DHBT processes to overcome the limitations of these two manufacturing processes, which has a porous structure with both high surface area and superior 3D porous structure. The effects of the manufacturing

parameters on the surface area, the mass transfer performance and the glucose detection performance of the LCS and LCS/DHBT porous Ni are investigated.

Mass transfer is an important factor for porous metals in an electrochemical application, because it determines the reaction speed of the electrochemical process (Brown et al. 1992). The main methods to improve the mass transfer performance of porous metals include increasing the surface area of the electrode, increasing the mass transfer coefficient and increasing the fluid flow velocity (Recio et al. 2013, Zhu et al. 2017).

Porous metal electrodes have higher mass transfer coefficients than solid plate electrodes (Zhu 2018, Diao et al. 2015). However, if the tortuosity of the porous electrode is too high, a powerful pump is required to overcome the high pressure drop inside the electrode (Zhu and Zhao 2017). Increasing the electrolyte flow rate can change the flow state from laminar to turbulent flow, which can improve the mass transfer performance (Recio et al. 2013, Griffiths et al. 2005). However, when the flow rate is beyond 33 cm/s, the mass transfer performance no longer increases (Griffiths et al. 2005). In addition, high flow rates require high pumping powers and stronger electrodes. However, increasing the surface area of the electrode improves the mass transfer performance without causing any pressure drop issue.



Non-enzyme electrochemical sensors have attracted much attention in recent years as a supplement to enzyme sensors. Ni-based electrodes are one potential candidate for accuracy and economic considerations. In this study, the LCS and LCS/DHBT porous Ni samples are assessed for electrochemical non-enzyme glucose analysis. The relationship between the current and the glucose concentration in typical detection ranges is investigated. The sensitivity, limit of detection (LOD) and linear range are studied and compared to the other Ni-based electrodes in the literature.

## **1.2 Project Aim and Objectives**

The aim of this project is to study the effects of the manufacturing parameters of the LCS and DHBT processes on the surface area, the mass transfer performance and the relationship between the current and glucose concentration of the LCS and LCS/DHBT porous Ni. The effects of parameters of the LCS process, including pore size, porosity, fine Ni powder ratio, compaction pressure and sintering temperature, on surface area and mass transfer performance are studied. The parameters of the DHBT process studied include type of Ni salt, concentration of Ni salt, concentration of H<sup>+</sup> source, deposition potential and deposition time.

The objectives are:

- To measure the surface areas of the LCS porous metals manufactured with different parameters (pore size, porosity, fine Ni powder ratio, compaction pressure and sintering temperature).
- To measure the surface areas of the LCS/DHBT porous metals manufactured with different parameters (type of Ni salt, concentration of Ni salt, concentration of H<sup>+</sup> source, deposition potential and deposition time).
- To measure the mass transfer performance (product of mass transfer coefficient and active electrode area) of the LCS porous Ni samples manufactured with different fine Ni powder ratios and of the LCS/DHBT porous Ni samples manufactured with different deposition potentials and times.
- To correlate the current with glucose concentration for the Ni plate, the LCS porous Ni and the LCS/DHBT porous Ni electrodes in electrochemical cyclic voltammetry.

### **1.3 Structure of Thesis**

Chapter 2 is a review of the literature relevant to the research of this study, including the manufacture methods, properties, characterization techniques and applications of porous metals. The principles of electrochemical

measurement of surface area are introduced. The electrochemical applications of open-cell porous metals are briefly reviewed.

Chapter 3 describes the details of the fabrication processes of the porous metal samples used throughout the PhD project. The procedures for the electrochemical measurements of the surface area, mass transfer performance and current-glucose relationship are presented. The chemical reagents and equipment used for the measurements are also described.

Chapter 4 presents the results of the surface areas of the LCS porous metals and discusses the effects of the manufacturing parameters, including pore size, porosity, fine Ni powder ratio, compaction pressure and sintering temperature.

Chapter 5 presents the results of the surface areas of the DHBT porous Ni and discusses the effects of the manufacturing parameters, including type of Ni salt, concentration of Ni salt, concentration of H<sup>+</sup> source, deposition potential and deposition time.

Chapter 6 presents the results of the mass transfer performance of the Ni plate, the LCS porous Ni and the LCS/DHBT porous Ni samples. The effect of the fine Ni powder ratio in LCS porous Ni, the effects of the deposition potential and

deposition time in LCS/DHBT porous Ni, and the effect of electrolyte flow rate on the mass transfer performance are discussed.

Chapter 7 presents the results on the correlations between the current and glucose concentration of the Ni plate, the LCS porous Ni and the LCS/DHBT porous Ni samples. The effects of the scan rate, deposition potential and deposition time in LCS/DHBT porous Ni on the correlation are analysed. The linear range, LOD and sensitivity of the plate, LCS and LCS/DHBT Ni electrodes are compared to the Ni-based electrodes reported in the literature.

Chapter 8 presents the conclusions drawn in this thesis and the recommendations and directions for future research.

## **Chapter 2 Literature Review**

### **2.1 Introduction to Porous Metals**

Porous metals are multi-functional materials and have received much attention in industry over the past few decades. They can be classified into two types, closed-cell and open-cell, according to the pore structure. As the names suggest, closed-cell means the pores inside the porous media are sealed and the pores in the open-cell porous media are interconnected.

The first closed-cell porous metal was manufactured by a gas injection method, developed by Meller in 1926 (Ashby 2000). An inert gas is injected into a molten metal and with the solidification of the metal, bubbles are left inside. Closed-cell metals can absorb a large amount of impact energy through plastic deformation. Hence, they are applied widely in structural and functional products, like crash boxes and buffer material in vehicles for passenger safety (Zhang and Zhao 2008). Closed-cell porous metals have high mechanical strength and lightweight, which are highly desirable for some aerospace products to reduce the self-weight of aircraft.

Open-cell porous metals have an interconnected porous structure, which permits fluids to flow through the media. Hence, they have applications in many fields where closed-cell porous metals are not applicable. Open-cell porous

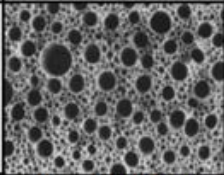
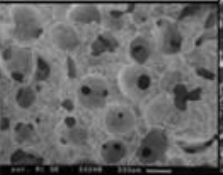
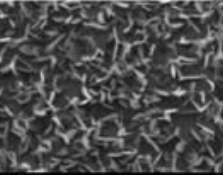
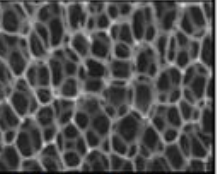
metals have the potential for applications in high-temperature filtration, heat exchange and flow diffusion, due to their high surface area and good mass/heat transfer performance (Kleperis et al. 2001, Kieback et al. 2003, Nart et al. 2003). Their applications are expanding rapidly in recent years. Recently, open-cell porous metals have been employed in various electrochemical applications, such as current collectors, battery electrodes and electrochemical sensors (Hamnett 1997, Zhang et al. 2009, Niu et al. 2014, Li et al. 2015, Zhu and Zhao 2017). They are also excellent structural-functional materials, as they can provide a large amount of active site and space to carry nano-active materials such as metal oxides/hydroxides for different requirements, which can be deposited onto the surface of the porous matrix by physical, chemical and other manufacturing techniques (Niu et al. 2014, Li et al. 2015).

## **2.2 Manufacturing Methods for Open-cell Porous Metals**

A range of techniques has been developed for manufacturing porous metals in the last few decades (Dukhan 2012). Because open-cell porous metals have numerous advantages in some industrial applications, this section provides a review of the manufacturing methods for open-cell porous metals that have been reported or are currently employed in the industry. Manufacturing methods for closed-cell porous metals are not discussed here because this project is focused on open-cell porous metals.

The manufacturing methods for porous metals can be classified by the state of the metal during manufacturing, namely liquid, solid, vapour or ionic state processes (Banhart 2001, Dukhan 2013). Liquid state manufacturing uses molten metals and is generally carried out by casting techniques. Solid-state manufacturing usually uses metallic powders and fibers as raw materials, followed by sintering. In a vapour state process, a metal vapour is generated by sputtering and deposits on a sacrificial preform which is removed to leave voids and pores. In an ionic state method, metal ions in the electrolyte are deposited on a preformed substrate by a redox reaction. Table 2.1 presents the characteristics of these classes of manufacturing methods using one example for each category.

Table 2. 1 Characteristics of different fabrication methods for porous metals  
(Banhart 2001).

Class	Liquid State	Solid State	Vapour State	Ions State
<b>Example</b>	Solid-gas eutectic solidification	Space holder method	Chemical vapour deposition (CVD)	Electrodeposition
<b>Pore Structure</b>				
<b>Pore Type</b>	Closed-cell pore	Open-cell pore	Open-cell pore	Open-cell pore
<b>Porosity Range</b>	5-95%	20-90%	70-98%	80-99%
<b>Applicability</b>	Copper, Nickel, Aluminum etc.	Copper, Nickel, Aluminum, Titanium, Metallic Alloys etc.	Silver, Gold, Nickel etc.	Nickel, Copper, Zinc, Gold, Platinum etc.
<b>Pros</b>	Directional pores	Good mechanical strength Pore size and porosity controllable	Pore morphology can be tailored	Pore structure tailorable
<b>Cons</b>	Closed-cell pores Process need to be carefully controlled	Residual of filler Low surface area	The porosity range is high High production costs	Porosity range is relatively high Short-life of electrolytes Waste electrolytes need to be carefully treated
<b>References</b>	Shapovalov 2007	Ashby 2000	Queheillalt et al. 2001	Liu et al. 2001

## 2.2.1 Liquid State Process

Liquid state processes for the manufacture of open-cell porous metals may involve pouring molten metal into a mould with a removable sacrificial preform, direct foaming by injecting gases into the molten metal or using a gas-releasing blowing agent to create a cellular structure, followed by metal solidification. The



main methods include direct foaming, space holder casting, investment casting and spray foaming. This section describes these fabricating processes and discusses their characteristics.

### **2.2.1.1 Direct Foaming**

The direct foaming process is a widely used fabrication method because it provides economic and ecological products compared to other fabrication processes (Luthardt et al. 2015). In this process, the air is employed to generate the porous structure inside the matrix. As shown in Fig. 2.1, the melt is input into a cylinder by a peristaltic pump (1); the gas (2) is injected into the melt from and through the porous membrane (3) static mixing elements (4) provide a good distribution of pores by mixing the melt with the air. The foam solidifies after leaving the cylinder and produces an open-cell metal foam. The rheological parameter is a significant factor in the direct foaming process. To ensure foam stability, silicon carbide, aluminum oxide or magnesium oxide particles are added to the molten metal to enhance the viscosity of the melt, which can hinder the mobility of air bubbles. Fig. 2.2 represents a typical directly foamed open-cell porous structure. The foam fabricated by this method has a porosity range of 70%-95% with a pore size in the range of 0.1-6 mm.

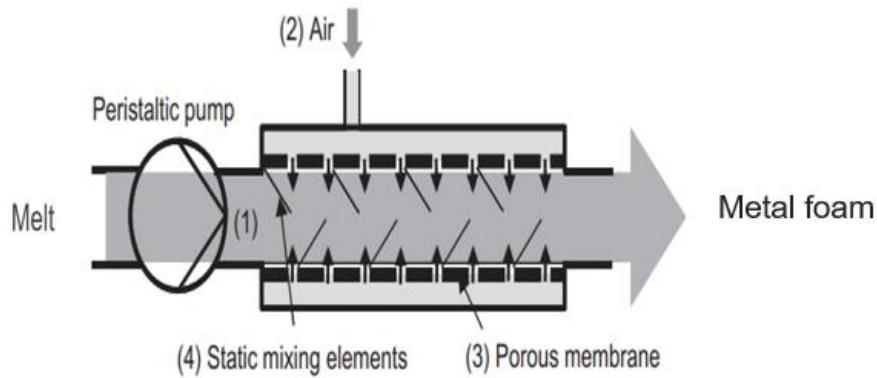


Fig. 2. 1: Schematic of the direct foaming device (Luthardt et al. 2015).

The direct foaming technique has many advantages. It does not release a large amount of waste because it is a template-free process, which allows it to become a cost-effective, ecological and simple process. Moreover, it provides a process for the mass production of metal foam with low density. For example, products of 1.5 m wide and 15 cm thick were produced by a Canadian company and the production line delivered 1000 kg of the products per hour (Banhart 2001). However, the pore structure and distribution of the foam are difficult to be controlled. It is mainly suitable for the production of closed-cell foams.

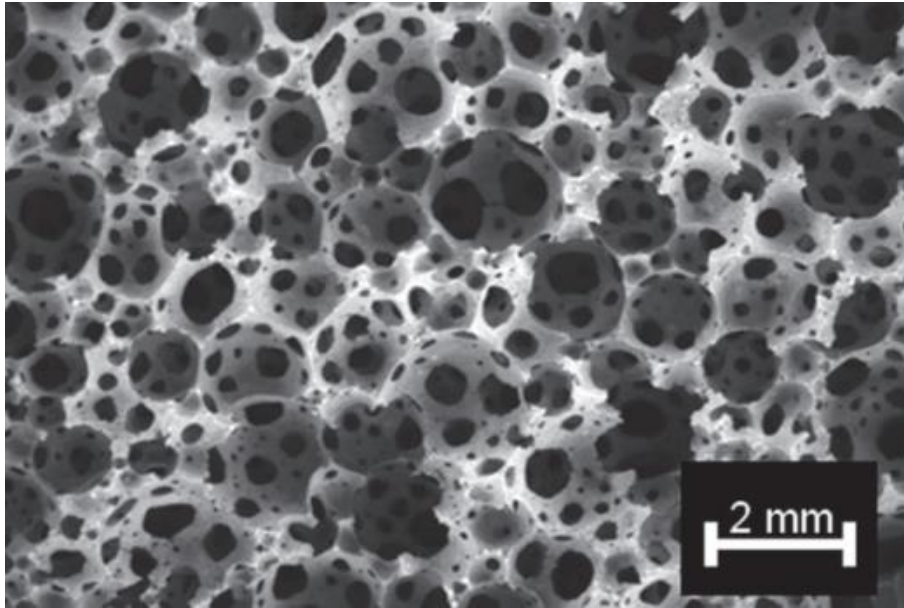


Fig. 2. 2: A typical directly foamed open-cell structure with big pores (Luthardt et al. 2015).

### **2.2.1.2 Space Holder Casting**

Porous metals can be formed by casting molten metal in a mould with a sacrificial space filler in particulate form. The molten metal is cast around a filler which is removed by thermal, dissolution or chemical treatment. To ensure that the filler can be eliminated completely, it should occupy a high proportion of space and the granules are interconnected. Many space filler materials have been developed, such as soluble salts, polymers, glasses and aluminum oxide hollow spheres (Banhart 2001, Chen et al. 1999, Grote et al. 1999, Thiele 1971). Fig. 2.3 represents a typical process of the space holder casting method. The space holders are first accumulated in a mould and preheated to a specific

temperature. The melt is then infiltrated into the space holder preform by external pressure. After the solidification of the molten metal, the space holders are removed by further treatment.

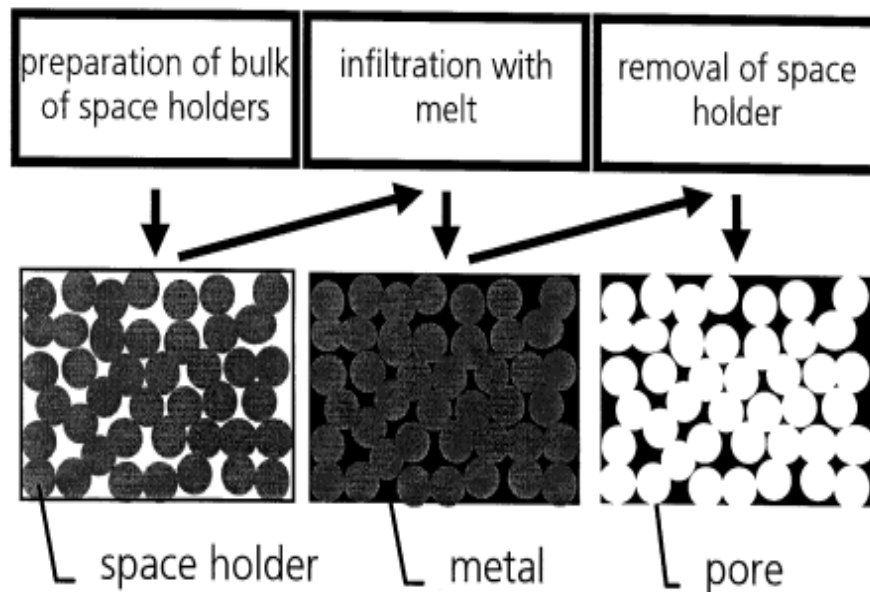


Fig. 2. 3: A typical process of space holder casting methods (Banhart 2001).

As a large number of space filler granules are stacked together and the melt may have a high viscosity and surface tension, it is difficult to cast around these granules. Defects are often present. A porous structure may even not be created. Negative pressure or vacuum is often needed to promote infiltration. Pre-heating of the mould and space holder is necessary to prevent the melt from solidifying before a complete cellular structure is formed.

A wide range of metals, such as copper, aluminium and zinc, can be processed by the space holder casting method. The pore size, porosity and pore distribution can be controlled by designing the shape, amount and size of the

space filler granules in this process, because the porous structure is a negative replica of the granules as shown in Fig. 2.4. The maximum porosity of the space holder casting products is up to 80%.

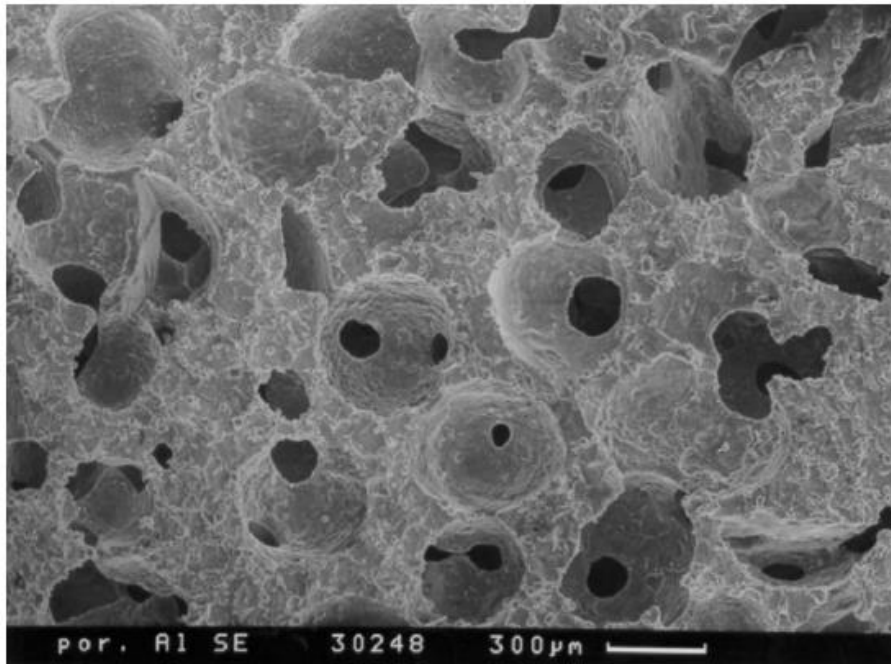


Fig. 2. 4: Cellular aluminium manufactured by a space holder process  
(Banhart 2001).

The space holder casting method provides uniform porous structures and low-density products with isotropic properties. It can also produce compound structures like sandwich structures, in which porous and dense regions are sandwiched into each another. For example, the products can have dense surfaces and porous cores. Threads can be machined in the dense part for connecting to other devices.

### 2.2.1.3 Investment Casting

Porous metals can be made by the investment casting method. A schematic process of the method is shown in Fig. 2.5. In this process, a removable polymer scaffold with interconnected cells is employed. The open-cell polymer scaffold is dipped in a slurry of high heat-resisting material like calcium carbonate in a container (Yosida et al. 1990). The container is vibrated to eliminate the bubbles trapped in the mixture. After the slurry is cured, the polymer scaffold is removed by a thermal treatment. The molten metal is poured into the mould formed by the removal of the polymer scaffold. An external pressure is usually applied to ensure the formation of a complete porous structure. The porous structure is obtained after the demoulding process, which is a replica of the polymer scaffold. Fig. 2.6 shows an open-cell aluminium foam made by the investment casting method.

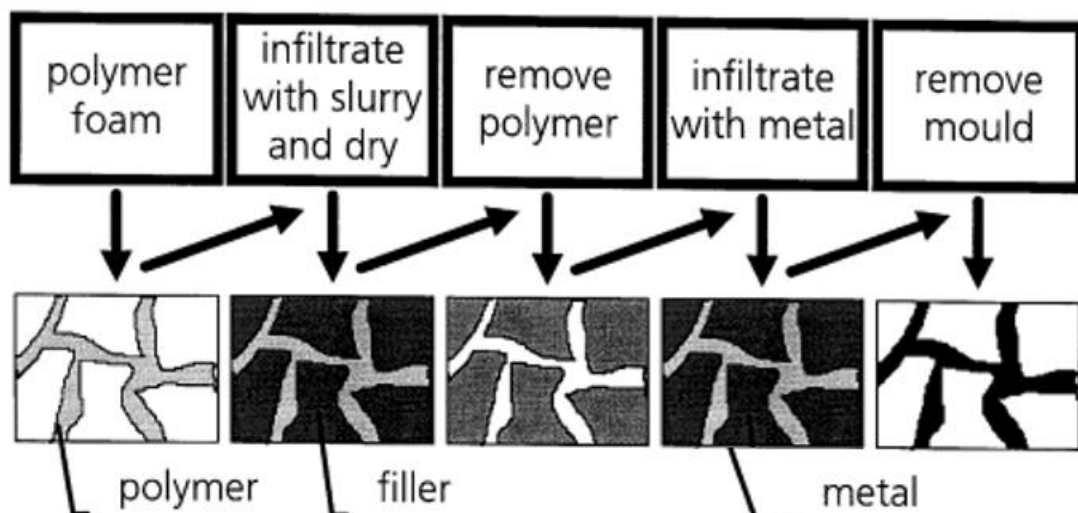


Fig. 2. 5: A schematic process of the investment casting (Banhart 2001).

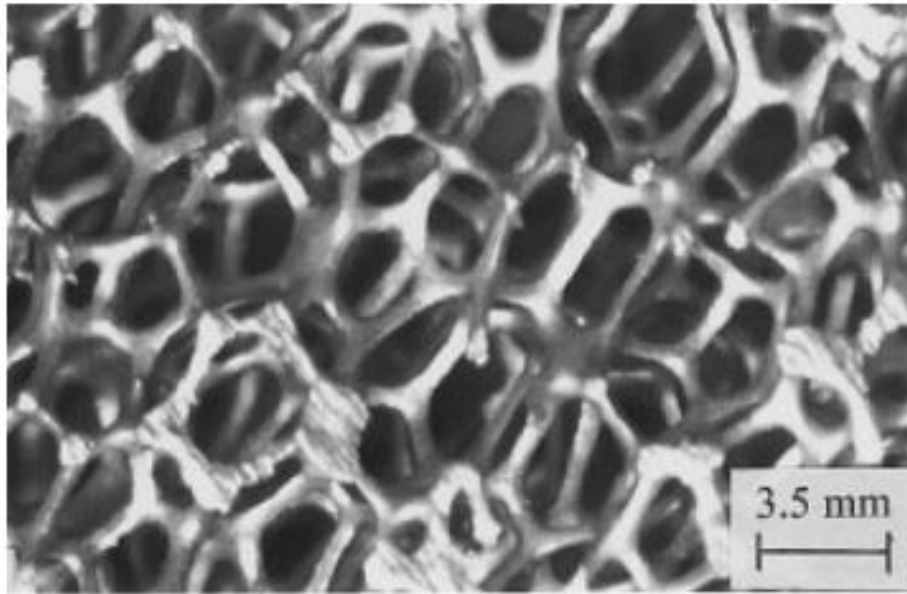


Fig. 2. 6: Micrograph of an aluminium foam produced by the investment casting method (Harte et al.1999).

The investment casting technique can be applied to most metals. The porosity is normally in the range of 80-97%. The cellular structure, cell size, and porosity can be tailored by choosing an appropriate polymer precursor. However, this method has some disadvantages. Firstly, each porous structure uses one mould. Secondly, the demoulding process is very time-consuming and it is difficult to avoid the occurrence of damages to the delicate parts of the structure during this process. Thirdly, it is difficult to ensure a completely filled filament, because the casing process is directional solidification. As the process is time and cost-consuming, the price of the as-manufactured structure is relatively high and the yield is low (Hintz et al. 1999, Moore 1999).

### 2.2.1.4 Spray Forming

Spray forming is also called the Osprey process. Fine molten metal droplets are formed by a spraying or atomizing process, travelled to the surface of a substrate and solidify on the surface to form a deposit (Barnhart 2001). The materials used in this process can be pure metals or alloys. Adding a decomposable powder agent into the process can release a large amount of gas in the deposit, which can create a porous structure, as shown in Fig. 2.7. Many porous alloy structures, including copper-zinc alloy and carbon steel, have been developed (Kelley et al. 1993, Barnhart et al. 1998). However, the pore generation of the spray foaming method is not uniform and the pores are not well interconnected. The maximum porosity is about 60%.

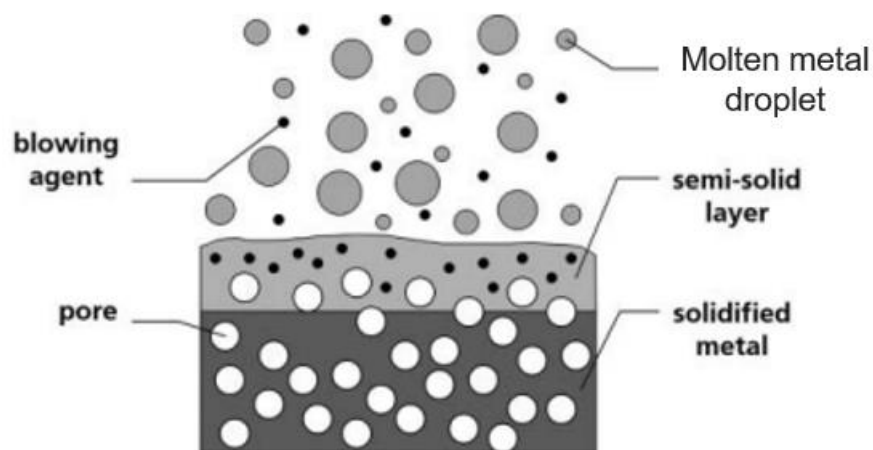


Fig. 2. 7: Schematic of pores generated in the spray foaming process

(Barnhart 2001).

### 2.2.2 Solid State Process



Solid-state processes are another pathway to fabricate porous structures. Different from the liquid-state processes, the materials used in the solid-state processes are not molten over the whole process and partly maintain their shape and morphology. Hence, the microstructure of the products made by these processes is markedly different. The raw materials are in powder form. The powder particles are connected by sintering, binder or other solid-state operations. The solid-state processes for manufacturing open-cell porous structures include powder metallurgy, foaming of slurries, the metal powder/binder process and the space holder process. The slurry foaming process is similar to the liquid process mentioned in section 2.2.1.1, except that molten metal is replaced with a metal slurry. This section introduces the two main solid-state processes.

### **2.2.2.1 Powder Metallurgy Process**

Powder metallurgy (PM) is a conventional solid-state manufacturing technique. With the development of modern PM techniques, this technology has been employed in commercial mass production (Upadhyaya 1997). It is simple, rapid, flexible, low-cost, and can be used to fabricate materials difficult to form by other techniques, such as high-melting-point metals. PM technology is widely used also because surface treatment is not necessary (Selcuk et al. 2010).

PM technology is particularly popular for manufacturing small components with

complex geometries. It has four main advantages (Dewidar et al. 2006):

- (1) Waste-free forming (does not need secondary operation);
- (2) Easy forming of high-melting hard-to-machine materials;
- (3) Homogeneous compositional distribution;
- (4) Appropriate porosity provides suitable strength.

Fig. 2.8 shows a schematic process of the PM method. The metal powder and the binder are blended and then compacted under a pressure to make a preform. The preform is sintered under a high temperature to form a metal component.

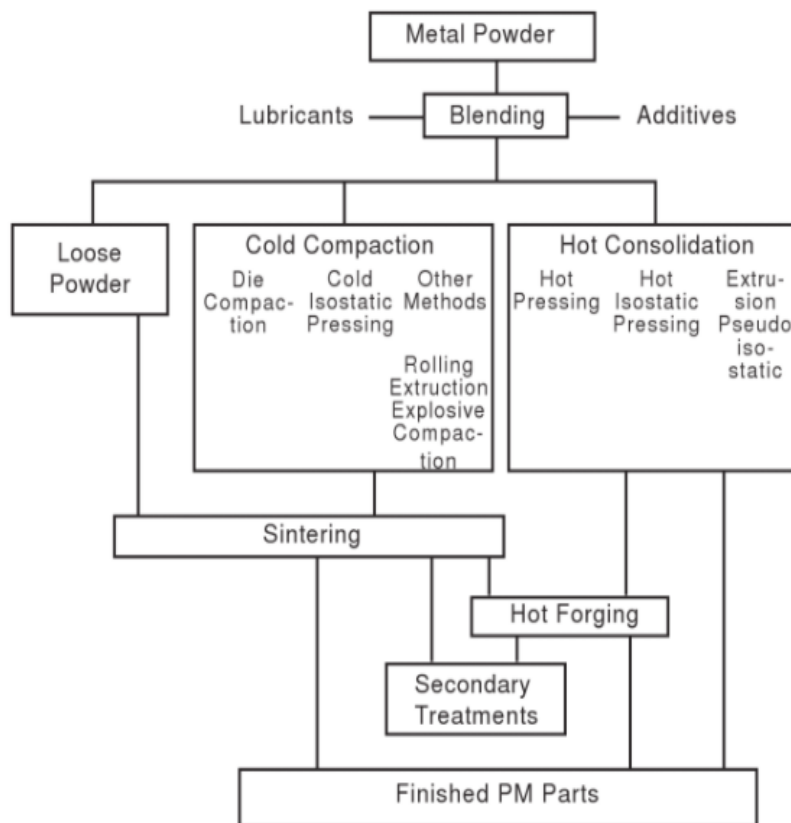


Fig. 2. 8: Basic steps of the PM process (Upadhyaya 1997).

The PM technique can be used to produce porous metals if a significant amount of porosity is left inside the metal matrix by controlling the manufacturing process. Fig. 2.9 demonstrates a typical porous bronze produced by the PM manufacturing method. The porous structure of the PM products is determined by the porosity of the compact, compact pressure and sintering temperature. Sintering reduces the porosity of the sintered preform due to the diffusion of metal atoms at high temperatures, normally occurring at a temperature over 50%-90% of the material's melting point to ensure that the powder is not fully densified (Ashby 2000). The porosity of loose-powder sintered porous metals is normally in the range of 40%- 60%, depending on the size and shape of the powder particles (Banhart 2001).

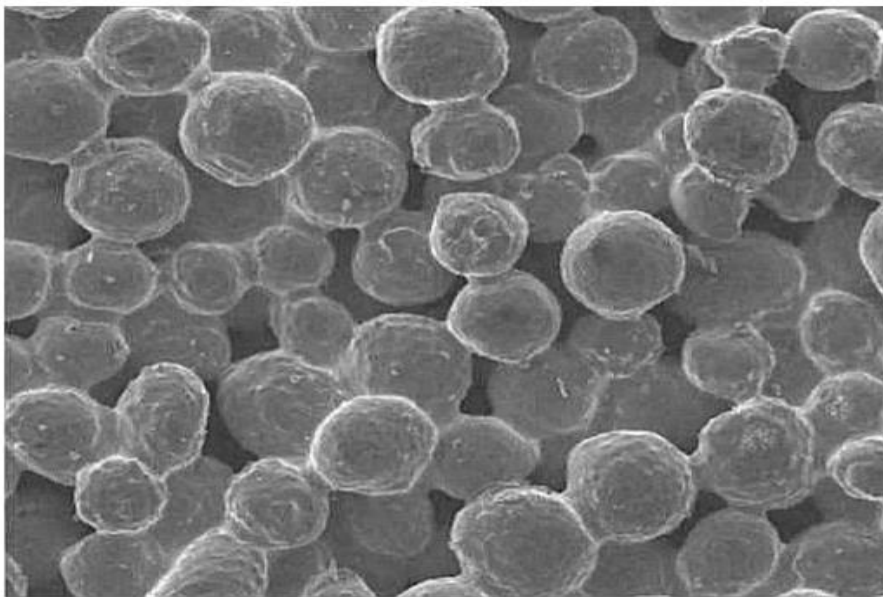


Fig. 2. 9: Loose powder sintered porous bronze (Eisenmann 1998).

### **2.2.2.2 Space Holder Process**

To increase the porosity of PM porous metals, space fillers can be used to form extra pores. The space holder powder is uniformly blended with the metal powder to make the preform. After sintering, the space holder is removed by thermal or leaching treatment, such as dissolution or decomposition, leaving pores inside the porous metal. Many space holder materials, such as carbonates, sodium chloride, carbamide, polystyrene, magnesium, saccharose and ice, have been used (Adamek et al. 2015, Arifvianto et al. 2014, Zhang and Zhao 2008, Papantoniou et al. 2018). The space holder material needs to be eliminated easily and not react with the metallic powder. The space holder process has a good control over porosity and pore size and is therefore more flexible than the traditional loose-powder sintering process.

### **2.2.3 Vapour State Process**

Metal or compound vapours can be sputtered or deposited onto sacrificial porous substrates to form porous metal structures by removing the substrates. The majority of pure metals and alloys have been successfully deposited by vapour deposition techniques (Sherman 1987, Park et al. 2001). There are two main vapour deposition techniques, which are chemical vapour deposition (CVD) and physical vapour deposition (PVD).

### 2.2.3.1 Chemical Vapour Deposition (CVD)

CVD is a deposition method that forms a dense film on the surface of a substrate in a chamber filled with evaporated target metal compounds. Several gaseous compounds react and deposit on the substrate surface to form a coating (Powell et al. 1966). There are three main ways of CVD, namely thermal decomposition, chemical synthesis and chemical transport reaction. Fig 2.10 shows a schematic diagram of a typical CVD reactor.

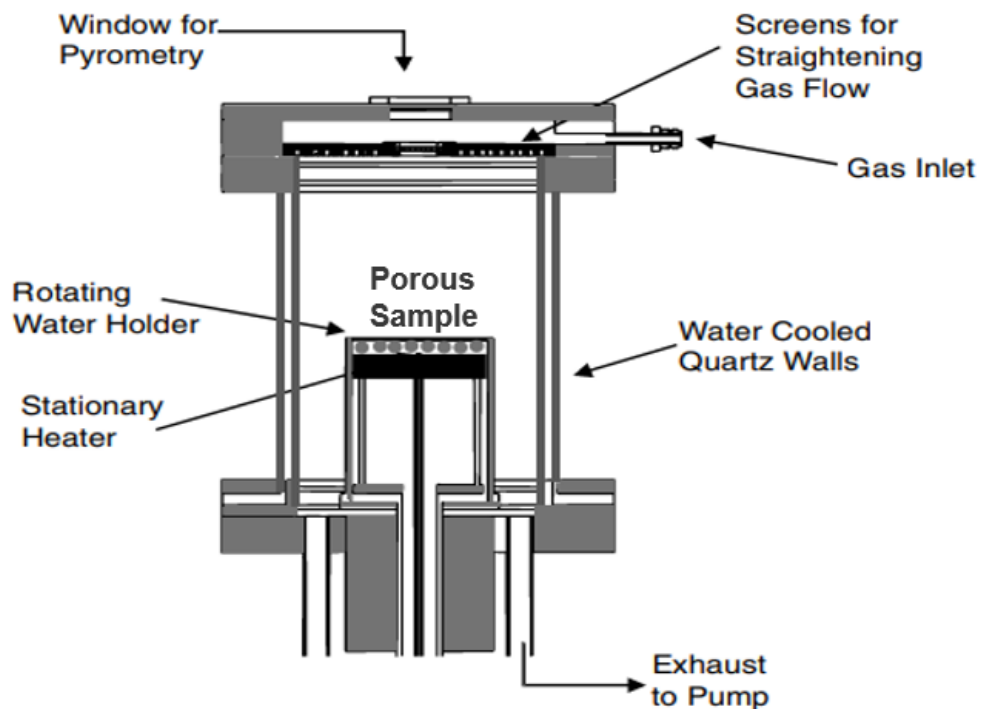


Fig. 2. 10: Schematic diagram of a typical CVD reactor (Park et al. 2001).

The principle of a thermal decomposition reaction is that a gaseous metal compound decomposes into the solid target product and a gaseous by-product when heated to a certain temperature. The reaction gas is introduced into a chamber furnace under a vacuum or inert atmosphere. The furnace

temperature is raised to the decomposition temperature of the compound to make it decompose, and the target metal is deposited on the substrate. The key to the thermal decomposition reaction lies in the selection of a suitable volatilization source and decomposition temperature. Fig 2.11 shows a typical Ni foam manufactured by this method.

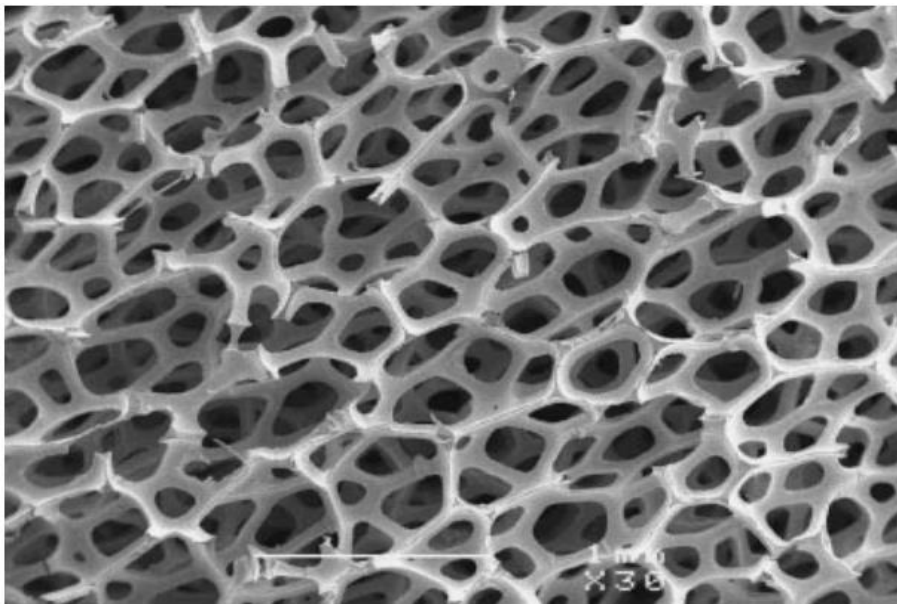


Fig. 2. 11: SEM micrograph of Inco Ni foam (Paserin et al. 2004).

Chemical synthesis is a process where a variety of reactive gases react with each other to produce a metal that deposits on the surface of a substrate to form a solid coating. Normally, several reaction gases are fed into a tube furnace under a vacuum or inert atmosphere. The furnace temperature is raised to facilitate the synthesis reaction on the substrate. The key to chemical synthesis are the selection of reaction agents and avoiding the formation of by-products.

The chemical transport reaction process uses the target product as a source and deposits it using an equilibrium reaction. The target metal first reacts with a gas to generate a gaseous compound, which is transported to the deposition zone at a temperature different from the volatilization zone by a carrier gas. The decomposition reaction deposits the source metal on the substrate.

The CVD processes can create fine porous metals with complex shapes and structures if a porous removable scaffold is used as the substrate. The porous structure obtained from the CVD process goes through a thermal treatment to eliminate the substrate and a porous metal structure is produced. The porous structure and morphology can be controlled by selecting the right polymer substrate. The porosity achieved can be up to 98% (Ashby et al. 2000). However, this process has to be operated in a high-temperature environment, which brings a great challenge to the substrate and equipment. In addition, gaseous metals can be harmful and toxic.

### **2.2.3.2 Physical Vapour Deposition (PVD)**

PVD is similar to CVD, except that the metal source is from the evaporation or sputtering of the target metal. It can be applied to most metals, alloys and even organic materials. It can be categorized into four types: vacuum evaporation, sputter deposition, arc vapour deposition and ion plating (Mattox 1999). The

differences between these techniques are shown in Fig 2.12.

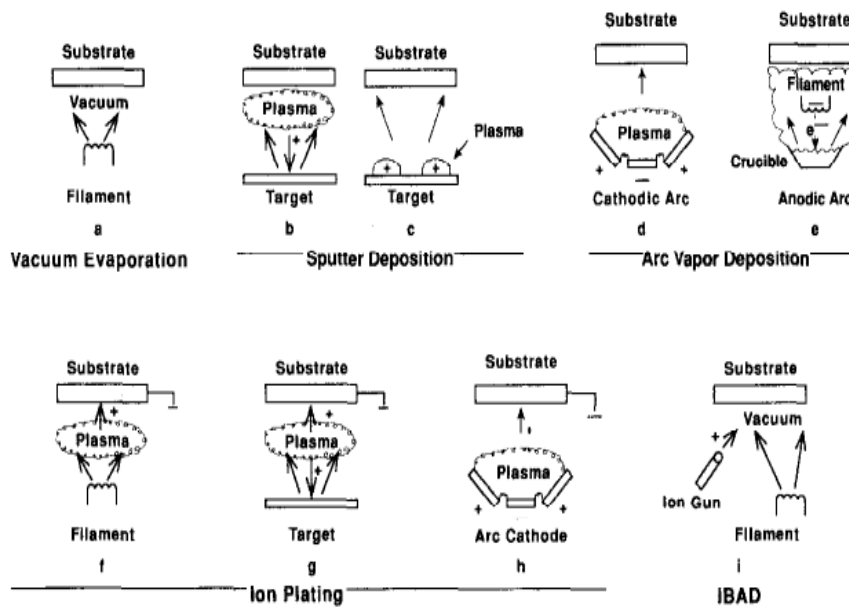


Fig. 2. 12: Various PVD processes: a) vacuum evaporation, b-c) sputter deposition, d-e) arc vapour deposition and f-i) ion plating (Mattox 1999).

Vacuum evaporation takes place in a vacuum or near vacuum condition. The material source is heated to form vaporized molecules which directly deposit on the surface of a substrate without contacting any contamination even gas. The material utilization of this method is relatively poor.

Sputter deposition is a non-thermal vaporization process. It uses atomic-sized energetic bombarding particles, generated and accelerated by plasma, to bombard the surface of a target, causing the ejection of the surface atoms by momentum transfer, which then deposit on a substrate (Mattox 1999). If a porous sacrificial substrate is used and is later removed by a heating process, a porous metal is formed. The production rate of sputter deposition is relatively



low compared to thermal evaporation. The flux distribution is difficult to control, which can cause a nonuniform coating in most simple plasma configurations. In addition, those bombarding particles that do not have enough energy to cause sputter-vaporization of target surface atoms will convert impact energy into thermal energy. This raises the temperature of the substrate, which may affect the quality of the products.

In the arc vapour process, a low-voltage high-current direct current (DC) is applied between a cathode and an anode in a low-pressure atmosphere to generate an arc, as shown in Fig. 2.13. The arc causes the local material to melt and vaporize to produce gaseous metal atoms.

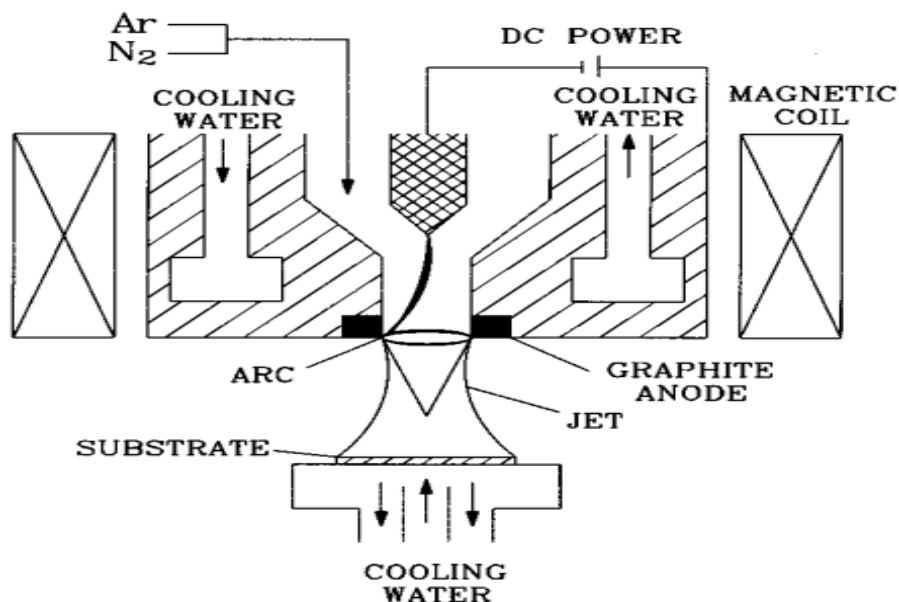


Fig. 2. 13: Schematic diagram of a typical arc PVD reactor (Yen et al. 1995).

Ion plating is another PVD process. The difference with the other PVD methods

is the bombarding source, which is usually an ion of inert or reactive gas. The high-energy bombarding ions are positively charged and are accelerated towards the substrate, which is at a negative potential concerning the bombarding ion particles. The energy of the bombarding ions is in the range of 50 – 300 eV to guarantee good properties of the deposit (Mattox 1999). The as-produced porous metals have a uniform thickness and a smooth surface morphology due to gas scattering and atomic peening effects and independence of the angle of incidence of the material source. However, uniform ion bombardment is hard to obtain. Furthermore, the bombarding ions can be incorporated into the coating and cause residual compressive stresses to influence the mechanical properties of the coating.

## **2.2.4 Ionic State Process**

Metals in their ionic state can be transported to porous substrates and form porous structures. The ionic state methods mainly include electroless plating (also called a chemical deposition) and electrodeposition (also called electroplating).

### **2.2.4.1 Electroless Plating Process**

A metal coating on a sacrificial foam substrate is formed in an aqueous solution

of a target metal salt. Both oxidation and reduction reactions take place in the electrolyte and metal deposits on the substrate by reduction. To meet the requirement of commercial batch production, the material of the sacrificial substrate needs to be mechanically processible and easy to be removed by dissolution or decomposition. The precursor is first coarsened in an acidic solution and then immersed into an electrolyte with noble ions to produce active catalytic centers for promoting the subsequent redox reaction. During deposition, the precursor is immersed in the pre-formulated electrolyte for several seconds for ion layer adsorption and reaction. Reducing agents (e.g. hydrazine) are used for the reduction of the metal ion on the surface of the substrate. (Nobari et al. 2016)

#### **2.2.4.2 Electroplating Process**

Electroplating is another electrodeposition method for porous metal production (Schwarzacher 2006, Gamburg et al. 2011). Same to other deposition methods, a coating is formed on a precursor, followed by removing the substrate. Different from electroless plating, the precursor in electroplating must be conductive. In the electroplating of metal, metallic ions ( $M^{n+}$ ) in the solution are reduced by obtaining electrons from the cathode and metal deposits on the surface of the cathode, while the anode is dissolved due to the oxidation reaction. The redox reactions are simply (Jeske et al. 1995):



The overall process of electrochemical deposition is complex. It includes mass transfer, charge transfer and crystallization. Mass transfer is the first step, where the electroactive species move to the surface of the cathode from bulk solution due to electrical potential difference with the anode. The metal ions are reduced and metal atoms are absorbed in the substrate surface by electron transfer. The crystals of the deposit grow step by step, as shown schematically in Fig. 2.14.

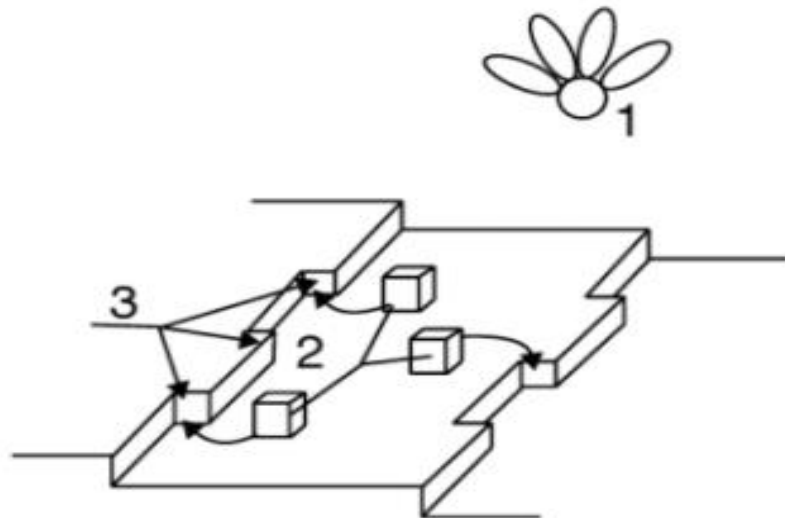


Fig. 2. 14: Fundamental steps of electrodeposition at an electrode surface, where 1 refers to the hydrated ions, 2 refers to the diffusion of ions to activated sites and 3 refers to the growth of the deposit (Schwarzacher 2006).

In electrodeposition, the properties and quality of the coatings can be controlled

by various manufacturing parameters and electrolyte conditions such as concentration of a solution, potential intensity/current density, operating temperature and pH of the solution (Gamburg et al. 2011, Schwarzacher 2006). In some cases, various compounds are added to the electrolyte to obtain a smooth and homogeneous metal surface. Heat treatment is applied in the deposition of most metals and alloys, as it can remove the surface stress in the deposits and improve the mechanical strength of the finished products. One disadvantage of electrodeposition, however, is that the electrolyte wastes can cause health and environmental issues and treatment of wastes must be strictly implemented.

### **2.2.5 Other Methods**

There are other pathways which are not mentioned above and can fabricate porous metals. For example, the chemical etching process can be employed to make porous metals (Erlebacher et al. 2001, Sieradzki et al. 2002). In a corrosive condition, metal surfaces are oxidized, especially where energy density is high. For alloys of metals with very different reactivities, chemical etching can remove only the metal with a higher reactivity rather than all of them. Such a process is called dealloying, which provides a new pathway to manufacturing nanoporous metal structures (Erlebacher et al. 2001, Sieradzki et al. 2002). The dealloying process is a corrosion process to selectively

dissolve electrochemically active elements, normally with a lower activity than hydrogen (e.g. zinc) in alloys. The corrosion reaction can be promoted by either a chemical reaction (acids or alkali etching) or an electrochemical reaction (anodizing). Fig 2.15 shows a typical porous structure produced by a dealloying method.

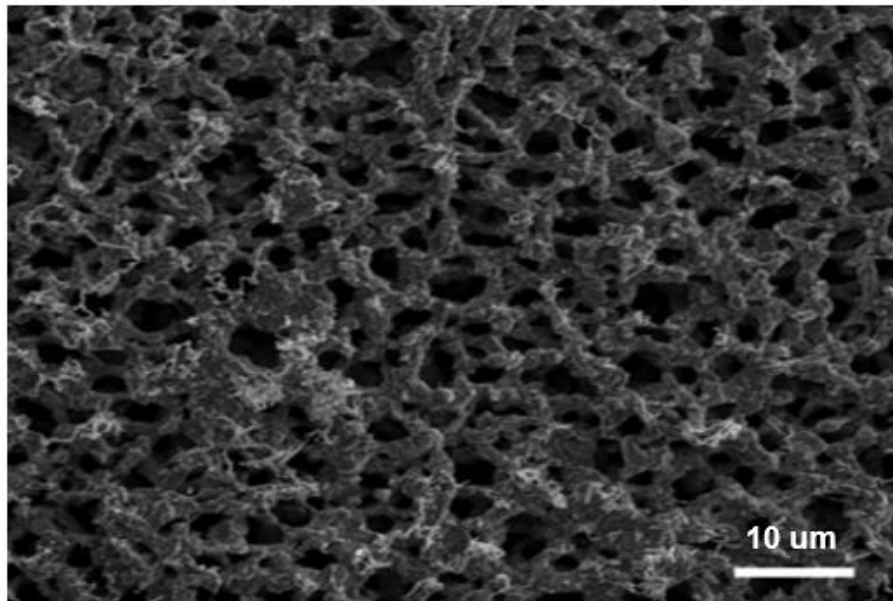


Fig. 2. 15: SEM macrograph of a dealloyed porous metal (Chen et al. 2013).

### **2.2.6 Lost Carbonate Sintering (LCS)**

Lost Carbonate Sintering (LCS) is one of the space filler manufacturing methods to fabricate porous metals, developed by Zhao et al. (2005). The LCS method employs  $K_2CO_3$  powder as the space filler material. Moistened  $K_2CO_3$  powder is well blended with a metallic powder at a volume ratio calculated according to the intended porosity. The mixture is then transferred to a container and compacted under a pressure, typically 200 MPa, to make the green preform.

The preform is then sent to a furnace and sintered at a high temperature for several hours. The pore fillers in the sintered preform are then removed by dissolving in water or decomposing in high temperature atmosphere to form a porous structure. Fig. 2.16 shows the LCS process schematically.

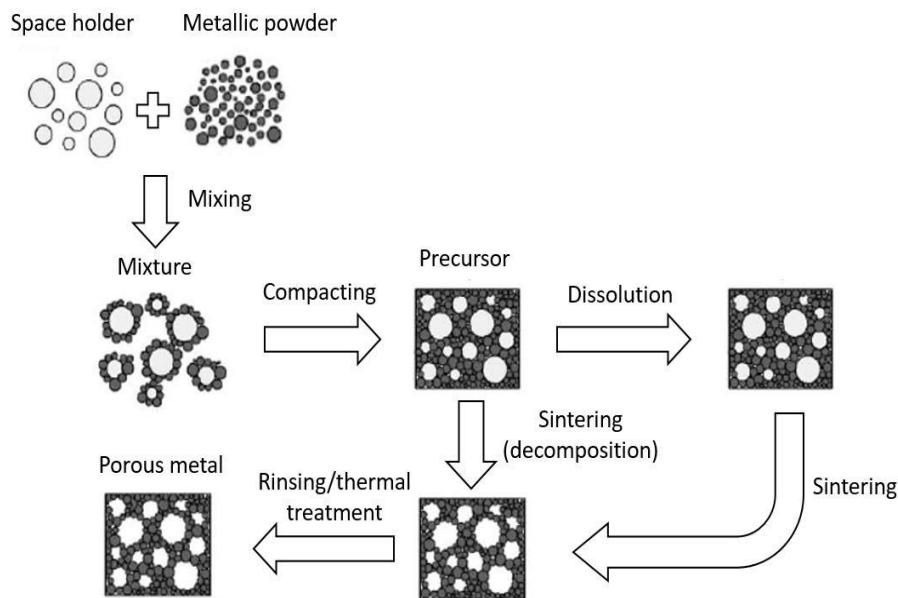


Fig. 2. 16: Schematic of the LCS process (Zhao et al. 2005).

$K_2CO_3$  is an ideal space filler for fabricating porous metals. It is very soluble in water, especially in hot water, with a solubility of 149.2 g per 100 mL in 100°C water (Haynes et al. 2016). This feature allows it to be fully eliminated from the porous matrix. The melting point of  $K_2CO_3$  is 891°C, which allows it to maintain a stable condition during the process without reacting with the metal (Haynes et al. 2016). At the same time, it provides strong support so the metal particles can form a strong bonding with each other. In addition,  $K_2CO_3$  does not release toxic substances during the high-temperature sintering process. Fig. 2.17 shows a typical SEM micrograph of an LCS porous metal.

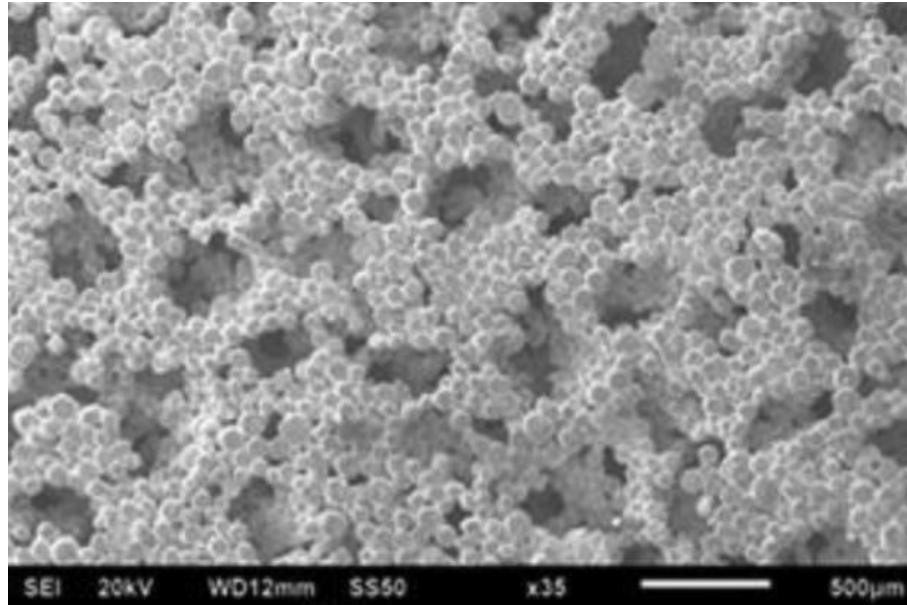


Fig. 2. 17: Porous copper produced by LCS method (Diao et al. 2015).

### **2.2.7 Dynamic Hydrogen Bubble Template (DHBT)**

The Dynamic Hydrogen Bubble Template (DHBT) method is one of the electrodeposition techniques (Shin et al. 2003, Li et al. 2007, Tong et al. 2009).

In the DHBT process, hydrogen evolution is intended and the bubbles play an important role in the production of a porous structure by acting as a dynamic soft template. As the electrolyte cannot enter the hydrogen bubbles, no metallic crystallization takes place in the bubbles and hence pores form. The pore size increases with deposition time because of the agglomeration of small gas bubbles, as shown schematically in Fig. 2.18. Even though the DHBT method provides even distribution and considerable micropores in the porous metals, the pore size of the porous structure cannot be controlled (Shin et al. 2003, Li et al. 2007).



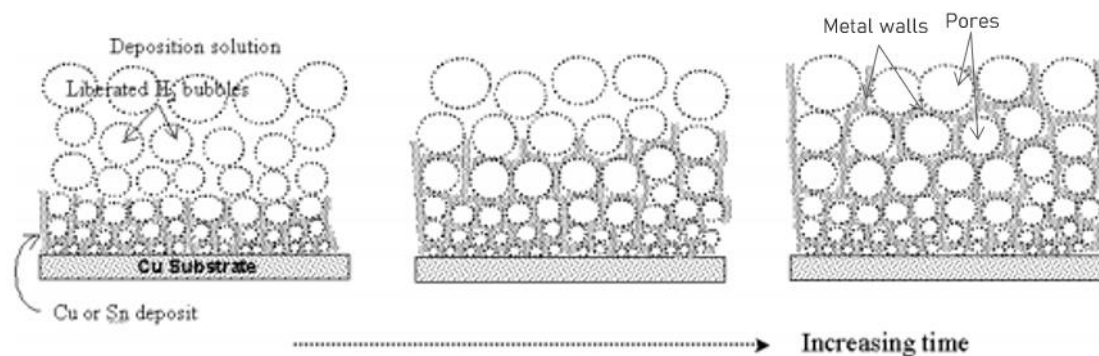


Fig. 2. 18: Schematic of DHBT for porous membrane production (Shin et al. 2003).

The surface morphology and pore structure of DHBT porous films depend on the processing parameters. The parameters include concentrations of metal salt and H<sup>+</sup> source, deposition potential and time, the value of solution pH and type and concentration of surfactant (Shin et al. 2003, Sengupta et al. 2018).

Deposition time has a significant effect on the morphology and pore structure of DHBT porous foams (Cherevko et al. 2010, Plowman et al. 2015). Increasing the deposition time, the foam wall gradually becomes thick. In addition, the hydrogen bubbles generated on the substrate surface have a long pathway to escape the porous film, which causes collision and agglomeration of bubbles, leading to the formation of big bubbles and pores.

DHBT porous metals have been used in electrochemical applications, due to their unique microporous structure and superior electrochemical properties. Hao et al. (2019) reported that the Oxygen Evolution Reaction (OER) property

of DHBT porous Ni electrodes is improved compared to Ni plate electrodes because the electroactive surface area of DHBT porous Ni is 270 times larger than that of Ni plate. Li et al. (2007) developed a gold-filmed DHBT sensor to detect ascorbic acid (AA), uric acid (UA) and p-acetaminophen (AP) in biological samples using electrochemical characterization methods. They pointed out that the sensor has a wide glucose detection range of 2-10 mM with a high sensitivity of  $11.8 \mu\text{Acm}^{-2}\text{mM}^{-1}$ . Plowman et al. (2015) investigated a Li-ion battery using DHBT modified copper foil as the electrode and showed that the battery has a high reversible capacity and cycling stability. The electrode was fabricated by in-situ production without using additives and binders between the substrate and the porous film. Xia et al. (2011) developed a novel super-capacitor based on the DHBT porous Ni/Co(OH)<sub>2</sub> electrode. This composite electrode has a high specific active surface area, which provides high energy density, a specific capacitance of 1920 F/g, and good cycling stability.

## **2.3 Properties of Porous Metals**

### **2.3.1 Surface Area**

The surface area of porous metal is a significant parameter in many fields (Woods et al. 1976, Trasatti and Petrii 1991, Jarzabek et al. 1997, Takasu et al. 2000, Diao et al. 2015, Zhu and Zhao 2017). Particularly in electrochemical

applications, a high surface area electrode can generate/store more electrical energy because a large surface area provides more reaction sites for electrochemical reactions (Shivkumar et al. 1998, Wang et al. 2009, Zhu and Zhao 2017). Hence, measurement of an electrode's surface area has attracted much attention.

Surface areas can be classified as geometric, electrochemical and real surface areas (Diao et al. 2015). The geometric surface area only counts the surface of the pore geometry, disregard the contributions of the micro-features on the surface. Electrochemical surface area is the area where an electrochemical reaction takes place. It is sometimes also called effective surface area (Mund et al. 1974). Real surface area is the whole area of every surface feature. Compared to electroactive surface area, the real surface area is several times larger because of the smaller length scale under detection (Trasatti and Petrii 1991, Diao et al. 2015, Smith et al. 2015).

### **2.3.1.1 Electrochemical Measurement Method**

Different measurement methods for a porous material can result in different surface area values. For example, Trasatti and Petrii (1991) pointed out that the real surface area is sensitive to the condition of the measurement method and the probe scale in a given measurement system. Therefore, an appropriate

measurement method should be employed according to the material and porous structure of the specimen. This section introduces the main electrochemical methods used to measure real and electroactive surface areas.

### **2.3.1.1.1 Double Layer Capacitance Method**

The double-layer capacitance (DLC) method is widely adopted for the measurement of the surface area of a porous structure made of the same material (Trasatti and Petrii 1991). In an electrochemical cell, there is a well defined interface between the solid electrode and the liquid electrolyte. When the solid surface possesses a charge, the liquid must have a balancing counter charge. Charged particles or electrons adsorbing and desorbing on the surface of the electrode will cause a change of charge. The capacitance of this process can be determined by (Gagnon 1976):

$$C = \frac{Q}{E} = \frac{I}{v'} \quad 2.3$$

where  $C$  is the capacitance,  $Q$  is the charge stored on the electrode,  $E$  is the potential applied on the electrode,  $I$  is the current and  $v'$  is potential sweep rate.

The double layer formed by the non-faradaic process is shown in Fig. 2.19. The thin layer most close to the electrode is called the compact layer or inner Helmholtz plane (IHP), which is caused by specific adsorption. The layer outside the IHP is the outer Helmholtz plane (OHP) formed by the solvated ions,

which attract charged particles and are adsorbed to a distance from the electrode surface. The layer of non-specifically adsorbed ions that distribute between OHP and the bulk electrolyte is the diffusion layer.

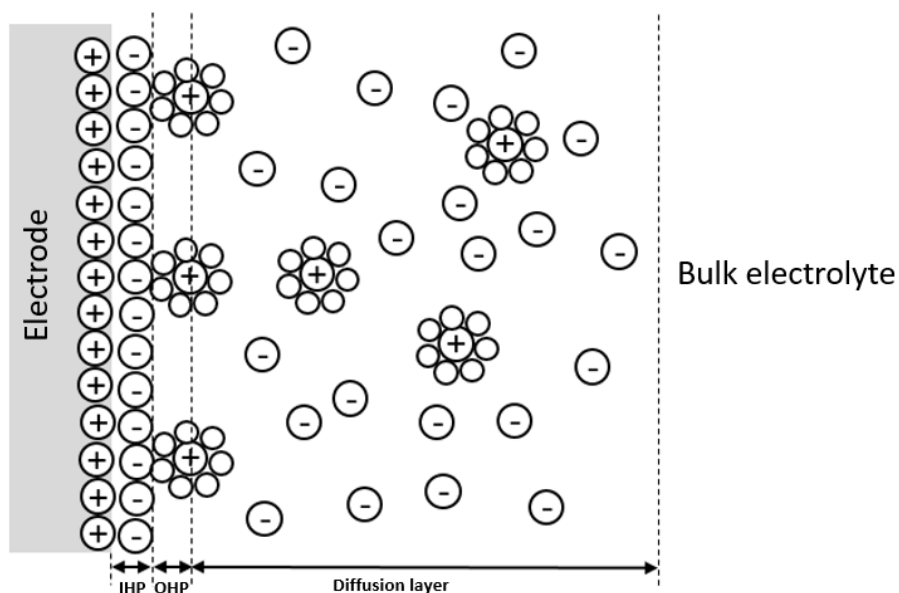


Fig. 2. 19: Schematic diagram of Helmholtz layer and the inner and outer plane (Bard 2002).

The DLC method obtains the real surface area of a porous electrode by measuring its apparent total capacitance of the double layer through the current/potential curves at different sweep rates (Campbell et al. 2004). The real surface area can be calculated from the capacitance by (Gagnon 1976):

$$A = \frac{\Delta C}{C'} = \frac{I}{v' C'} \quad 2.4$$

where  $\Delta C$  is the differential capacitance,  $I$  is the charging current,  $C'$  is the reference capacitance per unit area and  $v'$  is the scan rate. Fig. 2.20 shows the typical current-potential plots obtained in the double-layer capacitance method and the current-scan rate plot. The DLC method has been employed to

measure the real surface areas of LCS porous copper and LCS porous copper (Diao et al. 2015, Zhu and Zhao 2017).

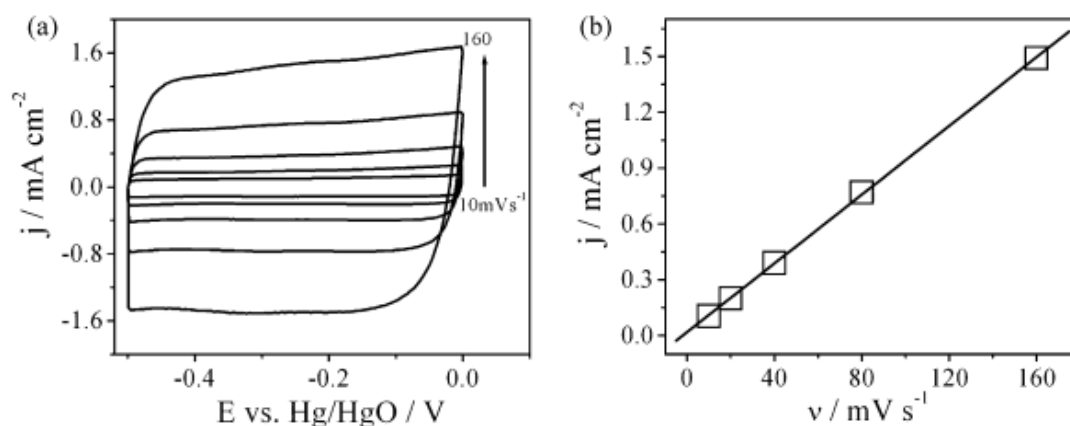


Fig. 2. 20: (a) Typical current-potential plots obtained by the double layer capacitance method and (b) the corresponding dependence of current on scan rate (Cherevko et al. 2010).

The DLC method is an in-situ measurement to obtain surface area during the reaction, which is very useful in the electrochemical field. However, this method has several limitations. The specific capacitance of the metal must be known. The ions in the electrolyte have to adsorb on the electrode metal. For example, fluorine ions can adsorb on silver but not on mercury (Trasatti and Petrii 1991). Moreover, the oxide film and impurities on the electrode surface have to be cleared fully to ensure the accuracy of the result (Trasatti and Petrii 1991).

### 2.3.1.1.2 Hydrogen Adsorption Method

The hydrogen adsorption method can be used to measure the surface area of

metals which have the hydrogen adsorption phenomenon (Michri 1972, Woods 1976, Beden et al. 1990). Cyclic voltammetry and chronopotentiometry are two common techniques in hydrogen adsorption measurement (Trasatti and Petrii 1991). Fig. 2.21 shows the current-potential curve of hydrogen adsorption and desorption at the voltammogram peaks (Lukaszewski et al. 2016).

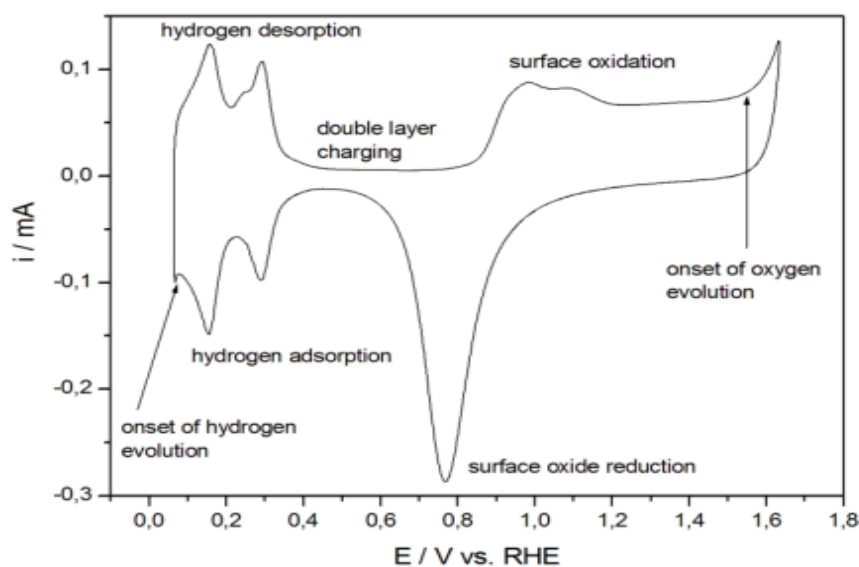


Fig. 2. 21: Various reactions under different potential ranges at Pt electrode in 0.5 M H<sub>2</sub>SO<sub>4</sub> (Lukaszewski et al. 2016).

The charge at the adsorption voltammetric peak can be assumed to correspond to the adsorption of hydrogen atoms on the metal surface. The amount of hydrogen adsorption can be determined quantitatively by measuring the charge transferred from the solution to the electrode surface. The surface area of the electrode can be derived from:

$$A = Q_H / Q_H^* \quad 2.5$$

where  $Q_H$  is the measured charge due to the hydrogen adsorption for a given

potential and  $Q_H^*$  is the charge of a monolayer of hydrogen adsorption per unit area.

The surface area measured by the hydrogen adsorption method is close to the true surface area of the metal because the hydrogen atom is the smallest particle that can be regarded as an adsorbate (Lukaszewski et al. 2016). The inaccuracy and unreproducibility of the surface area in the hydrogen adsorption method is around 10% (Hayes and Kuhn 1980). However, some assumptions have been made before using this method, which are not always valid for every condition. 1. The coverage of the adsorption is complete on the surface with a monolayer of hydrogen. 2. A defined quantitative relationship between the measured charge and the adsorbed atoms. 3. No surface alteration during the hydrogen adsorption and desorption process. 4. The metal does not absorb hydrogen.

The hydrogen adsorption method can be applied to porous metals at low potential scan rates (Kessler et al. 1985). It cannot be used to measure the surface area of transition metals including Ni, Cu and Fe, because of a distortion of the voltammogram caused by the ohmic resistance and kinetic restriction at high potential scan rates. A spillover effect in powder electrodes due to the diffusion of hydrogen along the surface is also uncovered, which results in invalid charge in the measurement (Tareasewich et al. 1967). Another



shortcoming of this method is the ionic adsorption during the hydrogen adsorption process, which also results in invalid charge (Aemand and Claviliver 1989).

### **2.3.1.1.3 Underpotential Deposition (UPD) Method**

Underpotential deposition (UPD) refers to deposition of a metal on the surface of another metallic substrate when the deposition potential is more positive than its bulk deposition potential. It happens because the interaction between the adsorbing metal and the substrate is larger than that of the adsorbing metal particles themselves. It is in fact the initial step of the bulk deposition of the metal. The deposition layer can be a monolayer or multilayer, depending on the interaction of the adsorbing metal and the substrate.

UPD has been widely used in surface area measurement since Franklin et al. (1976) firstly applied the method. Many metals, including Pd on Ag, Cu on Pd, Cu on Ru and Pb on Au, have been found to possess the UPD phenomenon (Franklin et al. 1976, Zhang et al. 2004, Deakin et al. 1988, Chierchie et al. 1988). The UPD surface area can be measured by cyclic voltammetry, chronoamperometry (CHR), electrochemical impedance spectroscopy (EIS) and electrochemical quartz crystal microbalance (EQCM) techniques. It can be calculated by the following equation:

$$A = Q_M / Q_M^*$$

2.6

where  $Q_M$  is the charge consumed in the range of voltammetric stripping of the adatoms and  $Q_M^*$  is the charge corresponding to a monolayer of deposited metal per unit area.

The most notable advantage of UPD is its high reproducibility (Trasatti and Petrii 1991). In addition, this method can be used for some cases where other adsorption methods are not suitable. For example, for metal Ru, the contributions of hydrogen and oxygen are hard to separate; therefore the hydrogen adsorption method cannot be applied. However, a monolayer of Cu can be formed on the surface of a Ru metal electrode (Trasatti and Petrii 1991), so the UPD technique is viable in this case.

The coverage of the surface by the adatom layer is strongly dependent on the deposition condition, the type of metals and the cleanliness of the electrolyte and the electrode surface (Dall'Antonia et al. 2001). Hence, several iterations of cyclic voltammetry are usually operated to record the condition of the blank background electrolyte and to clean the electrode surface. Similar to the other adsorption techniques, several main problems can occur in the determination of the UPD surface area. Firstly, the boundary of the voltammetric stripping region is not distinct, making it difficult to quantify the charge of adatoms accurately. Secondly, the formation of a complete monolayer is not possible,

because multilayer and clusters of metal adatoms usually form before the full monolayer coverage is completed (Podlovchenko et al. 1987). Finally, the contributions of double layer capacitance, hydrogen and oxygen adsorption are difficult to distinguish in the voltammetric stripping region, resulting in an underestimation of the UPD surface area.

#### **2.3.1.1.4 Peak Current Method**

The electrochemical peak current method can be used to determine the effective surface area of metals (Diao et al. 2015, Zhu and Zhao 2017, Tan et al. 2102). Fig. 2.22 shows a typical current-potential plot of the voltammogram used in the peak current surface area measurement. The method is based on the semi-infinite controlled process, where the value of the peak current in the voltammogram has a linear relationship with the surface area of the electrode if the other factors which can affect the peak current are not varying. The electroactive surface area of the porous metal can therefore be calculated from the peak current.

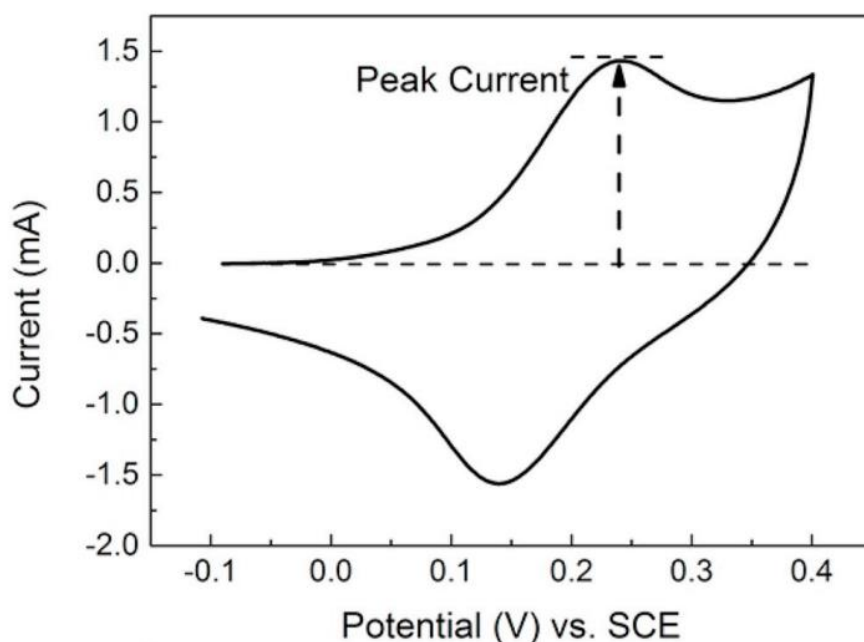


Fig. 2. 22: A typical current-potential plot of the oxidation of ferrocyanide on the surface of an LCS porous Ni sample (Zhu and Zhao 2019).

More specifically, the peak current occurs in the diffusion-controlled region when the diffusion process becomes the rate-determining step and the electroactive surface area is determined by the Randles - Sevcik equation (Bard 2002, Delahay 1954) as follows:

$$i_p = 268600 \times n^{\frac{3}{2}} \times A c D^{\frac{1}{2}} v^{\frac{1}{2}} \quad 2.7$$

where  $n$  is the number of electrons transferred in the redox process,  $A$  is the active surface area,  $c$  is the concentration of the reactive species in the bulk solution,  $D$  is the diffusion coefficient of the electrolyte,  $v$  is the scan rate.

The electrochemical peak current method is an in-situ surface area measurement. It is useful for the measurement of effective surface areas in

reaction (Zhu and Zhao 2017). The peak of the voltammogram is easy to be obtained, and electrochemical surface area can be determined by the peak current. However, in the hydrogen adsorption method, the hydrogen adsorption and evolution take place in the same region without an observable division, which causes misestimation of the current by hydrogen adsorption.

where the regions of hydrogen adsorption and evolution are hard to be distinguished due to no observable division between them. One limitation of this method is that the measured surface area depends on the relative magnitudes of the diffusion layer thickness and the roughness of the electrodes (Zhu and Zhao 2019). The structural features smaller than the diffusion layer thickness cannot be detected. Diao et al. (2015) indicated that the diffusion layer thickness is approximately 30  $\mu\text{m}$ .

### **2.3.1.2 Effect of Structural and Processing Parameters on Surface Area**

Many factors, including the manufacturing process and its processing parameters, can affect the surface area of porous metals (Trasatti and Petrii 1991, Lukaszewski et al. 2016, Diao et al. 2015). The surface morphology and porous structure are different for the porous metal products manufactured by different processes. Porous metals produced by CVD have flat surfaces; porous metals produced by space holder methods have relatively low porosity; porous

metals produced by DHBT have a very rough surface morphology and high porosity (Banhart 2001, Diao et al. 2015, Shin et al. 2003). The different surface morphology and porous structure can have a significant effect on the surface area. For example, the surface area of a CVD Ni foam, measured by Brunauer-Emmett-Teller (BET), is 292 cm<sup>2</sup>/g, while the surface area of a slurry foamed Ni foam with a similar pore size and porosity is 19710 cm<sup>2</sup>/g (Bidault et al. 2009, Duki et al. 2013).

Pore size is an important factor affecting the surface area of porous metals. For a given porosity, smaller pores mean more pores in the metal matrix and therefore a larger surface area. Zhu and Zhao (2017) investigated the effect of porous structure on surface areas of LCS porous copper and reported that the specific surface area increases with decreasing pore size.

Porosity is another factor affecting the surface area of porous metals. A high porosity represents a large amount of pores inside the metal matrix and, for the same pore size, brings about a high surface area. Studies on LCS porous copper and Ni (Diao et al. 2015, Zhu et al. 2017) showed that increasing porosity leads to an increase in the surface area.

Surface morphology has a significant effect on the surface area, especially for those measured by a sensitive method like DLC (Zhu et al. 2015, Grden et al.

2012, Stanislaw et al. 2019). A rough surface results in a high surface area. Stanislaw et al. (2019) electroplated Ni nanomesh on an aluminium oxide substrate, which was subsequently removed using a KOH solution. They reported that the electroactive surface area of the 3.3  $\mu\text{m}$  thick porous Ni samples was 87-107 times of that of a planar Ni, because the 3D porous Ni structure provides a large internal surface area. Grden et al. (2012) studied the effects of thermal, chemical and electro-oxidizing surface treatments on the surface morphology and surface area of porous Ni. They found that chemical etching resulted in a higher surface area because it produced a rougher surface and a clean surface condition without changing the porous structure. Zhu and Zhao (2017) reported that the real surface area of the LCS porous copper was reduced by 31-61% and 9-25% by chemical and thermal treatments, respectively, due to smoothed surface.

The processing parameters of various manufacturing methods can also affect the surface area of the as-produced porous metals. The factors include operation temperature, operation time, pressure, atmosphere, type and concentration of reactant, and intensity of potential and current (Zhu and Zhao 2017, Diao et al. 2015, Li et al. 2007). Temperature is an important factor in powder metallurgy methods. A higher sintering temperature decreases the real surface area of the LCS porous copper (Zhu and Zhao 2017).

### 2.3.2 Mass Transfer Performance

Mass transfer in electrochemistry refers to the movement of a reactant from the bulk electrolyte to the electrode surface. Mass transfer performance is an important parameter for electrochemical reactors, especially for those reactors having fast electrode reaction kinetics (Bard 2002). In such reactors, the electrochemical reaction rate is controlled by the mass transfer process (Recio et al. 2013, Zhu and Zhao 2017). Fig. 2.23 is a schematic diagram of a typical electrode reaction pathway. A general redox process involves mass transfer from the bulk solution to the electrode surface, charge transfer on the electrode and other intermediate reactions (e.g. adsorption/desorption). In an electrochemical redox reaction with a fast reaction kinetic, the diffusion process is the rate-determining step (Zhu and Zhao 2017).

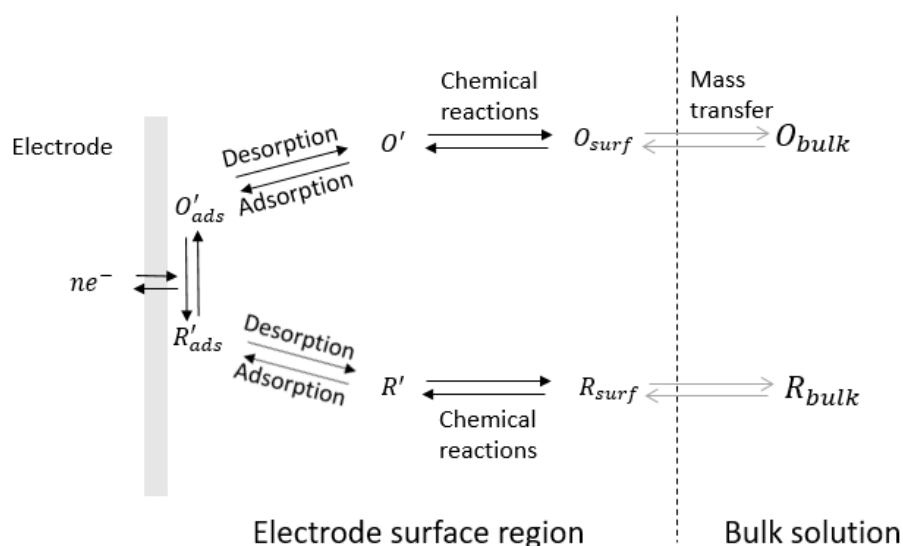


Fig. 2. 23: Schematic diagram of electrode reaction pathway (Bard 2002).



The rate of mass transfer is proportional to the concentration gradient in the bulk solution, which is described by Fick's law (Compton 2012, Compton et al. 2013). Fick's second law states that the flux of the species,  $J_0$ , is proportional to the concentration gradient:

$$J_0 = -D \frac{\partial^2 c}{\partial x^2} \quad 2.8$$

where  $D$  is the diffusion coefficient,  $c$  is the concentration of bulk solution and  $x$  is the distance away the electrode surface.

The mass transfer performance can be characterized by the voltammogram method, also called the limiting current method (Recio et al. 2013, Zhu and Zhao 2017). Fig. 24 shows a typical current-potential profile in a voltammogram. It has three kinetic regions, including hydrogen evolution region, mass transfer control region and mixed control region. The limiting current,  $I_L$ , is determined by:

$$I_L = kAnFc \quad 2.9$$

where  $k$  is the mass transfer coefficient,  $A$  is the active electrode area,  $n$  is the number of electron transfer in the reaction,  $F$  is the Faraday constant, and  $c$  is the concentration of the bulk solution.

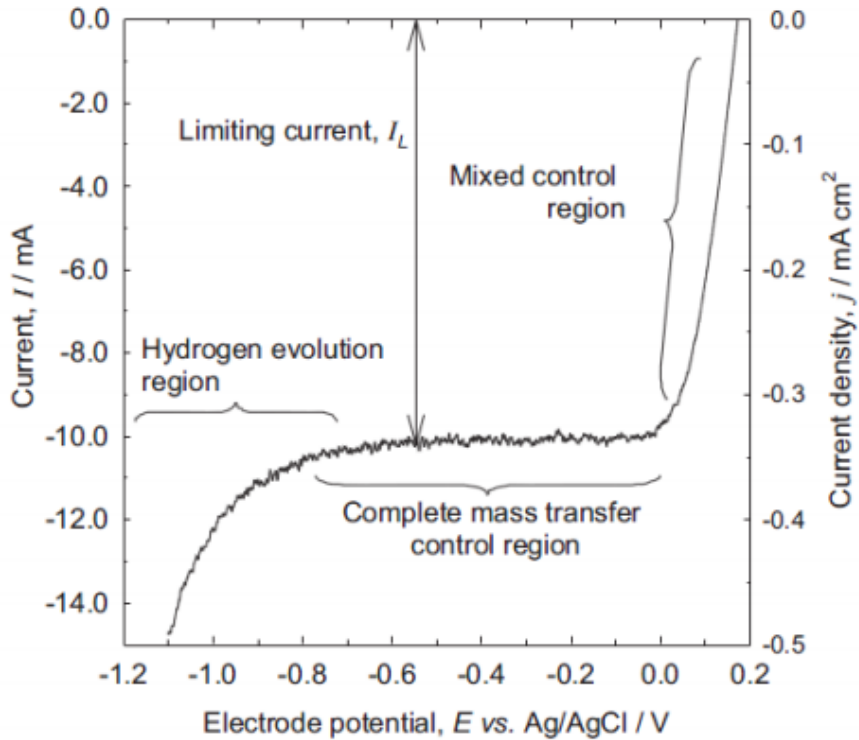


Fig. 2. 24: Typical voltammogram for the reduction of 1 mM  $\text{K}_3\text{Fe}(\text{CN})_6$  in 1 M  $\text{Na}_2\text{CO}_3$  (Recio et al. 2013).

The study of mass transfer performance in porous electrodes is particularly important because they have high surface areas and complicated structural characteristics which exhibit a superior mass transfer performance. There are three pathways to improve the mass transfer performance of the electrode, including increasing the surface area, increasing the mass transfer coefficient and increasing the electrochemical catalysis of the electrode (Zhu and Zhao 2017).

Recio et al. (2013) studied the mass transfer in plate electrodes with smooth and rough surfaces. They reported that the mass transfer performance of an

electrode with a rough surface is 11 times higher than that with a smooth surface. They also employed a turbulence promoter in the experiment to study the effect of the fluid state on the mass transfer performance. The mass transfer performance was further increased by 23 times compared with those without a promoter. This is because using a turbulence promoter changes the fluid flow from laminar to turbulent.

Zhou et al. (2015) studied a series of porous copper-fibre electrodes with different porosities of 0.7, 0.8 and 0.9, made by sintering. The best mass transfer performance appears at the porosity of 0.8. They indicated that the mass transfer depends on the residence time of the electrolyte inside the porous metal. If the porosity is too low, the electrolyte inside the porous electrode is exhausted quickly. If the porosity is too high, the electrolyte leaves the porous metal rapidly without sufficient reaction. Both result in a low mass transfer performance.

Zhu and Zhao (2017) studied the mass transfer performance of the LCS porous Ni electrode. They found that the mass transfer coefficient increases with increasing pore size and decreases with increasing porosity. The mass transfer performance is up to 300 times higher than the Ni plate. Langlois and Coeuret (1989) reported that the mass transfer performance of a Ni foam decreases with increasing pore size. They used three grades of Ni foam, G100, G60 and

G45, and found that the BET surface area of the G100 Ni foam is 2.16 times higher than the G45 Ni foam, which has the largest pore size.

The effect of electrolyte flow rate on the mass transfer can be expressed by (Recio et al. 2013):

$$kA = av^b \quad 2.10$$

where ' $kA$ ' is the mass transfer performance, which is the product of ' $k$ ', the mass transfer coefficient and ' $a$ ', active electrode surface area, ' $a$ ' is a constant associated with the structural properties of the electrode,  $v$  is the electrolyte flow velocity and ' $b$ ' is a constant associated with the mass transport condition. The mass transfer performance increases with increasing the electrolyte velocity. However, the highest mass transfer performance appears at a velocity around 33 cm/s, beyond which the fluid resistance limits further enhancement of the mass transfer (Brown et al. 1993).

In the investigations into the mass transfer, several dimensionless numbers, including Sherwood number (Sh), Reynolds number (Re) and Schmidt number (Sc), are used (Recio et al. 2013):

$$Sh = \frac{kd_e}{D} \quad 2.11$$

$$Re = \frac{vd_e}{\nu} \quad 2.12$$

$$Sc = \frac{\nu}{D} \quad 2.13$$

where  $d_e$  is the equivalent diameter of pores,  $D$  is the diffusion coefficient of the reactive species and ' $u$ ' is the kinematic viscosity of the electrolyte. The relationship among these parameters can be expressed as (Brown et al. 1992, Park et al. 2007):

$$\text{Sh} = \alpha \text{Re}^\beta \text{Sc}^{0.33} \quad 2.14$$

where ' $\alpha$ ' is a constant associated with the geometrical structure of the electrode and ' $\beta$ ' is a constant depending on the hydrodynamic regime. The Sherwood number can be used to compare electrodes with different geometrical and physical properties.

## 2.4 Electrochemical Applications

Open-cell porous metals, especially those with modified functional surfaces, have received much interest over the past three decades due to their great combinations of properties of electrocatalysis, specific capacitance, specific surface area, and mass transfer coefficient (Zhu and Zhao 2017, Diao et al. 2015, Recio et al. 2013). They have found increasing applications in a wide range of new fields, including electrochemical sensors, electrochemical batteries, fuel cells and so on (Lu et al. 2011, Niu et al. 2013, Noelle et al. 2018, Krishnamoorthy et al. 2014). The development of manufacturing technologies, e.g., electrochemical, hydrothermal, physical deposition and other methods as complements of conventional metallurgical techniques, has further advanced

the applications.

### **2.4.1 Electrochemical Glucose Sensors**

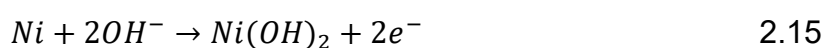
One of the most significant attributes of porous metals is their electrocatalysis of bio-detection of redox substances (e.g. glucose, dopamine etc). They can be employed as non-enzyme bio-detectors for medical instruments to improve the user experience as well as the accuracy and selectability of products. Non-enzyme bio-detectors possess many advantages over enzyme detectors. They have a significant market potential because of long life-span, easy fabrication, low cost, low requirements for storage environment as well as high reproducibility and stability (Niu et al. 2013, Zhu et al. 2018, Chakraborty et al. 2020, Jagadeesan et al. 2019).

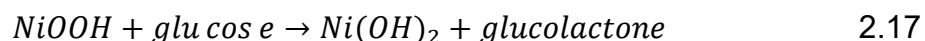
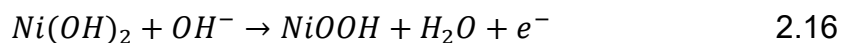
In the recent few decades, fast detection of glucose in humans become an important issue, because of a rapidly growing number of people with diabetes (Stefan-van Staden et al. 2018). Since the development of the first enzymatic glucose detector, glucose oxidase (GOx) glucose sensors have been widely used in the production of blood glucose test paper due to their high selectivity and accuracy (Park et al. 2006, Toghil et al. 2010). However, because GOx is affected by oxygen content, dehydrogenase is employed to substitute GOx in many glucose detection sensors. Although enzymes possess a high selectivity,

accuracy and wide detection range in glucose detection, enzyme-based sensors have obvious limitations. The production and storage of the GOx enzyme are costly to guarantee the activity of the enzyme. Moreover, the immobilization of enzymes on the electrode is a time-consuming process, and the processing temperature must be controlled (Tang et al. 2014).

Non-enzyme bio-detector can avoid the shortcomings of enzyme-based detectors, including high-pricing and storage issues. Noble metals such as gold show a great catalytic performance in glucose detection, but the high-cost prevents their mass production (Chen et al. 2021). Transition metals and their oxides have been investigated extensively in academia and industry in order to reduce the cost and implement mass-production goals. To improve the detection accuracy, it is necessary to use a high surface area electrode, which can output a relatively high signal to increase the signal-to-noise ratio in the measurement.

The principle of glucose detection is based on the redox reaction of glucose at the electrode. The oxidation of glucose to gluconolactone occurs on a transition metal surface in an alkaline solution (e.g. 0.1 M NaOH solution), and the equilibrium reaction can be described as (e.g. for Ni electrode) (Safavi et al. 2009):





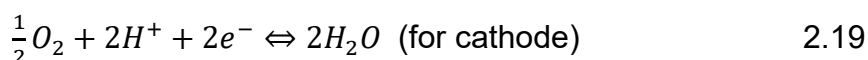
Niu et al. (2013) developed a highly-sensitive and selective glucose detector using a porous Ni electrode manufactured by the DHBT method. This electrode has a wide linear concentration range of 0.0005-4 mM with a high sensitivity of 2900  $\mu A/(cm^2mM)$ ; its limit of detection (LOD) for glucose is 0.07  $\mu M$ . Guo et al. (2015) reported a three-dimensional nanostructured porous CNT/MnO<sub>2</sub> composite electrode with a superior sensitivity of 3406.4  $\mu A/cm^2mM$  and a low LOD of 0.5  $\mu M$  for glucose detection.

Porous metal structure carrying catalytic material provides a high specific surface area and allows the reactant to flow through to improve the performance of sensors. Kung et al. (2014) synthesized Ni hydroxide nanoparticles in-situ on a Ni foam electrode by an electrochemical cyclic voltammetric method. This composite electrode possessed superior electrocatalytic performance in glucose detection, with a high sensitivity of 1950.3  $\mu A/cm^2mM$ , a wide linear range of 0.6 - 6 mM and a low LOD of 0.16  $\mu M$ . The electrode was still stable after storage in the atmosphere for over a month, which indicates excellent reproducibility.

## 2.4.2 Electrochemical Batteries



Electrochemical batteries are devices that can efficiently convert chemical energy into electrical energy. They have received much interest in both academia and industry due to the shortage of fossil fuels and environmental issues. Using fuel cells as an example, fuels like methanol and hydrogen gas are directly converted into electrical energy through fuel cells based on a redox reaction (Chen et al. 2007, Chung et al. 2013). The configuration incorporates an anode, a cathode and an electrolyte. The fuels and oxidizing agent or source flow by/through the anode and cathode, respectively. At the surface of the anode, oxidation of the fuel occurs, which generates electrons and produces an electric current to the cathode along with the external circuit. The ions formed by the anode reaction are transferred to the cathode through an electrolyte and react with oxygen and electrons on the surface of the cathode to generate new products. Fig. 2.25 shows a schematic diagram of a simple hydrogen-oxygen fuel cell. The reaction is split into two half-reactions:



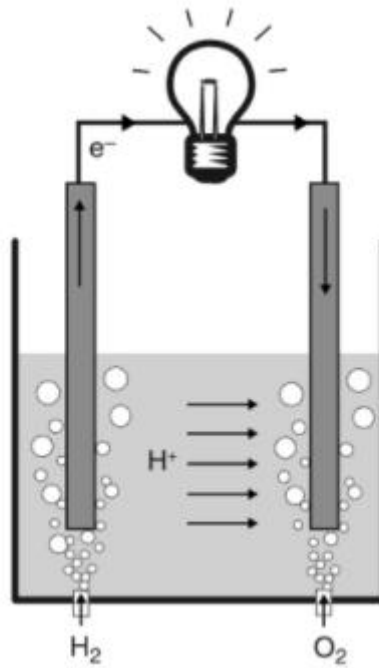


Fig. 2. 25: Schematic diagram of a simple hydrogen-oxygen fuel cell (O'Hayre et al. 2016).

Fuel cells have a high energy conversion efficiency due to direct electrochemical energy conversion. The energy capacity of fuel cells is determined by the fuel reservoir size. The electricity is generated continuously while the fuel is supplied.

Fuel cells can be classified by their electrolyte and the major types of fuel cells are listed in Table 2.2. Solid state electrolytes can provide a highly reliable and long-lasting reactor without emissions of polluted gases such as  $\text{NO}_x$  and  $\text{SO}_x$ .

Table 2. 2 Major fuel cell types: proton exchange membrane fuel cell (PEMFC), phosphoric acid fuel cell (PAFC), alkaline fuel cell (AFC), molten carbonate fuel cell (MCFC) and solid oxide fuel cell (SOFC) (O'Hayre et al. 2016).

	PEMFC	PAFC	AFC	MCFC	SOFC
Electrolyte	Polymer membrane	Liquid H <sub>3</sub> PO <sub>4</sub> (immobilized)	Liquid KOH (immobilized)	Molten carbonate	Ceramic
Charge carrier	H <sup>+</sup>	H <sup>+</sup>	OH <sup>-</sup>	CO <sub>3</sub> <sup>2-</sup>	O <sup>2-</sup>
Operating temperature	80°C	200°C	60–220°C	650°C	600–1000°C
Catalyst	Platinum	Platinum	Platinum	Nickel	Perovskites (ceramic)
Cell components	Carbon based	Carbon based	Carbon based	Stainless based	Ceramic based
Fuel compatibility	H <sub>2</sub> , methanol	H <sub>2</sub>	H <sub>2</sub>	H <sub>2</sub> , CH <sub>4</sub>	H <sub>2</sub> , CH <sub>4</sub> , CO

The reaction rate in fuel cells is determined by the fluid's transport, i.e., the mass transfer performance. Mass transport in the fuel cell is dominated by fluid flow velocity, mass transport condition (e.g. convection or diffusion) and surface area of the electrode. Because the electrochemical reactions take place at the surface of the electrode/current collector, and the fast flow allows a large number of reactant molecules to transfer to the surface, as shown in Fig. 2.26, a diffusion layer (concentration gradient of reactant from the fuel tank to the interface between electrode and electrolyte) develops at the anode of an operating hydrogen-oxygen fuel cell.

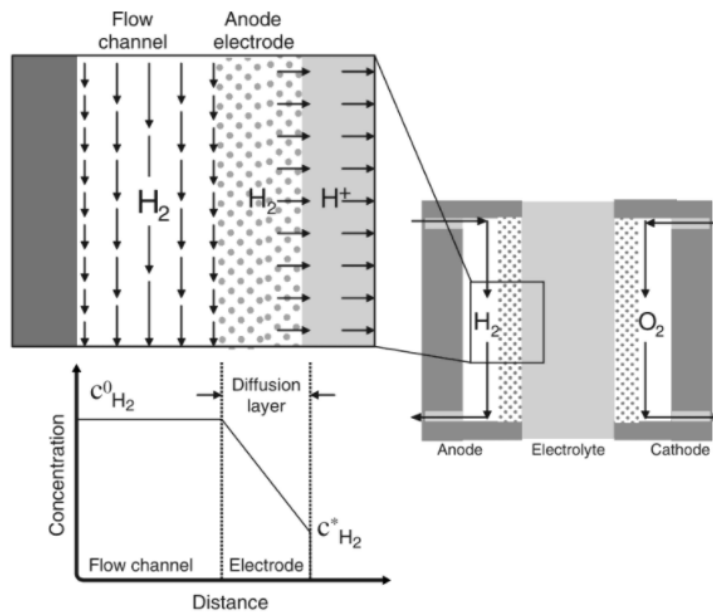


Fig. 2. 26: Schematic diagram of the diffusion layer that develops at the anode of an operating hydrogen-oxygen fuel cell configuration (O'Hayre et al. 2016).

In electrochemical batteries, the specific surface area of the electrode is an important parameter because of the large number of active materials loading on the electrode surface. Therefore, high surface area porous current collectors are often employed in these electrochemical battery applications. Yun et al. (2016) developed a porous copper current collector by the dealloying method. The porous electrode was first made from a Cu-Zn alloy and the Zn component was removed by chemical etching, leaving behind micropores to accommodate the lithium metal. The electrode exhibited a high energy capacity and high-reliability. Lu et al. (2016) plated the active materials onto a copper nanowire current collector as the anode and showed that it has a high coulombic efficiency, superior rate performance and conductivity. Li et al. (2017) fabricated a porous copper foam current collector and demonstrated that, compared to

planar copper foil, the porous copper foam provides a high specific surface area and therefore improved the electrochemical reaction kinetics. They reported that the porous copper foam/lithium composite electrode has a lower resistance than bare lithium metal (Fig. 2.27). Noelle et al. (2018) reported that a structural electrochemical battery based on porous metal current collectors possessed a high safety margin and energy density. Jin et al. (2017) investigated the effect of the current collector contact area on the cell resistance of the SOFC cathode and reported that the cell resistance decreased from 1.43 to 0.019  $\Omega\text{cm}^2$  at 800°C when the contact area of the current collector increased from 4.6% to 27.2%.

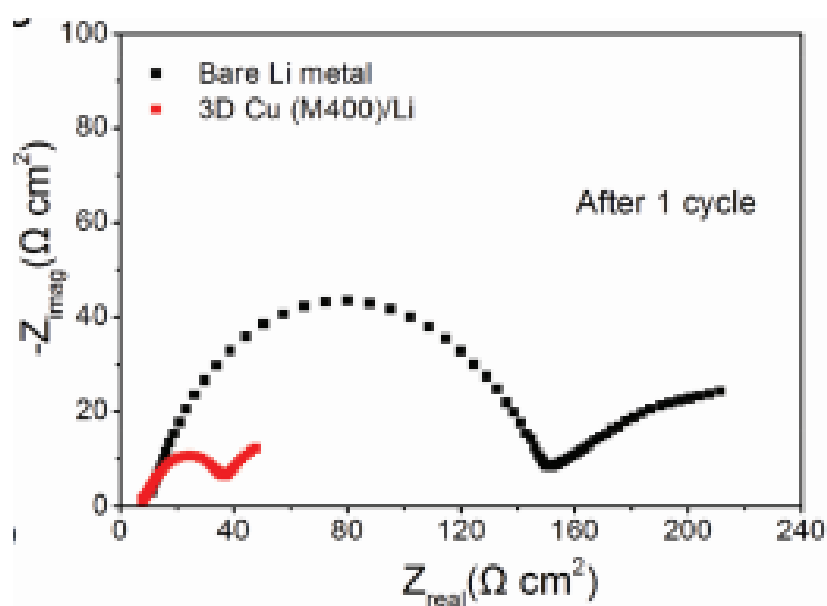


Fig. 2. 27: Contrast of resistance in Nyquist plots of the composite electrode and bare lithium metal (Li et al. 2017).

## **2.5 Summary**

This chapter reviews the manufacturing methods, electrochemical properties and applications of open-cell porous metals. The four different manufacturing pathways and their characteristics are summarized. The effects of surface condition and porous structure on surface area and mass transfer performance of porous metals are discussed and summarized. The LCS porous metals have superior 3D porous structure and good mass transfer coefficient. However, such manufactured porous structures have relatively low surface area, which cause the limitations of the LCS porous metals in electrochemical applications. Therefore, the methods and processes to increase the surface area of the LCS porous metals is necessary to study. The investigations on the electrochemical characterizations of important properties of porous metals are reviewed. Two electrochemical applications of open-cell porous metals, sensors and batteries, are introduced.

## **Chapter 3 Experimental Methods**

### **3.1 Introduction**

This chapter describes the fabrication procedures used to manufacture the porous metal samples and the methods used to characterize the samples. The porous metal samples were manufactured by the Lost Carbonate Sintering (LCS) and the Dynamic Hydrogen Bubble Template (DHBT) methods. The surface areas and mass transfer performance of the porous metal samples were characterized by cyclic and linear voltammetry methods. The correlations of electrode current with glucose concentration using porous metal electrodes were investigated by cyclic voltammetry technique.

### **3.2 Preparation of LCS Porous Ni**

The LCS process is a space holder method for manufacturing porous metals, developed by Zhao's group at the University of Liverpool in 2005 (Zhao et al. 2005). In LCS,  $K_2CO_3$  powder is used as the space holder agent, which is subsequently eliminated by the dissolution treatment. The pore size of the LCS porous metals is normally in a range of 250 – 1500  $\mu\text{m}$  and the porosity is in a range of 60 – 85%. The LCS process for manufacturing porous metals is shown schematically in Fig. 3.1.

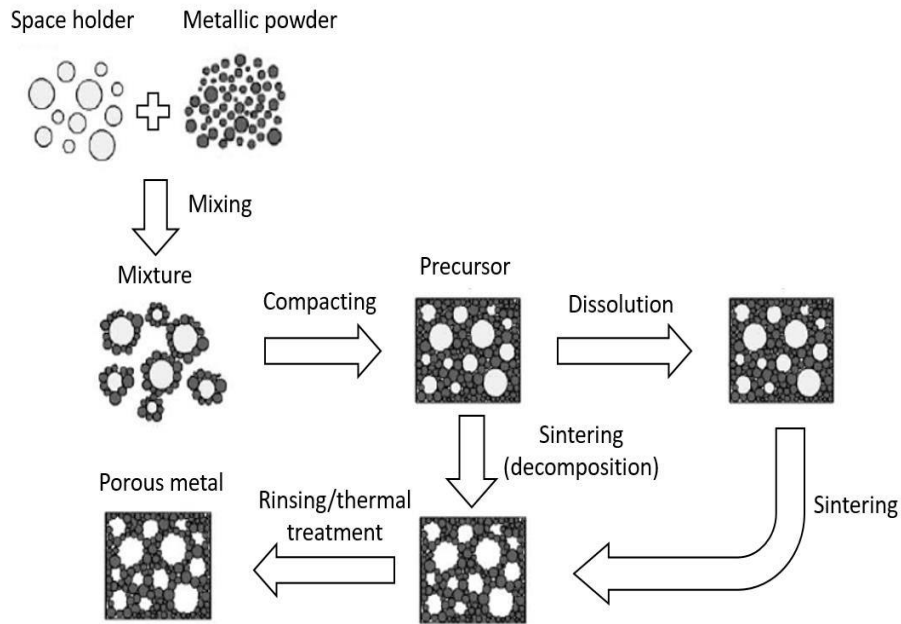


Fig. 3. 1: The schematic diagram of the LCS process (Zhao et al.2005).

### 3.2.1 Raw Materials

All chemicals used in the experiments were analytical grade without further purification. The coarse and fine Ni powders with spherical particles and a purity of 99.5% were supplied by Changsha Tianjiu Ltd. China. The mean particle size of the coarse and fine Ni powders were 100  $\mu\text{m}$  and 10  $\mu\text{m}$ , respectively. The fine powder was mixed with the coarse powder with contents of 0%, 20%, 40%, 60%, 80% and 100% in weight to study the effect of metal particle size on the surface area and mass transfer performance of the as-manufactured LCS porous Ni. The space filler is a food-grade spherical  $\text{K}_2\text{CO}_3$  powder with a purity of 99% supplied by E&E Ltd., Australia. The  $\text{K}_2\text{CO}_3$  powder was sieved and divided into four different particle size ranges of 250-425  $\mu\text{m}$ , 425-710  $\mu\text{m}$ , 710-



1000  $\mu\text{m}$  and 1000-1500  $\mu\text{m}$  for fabricating porous metal samples with different pore sizes and porosities.

### 3.2.2 Mixing and Compaction

The Ni powder was mixed with the  $\text{K}_2\text{CO}_3$  powder at a pre-determined volume ratio according to the target porosity and pore size. To disperse particles and prevent particle agglomeration, 1 wt.% ethanol was employed as an additive. A stainless-steel cylindrical tube (with  $\Phi = 50$  mm) was used as the mould to accommodate the powder mixture. The thickness of the final porous Ni samples was 5 mm, and the mass of  $\text{K}_2\text{CO}_3$ ,  $m_{\text{K}_2\text{CO}_3}$  and the mass of Ni,  $m_{\text{Ni}}$ , can be determined by:

$$m_{\text{Ni}} = (1 - \varepsilon)V\rho_{\text{Ni}} \quad 3.1$$

$$m_{\text{K}_2\text{CO}_3} = \varepsilon V\rho_{\text{K}_2\text{CO}_3} \quad 3.2$$

where  $\varepsilon$  is the porosity,  $V$  is the volume of the porous Ni sample, and  $\rho_{\text{Ni}}$  and  $\rho_{\text{K}_2\text{CO}_3}$  are the densities of Ni and  $\text{K}_2\text{CO}_3$ , respectively.

The powder mixture in the mould was compacted by a hydraulic press (Moore Hydraulic Press, UK) at pressures of 0, 50, 100 or 200 MPa for 30 seconds to form a preform for subsequent heat treatment. Fig. 3.2 shows a schematic diagram of the compaction process for manufacturing the preforms.

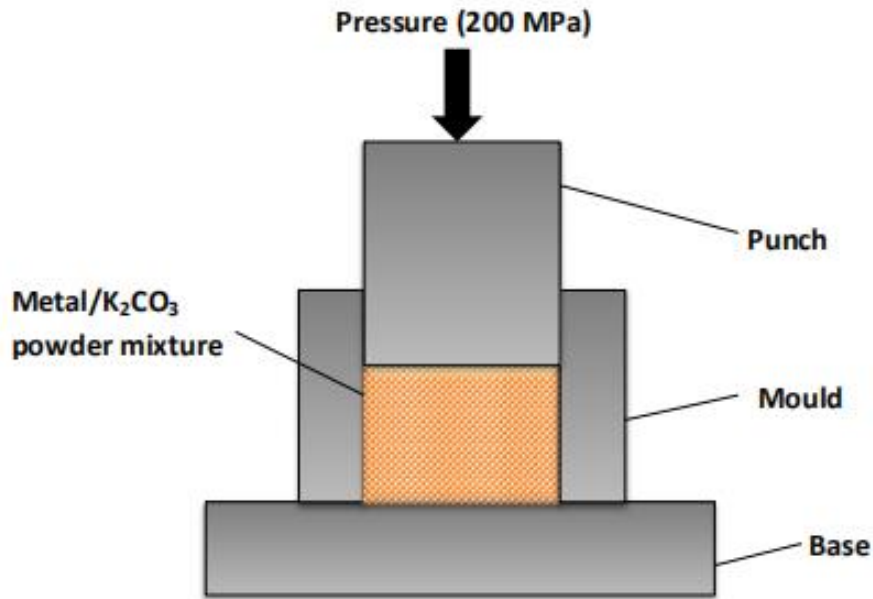


Fig. 3. 2: Schematic diagram of the compaction process for manufacturing the preforms (Diao et al. 2015).

### 3.2.3 Sintering and Dissolution

The preform was transferred to a vacuum furnace for sintering. The temperature was raised from room temperature to 200°C and stayed at 200°C for 30 minutes to eliminate the ethanol in the preform. The temperature was then increased to the sintering temperature of 850°C and kept for 4 hours. The temperature profile of the sintering process is shown in Fig. 3.3. After sintering, the sample was taken out from the stainless steel tube by extrusion and immersed in hot water for dissolution. The  $K_2CO_3$  particles inside the sample were completely removed by the dissolution process, resulting in a LCS porous Ni sample.

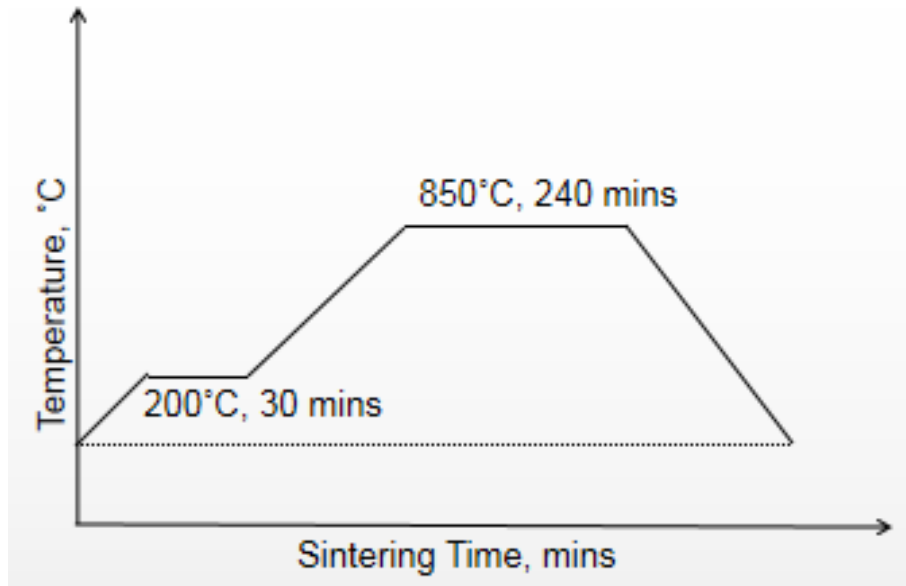


Fig. 3. 3: Temperature profile of the sintering process (Zhu and Zhao 2017).

### 3.2.4 Taguchi Design in the Manufacture of LCS Porous Ni Samples

Taguchi orthogonal array design was used to investigate the effects of LCS processing parameters on the surface areas of the porous Ni. Based on previous research on processing conditions (Diao et al. 2015), five key factors were selected:  $K_2CO_3$  particle size,  $K_2CO_3$  volume percentage, fine Ni powder ratio, compaction pressure and sintering temperature. As the particle size and the volume percentage of the  $K_2CO_3$  powder determine the pore size and porosity of the resultant porous Ni sample, these two parameters are labelled as pore size and porosity, respectively, for convenience. Each of the five factors had four levels and an L16 orthogonal array was designed, as shown in Table 3.1.

Table 3. 1 L16 orthogonal array design of experiments.

Experiment No.	Pore size (µm)	Porosity (%)	Fine powder ratio (%)	Compaction Pressure (MPa)	Sintering Temperature (°C)
1	250-425	65	0	0	700
2	425-710	70	20	0	750
3	710-1000	75	40	0	800
4	1000-1500	80	60	0	850
5	250-425	75	60	50	750
6	425-710	80	40	50	700
7	710-1000	65	20	50	850
8	1000-1500	70	0	50	800
9	250-425	80	20	100	800
10	425-710	75	0	100	850
11	710-1000	70	60	100	700
12	1000-1500	65	40	100	750
13	250-425	70	40	200	850
14	425-710	65	60	200	800
15	710-1000	80	0	200	750
16	1000-1500	75	20	200	700

Notes: Pore size refers to the particle size of the  $K_2CO_3$  powder. Porosity refers to the volume fraction of the  $K_2CO_3$  powder in the metal/  $K_2CO_3$  mixture. Fine powder ratio refers to the weight ratio of fine powder in the whole metal powder mixture.

In this study, the fine Ni powder ratio was identified as the most important parameter affecting the surface area of the porous Ni samples. Further experiments for the effect of fine powder ratio were carried out because this factor shows to have an important effect on the surface area of the LCS porous Ni in the pre-experiments. In this set of experiments, the pore size (425 – 710  $\mu\text{m}$ ), porosity (70%), compaction pressure (200 MPa) and sintering temperature (850°C) were fixed and six fine Ni powder ratios (0%, 20%, 40%, 60%, 80% or 100%) were investigated.

### **3.3 Preparation of DHBT and LCS/DHBT Porous Ni**

#### **3.3.1 Raw Materials**

Ni strips were used as substrates to manufacture the DHBT porous Ni films to study the effect of DHBT manufacturing parameters on surface area. They have a purity of 99.99% and a size of 1 mm x 45 mm. They were polished to mirror-like smooth surface using metallographic techniques to make substrates. The LCS porous Ni samples were used as substrates to manufacture the composite LCS/DHBT porous Ni samples. The samples have a porosity of 80% and pore

size in the range of 710-1000  $\mu\text{m}$ . The Ni substrates were then cleaned with 10% dilute NaOH and HCl, respectively, to remove the grease and oxides on the surface. The substrates were washed with distilled water and ethanol in turn and dried using nitrogen gas. All the cleaning processes were carried out in an ultrasonic cleaner. The Ni salts used in this study were  $\text{Ni}(\text{CH}_3\text{COO})_2$  (99.5% purity) and  $\text{Ni}(\text{SO}_3\text{NH}_2)_2$  (99.5% purity).  $\text{NH}_4\text{Cl}$  (99% purity) was used to generate hydrogen bubbles. All raw materials were supplied by Simga-Alrich Co. Ltd.

### **3.3.2 Electro-deposition**

The Ni strip substrates were then numbered and electrodeposited with different manufacturing parameters in two different electrolytes,  $\text{Ni}(\text{CH}_3\text{COO})_2$  and  $\text{Ni}(\text{SO}_3\text{NH}_2)_2$  as shown in Tables 3.2 and 3.3, respectively. A three-electrode configuration was used in this experiment. A Pt plate with a surface area of 1  $\text{cm}^2$  was used as the counter electrode, a saturated calomel electrode (SCE) was employed as the reference electrode and the Ni substrate was used as the working electrode. The electrodeposition process was driven by a potentiostat (Autolab PGSTAT 101). The experiments were carried out in a 50 mL electrolytic tank at room temperature. The distance between the electrodes was 20 mm in all experiments. The solutions for experiment were degassed by aerating plenty of nitrogen gas. After deposition, the DHBT porous Ni samples

were cleaned by plenty of distilled water and ethanol without using ultrasonic cleaner to avoid damage of samples, because the DHBT porous Ni samples have extremely high porosity; the metal walls are thin and the strength of the DHBT porous Ni is limited. The cleaned samples were dried and then characterized using the potentiostat and a Scanning Electron Microscope (SEM).

Tables 3.2 and 3.3 show the bath compositions and deposition parameters used to manufacture the DHBT films in the  $\text{Ni}(\text{CH}_3\text{COO})_2$  and  $\text{Ni}(\text{SO}_3\text{NH}_2)_2$  electrolytes, respectively. Each parameter has 3 levels.

Table 3. 2 Bath compositions and deposition parameters in  $\text{Ni}(\text{CH}_3\text{COO})_2$  electrolyte.

Number	$\text{Ni}(\text{CH}_3\text{COO})_2/\text{M}$	$\text{NH}_4\text{Cl}/\text{M}$	Potential/V	Time/s
1	0.2	0.5	-1.35	150
2	0.2	1	-1.35	150
3	0.2	1.5	-1.35	150
4	0.1	1.5	-1.35	150
5	0.4	1.5	-1.35	150
6	0.2	1.5	-1.5	150
7	0.2	1.5	-1.7	150
8	0.2	1.5	-1.35	60
9	0.2	1.5	-1.35	300

Table 3. 3 Bath compositions and deposition parameters in  $\text{Ni}(\text{SO}_3\text{NH}_2)_2$  electrolyte with 1.5 M  $\text{NH}_4\text{Cl}$ .

Number	$\text{Ni}(\text{SO}_3\text{NH}_2)_2$ (M)	Potential (V)	Time (s)
1	0.1	-1.7	150
2	0.2	-1.7	150
3	0.4	-1.7	150
4	0.2	-1.9	150
5	0.2	-2.1	150
6	0.2	-1.7	100
7	0.2	-1.7	200

The composite LCS/DHBT porous Ni samples used for mass transfer performance study were manufactured in the same electrodeposition process, except that the substrates were LCS porous Ni samples. The electrolyte contained 0.2 M  $\text{Ni}(\text{CH}_3\text{COO})_2$  and 0.5 M  $\text{NH}_4\text{Cl}$ . The deposition potentials were -1.35, -1.5 and -1.7 V and the deposition times were 60, 150 and 300 s, as shown in Table 3.4.



Table 3. 4 Deposition potential and time for manufacturing the LCS/DHBT porous Ni samples for mass transfer study.

Number	Potential (V)	Time (s)
1	-1.35	60
2	-1.5	60
3	-1.7	60
4	-1.35	150
5	-1.5	150
6	-1.7	150
7	-1.35	300
8	-1.5	300
9	-1.7	300

The composite LCS/DHBT porous Ni samples used for glucose detection study were manufactured in the same electrodeposition process using LCS porous Ni samples as the substrates. The porous Ni substrates have a porosity of 80% and a pore size range of 710 – 1000  $\mu\text{m}$ , and were cut into cuboids (4×5×6 mm). A thin porous Ni film was electrodeposited on each of the substrates by the DHBT method. The electrolyte contained 0.2 M  $\text{Ni}(\text{CH}_3\text{COO})_2$  and different concentrations of  $\text{NH}_4\text{Cl}$ , as shown in Table 3.5. The deposition potentials were -1.35, -1.5 and -1.7 V, as shown in Table 3.5, and the deposition time was set at 300s.

Table 3. 5 NH<sub>4</sub>Cl concentration and deposition potential for manufacturing the LCS/DHBT porous Ni samples for glucose detection study.

Number	NH <sub>4</sub> Cl /M	Potential /V
1	0.5	-1.35
2	1	-1.35
3	1.5	-1.35
4	0.5	-1.5
5	1	-1.5
6	1.5	-1.5
7	0.5	-1.7
8	1	-1.7
9	1.5	-1.7

### 3.4 Measurement of Electroactive Surface Area

#### 3.4.1 Experimental Apparatus

All electrochemical experiments were performed using a potentiostat (Auto lab PGSTA101). The experiments took place in a sealed glass vial, with a three-electrode configuration consisting of a porous metal working electrode, a saturated calomel electrode (SCE) reference electrode and a Pt coil wire counter electrode. A schematic diagram of the three-electrode electrochemical cell used for the cyclic voltammetry (CV) measurements is shown in Fig. 3.4.

The measurements were carried out in 1 mM  $K_4[Fe(CN)_6]$  in a 0.1 M KOH background solution. A series of mirror-polished Ni plates with known surface areas were employed to calibrate the measurements.

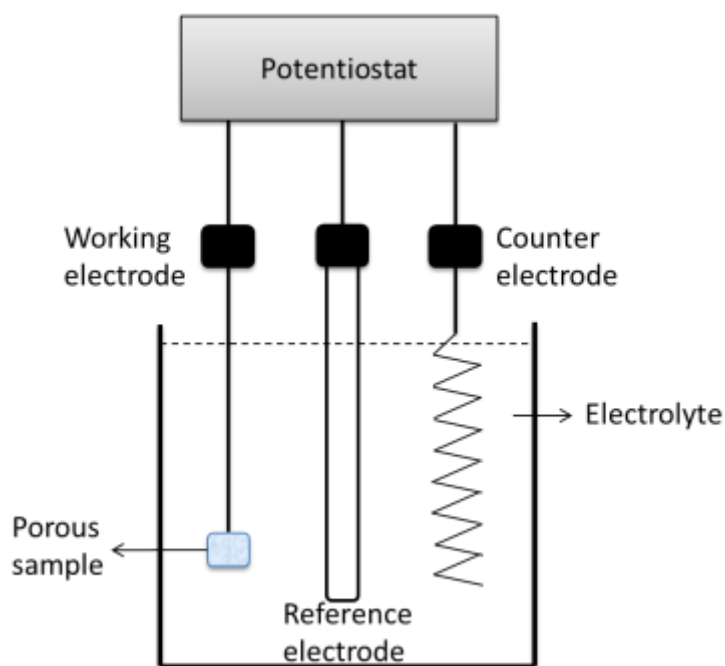


Fig. 3. 4: Schematic diagram of the three-electrode electrochemical cell used for the CV measurement (Zhu and Zhao 2017).

### 3.4.2 Procedure of Measurement

The electroactive surface area of the porous Ni samples was measured by the peak current method (Rohatgi 2000), the details of which were reported in (Diao et al. 2015). This cyclic voltammetry method is based on the fact that the peak current for a reversible electron transfer reaction is proportional to the surface area and the proportionality coefficient can be determined experimentally using samples with known surface areas.

The measurement was carried out on an electrochemical workstation with the three-electrode configuration at room temperature. The working electrode was the porous Ni sample. The reference electrode was a saturated Calomel Electrode (SCE, +0.241V vs standard hydrogen electrode) and the counter electrode was a platinum wire. The electrolyte was a 1 mM  $K_4[Fe(CN)_6]$  in 0.1 M KOH solution, which was de-aerated with argon for 5 minutes before the measurement. The potential window was from -0.2 to 0.4 V vs. SCE and the scan rate range was from 0.005 to 0.3 V/s. The anodic peak appears at around 0.25 V, as shown in Fig. 3.5. The electrochemical reaction during the scan was in the form of:

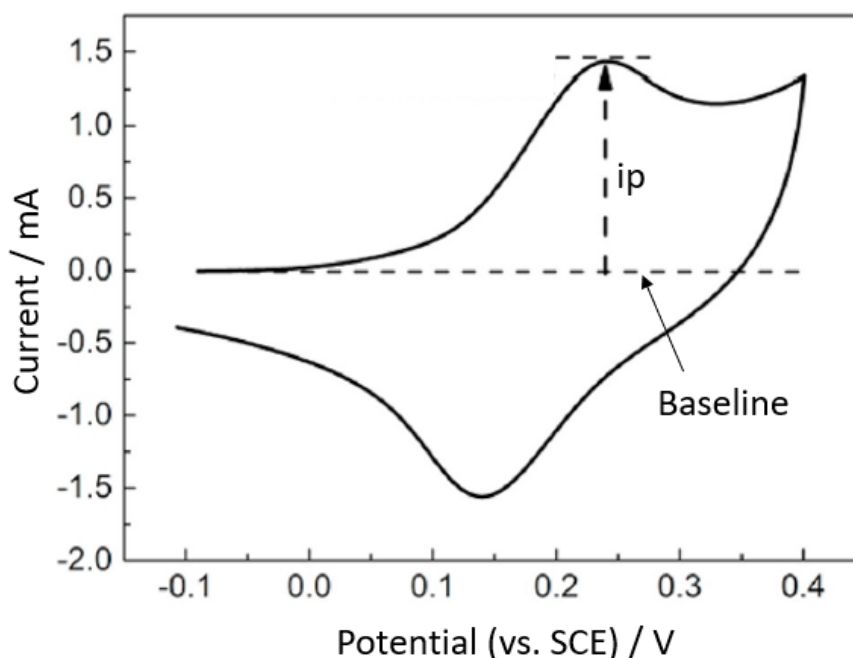
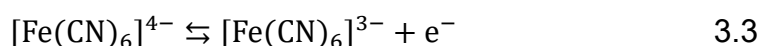


Fig. 3. 5: A typical current-potential plot of redox reaction of ferrocyanide (Zhu and Zhao 2019).

The peak current,  $i_p$ , predicted for a reversible electron transfer in the diffusion-controlled regime can be calculated by the equation 2.7.

In order to eliminate the effect of electrolyte's resistance, compensated work was considered in this study, because a significant distortion in the voltammetry will appear if the resistance of the electrolyte is not compensated (Diao et al. 2015). The potential at the peak current could shift positively and affect the kinetics of the reaction, the details of which will be discussed in Chapter 7. The 'IR-compensation' feature of the potentiostat was set up to compensate for the resistance of the electrolyte automatically.

### **3.5 Measurement of Real Surface Area**

The real surface area of the porous Ni samples was measured by the double layer capacitance (DLC) method, a voltammetry approach which can obtain the real surface area by determining the apparent total capacitance of a porous electrode (Diao et al. 2015, Trasatti and Petrii 1991, Campbell et al. 2004). The real surface area can be determined by equation 2.4. The reference capacitance per unit area is  $28 \mu\text{Fcm}^{-2}$  for Ni in 8 M KOH, and therefore the real surface area of porous Ni can be calculated by dividing the capacitance obtained by adsorption/desorption by  $28 \mu\text{Fcm}^{-2}$  (Gagno 1976).

The measurement was carried out on the electrochemical workstation with the same three-electrode configuration as for the electroactive surface area measurements, at room temperature. The electrolyte was an 8 M KOH solution, which was de-aerated with argon for 5 minutes before the measurement. The potential window was chosen in a non-redox reaction potential range from -0.8 to -0.7 V vs. SCE and the scan rate was set in the range of 0.05 to 1 V/s.

### **3.6 Measurement of Mass Transfer Performance**

The mass transfer performance of the porous metals was measured by the limiting current method (Recio et al. 2013, Zhu and Zhao 2017). The LCS porous Ni sample with a porosity of around 80% and pore size in the range of 1000 – 1500  $\mu\text{m}$  was used as the substrates for this measurement. The mass transfer performance of the LCS porous Ni samples with different fine Ni powder ratios of 0%, 20%, 40%, 60%, 80% and 100% and the LCS/DHBT porous Ni samples with different manufacturing parameters (as shown in section 3.3.2) were investigated under various electrolyte fluid velocities of 1.32 – 6.66 cm/s.

#### **3.6.1 Experimental Apparatus**

The electrochemical configuration used to characterize the mass transfer

performance consisted of two electrolyte tanks, a three-electrode system, and a fluid transport system as shown in Fig. 3.6. The workstation and the three-electrode configuration were the same as for the surface area measurements.

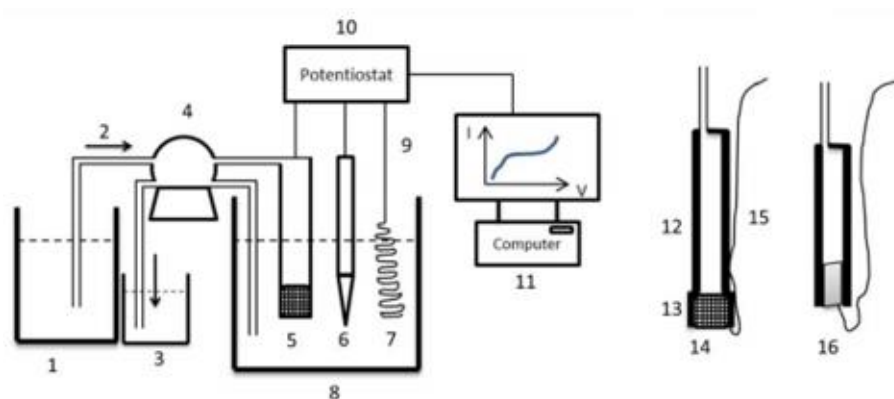


Fig. 3. 6: Schematic of the electrochemical configuration for the mass transfer measurement. 1 is electrolyte reservoir, 2 is the solution input pipe, 3 is waste solution tank, 4 is a peristaltic pump, 5 is working electrode, 6 is SCE reference electrode, 7 is Pt coil counter electrode, 8 is the glass vial, 9 is conducting wire, 10 is potentiostat, 11 is computer monitor, 12 is an acrylic tube, 13 is water barrier film, 14 is porous working electrode, 15 is conducting wire and 16 is mirror-polished Ni plate (Zhu and Zhao 2017).

### 3.6.2 Determination of Mass Transfer Performance

The measurement was carried out at room temperature. The electrolyte was a 1 mM  $K_4[Fe(CN)_6]$  in 1 M  $Na_2CO_3$  solution, which was de-aerated with argon for 5 minutes before the measurement. The potential window was from -1.2 to 0.2 V vs. SCE, because the mass-transfer controlled regime is at a potential range

of around -0.8 to 0 V vs. Ag/AgCl as shown in Fig 3.7. The scan rate was set at 0.005 V/s. The fluid flow velocities were 1.32, 2.22, 4.38 and 6.6 cm/s.

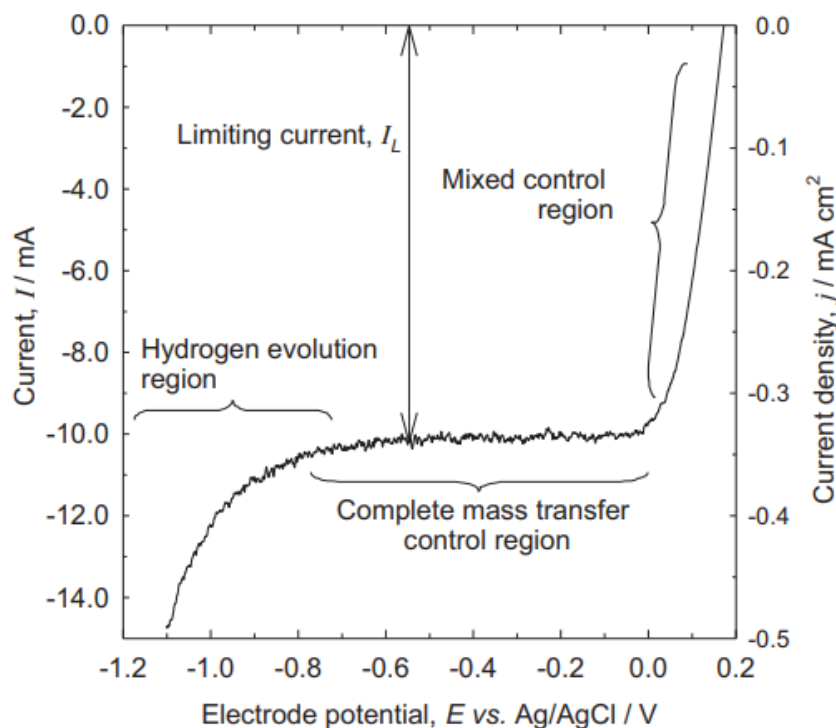


Fig. 3. 7: Typical current vs potential plot for the reduction of  $\text{Fe}(\text{CN})_6^{3-}$  in  $10^{-4}$  M  $\text{K}_3\text{Fe}(\text{CN})_6$  +  $10^{-3}$  M  $\text{K}_4\text{Fe}(\text{CN})_6$  + 1 M  $\text{Na}_2\text{CO}_3$  at a porous Ni electrode with a scan rate of 0.005 V/s (Recio et al. 2013).

In mass transfer controlled regimes, the reaction depends on the rate of reactant transport to the electrode surface. The mass transfer performance,  $kA$  can be characterized by the product of mass transfer coefficient,  $k$ , and active electrode area,  $A$ :

$$kA = \frac{I_L}{nF\Delta C} \quad 3.4$$

where  $I_L$  is the limiting current,  $n$  is the number of electrons exchanged in the reaction,  $F$  is the Faraday constant and  $\Delta C$  is the concentration difference of



the electroactive species between the bulk solution and the electrolyte at the electrode surface.

### 3.7 Correlation between Peak Current and Glucose Concentration

The catalytic activity of the  $\text{Ni}^{2+}/\text{Ni}^{3+}$  couple in an alkaline medium allows fast catalysis of glucose to gluconolactone as shown in equation 2.15 – 2.17. An anodic peak will form if glucose exists in the solution. The current and potential of the peak depends on the concentration of the glucose, as shown in Fig. 3.8. The peak current increases with increasing the concentration of glucose. It is worth to mention that with the increase of glucose concentration, the current peak shifts positively.

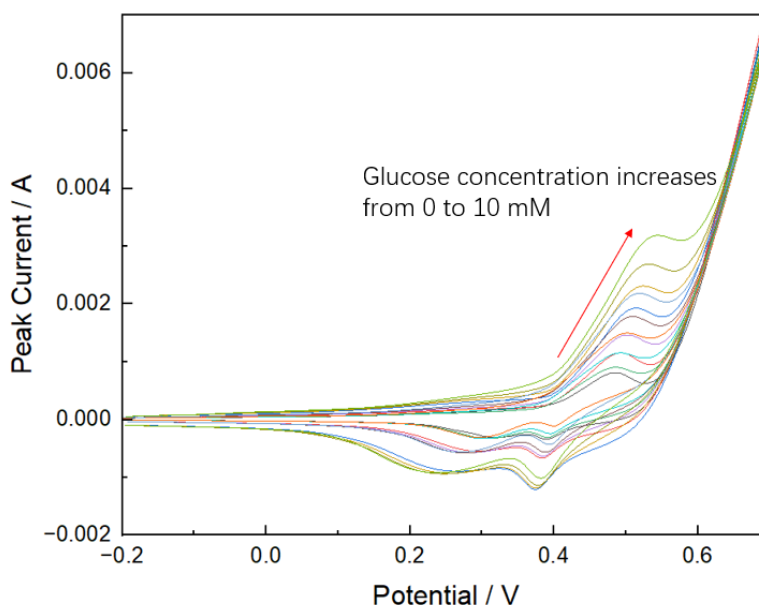


Fig. 3. 8: Current versus potential profiles as glucose concentration increases from 0 to 10 mM.

The Ni plate, LCS porous Ni and LCS/DHBT porous Ni with the same geometric surface area of 4 cm<sup>2</sup> were investigated in this experiment. The manufacturing parameters of the LCS/DHBT porous Ni samples were shown in section 3.3.2. The glucose measurement performance of the LCS/DHBT porous Ni samples was characterised in the same three-electrode electrochemical system (Autolab PGSTAT 101) by the cyclic peak current method. The electrolyte was a 0.1 M KOH background solution and the concentration of glucose was changed from 10 µM in a step of 50 µM to 500 µM and increased until a peak current could not be obtained. The sweep potential window was from -0.2 to 1 V and the scan rate was in the range of 25 to 300 mV/s. The anodic peak current was measured at each glucose concentration.

### 3.8 Error and Uncertainty

Mean values were used to characterize the errors in this study. Each experiment was repeated three times under the same conditions to obtain the mean value by:

$$X = \frac{1}{n} \sum_{i=1}^n x_i \quad 3.5$$

where  $X$  is the mean value,  $n$  is the number of measurements and  $x_i$  is the value of each measurement. The standard deviation was obtained by the following equation:

$$\frac{\Delta x}{X} = \frac{\sqrt{\sum_i (x_i - X)^2 / (n-1)}}{X} \times 100\% \quad 3.6$$

The error and standard deviation of measurements in this work were less than 5%.

In this thesis, propagation of uncertainty is used to estimate the uncertainty of the experiments. The uncertainty can be determined by the equation:

$$\omega_R = \sqrt{(\omega_1 \frac{\partial R}{\partial x_1})^2 + (\omega_2 \frac{\partial R}{\partial x_2})^2 + \dots + (\omega_n \frac{\partial R}{\partial x_n})^2} \quad 3.7$$

where  $\omega_1, \omega_2, \dots, \omega_n$  are the uncertainties in the independent variables  $x_1, x_2, \dots, x_n$ .

For example, in the gravimetric real surface area measurements, the sources of uncertainty are the mass of the sample, the current and the scan rate in the reaction. The uncertainty of the surface area can be obtained by

$$\omega_A = \sqrt{(\omega_I \frac{\partial A}{\partial I})^2 + (\omega_v \frac{\partial A}{\partial v})^2 + \dots + (\omega_m \frac{\partial A}{\partial m})^2} \quad 3.8$$

where  $\omega_I, \omega_v$  and  $\omega_m$  are the uncertainties in reaction current, scan rate and sample mass. The uncertainties of the parameters due to the measurement equipment are summarized in Table 3.6.

Table 3. 6 Uncertainty of physical parameters in this study.

Parameter	Uncertainty
Pore size	0.5 $\mu\text{m}$
Porosity	<0.25%
Mass	0.001 g
Volume	0.01 $\text{cm}^3$
Compaction pressure	0.05 MPa
Temperature	0.5 $^{\circ}\text{C}$
Time	0.01 s
Potential	0.01 mV
Current	0.01 mA
Fluid velocity	0.005 mL/s
Surface area	<5%

## **Chapter 4 Real and Electroactive Surface Areas of LCS Porous**

### **Ni**

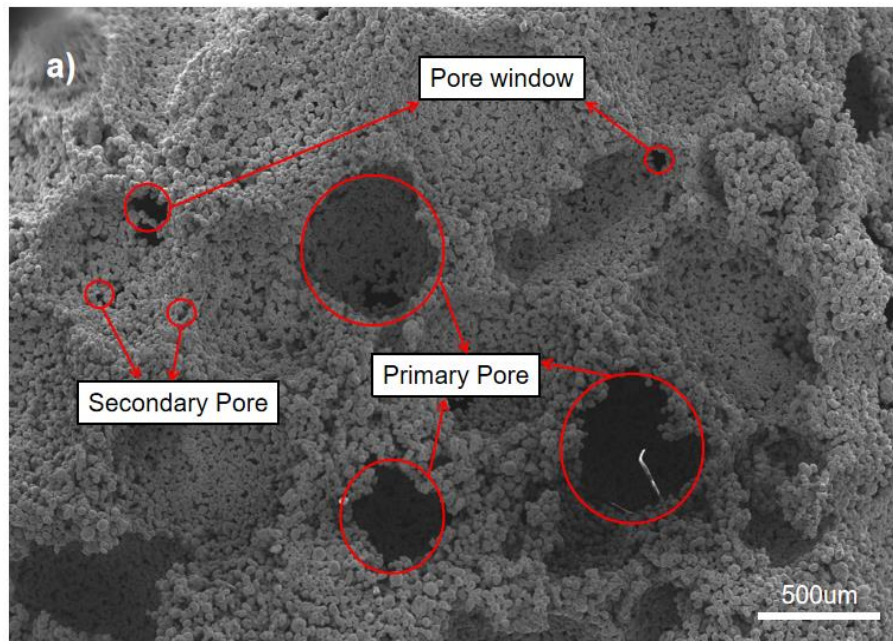
#### **4.1 Introduction**

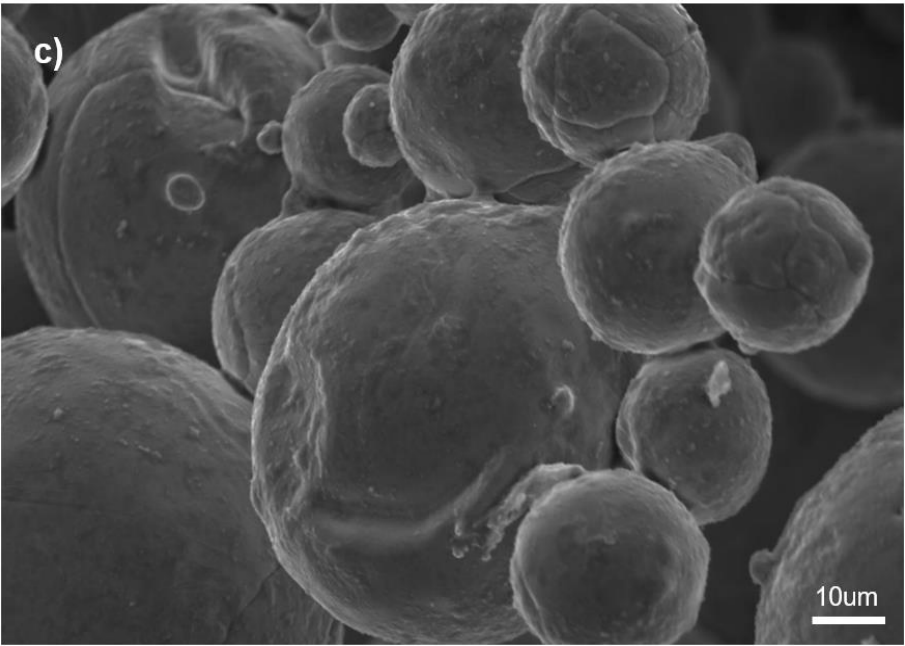
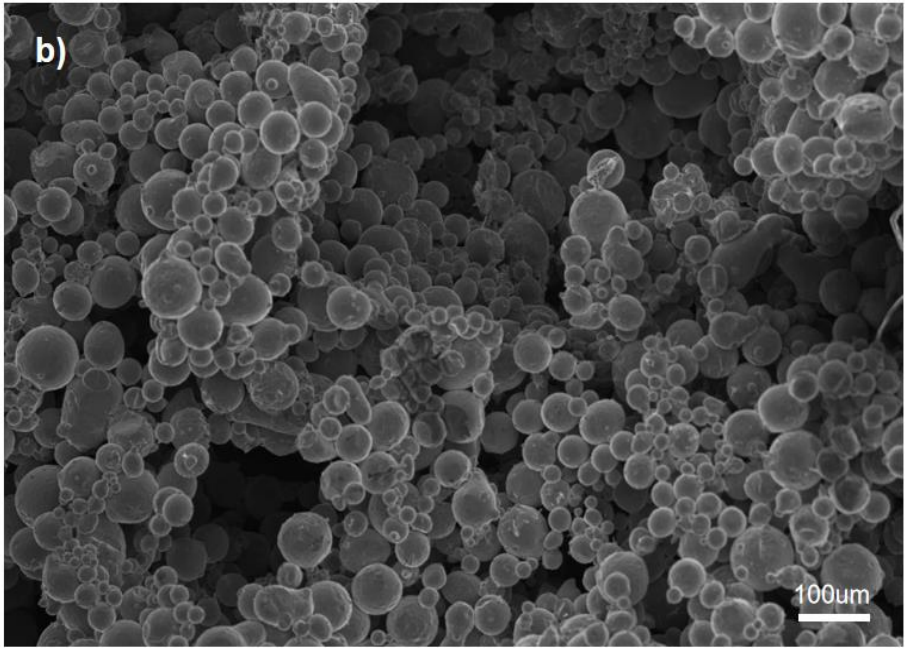
This chapter presents and discusses the experimental results on the real and electroactive surface areas of the porous Ni samples manufactured by the LCS process. The investigations include the effects of porous structure and manufacturing processing parameters on the surface morphology, real surface area and electroactive surface area. The structural and processing parameters studied include pore size, porosity, content of fine Ni powder, compaction pressure and sintering temperature. The Taguchi design method was employed to identify and rank the effects of parameters on the surface areas. The effects of fine Ni content were investigated further in detail.

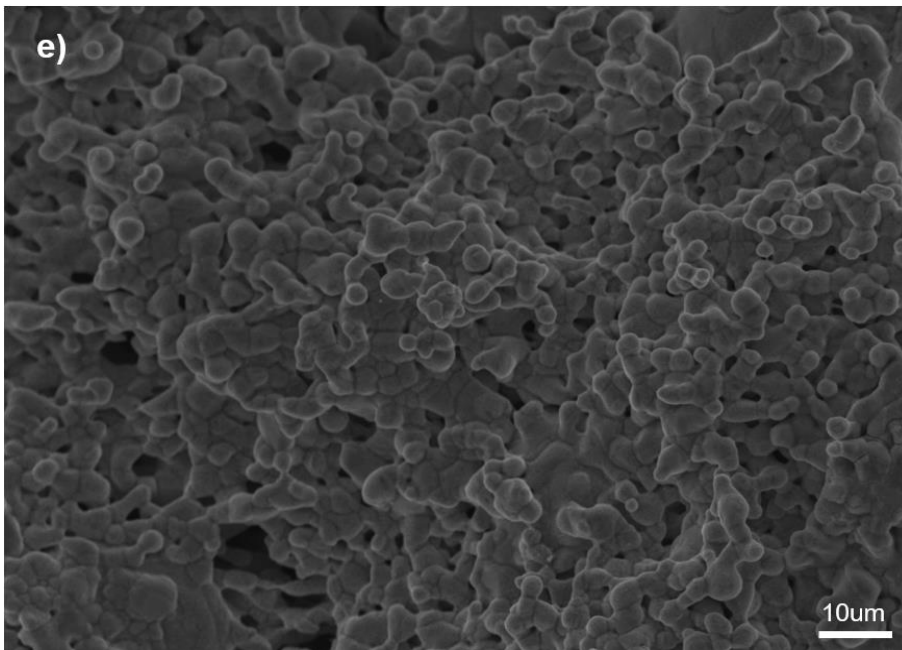
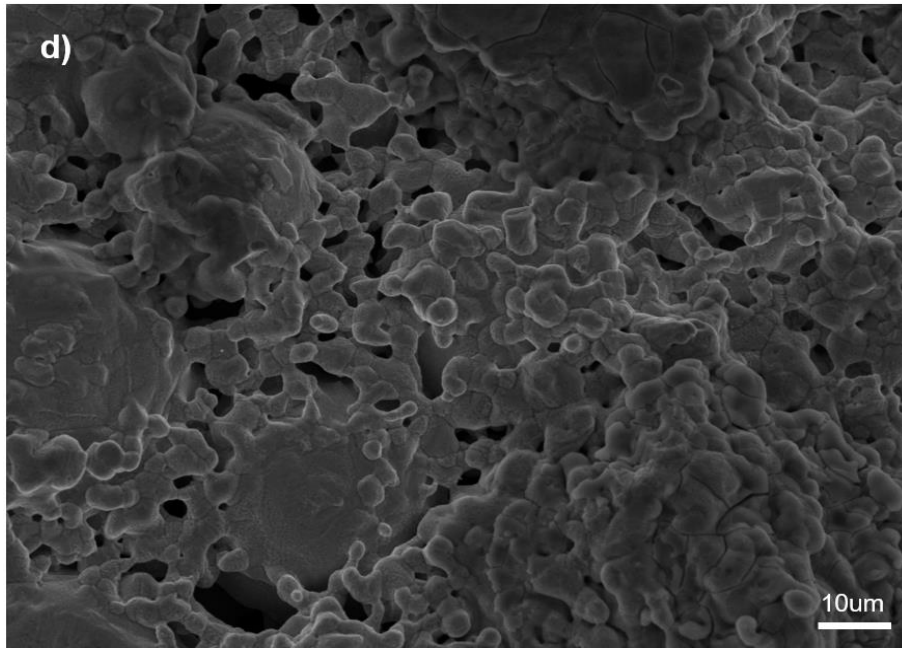
#### **4.2 Surface Morphology**

The microstructures of the LCS Ni samples manufactured under different processing conditions are shown in Fig. 4.1. It is observed that the LCS porous Ni samples have interconnected pores and rough surfaces. There are two different pore sizes, marked as primary pore and secondary pore (Fig. 4.1a). The primary pores are formed by eliminating the space holder  $K_2CO_3$  particles and the secondary pores are formed by the interstices and gaps between the

metal particles. The primary pores are interconnected through small windows because the  $K_2CO_3$  particles are randomly distributed in the metal matrix and in contact with each other during manufacturing. The shape and size of the primary pores are determined by the  $K_2CO_3$  particles, as they are negative replicas of the  $K_2CO_3$  particles. The secondary pores are much smaller than the primary pores as shown in Fig. 4.1a, because the metal particles are smaller than the space holder particles and the interstices are even much smaller after sintering.







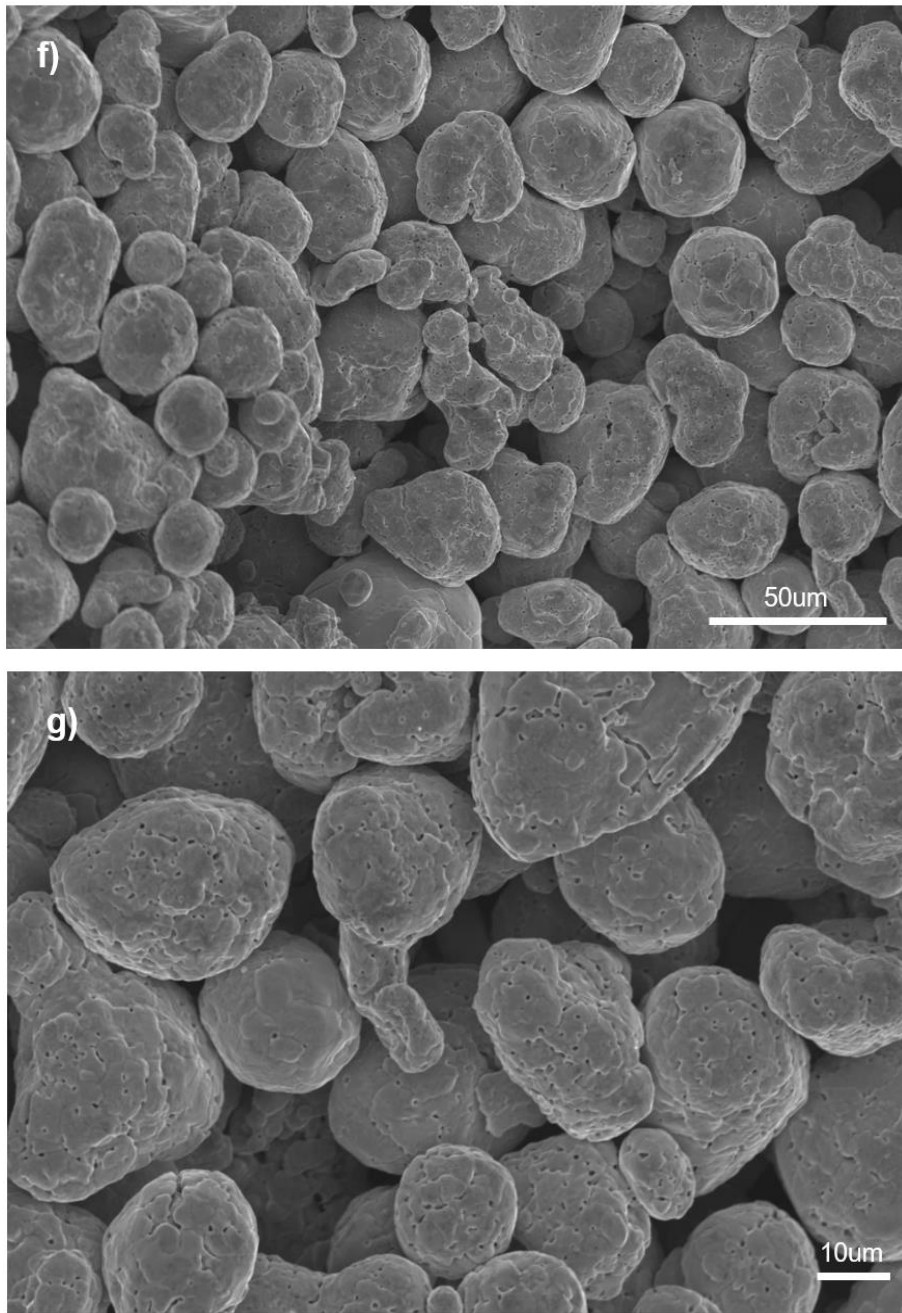


Fig. 4. 1:SEM micrographs of LCS porous Ni samples with benchmark processing parameters (pore size 425 – 710  $\mu\text{m}$ , porosity 60%, coarse Ni powder only, compaction pressure 200 MP and sintering temperature 850 $^{\circ}\text{C}$ ) or with one parameter different from the benchmark condition: a) benchmark, low magnification; b) benchmark, higher magnification, c) sintering temperature 850  $^{\circ}\text{C}$ , d) fine Ni content 60%, e) fine Ni content 100%, f) no



compaction and g) sintering temperature 700 °C.

Fig. 4.1c, d and e show the LCS porous Ni samples with no, 60% and 100% fine Ni powder ratio, respectively, sintered at 850°C for 4 hours. The samples formed with fine metal particles show a high degree of sintering with large sintering neck, because the high surface active energy promotes atomic diffusion under the high-temperature sintering condition. In contrast, the sample formed with only the coarse Ni powder shows narrower sintering necks between the metal particles.

Fig. 4.1f shows an LCS porous Ni sample manufactured without applying compaction pressure during the compaction stage. It shows that the metal particles are loosely sintered with very thin sintering necks. In comparison, the sample manufactured with a 200 MPa compact pressure shows stronger sintering necks (Fig. 4.1b, d). This is because the high compact pressure presses the metal particles closer, enhancing the contacts between the metal particles and reducing the voids and interstices inside the metal matrix.

Comparing Fig. 4.1c and g shows that sintering temperature significantly affects the surface morphology. The porous Ni sample manufactured by sintering at 700°C (Fig. 4.1g) shows very little sintering necking with the metal particles weakly sticking together due to slow atomic diffusion. Increasing the sintering

temperature to 850°C resulted in larger sintering necks, and flatter and smoother surfaces, due to faster atomic diffusion and reduction of voids and cavities.

Low compaction pressure or low sintering temperature can both result in insufficient sintering and therefore more secondary pores in the metal matrix (Fig. 4.1f and g). The secondary pores are voids or interstices between the metal particles. They are irregular in shape and are typically from submicron to a few dozen microns. The larger secondary pores exist at locations of loose metal particle packing due to low compaction pressure, while the smaller secondary pores are associated with places of closer particle packing due to high compaction pressure.

Surface morphology of LCS porous Ni can be altered by chemical treatments. Fig. 4.2 shows the surface morphology after chemical treatment by 20% diluted hydrochloric acid. The surface becomes flat and smooth as the small protrusions and defects are removed after the diluted hydrochloric acid treatment (Fig. 4.2). The treatment does not change the porous structure, as the mass loss was less than 1% of the porous sample.

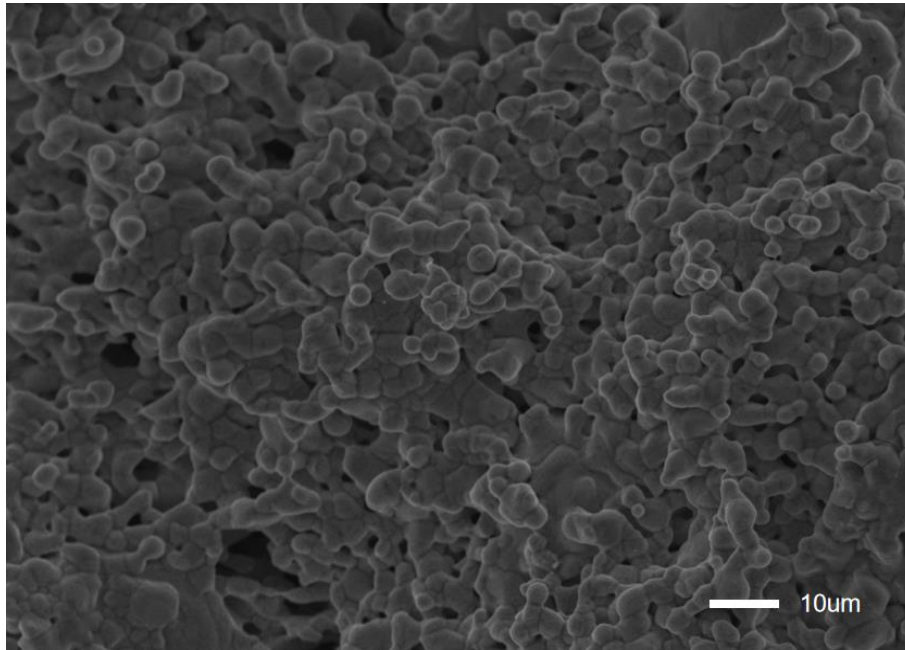


Fig. 4. 2: Surface morphology of porous Ni sample treated with 20% diluted hydrochloric acid for 60 mins.

Fig. 4.3 shows the surface morphology after chemical treatment by 98% concentrated sulfuric acid. The surface becomes rough after etching with the concentrated sulfuric acid (Fig. 4.3). However, the treatment of Ni in concentrated sulfuric acid can lead to oxidation of Ni, so further treatment is necessary to remove the oxide layer. In this experiment, the porous samples after the sulfuric acid etching were cleaned with plenty of distilled water and then soaked with the diluted hydrochloric acid for several seconds in an ultrasonic cleaner to remove the passivation film. The EDX analysis of the sample (Fig. 4.4) shows that only Ni element is detected, which indicates that the chemical treatment does not change the composition of the samples.

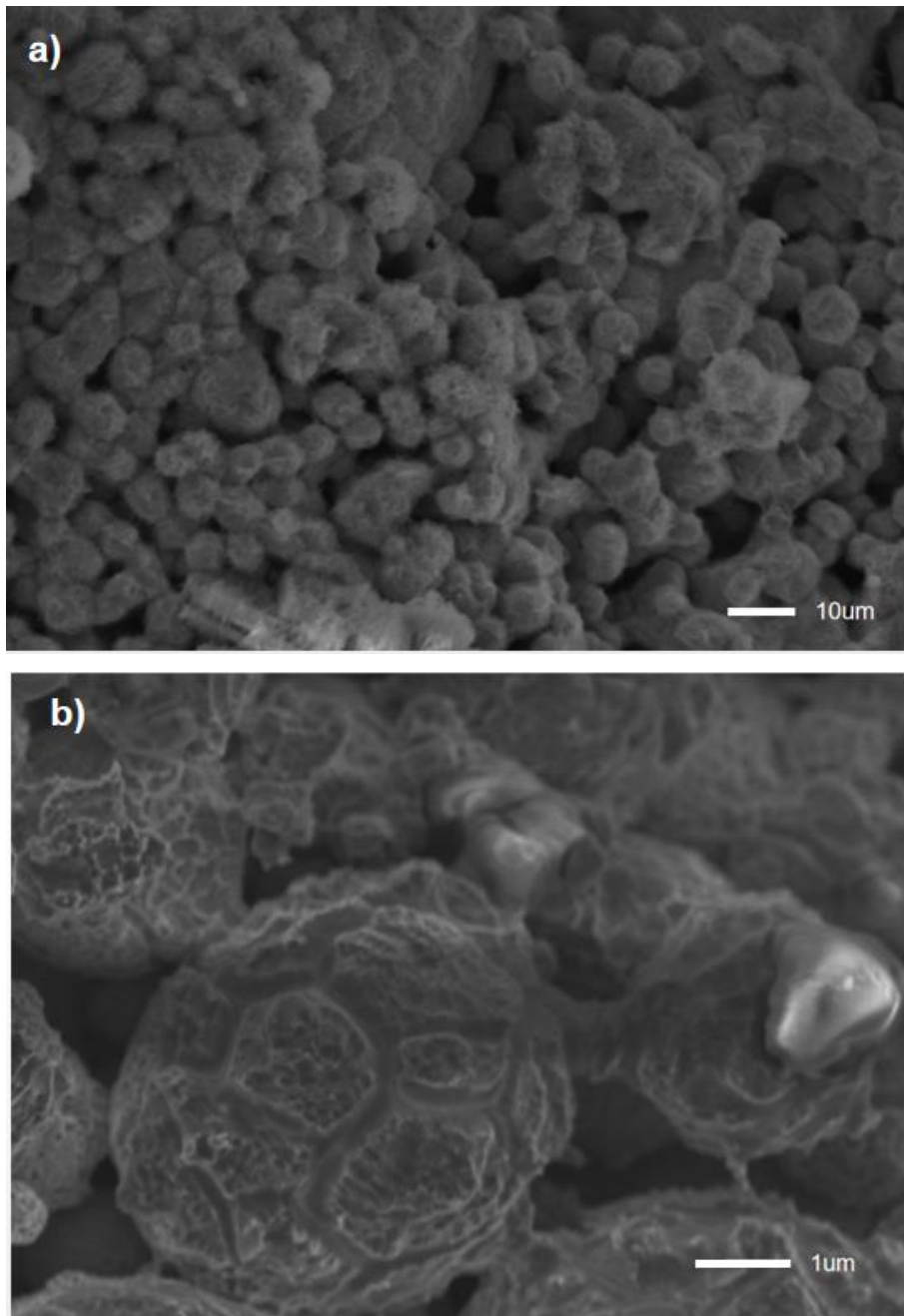


Fig. 4. 3: Surface morphology of porous Ni sample treated with concentrated sulfuric acid for 60 min, a) low magnification and b) high magnification.

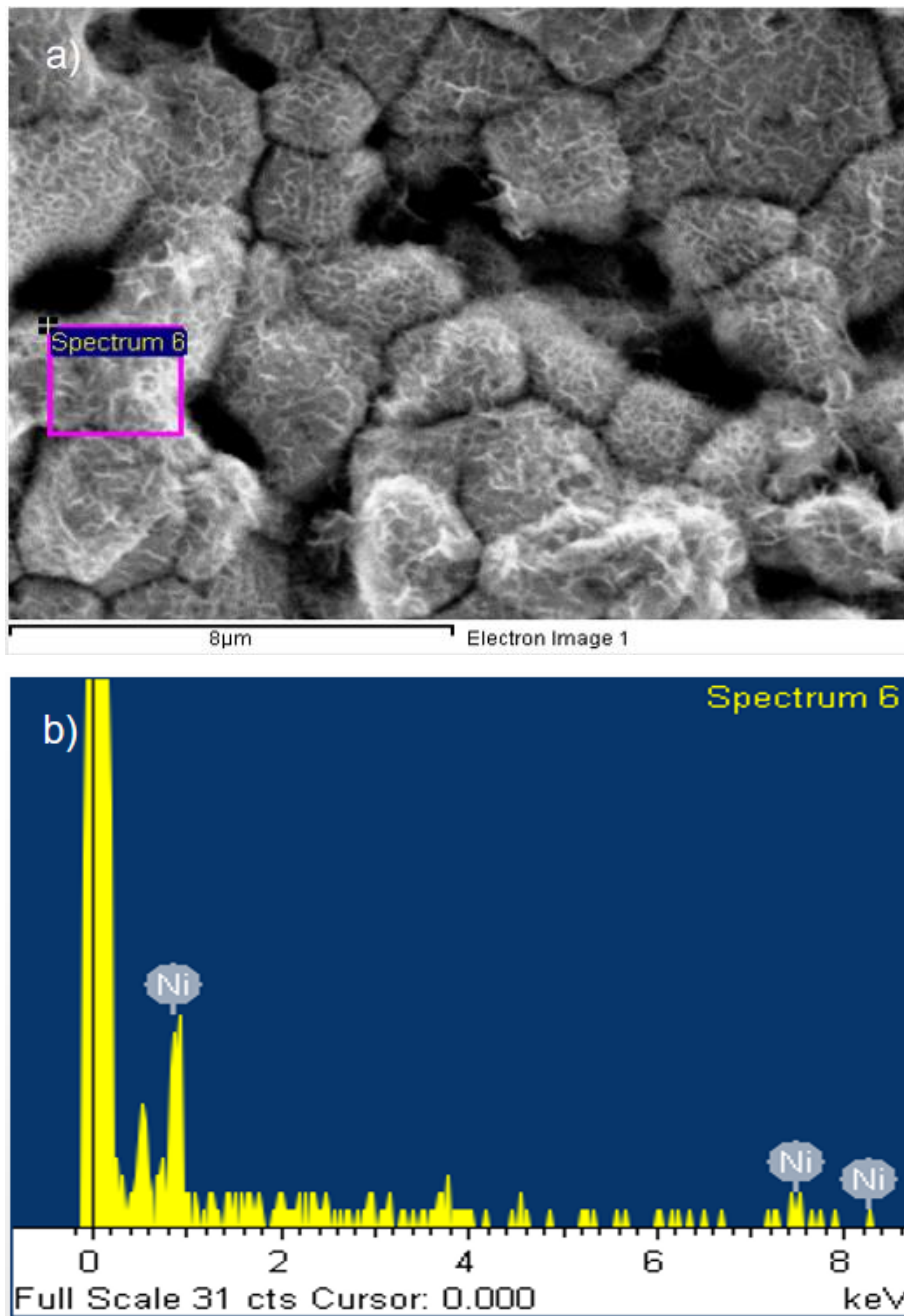


Fig. 4. 4: a) SEM micrograph and b) EDX spectrum of LCS porous Ni sample treated with concentrated sulfuric acid for 60 min and 20% diluted hydrochloric acid for 20 s.

### 4.3 Effect of Processing Parameters on Real Surface Area

Fig. 4.5 shows the effects of the pore size, porosity, fine Ni content, compaction pressure and sintering temperature on the volumetric and gravimetric real surface areas of the porous Ni samples. The volumetric and gravimetric real surface areas varied in the ranges of 540-1550  $\text{cm}^{-1}$  and 200-650  $\text{cm}^2/\text{g}$ , respectively, for the parameter values studied in this experiment. It is shown that the fine Ni powder ratio has a huge effect on the real surface area. The volumetric and gravimetric surface areas increased 2.96 and 3.25 times, respectively, when the content of fine Ni powder was increased. With increasing porosity, the volumetric real surface area decreased while the gravimetric real surface area increased slightly. Pore size, compaction pressure and sintering temperature had no significant effect on the real surface areas. In general, both volumetric and gravimetric real surface areas slightly decrease with increasing the pore size, compaction pressure and sintering temperature.

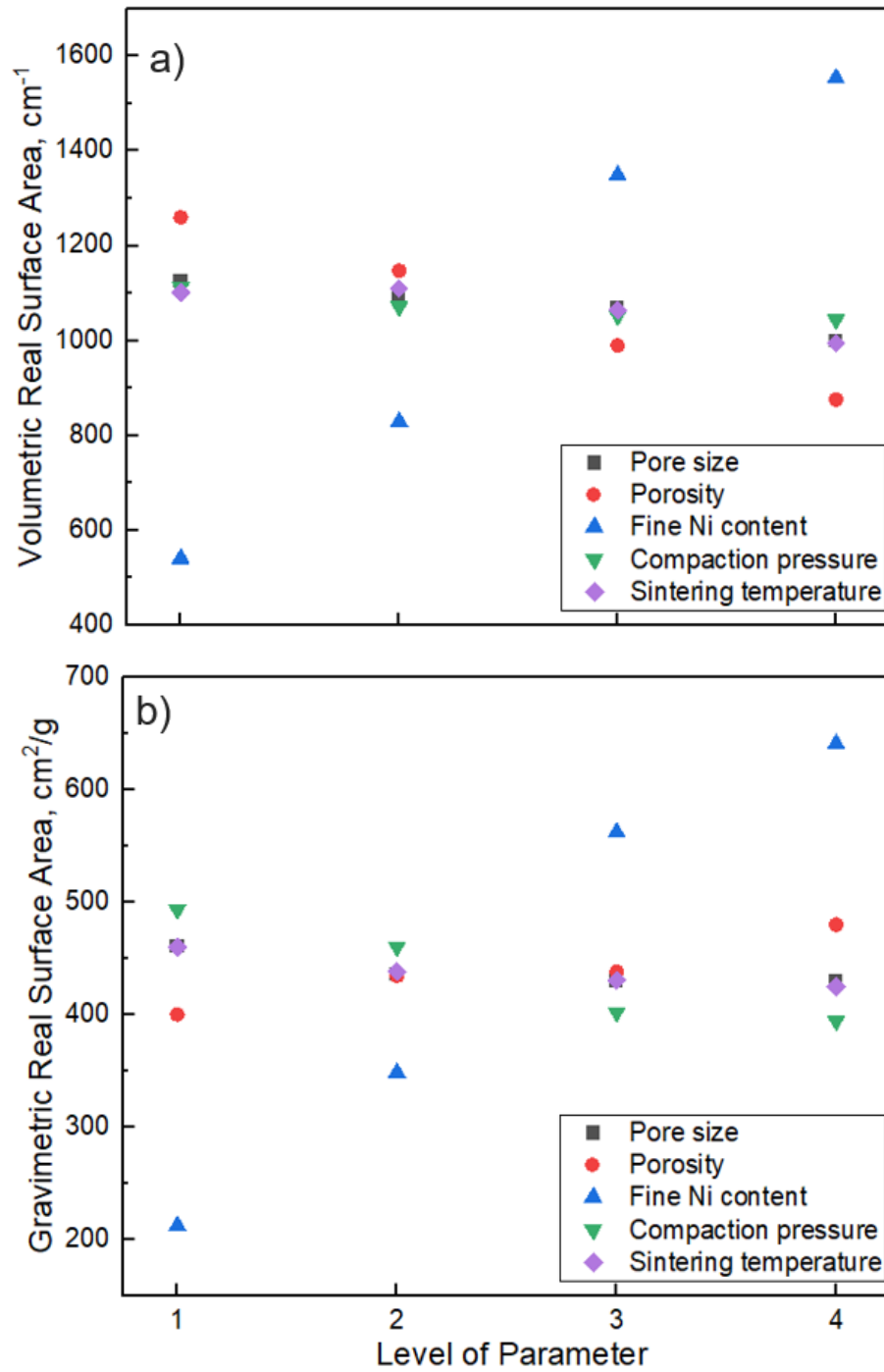


Fig. 4. 5: Variations of (a) volumetric and (b) gravimetric real surface areas with level of parameter.

Porosity and pore size are two structural parameters of the LCS porous Ni samples, which have different effects on the real surface area. The real surface

area is mainly determined by the amount of Ni particles in the porous Ni sample, because it is the total surface area of all the Ni particles accessible by the electrolyte, excluding the surface area loss due to the formation of sintering necks (Diao et al. 2015, Zhao et al. 2001). For any given volume of a porous Ni sample, a higher porosity means less metal and therefore a lower volumetric real surface area. For a given mass of porous Ni sample, porosity has little effect on the real surface area, i.e., the gravimetric real surface area is insensitive to porosity. For fixed porosity, the amount of metal particles is constant, and therefore, both volumetric and gravimetric real surface areas are insensitive to pore size. However, changing porosity or pore size can affect the electrolyte accessibility to secondary pores, which can have some small effects on the real surface area. The effects of porosity and pore size on the real surface area are consistent with the previous results reported by Diao et al. (2015).

Moreover, the detects and patterns on the particles would also provide a large number of activated sites for reaction during the electrochemical process. Hence, the different measurement methods in electrochemical processes would significantly affect the surface area for example, if the detection probe is thinner than the detection of the particle surface, the real surface area is obtained. The electrochemical surface area is obtained if the electrolyte can access all interstices and voids and the detection probe is thinner than the



interstices. If the scale of probe is thicker than the magnitude of the secondary pore but thinner than the primary pore, only the electroactive surface area of large pores can be detected.

#### **4.4 Effect of Processing Parameters on Electroactive Surface Area**

Fig. 4.6 shows the effects of the five processing parameters on the volumetric and gravimetric electroactive surface areas of the porous Ni samples. The volumetric and gravimetric electroactive surface areas varied in the ranges of 75-115  $\text{cm}^{-1}$  and 30-55  $\text{cm}^2/\text{g}$ , respectively, for the parameter values studied in this experiment. The electroactive surface area is approximately one order of magnitude lower than the real surface area, because of the scale of the diffusion layer is comparable to the size of the secondary pores. Both volumetric and gravimetric electroactive surface areas increased with porosity and fine Ni powder ratio and decreased with pore size, compaction pressure and sintering temperature.

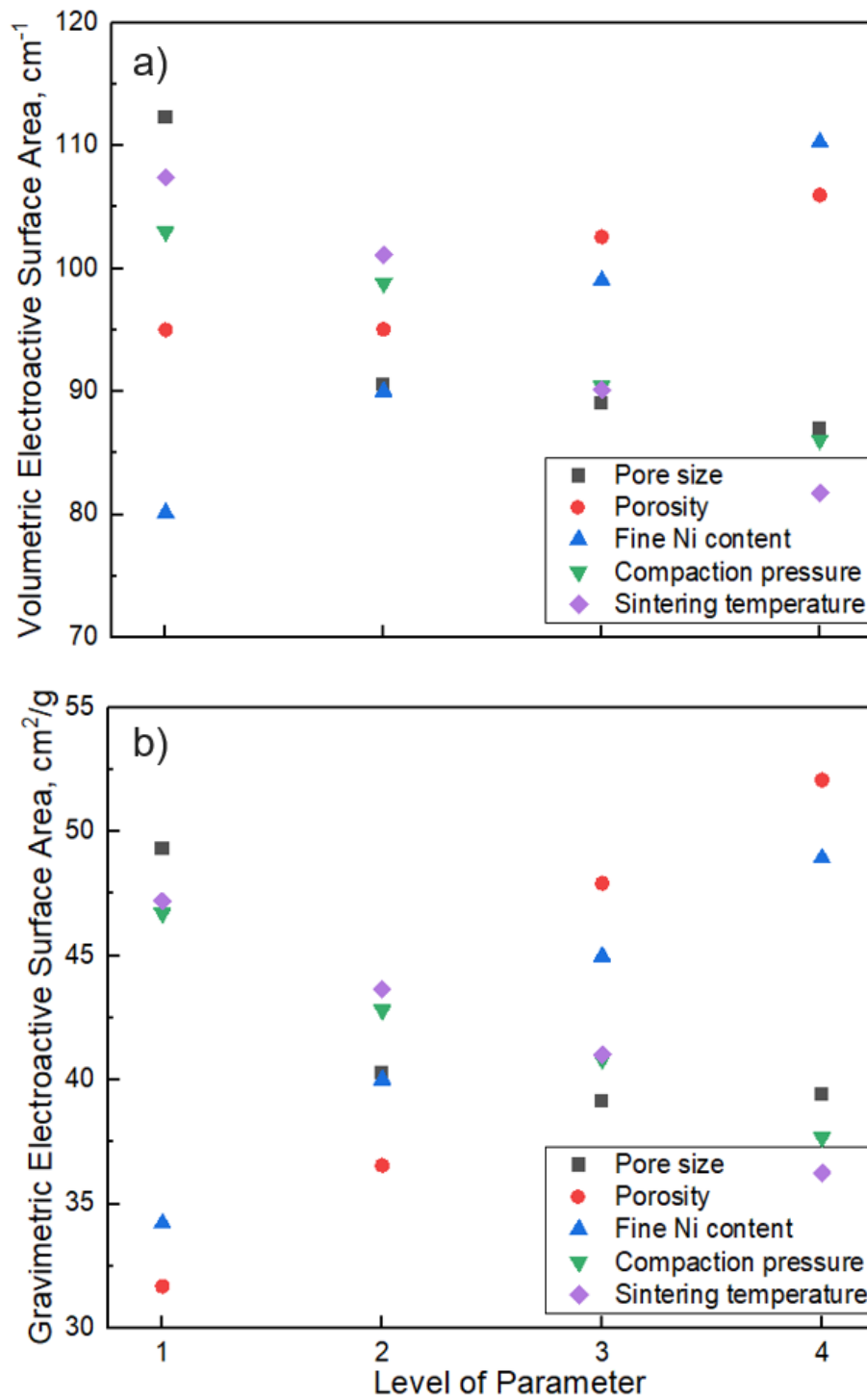


Fig. 4. 6: Variations of (a) volumetric and (b) gravimetric electroactive surface areas with level of parameter

For volumetric electroactive surface area, adding fine Ni powder had the most significant effect, with the electroactive surface area increasing by 40% when the fine Ni content increased from 0 to 40%. The electroactive surface area was increased by 11.6% when the porosity was changed from 65% to 80% and decreased by 17.9%, 16.5% and 25.9% when the pore size, compact pressure and temperature, respectively, were increased in the studied ranges. For gravimetric electroactive surface area, the effect of porosity is more noticeable. The electroactive surface area was increased by 62.5% and 44.1% when the porosity and fine Ni content, respectively, were increased in the studied ranges. It was decreased by 20.2%, 20.2% and 23.4% when the pore size, compact pressure and sintering temperature, respectively, were increased in the studied ranges. This is due to the decreases in the amount and size of the secondary pores.

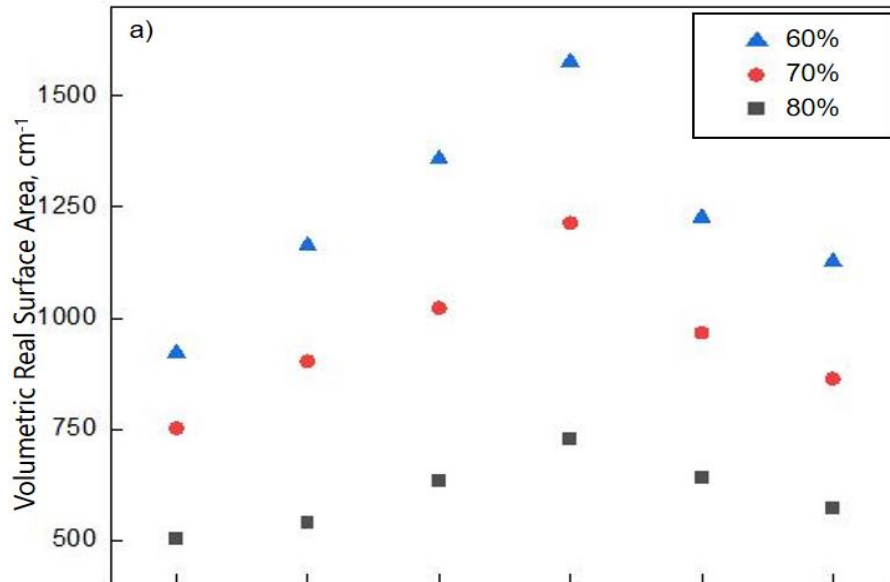
The electroactive area is determined by the internal porous structure and is sensitive to both primary and secondary pores. The primary pores are characterized by porosity and pore size. A higher porosity means more primary pores in the porous sample and therefore provides more total surface area. For a fixed porosity, larger pores lead to fewer primary pores in the porous sample and overall less specific surface per unit volume. In other words, increasing pore size results in a lower electroactive surface area.

The secondary pores can also contribute to the electroactive surface area, depending on the diffusion layer thickness. In many cases, the secondary pores can provide more electroactive surface area than the primary pores. At a fixed porosity, decreasing the pore size means more pores inside the metal matrix, and therefore larger internal surface area. Secondary pores are affected by compaction pressure, sintering temperature and Ni particle size. A higher compaction pressure removes or reduces more secondary pores, leading to reduced electroactive surface area. A higher sintering temperature promotes more rapid diffusion of Ni atoms on the surface of the Ni particles during sintering, which causes a smoother surface and therefore decreased electroactive surface area. The effects of fine Ni powder ratio (from 0% to 100%) will be discussed in the next two sections when further experimental data are presented.

#### **4.5 Effect of Fine Ni Powder ratio on Real Surface Area**

The variations of volumetric and gravimetric real surface areas with fine Ni powder ratio are shown in Fig. 4.7. The real surface areas increased with increasing fine Ni content from 0 to 60% and then decreased with increasing fine Ni content further. The specific real surface areas peaked at the fine Ni content at 60%. At low and intermediate fine Ni powder ratio, the metal matrix can be regarded as a skeleton of coarse Ni particles covered with fine Ni

particles. Most fine Ni particles distribute evenly at the surface of the space holder particles, i.e., primary pores. They are not much conglomerated and therefore most of the fine particles contribute to the real surface area. For the same amount of metal matrix, as discussed in Section 4.1, more fine Ni particles lead to a higher surface area. On the other hand, if the fine Ni powder ratio is too high, the fine particles tend to agglomerate and form thicker sintering necks during sintering. This is because small particles have higher surface energy and enlarged area of contact, the diffusion paths of the metal atoms are shorter, and therefore the fine particles can sinter more readily at high temperature (Qin et al. 2016). The high degree of sintering associated with fine Ni particles can result in reduced real surface area.



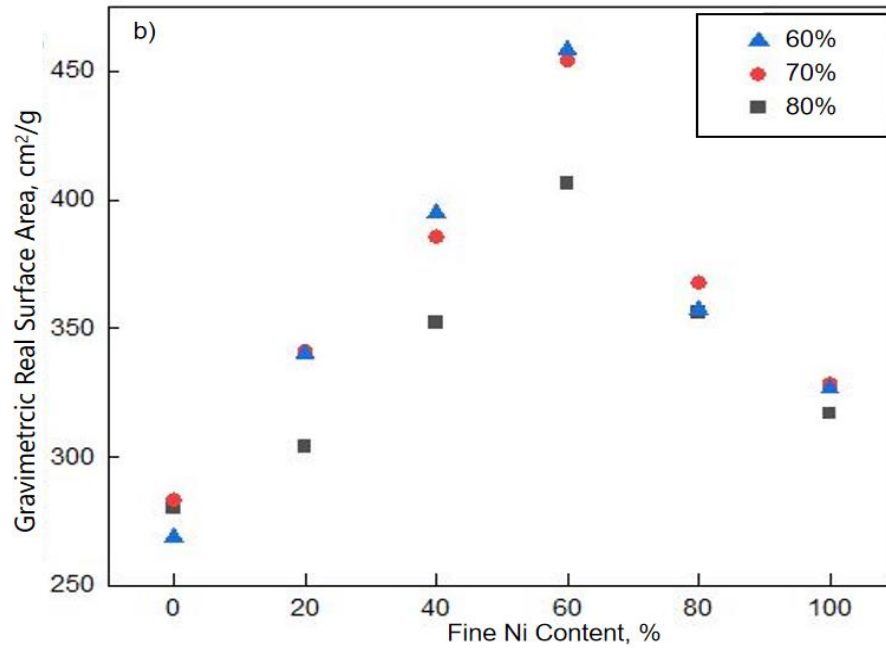


Fig. 4. 7: Variations of a) volumetric and b) gravimetric real surface areas with fine Ni ratio at different porosities (see inset). Other parameters: pore size 425 – 710  $\mu\text{m}$ , compaction pressure 200 MP and sintering temperature 850  $^{\circ}\text{C}$

#### 4.6 Effect of Fine Ni Powder ratio on Electroactive Surface Area

The variations of volumetric and gravimetric electroactive surface areas with fine Ni powder ratio at selected scan rates are shown in Fig. 4.8. At any given scan rate, the volumetric and gravimetric electroactive surface areas increased with increasing fine Ni content, especially more markedly at higher scan rates. At a scan rate of 0.4 V/s, for example, the electroactive surface area of the sample with 100% fine Ni powder is 1.7 times of the sample with 100% coarse Ni powder. This is because smaller particles provide a rougher surface morphology and produce smaller secondary pores. The diffusion layer is thin

and most of details on the surface of the porous Ni can be detected, which causes an increase in the electroactive surface area (Molina et al. 2013, Amatore et al. 2001). Increasing fine Ni powder ratio in the Ni powder mixture reduces the mean granularity of the mixture and therefore results in a reduced overall diffusion layer thickness. As a result, extra surface areas are detected which cannot be obtained under a thick diffusion layer.

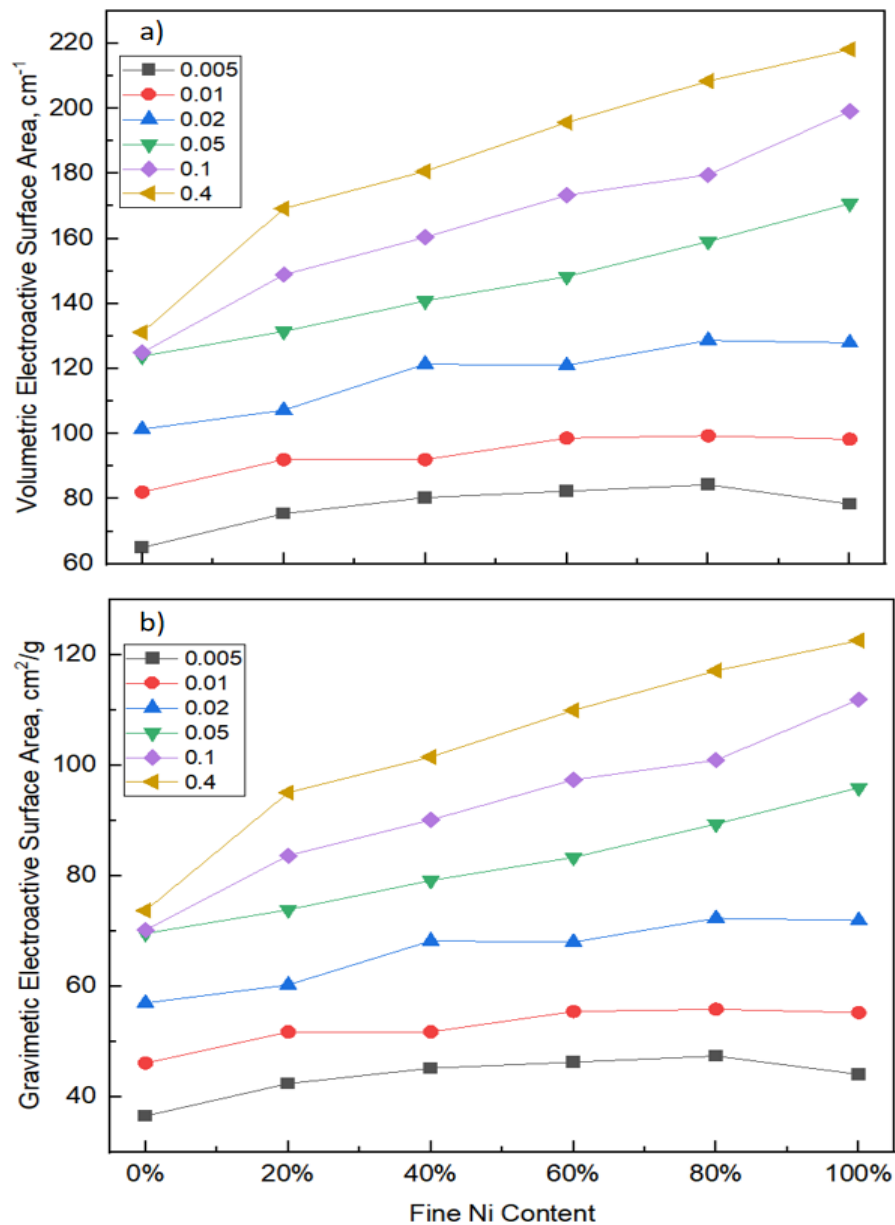


Fig. 4. 8: Variations of a) volumetric and b) gravimetric electroactive surface areas with fine Ni powder ratio at selected scan rates (see inset, V/s). Other parameters: pore size 425 – 710  $\mu\text{m}$ , porosity 60%, compaction pressure 200 MP and sintering temperature 850  $^{\circ}\text{C}$ .

Fig. 4.8 shows that the electroactive surface area is very sensitive to scan rate. This is because the electroactive surface area is obtained directly from peak current, which is a function of scan rate. The relationship between peak current and scan rate depends on the thickness of the diffusion layer, which is the region where the concentration of the reaction species increases from zero at the electrode surface to the bulk concentration at a distance into the electrolyte reservoir. The diffusion layer thickness,  $\delta$ , can be calculated from scan rate,  $v'$ , by (Scholz 2002, Diao et al. 2015):

$$\delta = \sqrt{\frac{DRT}{nFv'}} \quad 4.1$$

where  $D$  is the diffusion coefficient of the species involved in the redox reaction ( $6.4 \times 10^{-6} \text{ cm}^2/\text{s}$  for ferrocyanide),  $R$  is the gas constant,  $T$  is temperature,  $n$  is the number of electrons transferred in the redox process ( $n = 1$  for the ferrocyanide reaction),  $F$  is the Faraday constant.

If the diffusion layer is thin compared to the electrolyte reservoir, the redox reaction is more likely to be controlled by diffusion of the reacting species. In



the diffusion-controlled regime, the peak current,  $i_p$ , is proportional to the square root of scan rate and can be predicted by the equation 2.7.

If the diffusion layer is of a similar magnitude to the electrolyte reservoir (known as thin-layer condition), the redox reaction is more likely to be controlled by the quantity of the reacting species in the electrolyte reservoir. For a process with a thin-layer limited response, the peak current is proportional to the scan rate and can be calculated by (Bard 2002):

$$i_p = \frac{F^2 v V c}{4RT} \quad 4.2$$

where  $V$  is the volume of the electrolyte reservoir.

Fig. 4.8 also shows that the degree of effect of fine Ni powder ratio on the electroactive surface area is different at different scan rates. The electroactive surface area increases more pronouncedly with increasing fine Ni content at high scan rates. This behavior is due to the additional effect of diffusion layer thickness for electrodes with rough surfaces.

Fig. 4.9 plots peak current versus scan rate (bottom abscissa) and diffusion layer thickness (top abscissa, calculated from equation 4.1) in the logarithmic scale. It shows that the peak current is proportional to scan rate in the low scan rate region (thin-layer limited) and proportional to square root of scan rate in the high scan rate region (diffusion-controlled). It confirms that the factor controlling

the reaction indeed changed with scan rate in the current test conditions. In any case, the peak current increases as scan rate increases, initially proportionally and gradually transitioning to sublinear.

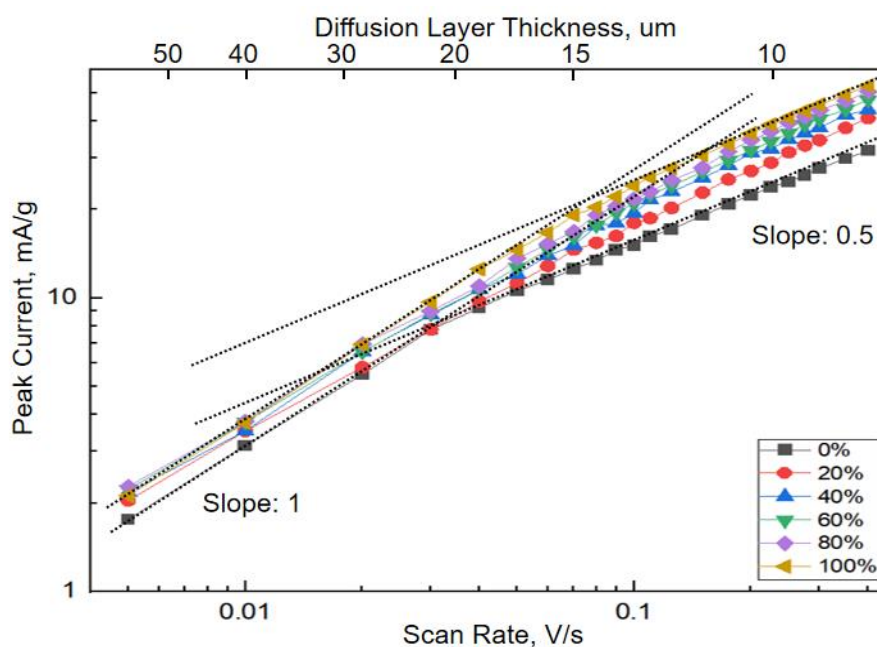


Fig. 4. 9: Variations of peak current with scan rate (bottom abscissa) or diffusion layer thickness (top abscissa) for different fine Ni powder ratios (pore size 425 – 710  $\mu\text{m}$ , porosity 60%, compaction pressure 200 MP and sintering temperature 850  $^{\circ}\text{C}$ ).

Fig. 4.10 is a schematic diagram showing how scan rate affects diffusion layer and how the diffusion layer thickness affects the measured electroactive surface area for samples with different surface morphologies or geometric features. The electroactive surface area can be regarded as the area of the outer surface of the diffusion layer (Diao et al. 2015, Zhu and Zhao 2017). It can be considerably smaller than the real surface of the porous structure, and

even smaller than the external contour of the surface. With increasing the thickness of the diffusion layer, the diffusion layer becomes flatter and the surface area of the samples is underestimated. The deviation depends on the relative magnitudes between the diffusion layer thickness and the surface roughness or geometrical features of the porous structure. The electroactive surface follows the contour of the surface features that are greater than or comparable to the diffusion layer thickness. Geometrical features on the surface are considerably smaller than the diffusion layer, or some small recessed cavities such as secondary pores, are submerged in the diffusion layer and do not contribute to the electroactive surface. The measured electroactive surface area is therefore always smaller than the real surface area. Increasing the scan rate decreases the diffusion layer thickness, resulting in better resolution of the surface morphology, i.e., better detection of finer surface features.

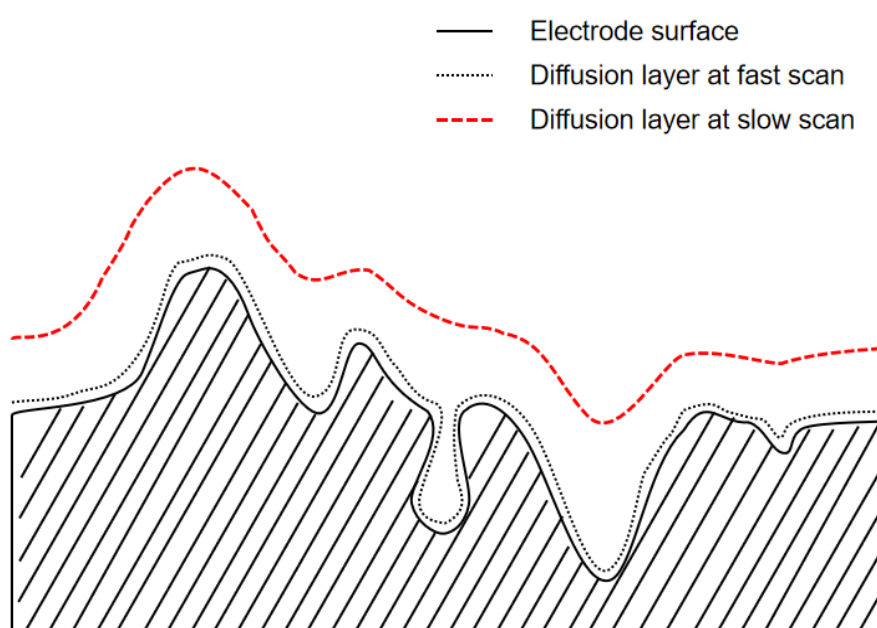


Fig. 4. 10: Schematic diagram showing how scan rate affects diffusion layer and electroactive surface area.

The porous Ni samples with the same primary pore size have similar internal surface contours, regardless of the fine Ni powder ratio. At a low scan rate, the diffusion layer is thick. The effect of surface morphology on the electroactive surface area is small, as the surface features smaller than the diffusion layer thickness is practically not detected. At a high scan rate, however, the diffusion layer becomes thin. More finer surface features are revealed. Samples with higher fine Ni contents will produce a more noticeable increase in electroactive surface area, because they have rougher surfaces and finer surface features.

It is worth noting that fine Ni powder ratio affects the transition of the  $i_p$  vs  $v$  curve from a slope of 1 to 0.5, in the logarithmic scale as shown in Fig. 4.9. Table 4.1 shows the transition range of scan rate, and the corresponding diffusion layer thickness, for the samples with different fine Ni powder ratios. The nominal mean Ni particle size for each sample is also listed in the table to give a qualitative indication of the magnitude of the diffusion layer relative to the surface morphology. It is shown that increasing fine Ni powder ratio, or decreasing nominal Ni particle size, the transition range of diffusion layer thickness decreases.

Table 4. 1 Nominal mean Ni particle size, range of scan rate and corresponding diffusion layer thickness of the transition region for samples with different fine Ni powder ratios.

Fine Ni content, %	Nominal mean Ni particle size, $\mu\text{m}$	Range of scan rate, V/s	Range of diffusion layer thickness, $\mu\text{m}$
0	100	0.02 – 0.04	27 – 19
20	82	0.02 – 0.07	27 – 15
40	64	0.03 – 0.08	22 – 14
60	46	0.04 – 0.09	19 – 13
80	28	0.05 – 0.11	17 – 12
100	10	0.06 – 0.125	16 – 11

## 4.7 Summary

The surface morphology of the LCS porous Ni samples manufactured with varying process parameters, including pore size, porosity, metal particle size, compaction pressure, sintering temperature and chemical treatment, were characterized and the real and electroactive surface area are measured.

The volumetric and gravimetric real surface areas of the LCS porous Ni samples are in the ranges of  $500\text{-}1650\text{ cm}^{-1}$  and  $200\text{-}650\text{ cm}^2/\text{g}$ , respectively.

The volumetric real surface area increases with increasing fine Ni powder ratio

and decreasing pore size and porosity. The gravimetric real surface area increases with increasing fine Ni powder ratio and porosity and decreasing compaction pressure.

The volumetric and gravimetric electroactive surface areas of the LCS porous Ni samples are in the ranges of 60-220 cm<sup>-1</sup> and 30-130 cm<sup>2</sup>/g, respectively. The electroactive surface area increases with increasing porosity, but it decreases with increasing pore size, compaction pressure and sintering temperature. The electroactive surface area also depends on the diffusion layer thickness associated with the electrochemical reaction. In the semi-infinite diffusion controlled regime, the thickness of the diffusion layer mainly depends on the sweep speed. A high sweep speed leads to a relatively thin diffusion layer and therefore provides a high electroactive surface area.

## **Chapter 5 Real Surface Area of DHBT Porous Ni**

### **5.1 Introduction**

Porous Ni has attracted many interests as electrodes for electrocatalysis, sensor and modified current collector for supercapacitors because of the high surface area and electrical conductivity (Drunen et al. 2014, Lu et al. 2016, Akhtar et al. 2014, Xu et al. 2010). The high surface area leads to large energy generation and storage, and the high electrical conductivity results in rapid electrochemical reactions and high energy transport density. This chapter investigates the morphology and real surface area of the porous Ni samples manufactured by the Dynamic Hydrogen Bubble Template (DHBT) method under different deposition and solution conditions. The effects of several key process parameters (including type and concentration of Ni salt, the concentration of H<sup>+</sup> source, deposition potential and time) are discussed.

### **5.2 Effect of Deposition Condition on Current Density**

Fig. 5.1 shows the nominal current density-time profiles for three Ni(CH<sub>3</sub>COO)<sub>2</sub> concentrations of 0.1, 0.2 and 0.4 M. In each case, there is a rapid decrease in nominal current density in the first 10 s. This is because a large number of hydrogen bubble formed and covered on the surface of the substrate, which hinder the redox reaction and causes a decreased current. After this period, the

nominal current density increases, due to increased hydrogen nucleation and evolution. The nearly linear increase in nominal current density over time as a whole is because of the increased surface area and the process is controlled by semi-infinite diffusion (Sengupta et al. 2018). The serration shape of the curve features fluctuation in nominal current density because the generated gas bubbles coalesce and break off on the surface, temporarily changing the effective surface area. When the bubbles stick on the surface, the effective surface area is decreased and the total current is decreased. When the bubbles break off from the surface, the effective surface area is increased and the total current is also increased. Comparing the three curves shows that the nominal current density increases with increasing the concentration of  $\text{Ni}(\text{CH}_3\text{COO})_2$  in the solution, because of the decreased internal electrical resistance.

Fig. 5.1 shows that the slope in the solution containing  $\text{Ni}(\text{SO}_3\text{NH}_2)_2$  is less steep than in the solution containing  $\text{Ni}(\text{CH}_3\text{COO})_2$ . This is because different reactions occur on the anode. Several hydrogen bubbles covered on the surface, and therefore doesn't decrease the effective area of the substrate. The oxidation of  $(\text{NH}_2\text{SO}_3)^-$  increases the pH of the solution, which slows hydrogen and metal evolution and impedes the rate of increase in nominal current density over time (Sengupta et al. 2018).



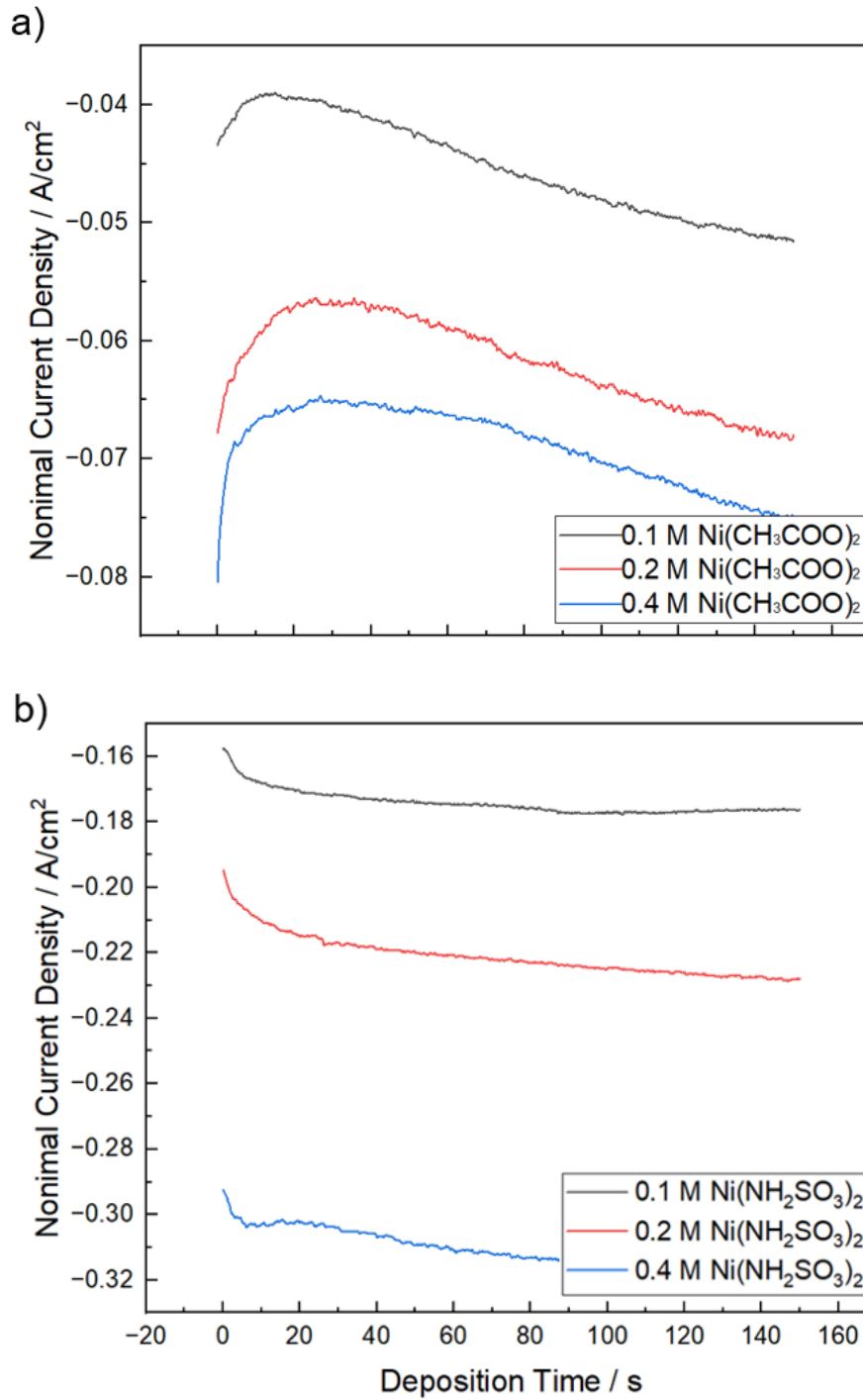


Fig. 5. 1: Deposition nominal current density versus deposition time for different concentrations of a) Ni(CH<sub>3</sub>COO)<sub>2</sub> and b) Ni(NH<sub>2</sub>SO<sub>3</sub>)<sub>2</sub> in the solution with 1.5 M NH<sub>4</sub>Cl, under a deposition potential of -1.5 V over 150 s.

Fig. 5.2 shows the nominal current density-time profiles for three different NH<sub>4</sub>Cl

concentrations of 0.5, 1.0 and 1.5 M. Again, in each case, there is a rapid decrease in nominal current density in the first 10 s and then a gradual increase over time. The nominal current density increases with increasing the concentration of  $\text{NH}_4\text{Cl}$ , which is because of the decreasing of the electric resistance. At a low concentration of  $\text{NH}_4\text{Cl}$ , the nominal current density is low, because Ni deposition is the predominant reaction. With increasing the concentration of  $\text{NH}_4\text{Cl}$ , the hydrogen evolution reaction plays a more important role.

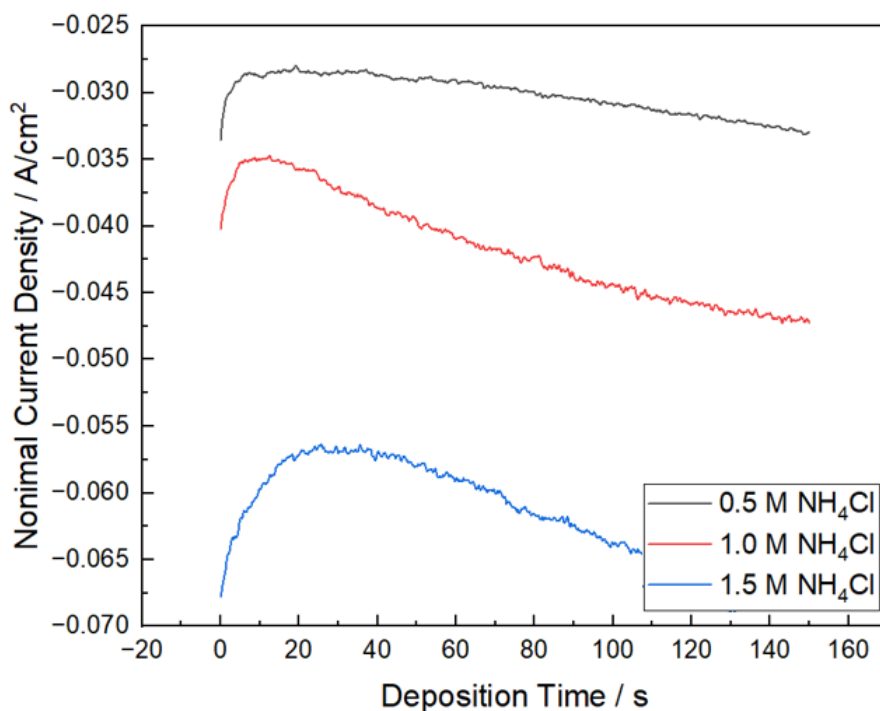


Fig. 5. 2: Deposition nominal current density versus deposition time for different concentrations of  $\text{NH}_4\text{Cl}$  in the solution with 0.2 M  $\text{Ni}(\text{CH}_3\text{COO})_2$  under a deposition potential of -1.5 V over 150 s.

Fig. 5.3 shows the nominal current density-time profiles for three different

applied deposition potentials of -1.35, -1.5 and -1.7 V in 0.2 M Ni(CH<sub>3</sub>COO)<sub>2</sub> and 0.2 M Ni(NH<sub>2</sub>SO<sub>3</sub>)<sub>2</sub> solutions. At a low deposition potential of -1.35 V in 0.2 M Ni(CH<sub>3</sub>COO)<sub>2</sub>, the nominal current density decreases at the beginning of deposition due to the hydrogen bubble on the surface of substrate as mentioned above. In all the other cases, the nominal current density increases with time all along. Increasing potential significantly increases the nominal current density, because of the increasing rate of hydrogen evolution and nucleation of metal crystals. Because diffusion is the rate-determinant step in the deposition reaction, the increasing hydrogen evolution results in more gas bubbles, which stirs the solution and hence increases the nominal current density.

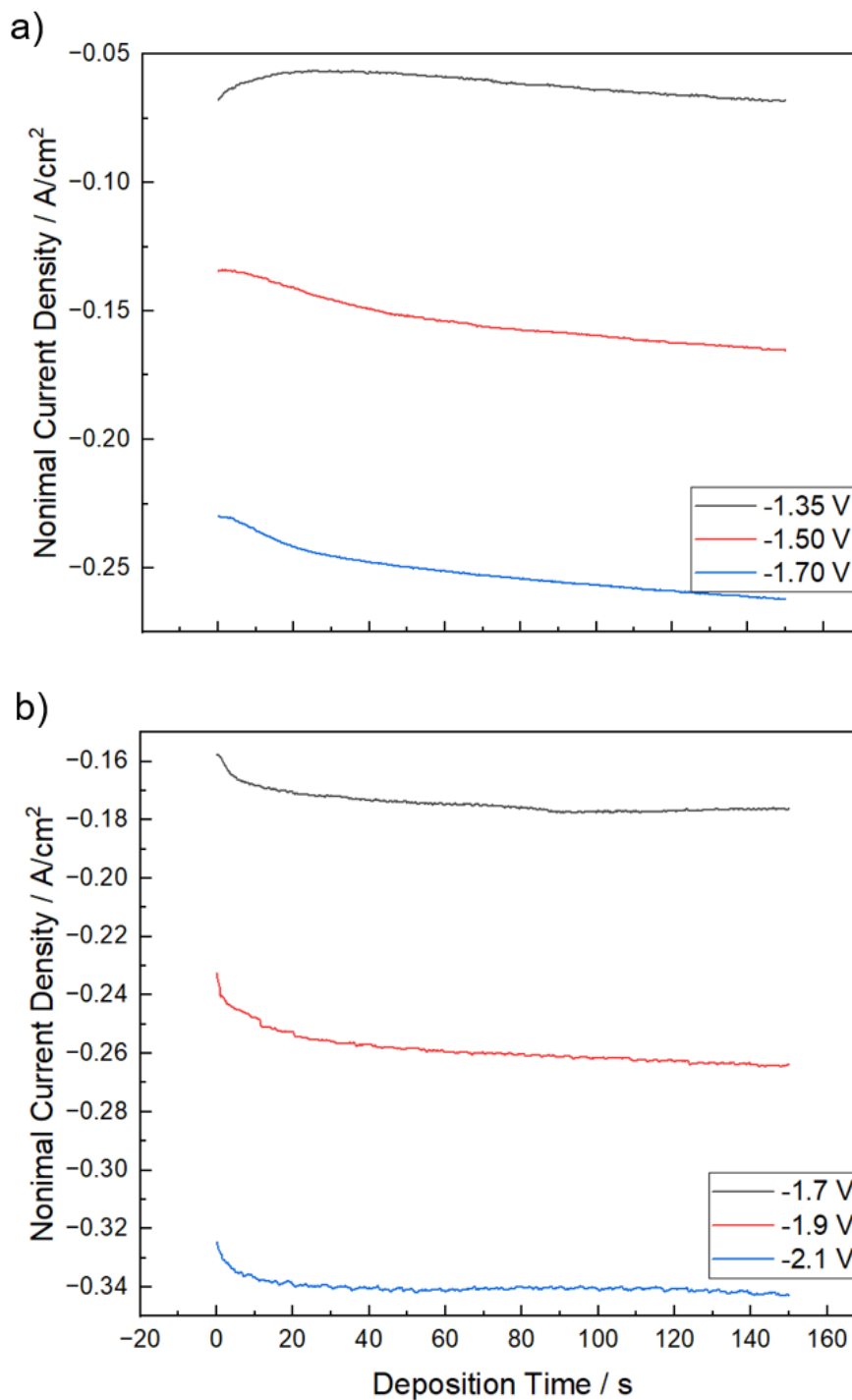


Fig. 5. 3: Deposition nominal current density versus deposition time for different applied deposition potentials in a) 0.2 M Ni(CH<sub>3</sub>COO)<sub>2</sub> and b) 0.2 M Ni(NH<sub>2</sub>SO<sub>3</sub>)<sub>2</sub> solutions with 1.5 M NH<sub>4</sub>Cl over 150 s.

Fig. 5.4 shows the nominal current density-time profiles for three samples with different lengths of deposition time in a) 0.2 M  $\text{Ni}(\text{CH}_3\text{COO})_2$  and b) 0.2 M  $\text{Ni}(\text{NH}_2\text{SO}_3)_2$  solutions. It shows that the deposition rate in the  $\text{Ni}(\text{NH}_2\text{SO}_3)_2$  solution is much more consistent than that in the  $\text{Ni}(\text{CH}_3\text{COO})_2$  solution. Unlike in the  $\text{Ni}(\text{CH}_3\text{COO})_2$  solution (Fig. 5.4 a), the deposition current increases dramatically at the beginning of deposition in the solution with  $\text{Ni}(\text{SO}_3\text{NH}_2)_2$ . This is because the presence of plenty of  $\text{SO}_4^{2-}$  ions in the solution prevents the gas bubbles to cover the surface of the substrate. This effectively increases the actual surface area, resulting in a great increase of deposition current.

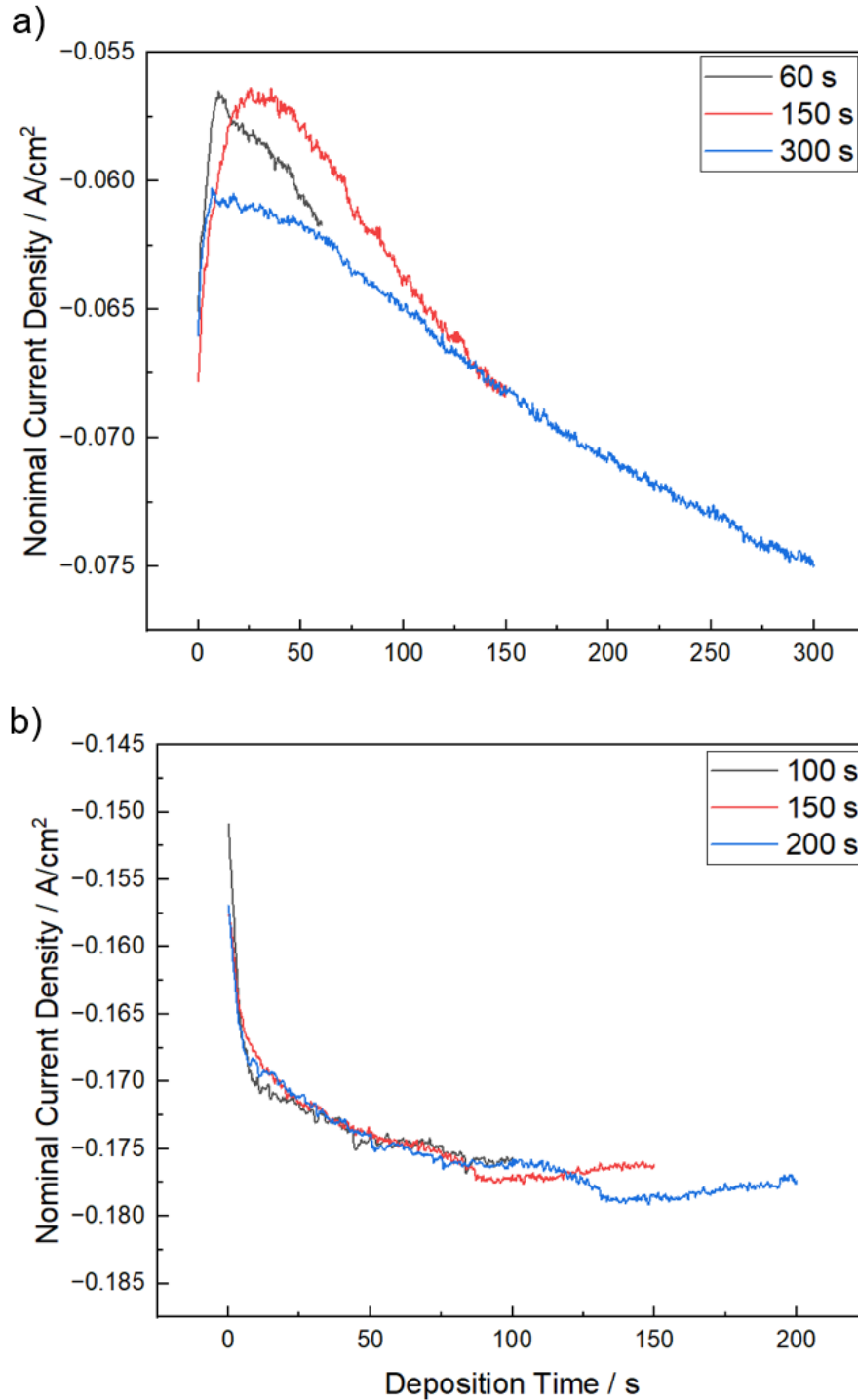
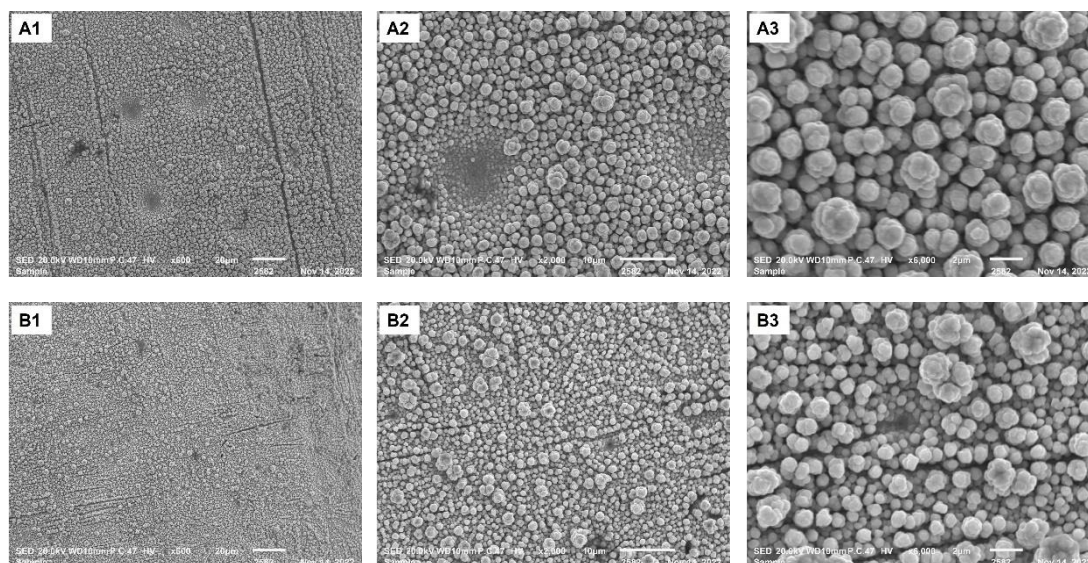


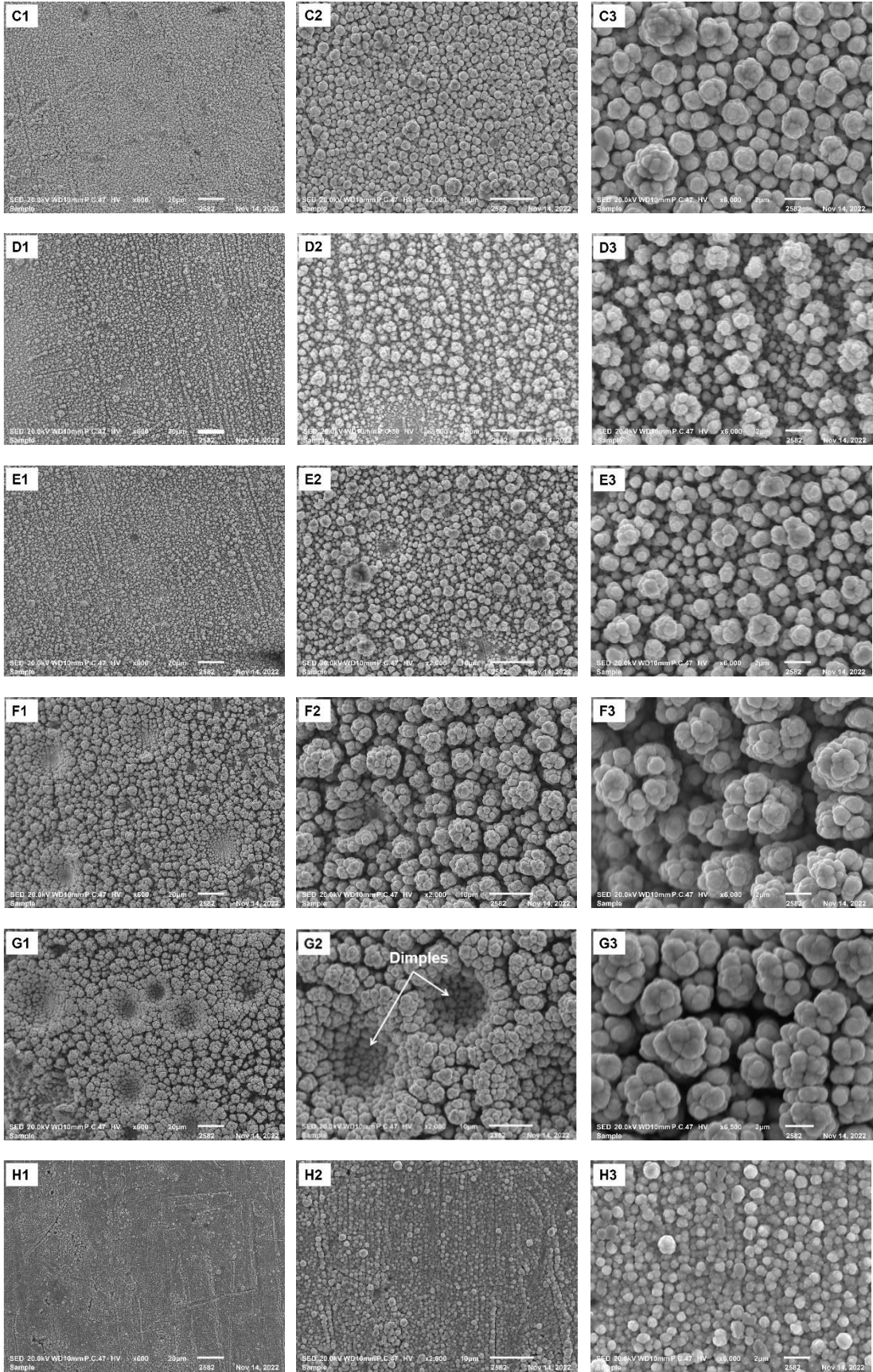
Fig. 5. 4: Deposition nominal current density versus deposition time for three samples with different lengths of deposition time in a) 0.2 M Ni(CH<sub>3</sub>COO)<sub>2</sub> and b) 0.2 M Ni(NH<sub>2</sub>SO<sub>3</sub>)<sub>2</sub> solutions with 1.5 M NH<sub>4</sub>Cl under a deposition potential of -1.5 V over 60 - 300 s.

## 5.3 Effect of Deposition Condition on Surface Morphology

### 5.3.1 Ni(CH<sub>3</sub>COO)<sub>2</sub> Solution

Fig. 5.5 shows the SEM micrographs of the samples with different process conditions with varying concentrations of Ni(CH<sub>3</sub>COO)<sub>2</sub>, the concentration of NH<sub>4</sub>Cl, deposition potential and deposition time, at three different magnifications denoted by suffixes 1, 2 and 3. Fig. 5.5 A1, A2 and A3 show the micrographs of the sample with the benchmark process condition: Ni(CH<sub>3</sub>COO)<sub>2</sub> concentration 0.2 M, NH<sub>4</sub>Cl concentration 1.5 M, deposition potential -1.35 V, and deposition time 150 s. The other micrographs have only one parameter changed from the benchmark condition with the other parameters kept unchanged. The morphology of the deposits is characterized by cauliflower-like crystals with sparsely distributed dimples where the crystals are much smaller, indicating a lack of growth due to gas bubbles (as shown in Fig. 5.5 I2).







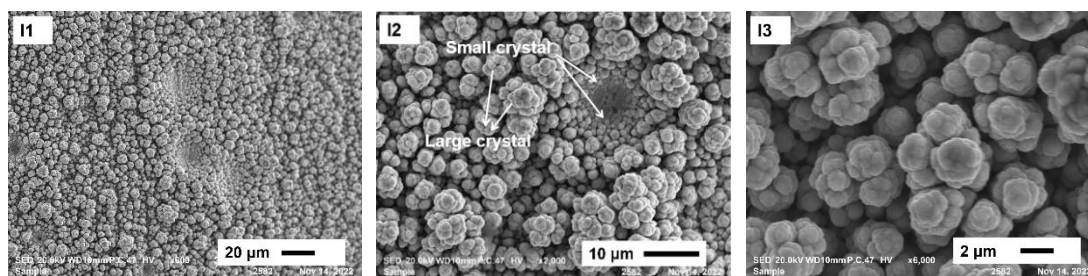
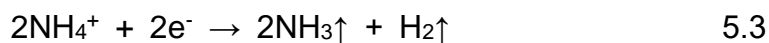


Fig. 5. 5: SEM micrographs of the deposits produced with benchmark process condition (0.2 M Ni(CH<sub>3</sub>COO)<sub>2</sub>, 1.5 M NH<sub>4</sub>Cl, -1.35 V, 150 s) or with one parameter different from the benchmark condition: A) benchmark, B) 0.1 M Ni(CH<sub>3</sub>COO)<sub>2</sub>, C) 0.4 M Ni(CH<sub>3</sub>COO)<sub>2</sub>, D) 0.5 M NH<sub>4</sub>Cl, E) 1.0 M NH<sub>4</sub>Cl, F) -1.5 V, G) -1.7 V, H) 60 s, I) 300 s. Suffixes 1, 2, 3 denote different magnifications.

In the Ni deposition process, the primary cathodic reactions are (Ito et al. 1980, Sengupta et al. 2018):



During the process, Ni is deposited on the substrate and the Ni crystals grow to form a deposit. Hydrogen gas is evolved at the surface of substrates to form gas bubbles.

The effect of the concentration of Ni(CH<sub>3</sub>COO)<sub>2</sub> on the morphology of the deposit can be seen by comparing Figs. 5.5 A, B and C, corresponding to

Ni(CH<sub>3</sub>COO)<sub>2</sub> concentrations of 0.2, 0.1 and 0.4 M. When the concentration is increased from 0.1 M to 0.2 M and then to 0.4 M, the average crystal size is increased from 0.8 μm (Fig. 5.5 B) to 1.6 μm (Fig. 5.5 A) and then to 2.1 μm (Fig. 5.5 C). At the low concentration of 0.1 M, the dimple (as shown in Fig. 5.5 G2) size is about 2 μm (Fig. 5.5 B), while at the intermediate concentration of 0.2 M, the dimple size is about 12 μm (Fig. 5.5 A). At the high concentration of 0.4 M, no dimples are observed (Fig. 5.5 C).

Crystal size increases with increasing the concentration of Ni(CH<sub>3</sub>COO)<sub>2</sub> because of the increased nominal deposition current density. At a higher Ni(CH<sub>3</sub>COO)<sub>2</sub> content, the reduction of Ni is promoted and there is sufficient formation and growth of Ni crystals due to adequate solution around the surface of the substrate. In terms of deposit morphology, the surface of the crystals is flat and smooth at a high Ni(CH<sub>3</sub>COO)<sub>2</sub> concentration but rough at a low Ni(CH<sub>3</sub>COO)<sub>2</sub> concentration. At a low Ni(CH<sub>3</sub>COO)<sub>2</sub> concentration, i.e., low Ni<sup>2+</sup> concentration in the solution, there is a high rate of hydrogen evolution, leading to the evident formation of dimples.

The change of dimple size with changing Ni(CH<sub>3</sub>COO)<sub>2</sub> concentration is due to its effect on hydrogen evolution and Ni crystal formation. At 0.1 M Ni(CH<sub>3</sub>COO)<sub>2</sub>, the nominal deposition current density is relatively low, and therefore the efficiency of the evolution of hydrogen and Ni is also low. The gas bubbles stuck

on the substrate are small and Ni crystals nucleate around these bubbles and form pores or dimples (Fig. 5.5 B). At 0.2 M  $\text{Ni}(\text{CH}_3\text{COO})_2$ , the nominal deposition current density is increased (see Fig. 5.1 a). More hydrogen is evolved and coalesces form bubbles. Although more Ni is formed, it is not enough to close the pores. Therefore, larger dimples with an average diameter of 12  $\mu\text{m}$  are left on the surface (Fig. 5.5 A). At 0.4 M  $\text{Ni}(\text{CH}_3\text{COO})_2$ , the high concentration of  $\text{Ni}^{2+}$  results in a relatively high nucleation rate of Ni. The high rate of Ni deposition results in growth of larger and thicker Ni crystals. The hydrogen evolution only forms small bubbles on the surface, leading to no evident formation of dimples (Fig. 5.5 C).

The effect of the concentration of  $\text{NH}_4\text{Cl}$  on the deposits morphology can be seen by comparing Figs. 5.5 A, D and E, corresponding to  $\text{NH}_4\text{Cl}$  concentrations of 1.5, 0.5 and 1.0 M. When the concentration is increased from 0.5 M to 1 M and then to 1.5 M, the average crystal size is increased from 1.1  $\mu\text{m}$  (Fig. 5.5 D) to 1.6  $\mu\text{m}$  (Fig. 5.5 A) and then to 1.9  $\mu\text{m}$  (Fig. 5.5 E), while the average dimple size is decreased from 15  $\mu\text{m}$  (Fig. 5.5 D) to 12  $\mu\text{m}$  (Fig. 5.5 A) and then to 3  $\mu\text{m}$  (Fig. 5.5 E).

The crystal size increases with increasing the  $\text{NH}_4\text{Cl}$  concentration, because the deposition current increases (Fig. 5.2). Increasing the  $\text{NH}_4\text{Cl}$  concentration promotes hydrogen gas evolution, which promotes the mixing of the solution.

The formation and float up of a large number of hydrogen bubbles result in a violent blend of the solution, facilitating the mass transfer of Ni salt. The diffusion layer between the electrode surface and the bulk solution is decreased, resulting in fast transport of Ni ions to the substrate surface to form a deposit with enlarged crystals and a smoother surface.

The decrease in the dimple size with increasing the  $\text{NH}_4\text{Cl}$  concentration is mainly due to its effect on hydrogen evolution. At the low  $\text{NH}_4\text{Cl}$  concentration of 0.5 M, the nominal deposition current density is low and therefore the evolution of hydrogen and the formation of Ni are slow. The growth of Ni crystals is slow before the gas bubbles break and leave the surface of the substrate. As a result, only a few shallow dimples are observed. At the intermediate  $\text{NH}_4\text{Cl}$  concentration of 1 M, the Ni deposition rate is increased, limiting the size of the dimples. At the high  $\text{NH}_4\text{Cl}$  concentration of 1.5 M, the evolution rate of hydrogen outweighs the deposition rate of Ni. The hydrogen bubbles leave the surface of the substrate more rapidly, leaving behind only some very small dimples.

The effect of deposition potential on the deposit morphology can be seen by comparing Figs. 5.5 A, F and G, corresponding to potentials of -1.35, -1.5 and -1.7 V. When the deposition potential is increased from -1.35 V to -1.5 V and then to -1.7 V, the average crystal size is increased from 1.6  $\mu\text{m}$  (Fig. 5.5 A) to

3.8  $\mu\text{m}$  (Fig. 5.5 F) and then to 5.6  $\mu\text{m}$  (Fig. 5.5 G), while the dimple size is increased from 12  $\mu\text{m}$  (Fig. 5.5 A) to 20  $\mu\text{m}$  (Fig. 5.5 F) and then remains 20  $\mu\text{m}$  (Fig. 5.5 G).

The crystal size increases with increasing the negative deposition overpotential, because the deposition current increases (Fig. 5.3 a). Increasing the negative deposition overpotential increases the hydrogen evolution and Ni deposition rates, increasing the crystal size. It is worth mentioning that the nominal current density at protrudes is higher than at the flat regions. Growth of Ni particles is easier than forming new particles. The particles grow larger and even diffuse to each other to form an even larger cauliflower-like particle. In addition, the hydrogen evolution promotes mass transfer to the substrate surface, which supplies sufficient Ni ions during the deposition and further facilitates the formation of larger Ni particles.

The increase in the dimple size with increasing the overpotential is mainly due to its effect on hydrogen evolution. Increasing the overpotential results in a high nominal current density. A large amount of gas is generated at the substrate to form large bubbles on the surface which serve as dimple/pore templates. Ni crystals form at a high rate around the bubbles to form dimples. At a low deposition potential, the nominal current density is relatively low and the Ni growth is sluggish. Walls of Ni crystals cannot establish around the bubbles

before they break. Therefore, only shallow dimples are formed in the deposit (Fig. 5.5 A). Increasing the deposition potential to -1.5 V facilitates both hydrogen evolution and Ni deposition. More bubbles form on the surface and fast Ni crystal growth causes a thicker wall around the bubbles, leading to larger dimples (Fig. 5.5 F). At the high deposition potential of -1.7 V, an equilibrium is established between hydrogen evolution and Ni deposition, and the dimple pores are formed because the gas bubbles have enough residence time on the surface.

The effect of deposition time on the deposit morphology can be seen by comparing Figs. 5.5 A, H and I, corresponding to times of 60, 150 and 300 s. When the deposition time is increased from 60 s to 150 s and then to 300 s, the average crystal size is increased from 0.8  $\mu\text{m}$  (Fig. 5.5 H) to 1.6  $\mu\text{m}$  (Fig. 5.5 A) and then to 4.8  $\mu\text{m}$  (Fig. 5.5 I), while the dimple size is increased from no sizeable dimples observed (Fig. 5.5 H) to 12  $\mu\text{m}$  (Fig. 5.5 A) and then 20  $\mu\text{m}$  (Fig. 5.5 I).

The mean Ni crystal size is increased by 8 times with increasing deposition time from 60 to 300 s. The Ni particles change from round and smooth to rough and cauliflower-like. At the beginning of the deposition, a large number of gas bubbles form and cover the surface of the substrate, resulting in a decrease in current or the nominal deposition current density (Fig. 5.4 a). With increasing

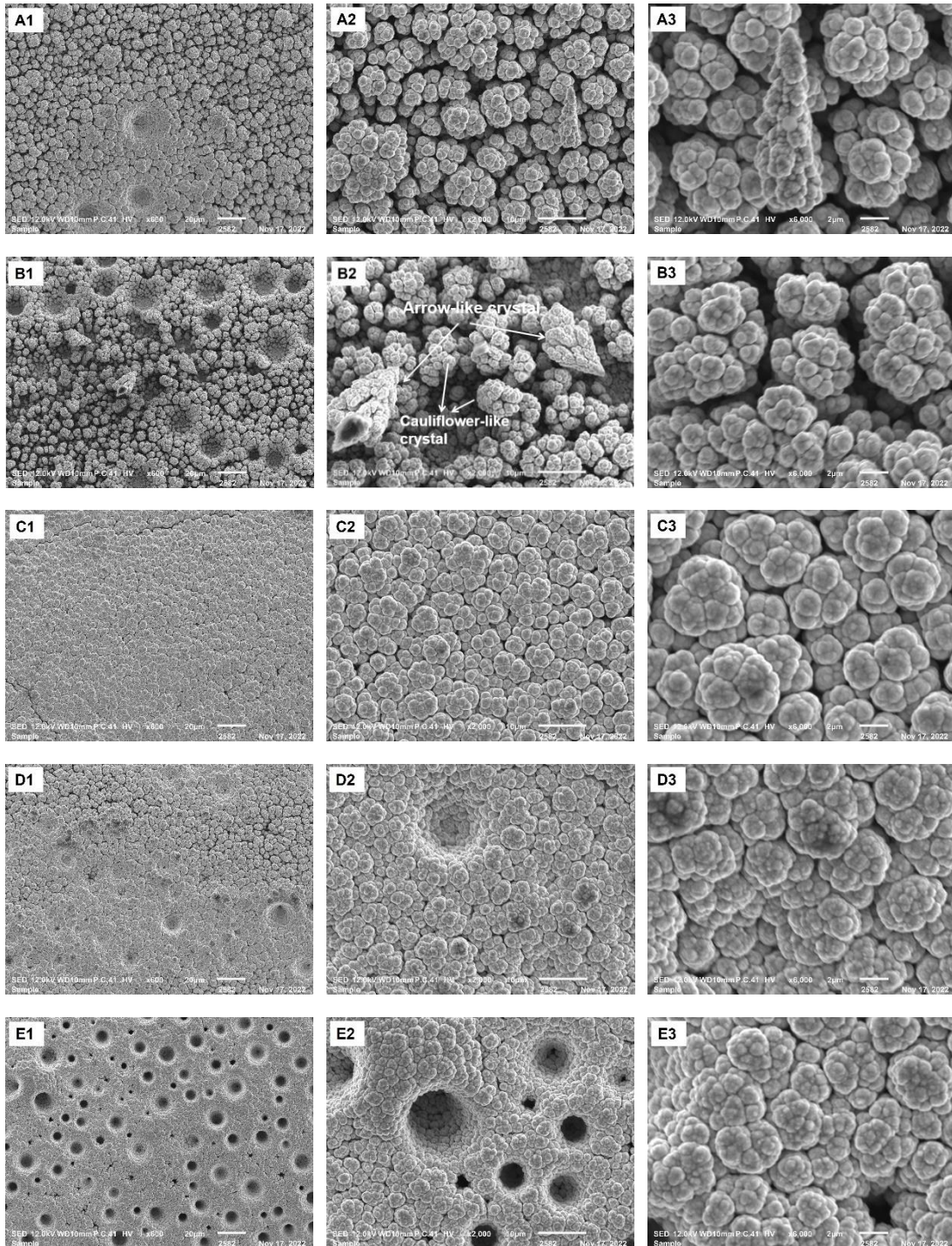
time, the bubbles coalesce and leave off the surface, providing more active sites for the evolution of hydrogen and formation of Ni as a result of increasing current. The growth of the Ni particles effectively increases the surface of the deposit and hence the current or the nominal current density.

The dimples in the deposit become large and deeper with increasing deposition time. No dimples are observed at the low deposition time (Fig. 5.5 H). This is because the current is low at the beginning of the deposition (Fig. 5.3). The evolution of gas bubbles too slow to form large dimples. With increasing deposition time further, however, some gas bubbles can grow and coalesce without leaving the substrate, thus forming dimples in the deposit. The dimples become larger and deeper over time, as the Ni crystals grow.

### **5.3.2 Ni(SO<sub>3</sub>NH<sub>2</sub>)<sub>2</sub> Solution**

Fig. 5.6 shows the SEM micrographs of the samples with different process conditions with varying concentrations of Ni(SO<sub>3</sub>NH<sub>2</sub>)<sub>2</sub>, deposition potential and deposition time, at three different magnifications denoted by suffixes 1, 2 and 3. Fig. 5.6 A1, A2 and A3 show the micrographs of the sample with the benchmark process condition: Ni(SO<sub>3</sub>NH<sub>2</sub>)<sub>2</sub> concentration 0.2 M, NH<sub>4</sub>Cl concentration 1.5 M, deposition potential -1.7 V, and deposition time 150 s. The other micrographs have only one parameter changed from the benchmark

condition with the other parameters kept unchanged. The morphology of the deposits is characterized by cauliflower-like crystals with sparsely distributed dimples where the crystals are more compact, indicating an increase of pH because of the reaction of ammonium sulfamate.





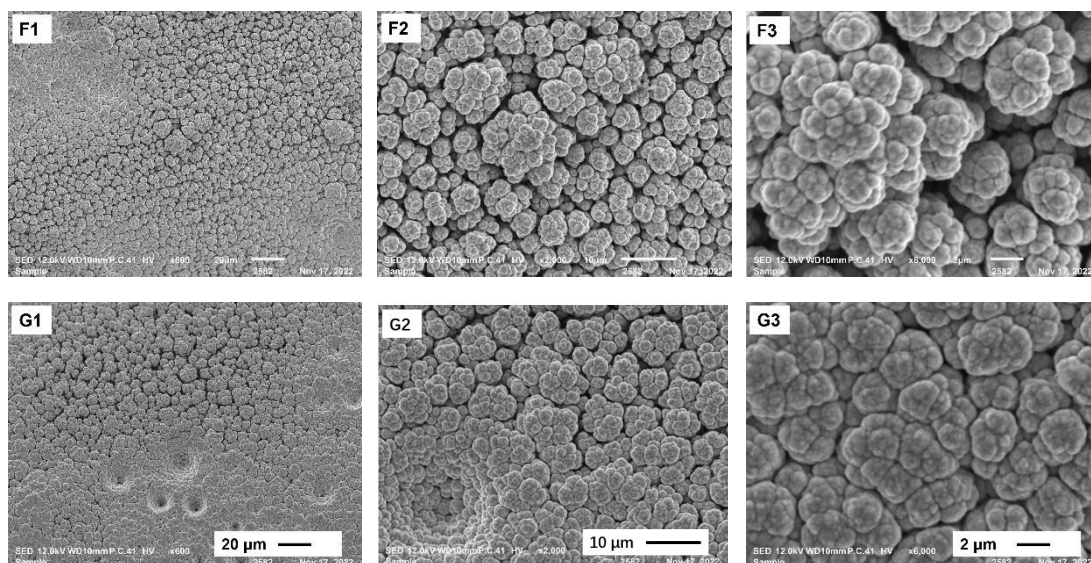


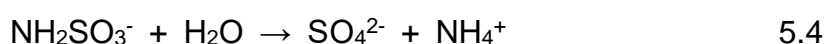
Fig. 5. 6: SEM micrographs of the deposits produced with benchmark process condition (0.2 M  $\text{Ni}(\text{NH}_2\text{SO}_3)_2$ , 1.5 M  $\text{NH}_4\text{Cl}$ , -1.7 V, 150 s) or with one parameter different from the benchmark condition: A) benchmark, B) 0.1 M  $\text{Ni}(\text{NH}_2\text{SO}_3)_2$ , C) 0.4 M  $\text{Ni}(\text{NH}_2\text{SO}_3)_2$ , D) -1.9 V, E) -2.1 V, F) 100 s, G) 200 s. Suffixes 1, 2, 3 denote different magnifications.

The effect of the concentration of  $\text{Ni}(\text{SO}_3\text{NH}_2)_2$  on the deposit morphology can be seen by comparing Figs. 5.6 A, B and C, corresponding to  $\text{Ni}(\text{SO}_3\text{NH}_2)_2$  concentrations of 0.2, 0.1 and 0.4 M. When the concentration is increased from 0.1 M to 0.2 M and then to 0.4 M, the average crystal size is increased from 4.6  $\mu\text{m}$  (Fig. 5.6 B) to 5.8  $\mu\text{m}$  (Fig. 5.6 A) and then to 6.1  $\mu\text{m}$  (Fig. 5.6 C), while the dimple size is reduced from 18  $\mu\text{m}$  (Fig. 5.6 B) to 16  $\mu\text{m}$  (Fig. 5.6 A) and then to no sizeable dimples observed (Fig. 5.6 C).

The Ni crystal size increases with increasing the concentration of  $\text{Ni}(\text{SO}_3\text{NH}_2)_2$ ,

similar to that observed in the case of the  $\text{Ni}(\text{CH}_3\text{COO})_2$  solution in section 5.3.1. The Ni particles also become more compact with increasing concentration. At the low concentration of  $\text{Ni}(\text{SO}_3\text{NH}_2)_2$ , two crystal shapes, arrow-like and cauliflower-like, are observed (Fig. 5.6 B). The particles are loose and small. At the intermediate concentration, the Ni crystals far away from dimples are loose and cauliflower-like, while those near the dimples are compact (Fig. 5.6 A). At a high concentration, the deposit is compact and only large cauliflower-like Ni particles are observed (Fig. 5.6 C). This is because Ni deposition is predominant and its deposition rate is faster than the evolution rate of hydrogen bubbles.

The number and size of dimples decrease with increasing the concentration of  $\text{Ni}(\text{SO}_3\text{NH}_2)_2$ . At the low concentration, the evolution of hydrogen and the formation of Ni are balanced, which leads to a loose deposit with dimples (Fig. 5.6 B). At the intermediate concentration, just a few small dimples are observed (Fig. 5.6 A). This is because increasing the concentration of  $\text{Ni}(\text{SO}_3\text{NH}_2)_2$  results in high resistance to bubble coalescence (Craig et al. 1993). In the solution with  $\text{Ni}(\text{SO}_3\text{NH}_2)_2$ , the sulfamate ion,  $\text{NH}_2\text{SO}_3^-$  hydrolyses in aqueous solution to provide ammonium and sulfate ions (Hammond 1971):



The  $\text{SO}_4^{2-}$  and  $\text{NH}_4\text{Cl}$  can prevent the coalescence of bubbles, and the ability of  $\text{SO}_4^{2-}$  is higher than  $\text{NH}_4\text{Cl}$  at the same concentration (Craig et al. 1993).

Increasing the concentration of  $\text{Ni}(\text{SO}_3\text{NH}_2)_2$  cuts down the residence time of the bubbles on the electrode surface, leading to smaller bubbles. At the high concentration of  $\text{Ni}(\text{SO}_3\text{NH}_2)_2$ , no dimples are observed (Fig. 5.6 C). This is because increasing the concentration of  $\text{Ni}(\text{SO}_3\text{NH}_2)_2$  in the deposition process decreases the current used for hydrogen evolution. Once the deposition rate of Ni becomes far higher than the rate of hydrogen evolution, no bubbles form.

The effect of the deposition potential on the deposit morphology can be seen by comparing Figs. 5.6 A, D and E, corresponding to deposition potential of -1.7, -1.9 and -2.1 V. When the potential is increased from -1.7 V to -1.9 V and then to -2.1 V, the average crystal size is increased from 5.8  $\mu\text{m}$  (Fig. 5.6 A) to 6.2  $\mu\text{m}$  (Fig. 5.6 D) and then to 7  $\mu\text{m}$  (Fig. 5.6 E). The deposition becomes more compact and denser with increasing deposition potential. The dimple sizes at the concentrations of 0.1, 0.2 and 0.4 M are around 16  $\mu\text{m}$  (Fig. 5.6 B), 3 - 12  $\mu\text{m}$  (Fig. 5.6 A) and 1-16  $\mu\text{m}$  (Fig. 5.6 C), respectively. Some Ni crystals have grown and diffused to each other and becoming large crystals.

The Ni crystals become larger and diffuse to each other to form cauliflower-like particles with increasing the deposition potential. At the low deposition potential, the hydrogen evolution and Ni growth are relatively slow because of the low deposition current (Fig. 5.1 b). Hence, the Ni crystal size is small. With increasing the applied potential, oxidation of  $\text{SO}_4^{2-}$  occurs, decreasing the

resistance to bubble coalescence. Some bubbles grow on the surface, leading to the formation of dimples at the intermediate potential and deeper dimples at the high potential.

The effect of the deposition time on the deposit morphology can be seen by comparing Figs. 5.6 F, A and G, corresponding to deposition time of 100, 150 and 200 s. When the deposition time is increased from 100 s to 150 s and then to 200 s, the average crystal size is increased from 6  $\mu\text{m}$  (Fig. 5.6 F) to 6.4  $\mu\text{m}$  (Fig. 5.6 A) and then to 6.8  $\mu\text{m}$  (Fig. 5.6 G). The crystal size does not change much, because it depends on the deposition current, which remain unchanged with time. The deposit, however, becomes more compact and denser with increasing deposition time. No dimples are observed on the surface at the low deposition time of 100 s (Fig. 5.6 F). At the intermediate and high deposition times of 150 and 200 s, the dimple sizes are around 16  $\mu\text{m}$  (Fig. 5.6 A) and 18  $\mu\text{m}$  (Fig. 5.6 G), respectively.

#### **5.4 Effects of Deposition Condition on Real Surface Area**

Figs. 5.7 and 5.8 show the variations of the real surface area with changing process parameters in the  $\text{Ni}(\text{CH}_3\text{COO})_2$  and  $\text{Ni}(\text{SO}_3\text{NH}_2)_2$  solutions, respectively. In  $\text{Ni}(\text{CH}_3\text{COO})_2$  solutions, the real surface areas are in a range of 4-27  $\text{cm}^2$ . However, the real surface areas in  $\text{Ni}(\text{SO}_3\text{NH}_2)_2$  solutions are in a

range of 31-58 cm<sup>2</sup>. The effects of these parameters, including type and concentration of the anion, the concentration of the cation, deposition potential and deposition time, on the real surface area are described and discussed in this section as follows.

#### **5.4.1 Type of Ni Salt**

Comparing Figs. 5.7 and 5.8 shows that the samples manufactured using different solutions have significantly different real surface areas. For fixed process parameters (1.5 M NH<sub>4</sub>Cl, deposition potential of -1.7 V and deposition time of 150 s), the real surface area of the sample manufactured using Ni(SO<sub>3</sub>NH<sub>2</sub>)<sub>2</sub> (38.5 cm<sup>2</sup>) is 47% higher than that manufactured using Ni(CH<sub>3</sub>COO)<sub>2</sub> (26.19 cm<sup>2</sup>). This is because the crystals in the sample manufactured using Ni(SO<sub>3</sub>NH<sub>2</sub>)<sub>2</sub> (Fig. 5.5 G3) are smaller, and smaller Ni particles provide a larger real surface area (Zhu and Zhao, 2017). In contrast, the crystals in the sample manufactured using Ni(CH<sub>3</sub>COO)<sub>2</sub> (Fig. 5.6 B3) are larger, resulting in a lower real surface area. In addition, the sample manufactured using Ni(CH<sub>3</sub>COO)<sub>2</sub> has some dimples in the deposit, while the sample manufactured using Ni(SO<sub>3</sub>NH<sub>2</sub>)<sub>2</sub> shows no dimples. More dimples mean less Ni and therefore a smaller real surface area.

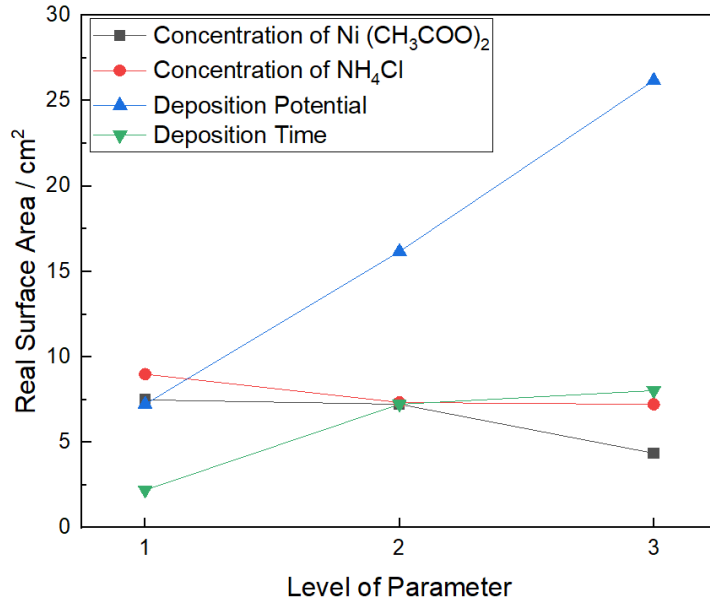


Fig. 5. 7: Variation of real surface area of the DHBT porous Ni with changing process parameters in the Ni(CH<sub>3</sub>COO)<sub>2</sub> solution. Levels 1, 2 and 3 correspond to 0.1, 0.2 and 0.4 M Ni(CH<sub>3</sub>COO)<sub>2</sub>; 0.5, 1 and 1.5 M NH<sub>4</sub>Cl; -1.35, -1.5 and -1.7 V deposition potential; 60, 150 and 300 s deposition time.

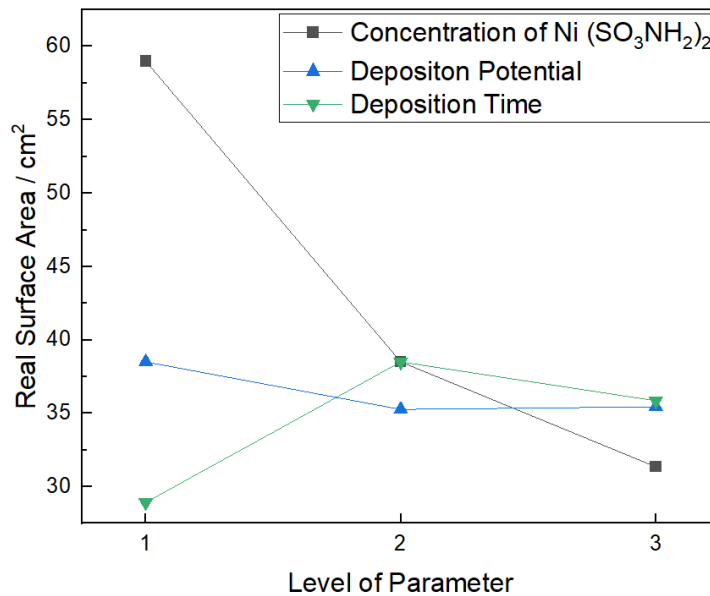


Fig. 5. 8: Variation of real surface area of the DHBT porous Ni with changing process parameters in the Ni(SO<sub>3</sub>NH<sub>2</sub>)<sub>2</sub> solution. Levels 1, 2 and 3

correspond to 0.1, 0.2 and 0.4 M  $\text{Ni}(\text{SO}_3\text{NH}_2)_2$ ; -1.7, -1.9 and -2.1 V

deposition potential; 100, 150 and 200 s deposition time.

#### 5.4.2 Concentration of Ni Salt

The real surface area decreases with increasing the concentration of the anion  $\text{Ni}^{2+}$  in both the solutions, as shown in Figs. 5.7 and 5.8. Increasing the concentration of anion from 0.1 to 0.4 M, for example, the real surface area is decreased by 42% and 47%, corresponding to the  $\text{Ni}(\text{CH}_3\text{COO})_2$  and  $\text{Ni}(\text{SO}_3\text{NH}_2)_2$  solutions respectively. A higher concentration of solution leads to a higher nominal deposition current density, which increases the production rate of Ni and hydrogen gas. With increasing the  $\text{Ni}^{2+}$  concentration, however, the production rate of Ni becomes higher than that with low  $\text{Ni}^{2+}$  concentration. The high production rate of Ni results in gas bubbles leaving the surface of the electrodes more quickly. This leads to larger Ni crystals and fewer dimples as observed in Figs. 5.5 C1 and 5.6 A1. The surface also becomes smoother and denser with the interstice porosity decreases. As a consequence, the real surface area decreases with increasing the concentration of the Ni salt.

In the  $\text{Ni}(\text{SO}_3\text{NH}_2)_2$  solution, the concentration of  $\text{SO}_3\text{NH}_2^-$  is also increased with increasing the Ni salt concentration. The  $\text{SO}_3\text{NH}_2^-$  ion is oxidized at the anode during the deposition process, according to equation 5.6. Many  $\text{NH}_4^+$

ions are generated, resulting in an increased pH of the solution. In high pH solutions, the crystals in the deposit tend to be globular rather than dendritic (Shin et al. 2003, Sengupta et al. 2018). While dendritic crystals have a large surface area due a large number of nano-dendrites, the globular crystals lead to a smoother surface and therefore a lower surface area. Therefore, the real surface area decreases with increasing the concentration of  $\text{Ni}(\text{SO}_3\text{NH}_2)_2$ .

### 5.4.3 Concentration of $\text{H}^+$ Source

The real surface area decreases with increasing the  $\text{NH}_4\text{Cl}$  concentration, as shown in Fig. 5.7. The real surface area of the deposit is decreased by 20% by increasing the concentration of  $\text{NH}_4\text{Cl}$  from 0.5 to 1.5 M. This is because the nominal deposition current density increases with increasing solution in the solution, as discussed above. Under a high nominal current density, the production rates of both metal crystals and hydrogen increase and the mean particle size of the crystals in the deposit increases, resulting in a lower surface area, as discussed in section 5.4.1. Furthermore, dimples are present in the deposit at the high  $\text{NH}_4\text{Cl}$  concentration (Fig. 5.5 A1), but not in the deposit at the low  $\text{NH}_4\text{Cl}$  concentration (Fig. 5.5 D1). These dimples are due to the formation of gas bubbles where metal ions cannot be reduced and the metal crystals cannot grow, resulting in less effective surface area. The real surface area, therefore, decreases with increasing the  $\text{NH}_4\text{Cl}$  concentration.



#### 5.4.4 Deposition Potential

The real surface area of the samples produced using  $\text{Ni}(\text{CH}_3\text{COO})_2$  increases with increasing the deposition potential, as shown in Fig. 5.7. For example, the real surface area of depositions with -1.7 V is 3.6 times of that with -1.35 V. This is because a higher overpotential results in a higher deposition nominal current density, which increases the production rates of both Ni crystals and hydrogen. The hydrogen gas bubbles coalesce on the deposit surface and the Ni crystals grow fast around the bubbles to form a porous structure. The gas bubbles float up in the solution by buoyancy and mix the solution, which promotes mass transfer of the solution and therefore results in more Ni deposits. The deposit grows thicker with the crystals becoming rougher and larger with increasing the overpotential, as shown in Figs. 5.5 C, G and H.

The real surface area of the samples produced using  $\text{Ni}(\text{SO}_3\text{NH}_2)_2$  has a different trend (Fig. 5.8) from that in the samples produced using  $\text{Ni}(\text{CH}_3\text{COO})_2$  (Fig. 5.7), when the deposition potential is increased. With increasing the overpotential from -1.7 to -1.9 V, the real surface area decreases slightly by 8%. This is because a high overpotential not only produces a high nominal current density, which increases the deposition rate of Ni and evolution of hydrogen, but also results in different reactions at the electrodes. Under an overpotential

of -1.7 V, the reaction taking place on the anode is shown in equation 5.5 (Karlsson and Cornell 2016), so the  $H^+$  ions in the solution are replenished and the pH value remains constant in a short deposition process. The reactions on the cathode are shown in equations 5.1 and 5.2, and therefore the deposit on the surface of electrode is loose with small crystals. With decreasing the potential to -1.9 V, partial reactions equations 5.4 and 5.6 occur on the anode, so the  $H^+$  ions decrease and the  $NH_4^+$  ions increase, resulting in an increased pH value. The change in the pH value causes the reaction on the cathode becoming equation 5.3. The deposition rate of Ni is low and the crystals can grow large, reducing the interstices between the crystals and decreasing the surface area.

There is no significant change in the real surface area when the overpotential is further increased to -2.1 V. This is because there are two competing factors. On one hand, reaction 5.6 is intensified at this potential so both reactions 5.4 and 5.6 become dominant on the anode. The surface becomes denser. On the other hand, the nominal current density also increases to a new level at this potential. The gas bubbles grow and coalesce on the surface to form dimples (Fig. 5.6 E1), which leads to the formation of fewer Ni crystals and thus a smaller real surface.

#### **5.4.5 Deposition Time**

The real surface area of the samples produced using  $\text{Ni}(\text{CH}_3\text{COO})_2$  increases with increasing the deposition time, as shown in Fig. 5.7. It increases markedly by 227% from 60 to 150 s, then slowly increases by 14% from 150 to 300 s. This is because at the beginning, a large amount of nano-structure crystals grow on the surface of the substrate. A new layer of crystals forms with time, up to a point. With a further increase in deposition time, the crystals become larger instead of forming new layers. Therefore, no significant change in surface area after 150 s.

The real surface area of the samples produced using  $\text{Ni}(\text{SO}_3\text{NH}_2)_2$  increases with increasing deposition time from 100 s to 150 s, but decreases from 150 s to 200 s, as shown in Fig. 5.8. This is because, during the initial stage of deposition, the nano Ni crystals deposit on the substructure and form new layers. With increasing the deposition time further, the surface morphology of Ni deposit becomes stable. The crystals grow larger and the deposit becomes denser, leading to decreasing real surface area.

## **5.5 Summary**

The effects of several deposition process parameters on the surface morphology and real surface area of the DHBT porous Ni samples have been investigated. The nominal deposition current density depends on the deposition

potential and the concentrations of the  $H^+$  source and Ni salt. The surface morphology is mainly affected by, in order of significance, deposition potential, type of anion, concentration of  $NH_4Cl$ , concentration of Ni precursor and deposition time. The real surface areas of the porous Ni samples manufactured by the DHBT porous method are in the range of 2.2 – 59  $cm^2$ .

The type of anion in the electrolyte has significant effects on the surface area of the DHBT porous nickel. In the electrolyte with  $CH_3COO^-$  anion, the real surface area of the DHBT porous Ni increases with increasing the deposition potential and deposition time. However, the surface area decreases with increasing the deposition potential in the electrolyte with  $SO_3NH_2^-$  anion. This is because of the hydrolysis of  $SO_3NH_2^-$  anion under high overpotential, which results in a dense deposit of the DHBT porous Ni and therefore low surface area. The real surface area of the DHBT porous Ni decreases with increasing the concentration of the Ni salt. However, the effect in the electrolyte with  $CH_3COO^-$  anion is minor but significant in the electrolyte with  $SO_3NH_2^-$  anion. The effect of concentration of  $NH_4Cl$  on the real surface area of the DHBT porous Ni is negligible.

## **Chapter 6 Mass Transfer Performance of LCS and LCS/DHBT**

### **Porous Ni**

#### **6.1 Introduction**

Mass transfer performance is an important parameter in electrochemical fields. Porous metal electrodes can be employed as superior electrochemical electrodes due to their highly active surface area and mass transfer coefficient (Recio et al. 2013, Zhu and Zhao 2017). Although the mass transfer coefficient of LCS porous Ni has been studied (Zhu and Zhao 2017), the studies have been limited in the effects of porous structure and fluid hydrodynamics. The effects of the surface morphology of the porous electrode on the mass transfer performance are still not well understood. Surface morphology has a significant effect on the surface area, which is an important factor characterizing the mass transfer performance. Hence, surface morphology can have a considerable influence on the mass transfer performance.

In this chapter, two methods to increase the surface area of the LCS porous Ni are studied. One is adding fine Ni powder during the manufacturing process in LCS and another one is forming a composite LCS/DHBT porous Ni structure by depositing a DHBT porous Ni film on the LCS porous Ni substrate. The increased surface area is expected to increase the limiting current, which is used to determine the overall mass transfer performance. The effect of fine Ni

powder ratio in LCS and the effects of deposition potential and time in DHBT on the mass transfer performance,  $kA$ , which refers to the product of mass transfer coefficient and active surface area, are studied. The effect of flow velocity is also investigated.

## 6.2 Effect of Fine Ni Powder ratio in LCS

Fig. 6.1 shows the mass transfer performance,  $kA$ , of the LCS porous Ni samples manufactured with different fine Ni powder ratio from 0 to 100%, at different electrolyte flow velocities. The mass transfer performance is in the range of 3 to 16  $\text{mm}^3/\text{s}$ . It increases with increasing the fine Ni powder ratio from 0 to 40% and decreases with increasing the fine Ni powder ratio from 60 to 100%.

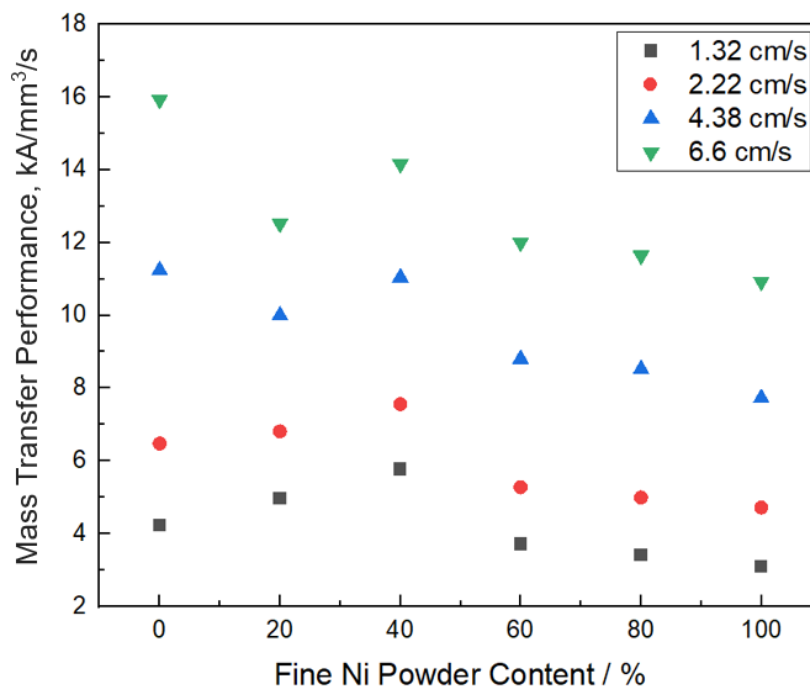


Fig. 6. 1: Mass transfer performance,  $kA$  of the LCS porous Ni as a function of

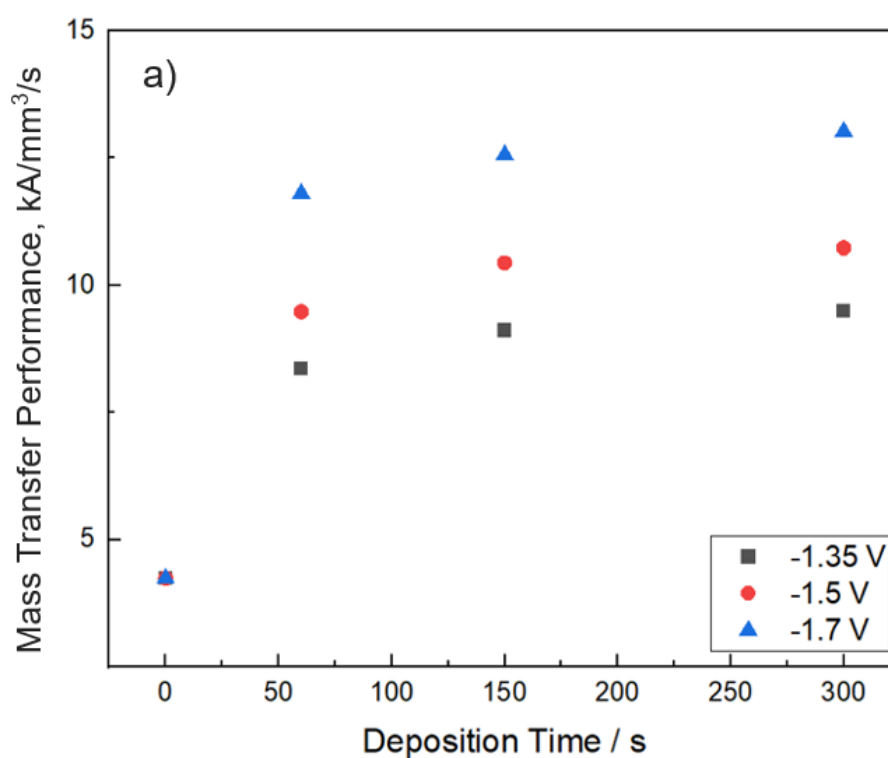
fine Ni powder ratio at different electrolyte flow velocities.

The effect of fine Ni powder ratio on the mass transfer performance can be explained by its effect on the morphology and surface area of the porous Ni electrode. As discussed in Chapter 4, with a low fine Ni powder ratio, the fine Ni particles are distributed on the surface of the coarse Ni particles and increase the surface area of the porous Ni sample. The limiting current is therefore increased. When the fine Ni powder ratio is higher than 40%, a large number of fine Ni particles are spread everywhere in the Ni matrix and the secondary pores in the matrix are decreased. The reduced amount and size of secondary pores decrease the pathways for the electrolyte to enter the porous Ni and decrease the effective surface area. In addition, the Ni walls become smoother and flatter due to the coalescence of the particles during sintering, which further decreases the surface area. The limiting current and the mass transfer performance are therefore decreased at a high fine Ni powder ratio in the metal matrix. The moderate content of fine powder have the highest effective surface area and therefore best grain in the limiting current.

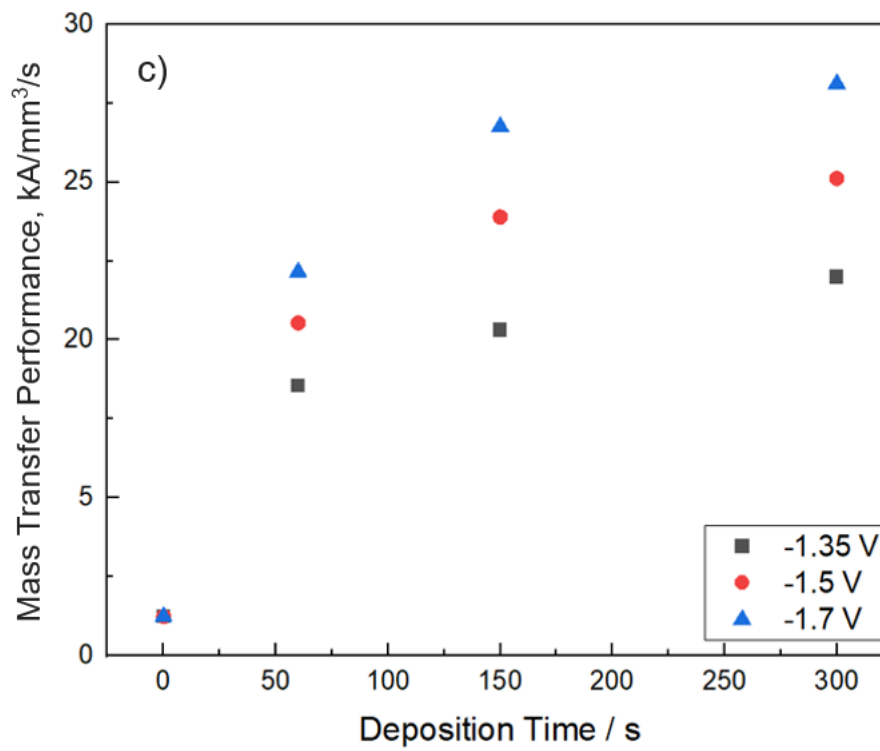
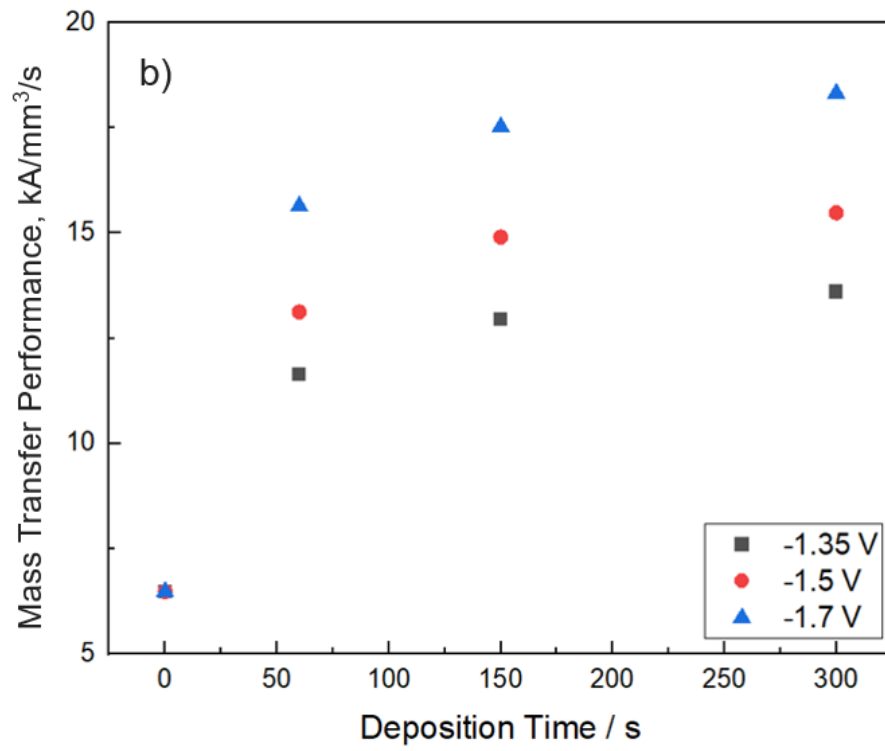
### **6.3 Effect of Deposition Potential and Time in LCS/DHBT**

Fig. 6.2 shows the variations of the mass transfer performance with the deposition time in a range of 60 to 300 s at different deposition potentials of -

1.35, -1.5 and -1.7 V for the LCS/DHBT composited porous Ni samples. The mass transfer performance is in the range of 4 – 38 mm<sup>3</sup>/s. The mass transfer performance is increased by up to 41% and 207% compared to the LCS porous Ni sample by increasing the deposition potential from -1.35 to -1.7 V and deposition time from 0 to 300 s, respectively.







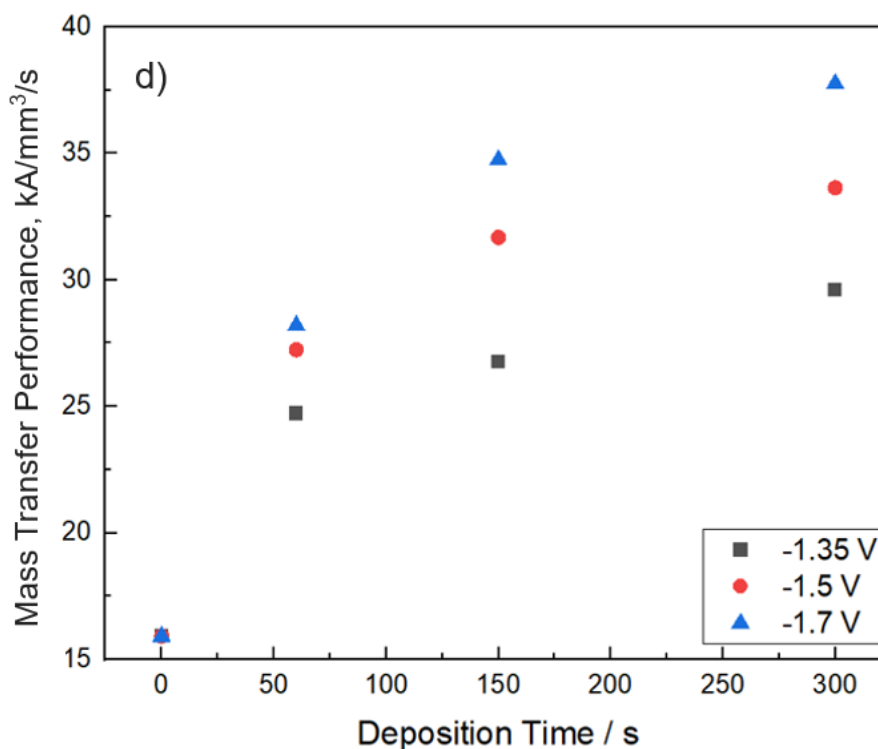


Fig. 6. 2: Mass transfer performance of the LCS/DHBT porous Ni as a function of deposition time under different deposition potentials of -1.35, -1.5 and -1.7 V and at different electrolyte flow velocities of (a) 1.32 cm/s, (b) 2.22 cm/s, (c) 4.38 cm/s and (d) 6.6 cm/s.

The effects of deposition potential and deposition time on the mass transfer performance can be explained by their effects on the surface area of the LCS/DHBT porous Ni electrode. Increasing the deposition potential increases the surface area of the deposit as discussed in Chapter 5. High deposition potential results in high deposition current and increases the Ni deposition rate. In addition, the hydrogen evolution rate is also increased at a high deposition current. The numerous micropores formed by enclosing the hydrogen bubbles in the deposit significantly increase the surface area of the porous Ni samples.

For any given deposition potential, increasing deposition time increases the number of Ni particles and the thickness of the deposit, which results in an increase in the surface area, as discussed in Chapter 5.

## 6.4 Effect of Flow Velocity

### 6.4.1 Fine Ni Powder ratio in LCS

In the mass transfer controlled region, the mass transfer performance,  $kA$ , can be calculated by equation 3.6. From the figures in the previous section, it is obvious that the mass transfer performance,  $kA$  is increased by increasing the electrolyte flow velocity. The relationship between the  $kA$  and electrolyte velocity can be expressed by (Langlois and Coeuret, 1989, Cognet et al., 1995):

$$kA = av^b \quad 6.1$$

where  $k$  is the mass transfer coefficient,  $A$  is the electrode active surface area,  $a$  is a constant associated with the structural properties of the electrode and  $b$  is a constant dependent on the hydrodynamic regime.

Fig. 6.3 shows the variations of the mass transfer performance with electrolyte velocity for the LCS porous Ni samples with different fine Ni powder ratios, plotted in logarithmic scale. It shows that there is a linear relationship between the mass transfer performance and the flow velocity in the logarithmic scale.

The effect of flow rate can indeed be described by equation 6.1.

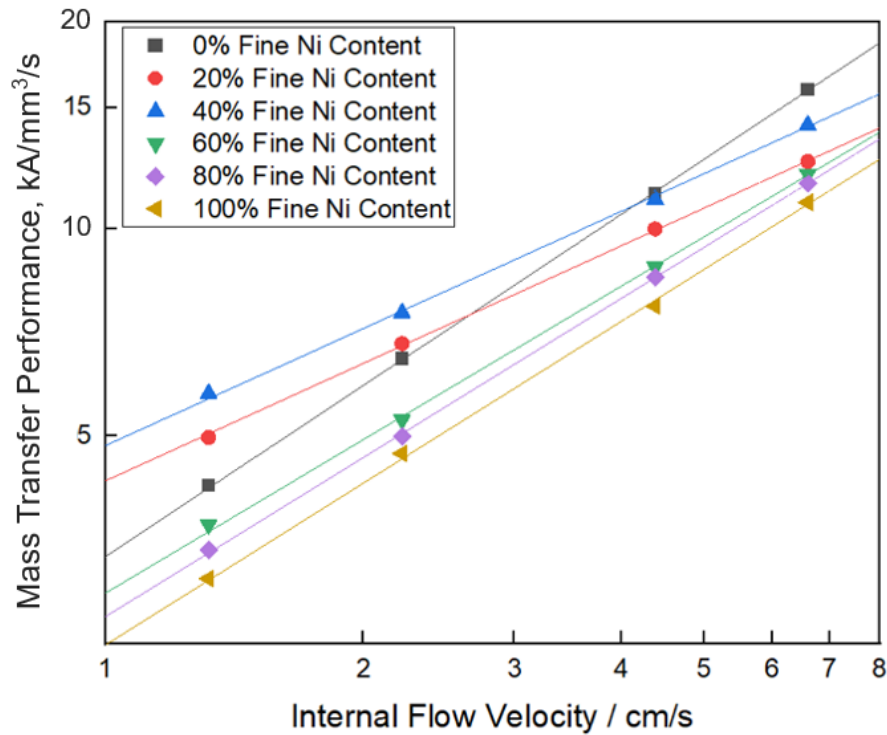


Fig. 6. 2: Logarithmic plots of the mass transfer performance, kA, versus electrolyte flow velocity for the LCS porous Ni samples manufactured with different fine Ni contents.

Table 6.1 lists the values of constants  $a$  and  $b$  for different fine Ni powder ratios, obtained by fitting the mass transfer performance data in Fig. 6.3 to equation 6.1. The values of the pre-exponential  $a$  are in the range of 0.0025 – 0.0049, while the values of the exponent  $b$  are in the range of 0.56 – 0.83. The constant  $a$  first increases with increasing fine Ni powder ratio, peaks at the fine Ni powder ratio of 40% and then decreases. The exponent  $b$  decreases with increasing the fine Ni powder ratio from 0 to 40% and then increases slightly from 40% to 100%.

Table 6. 1 Values of constants ‘*a*’ and ‘*b*’ for different fine Ni powder ratios, obtained by fitting the data to equation 6.1.

Constant \	Fine Ni Powder ratio of						
	Nominal mean Ni particle size, $\mu\text{m}$	0%	20%	40%	60%	80%	100%
		100	82	64	46	28	10
<i>a</i>		0.0033	0.0043	0.0049	0.003	0.0027	0.0025
<i>b</i>		0.83	0.57	0.56	0.74	0.76	0.78

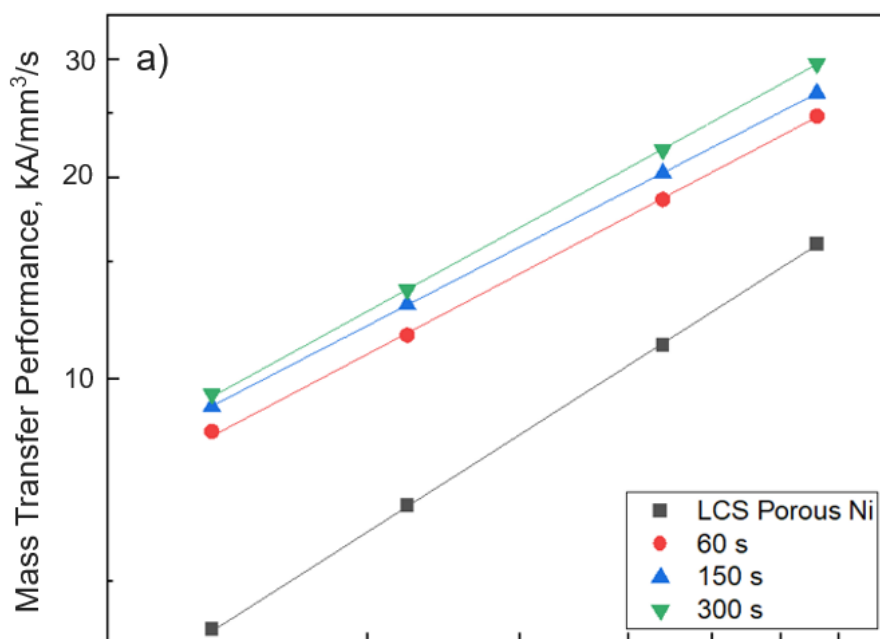
The pre-exponent ‘*a*’ is considered to be mainly affected by the electrode surface area. In the beginning of the reaction, the reactant close to the surface of the electrode is exhausted quickly. The larger surface area provides more reactive sites for reaction, and therefore results in a higher value of constant ‘*a*’. The effect of the fine Ni powder ratio on ‘*a*’ may arise from the magnitude of the electrolyte reservoir. A low content of fine Ni powder in the metal matrix does not affect the electrolyte distribution and provides a large number of active sites for reaction, therefore increasing the pre-exponential constant ‘*a*’. Increasing fine Ni powder ratio to above 40% can lead to particle agglomeration and blocked pores. The electrolyte cannot access some of the secondary pores, causing a decreased constant ‘*a*’.

The exponent ‘*b*’ is an indicator of hydrodynamics of the electrolyte (Recio et al. 2013, Zhu and Zhao 2017). Increasing fine Ni powder ratio can reduce the secondary pores and therefore the pathways of the electrolyte. For any porous

structure, less pathways mean decreased tortuosity (Diao et al. 2015) and therefore low turbulence, which can result in a decreased exponent value 'b'. With the fine Ni powder ratio increased over 60%, however, the surface morphology does not change much as explained in Chapter 4. The value of exponent 'b' becomes stable.

### 6.4.2 Deposition Potential and Time in LCS/DHBT

Fig. 6.4 shows the variations of the mass transfer performance with electrolyte velocity for the LCS/DHBT porous Ni samples with different deposition potentials and times, plotted in logarithmic scale. It shows that the mass transfer performance values of the LCS/DHBT samples are in the range of 8.36 – 37.76 mm<sup>3</sup>/s. They are much higher than those of the LCS samples, which are in the range of 4.24 – 15.92 mm<sup>3</sup>/s.



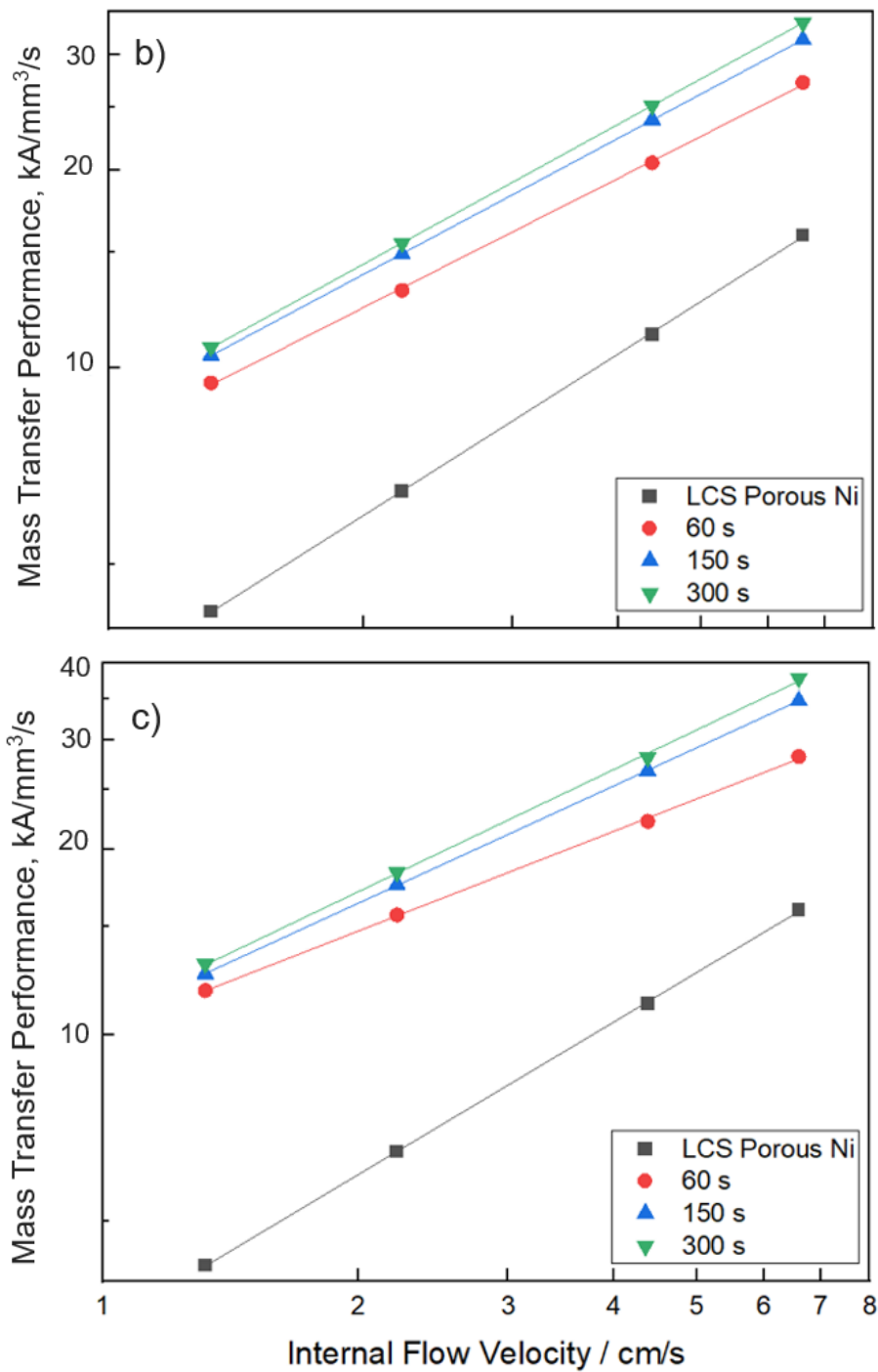


Fig. 6. 4: Logarithmic plots of the mass transfer performance, kA, versus the electrolyte flow velocity for the LCS/DHBT porous Ni samples manufactured under different deposition potentials of (a) -1.35 V, (b) -1.5 V and (c) -1.7 V, at different deposition times.

Table 6.2 lists the values of constants '*a*' and '*b*' for different deposition potentials and times, obtained by fitting the mass transfer performance data in Fig. 6.4 to equation 6.1. The values of constant '*a*' are in the range of 0.003 – 0.01, while the values of constant *b* are in the range of 0.41 – 0.83. The constant *a* generally increases with increasing the deposition potential, and increases with increasing the deposition time from 0 to 150 s and then decreases from 150 to 300 s. The constant '*b*' does not change much with deposition potential, and decreases with increasing the deposition time. The values of constant '*b*' are comparable to those of the LCS samples. The values of constant '*a*', however, are considerably higher than those of the LCS samples.

Table 6. 2 Values of constants '*a*' and '*b*' for different deposition potentials and deposition times, obtained by fitting the data to equation 6.1.

Deposition Potential (V)	Constants	Deposition Time (s)			
		0	60	150	300
-1.35	<i>a</i>	0.0033	0.0068	0.0092	0.0062
	<i>b</i>	0.8255	0.6820	0.6612	0.4422
-1.5	<i>a</i>	0.0033	0.0075	0.0102	0.0063
	<i>b</i>	0.8255	0.6772	0.6603	0.5014
-1.7	<i>a</i>	0.0033	0.0080	0.0066	0.0072
	<i>b</i>	0.8255	0.6622	0.4432	0.4115



The effects of deposition potential and deposition time on the constant ' $a$ ' can be explained by the magnitude of the electrolyte reservoir. A higher deposition potential produces a thicker deposit and larger dimples, which can accommodate more electrolyte and therefore lead to an increased constant ' $a$ '. Increasing deposition time increases the number of dimples and therefore increases the constant ' $a$ '. However, long deposition time causes an increase in the deposit thickness, which decreases the size of the primary pores. The pockets for the electrolyte become smaller, resulting in a reduced constant ' $a$ ' at an elongated deposition time. In addition, the interconnecting windows between the pores become smaller with increasing deposition time, which causes high resistance to electrolyte transfer. Furthermore, small pores have greater surface curvatures, which lead to thicker diffusion layers (Zhu and Zhao, 2017). A thick diffusion layer approaching the radius of the pore results in a quick depletion of the electrolyte and therefore decreases constant ' $a$ '.

## **6.5 Summary**

The mass transfer performance,  $kA$  of the LCS porous Ni samples with different fine Ni powder ratios of 0 – 100% and the DHBT porous Ni films with different deposition potentials of -1.35 – -1.7 V and deposition times of 60 – 300 s at different electrolyte flow velocities in the range of 1.32 – 6.6 cm/s were

investigated. The mass transfer performance values of the LCS porous Ni samples are in the range of 3 to 16 mm<sup>3</sup>/s. It increases with increasing the fine Ni powder ratio from 0 to 40% and decreases from 60 to 100%. The mass transfer performance values of the DHBT porous Ni films are in the range of 4 – 38 mm<sup>3</sup>/s. It increases by 41% when the deposition potential is increased from 0 to -1.7 V, and increases by 207% when the deposition time is increased from 0 to 300 s.

The mass transfer performance data were fitted to equation 6.1 and the values of constants 'a' and 'b' for different conditions were obtained. The LCS porous Ni with 40% of fine Ni powder ratio has the highest value of constant 'a', while the LCS porous Ni with no fine Ni powder has the highest value of constant 'b'. In the DHBT porous Ni samples, the constant 'a' generally increases with increasing the deposition potential and increases with increasing the deposition time first but decreases afterwards. The constant 'b' does not change much with deposition potential but decreases with increasing deposition time.

## **Chapter 7 Relationship between Current and Glucose Concentration for LCS/DHBT Ni Electrodes**

### **7.1 Introduction**

LCS porous metals have uniform porous structures and high specific surface areas, which potentially allow them to be used as electrochemical sensors. DHBT porous films can be easily formed on the surface of a substrate to increase the surface area markedly. In this chapter, composite porous Ni samples produced by the lost carbonate sintering/dynamic hydrogen bubble template (LCS/DHBT) method are used as electrodes and the relationship between electrode current and glucose concentration is investigated.

The electroactive surface areas of the Ni electrodes are measured. The effects of scan rate in cyclic voltammetry and the key DHBT process parameters (concentration of  $\text{NH}_4\text{Cl}$  and deposition potential) on the electrode current - glucose concentration profile for the composite LCS/DHBT porous Ni electrodes are investigated. The limit of detection (LOD) and the sensitivity of electrochemical detection of the LCS, LCS/DHBT, Ni plate and several other Ni-based electrodes in literature are compared.

The LCS porous Ni samples used as electrodes by itself or as the substrates for the composite LCS/DHBT electrodes in this work have a porosity of 80%, a

pore size of 710-1000  $\mu\text{m}$  and a constant volume of 0.12  $\text{cm}^3$ . The concentration of  $\text{Ni}(\text{CH}_3\text{COO})_2$  used in the DHBT fabrication is 0.2 M. The concentration of  $\text{NH}_4\text{Cl}$  is varied in three levels: 0.5, 1 and 1.5 M. The deposition potential is also varied in three levels: -1.35, -1.5 and -1.7 V. The deposition time is 300 s. The glucose concentration is varied from 10  $\mu\text{M}$  and increased until the peak current cannot be observed and measured. The scan rate in the cyclic voltammetry is in the range of 0.005 to 0.3 V/s. The density current in the chapter is the nominal current density.

## **7.2 Electroactive Surface Area**

Table 1 shows the electroactive surface areas of the composite LCS/DHBT porous Ni samples manufactured with different process parameters. The electroactive surface areas of these samples are in the range of 7.89 - 9.11  $\text{cm}^2$ . The composite LCS/DHBT porous Ni samples have higher electroactive surface areas than that of the pure LCS porous Ni. The electroactive surface area increases slightly with increasing the concentration of  $\text{NH}_4\text{Cl}$  or the deposition potential.

Table 7. 1 Electroactive surface areas of the LCS and composite LCS/DHBT porous Ni electrodes.

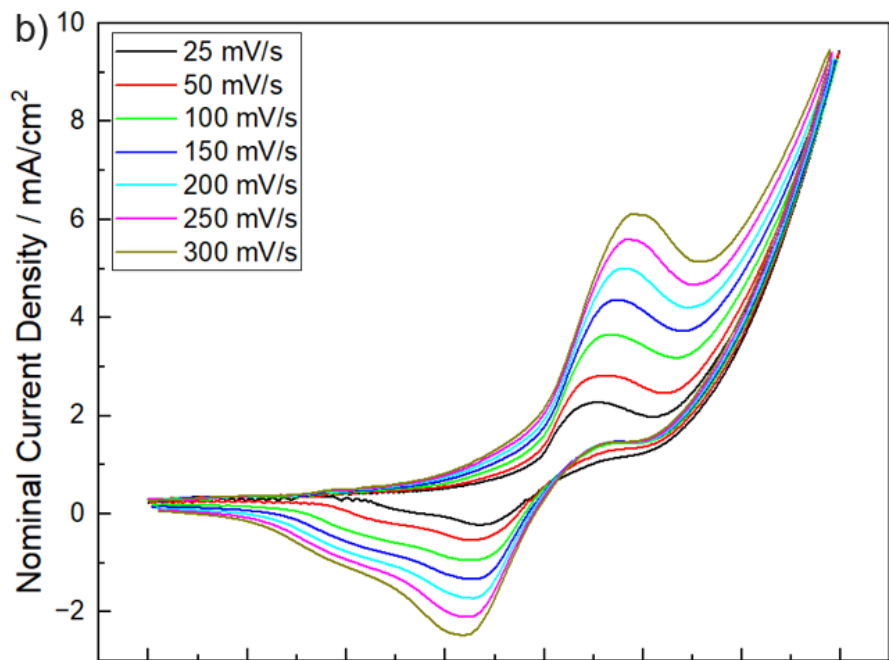
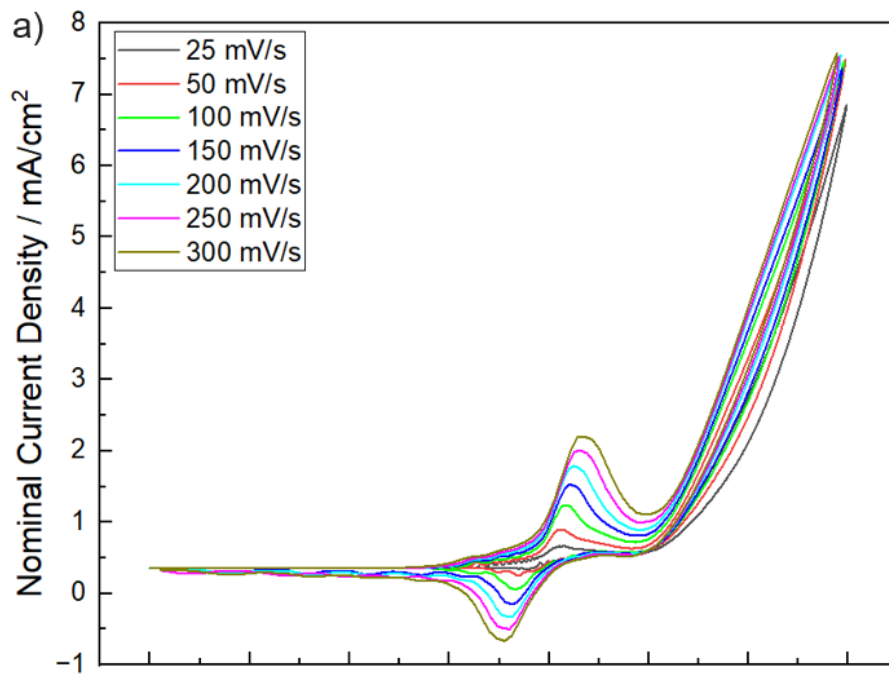
Sample No.	Concentration of NH <sub>4</sub> Cl (M)	Deposition Potential (V)	Peak Current (mA)	Electroactive Surface Area (cm <sup>2</sup> )
1	0	0	2.401	7.89
2	0.5	-1.35	2.598	8.53
3	1	-1.35	2.577	8.47
4	1.5	-1.35	2.523	8.29
5	0.5	-1.5	2.675	8.79
6	1	-1.5	2.654	8.72
7	1.5	-1.5	2.614	8.59
8	0.5	-1.7	2.774	9.11
9	1	-1.7	2.734	8.98
10	1.5	-1.7	2.694	8.85

Table 7.1 shows that the DHBT porous film has a moderate effect on the electroactive surface area. This is because the pores in the film are smaller or comparable to the thickness of the diffusion layer and the area provided by the nanostructures and nanopores on the electrode surface cannot be detected using the peak current method under the scan rate range used in this study. As a result, the effective surface area is much lower than the real surface area,

although the latter is significantly increased by the DHBT porous film. The current generated in the glucose measurement is due to the effective surface area rather than the real surface area. Hence, the electroactive surface area is more appropriate to reflect the effective surface area during the reaction.

### **7.3 Effect of Scan Rate on Current-Potential Profile**

Fig. 7.1 represent the cyclic voltammograms of the Ni plate, the LCS porous Ni sample (porosity: 80%, pore size: 710 - 1000  $\mu\text{m}$ ) and the composite LCS/DHBT porous Ni sample (1.5 M  $\text{NH}_4\text{Cl}$  and -1.7 V deposition potential), respectively, in 0.1 M KOH with 0.5 mM glucose at scan rates in the range of 25 – 300 mV/s. The nominal peak current densities for the Ni plate, the LCS porous Ni and the composite LCS/DHBT porous Ni electrodes are in ranges of 0.314 – 1.85, 1.92 – 5.57 and 3.43 – 13.94  $\text{mA}/\text{cm}^2$ , respectively.



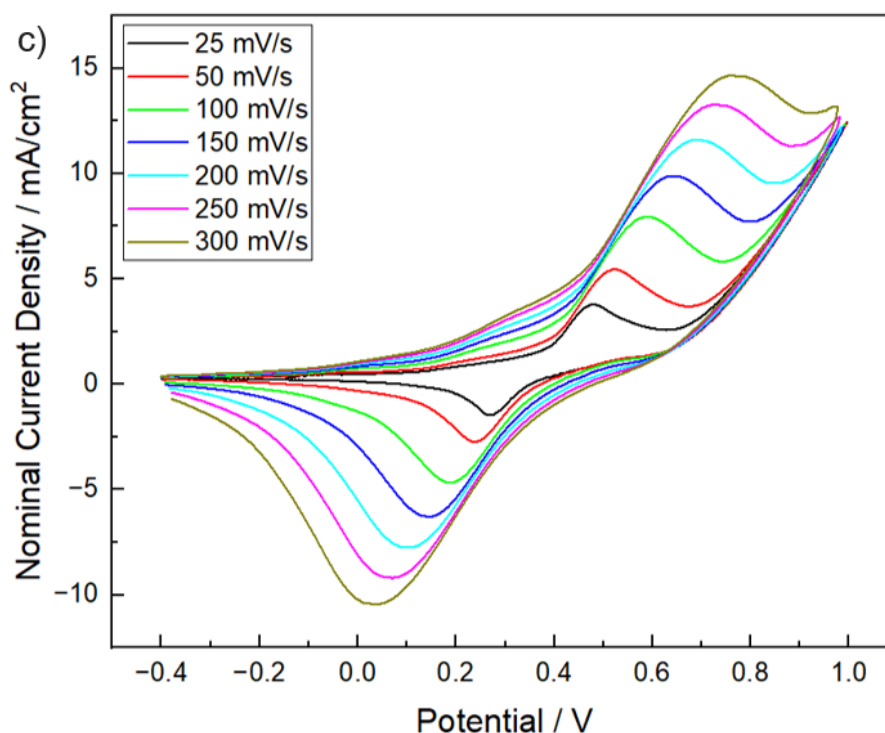


Fig. 7. 1: Cyclic voltammograms of a) the Ni plate electrode, b) the LCS porous Ni electrode (porosity: 80%, pore size: 710 - 1000  $\mu\text{m}$ ) and c) the LCS/DHBT porous Ni electrode (1.5 M  $\text{NH}_4\text{Cl}$  and -1.7 V deposition potential) in 0.1 M KOH and 0.5 mM glucose solution at scan rates of 25 – 300 mV/s.

The anodic peak occurs at a potential in the range of 0.4 to 0.8 V vs. SCE. The occurrence of the peak is due to the redox reaction of the  $\text{Ni}^{2+}/\text{Ni}^{3+}$  couple on the surface of the electrode (Reactions 2.15 – 2.17 in Chapter 2). The peak currents obtained by the LCS/DHBT porous Ni electrode are higher than those of the LCS porous Ni and Ni plate electrodes. It shows that, compared to the other two electrodes, the LCS/DHBT porous Ni electrode has more electron transfer reaction taking place on the surface.



It is noted that the anodic potential shifts positively with increasing scan rate. As the scan rate increases from 25 to 300 mV/s, the potential shifts for the Ni plate, the LCS porous Ni and the composite LCS/DHBT porous Ni electrodes are 0.058, 0.097 and 0.295 V, respectively. The anodic potential shift is due to the polarization of the increasing scan rate. Many factors including ohmic resistance in the three-electrodes configuration, electromotive force, as well as diffusional and electrochemical processes can induce polarization (Pu et. al 2021). The ohmic polarization caused by the ohmic resistance (inner resistance in the solution or the electrodes) is expressed by:

$$iR' = \varphi_{cathode} - \varphi_{anode} - \Delta V \quad 7.1$$

where  $i$  is the current through the circuit,  $R'$  is the ohmic resistance between the electrodes,  $\varphi_{anode}$  and  $\varphi_{cathode}$  are the potentials at anodic and cathodic peaks, and  $\Delta V$  is the potential shift.

Fig. 7.2 shows the anodic peak current density as a function of potential shift. The current density and potential shift have a good linear relationship, confirming that the potential shift is caused by the ohmic resistance.

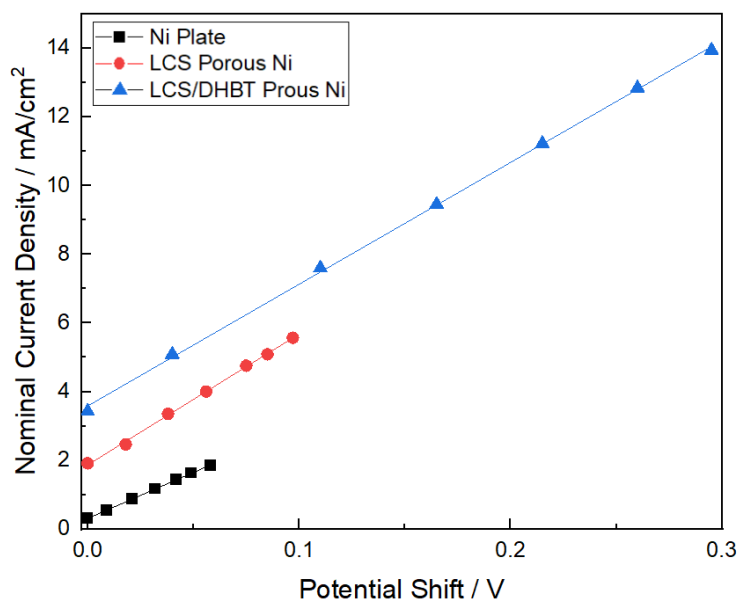


Fig. 7.2: Relationship between anodic peak current density and potential shift for the plate, LCS and LCS/DHBT Ni electrodes.

Table 7.2 shows the anodic peak current density and potential of the three electrodes at different scan rates. The anodic peak current of the Ni plate electrode is in the range of 0.314 to 1.848 mA/cm<sup>2</sup>. The low current densities show that the amount of glucose taking part in the reaction is small. The potential shift of the Ni plate electrode, however, is small and within 0.06 V, showing that the hindrance to the glucose diffusion to the electrode surface is small. This is because the concentration of products near the electrode surface is low for the Ni plate electrode, and therefore a thin diffusion layer is established between the Ni plate electrode and the bulk electrolyte. The glucose can pass the diffusion layer to reach the surface of the electrode with no difficulty.

Table 7. 2 Anodic current density and potential for plate, LCS and LCS/DHBT

Ni electrodes at different scan rates.

Scan Rate (V/s)	Plate		LCS		LCS/DHBT	
	Current Density (mA/cm <sup>2</sup> )	Potential (V)	Current Density (mA/cm <sup>2</sup> )	Potential (V)	Current Density (mA/cm <sup>2</sup> )	Potential (V)
0.025	0.314	0.42	1.922	0.50	3.428	0.48
0.05	0.546	0.43	2.474	0.52	5.09	0.52
0.1	0.885	0.44	3.363	0.54	7.597	0.58
0.15	1.176	0.45	4.013	0.55	9.448	0.64
0.2	1.436	0.46	4.762	0.57	11.22	0.70
0.25	1.644	0.47	5.094	0.58	12.84	0.73
0.3	1.848	0.48	5.569	0.59	13.94	0.78

The anodic peak current density of the LCS porous Ni is in the range of 1.922 to 5.569 mA/cm<sup>2</sup>. It is higher than that for the Ni plate. However, the LCS porous Ni electrode has an anodic peak potential of 0.5 V at a slow scan rate of 25 mV/s. It has the highest first-anodic-peak potential among the three electrodes. A high potential indicates a high inner resistance. This is because of the typical porous structure of the LCS porous electrode, which is made by sintering a compacted powder mixture. The Ni particles are connected to each other by

sintering necks. The small connecting area and interstices in the matrix can decrease the conductivity of the LCS porous Ni electrode. Additionally, there are oxides formed on the surface of the LCS porous Ni during the sintering process. Although the chemical treatment can remove most of the oxides, the residues can still affect the conductivity. The potential shift of the LCS porous Ni electrode is only 0.09 V, which is similar to that of the Ni plate electrode. It shows that the mode and rate of mass transport of glucose to the electrode surface are the same.

The composite LCS/DHBT porous Ni electrode has the highest anodic peak current density, which is in the range of 3.428 to 13.94 mA/cm<sup>2</sup>. The high peak current densities indicate a large amount of gluconolactone (oxidized product of glucose) is formed. The LCS/DHBT electrode has a much higher first-anodic-peak potential of 0.48 V than that of the Ni plate. As the ohmic resistance of the electrolyte is the same for all three electrodes, a high anodic peak potential indicates a high inner resistance (Pu et al. 2021). As all the electrodes are Ni based and have a similar conductivity, the main difference in the inner resistance can be attributed to the kinetics of the glucose redox reaction. Gluconolactone is formed by oxidation of the glucose and distributes near the surface of the electrode, which impedes the diffusion of the glucose from bulk electrolyte to surface of electrode and causes increased inner resistance.

The composite LCS/DHBT porous Ni electrode has the largest range of shifts of 0.3 V when the scan rate is increased from 25 to 300 mV/s. The increase in the potential shift is also the fastest among the three electrodes, indicating fast increase in the ohmic resistance of the electrolyte with increasing scan rate.

Fig. 7.3 shows the variations of the anodic peak current density with the square root of scan rate for the plate, LCS and LCS/DHBT porous Ni electrodes. The linear relationship shows that the oxidation of glucose on the electrode surfaces is a diffusion-controlled process, i.e., the diffusion rate is the rate-determining step. The active molecules are transported to the surface of the electrode by the spontaneous concentration difference because of the depletion of reactants at the electrode surface and a diffusion layer between the bulk solution and the electrode surface is established (Bard 2002).

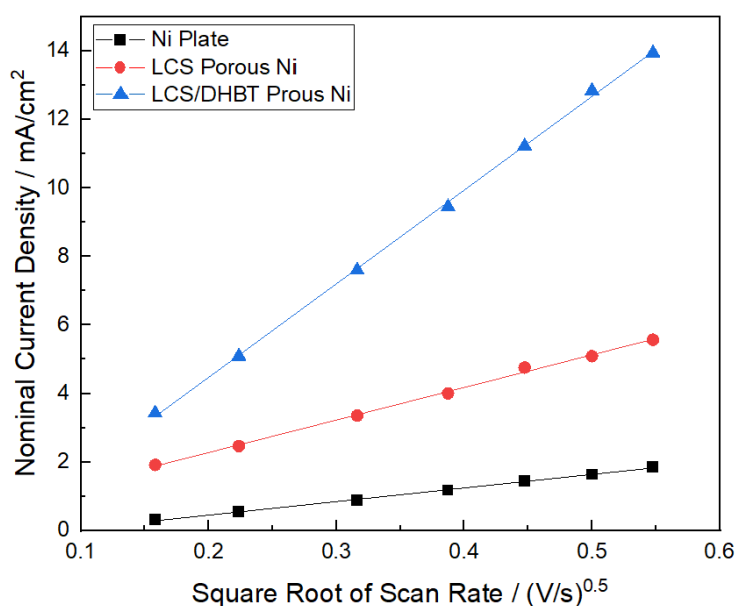


Fig. 7. 3: Variations of current density with square root of scan rate for the

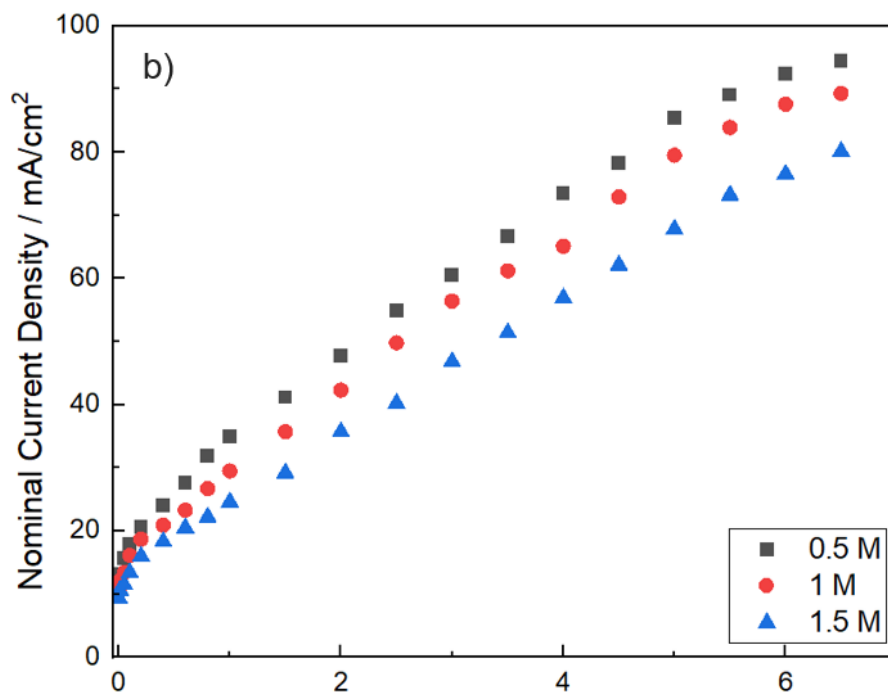
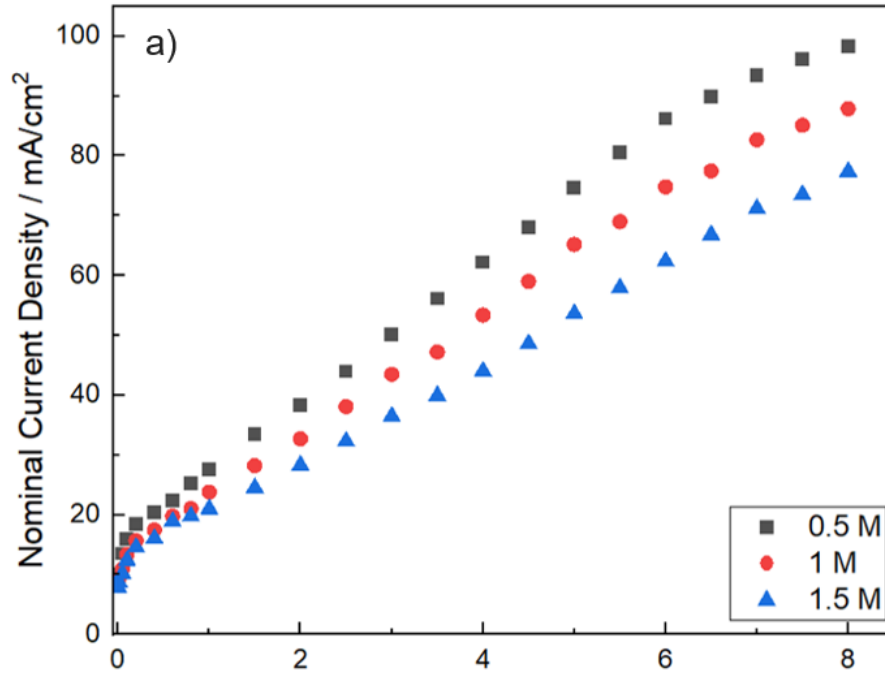
three different Ni electrodes.

Fig. 7.3 shows that there is a linear relationship between the nominal current density and square root of scan rate for all three electrodes, which indicates that the reaction is controlled by the semi-diffusion process. The LCS/DHBT porous electrode has the steepest slope and the highest intercept, indicating that the LCS/DHBT porous Ni electrode has the highest effective surface area. The electrodes with high surface areas can provide a high detection sensitivity because such electrodes provide high current density. The LCS porous Ni electrode has a similar slope to the Ni plate electrode, not as high as the LCS/DHBT electrode. However, its intercept is higher than the plate electrode, which shows that the LCS porous Ni electrode has a higher reaction current than the Ni plate electrode at any given condition. The Ni plate electrode has the lowest slope and intercept among the three electrodes, which indicates a very limited accuracy of measurement. This means that Ni plate electrodes are not a good choice for electrochemical measurement of glucose, especially when there are other species that interfere with the measurement, including ascorbic acid and uric acid (Niu et al. 2013, Ko et al. 2013).

## **7.4 Effects of Manufacturing Parameters on Current-Concentration Relationship**

### **7.4.1 Effect of Concentration of $\text{NH}_4\text{Cl}$**

Fig. 7.4 shows the current density profiles as a function of glucose concentration for the LCS/DHBT electrodes manufactured with different  $\text{NH}_4\text{Cl}$  concentrations of 0.5, 1 and 1.5 M in the electrolyte at a deposition potential of -1.35, -1.5 and -1.7 V, respectively. The current density decreases by increasing the concentration of  $\text{NH}_4\text{Cl}$  in the manufacturing process. For example, under a deposition potential of -1.35 V, the current density (0.5 M  $\text{NH}_4\text{Cl}$ ) is decreased by 23% and 41% when the concentration of  $\text{NH}_4\text{Cl}$  is increased from 0.5 M to 1 M and 1.5 M, respectively. The trend is similar for the electrodes manufactured under the deposition potentials of -1.5 and -1.7 V. This is because a higher concentration of  $\text{NH}_4\text{Cl}$  results in large Ni particles in the film and therefore a smaller effective surface area (Table 7.1). A low surface area provides less active sites for the electrochemical reaction and therefore a lower current density. Among the electrodes manufactured with electrolytes containing different concentrations of  $\text{NH}_4\text{Cl}$ , the composite LCS/DHBT porous Ni electrode manufactured with 0.5 M  $\text{NH}_4\text{Cl}$  electrolyte has the highest current density in this study.





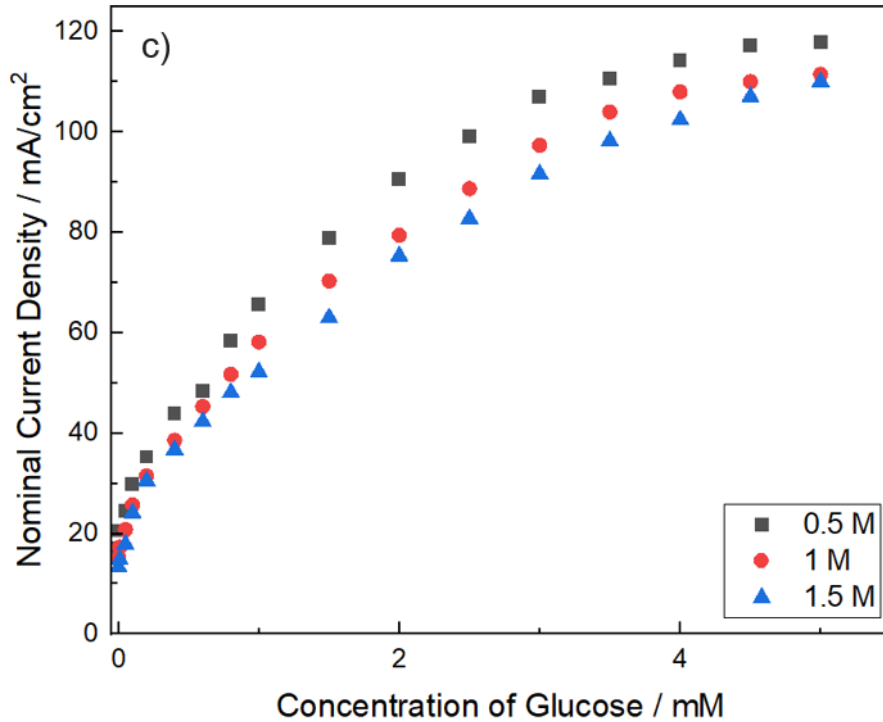
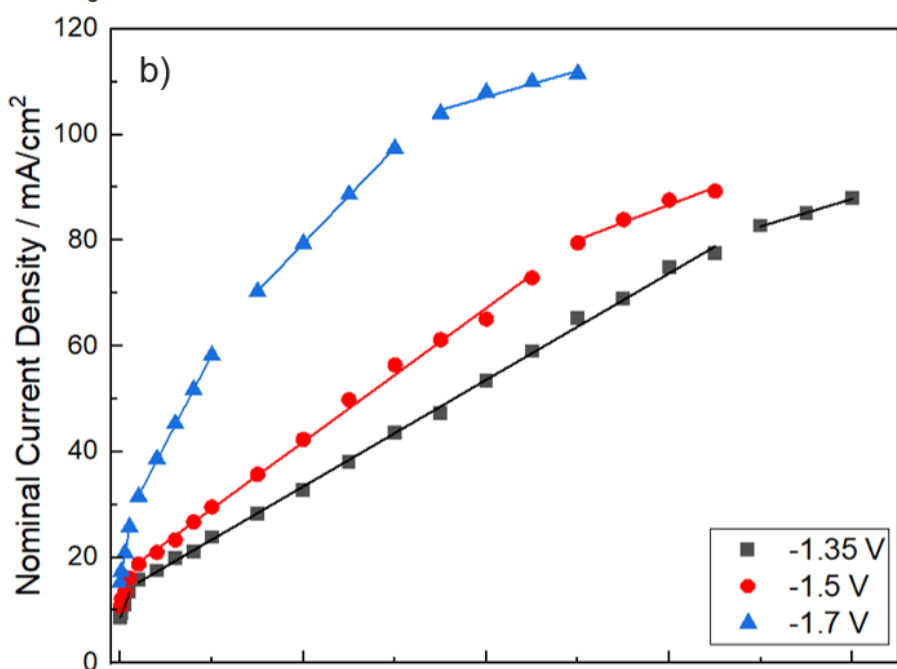
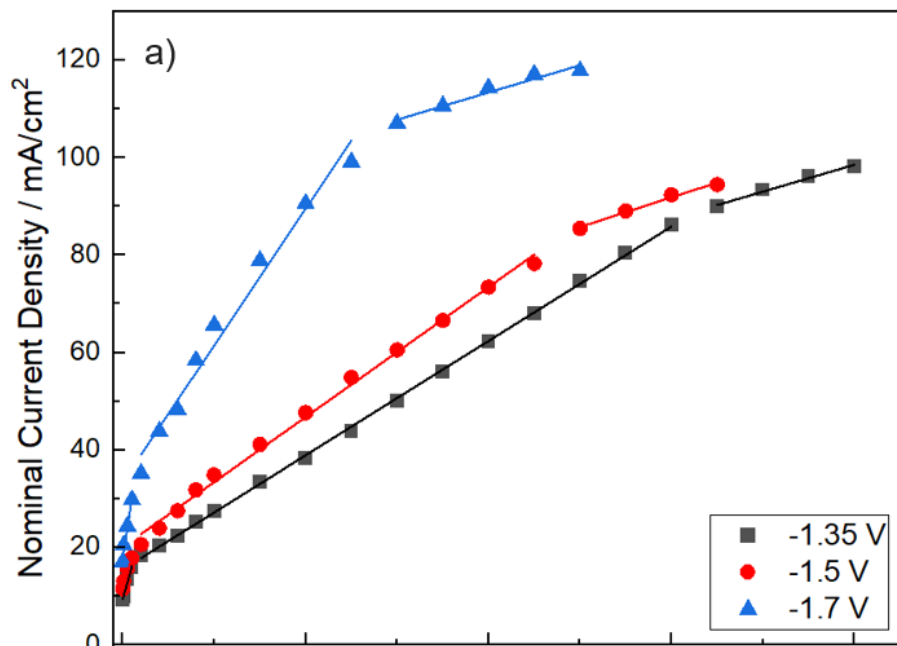


Fig. 7. 4: Current density as a function of glucose concentration for LCS/DHBT electrodes manufactured with different NH<sub>4</sub>Cl concentrations of 0.5, 1 and 1.5 M in the electrolyte at a deposition potential of a)-1.35 V, b) -1.5 V and c) -1.7 V.

### 7.4.2 Effect of Deposition Potential

Fig. 7.5 shows the current density profiles as a function of glucose concentration for the LCS/DHBT electrodes manufactured at different deposition potentials of -1.35, -1.5 and -1.7 V with a NH<sub>4</sub>Cl concentration of 0.5, 1 and 1.5 M in the electrolyte, respectively. The current density increases with increasing the deposition potential in the manufacturing process. For the electrolyte with a NH<sub>4</sub>Cl concentration of 0.5 M, for example, the current density is increased by 24% and 58% when the deposition potential is increased from

-1.35 V to -1.5 and then to -1.7 V. This is because a more negative deposition potential results in a larger specific surface area of the as-manufactured DHBT porous film, as discussed in Chapter 5, which in turn leads to a current density. For the electrolytes with a  $\text{NH}_4\text{Cl}$  concentration of 1 and 1.5 M, the trend is similar. It is noticed that the LCS/DHBT porous Ni sample with the highest surface area has the smallest linear range. This is because the high surface area is produced by the DHBT porous Ni coating. Under a high overpotential condition, the surface area of deposit is large and the structure of the surface is complex. After oxidation, the product is difficult to transport away from the electrode surface. As mentioned above, a high concentration of product at the electrode surface causes a distorted diffusion process, and therefore results in a potential shift. When the peak potential shifts positively and reaches to the potential of the oxygen evolution reaction, it is difficult to observe the peak current of the glucose reaction, and therefore leading to a narrow detection range.



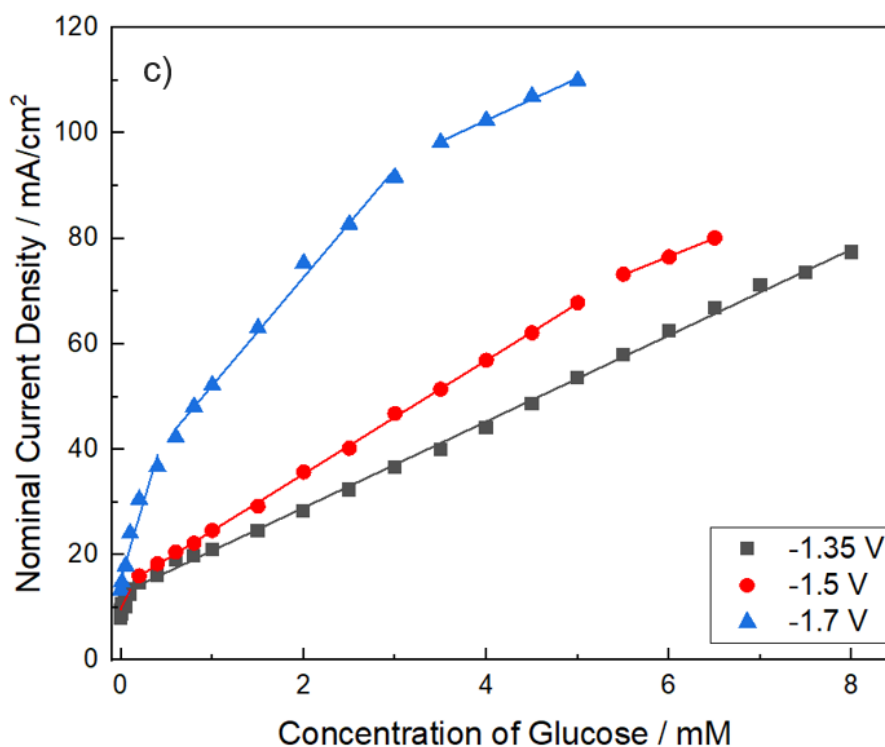


Fig. 7.5: Current density as a function of glucose concentration for LCS/DHBT electrodes manufactured with a) 0.5 M, b) 1 M and c) 1.5 M  $\text{NH}_4\text{Cl}$  in the electrolyte at different deposition potentials of -1.35, -1.5 and -1.7 V.

It is noticed that the slope and the intercept of the current density against glucose concentration curves vary with glucose concentration. For the electrode manufactured with 0.5 M  $\text{NH}_4\text{Cl}$  in the electrolyte, the slope decreases while the intercept increases with increasing glucose concentration. At a deposition potential of -1.35 V, the slope is decreased by 83% and 92% when the glucose concentration is increased from the range of 0.01 to 0.1 mM to the range of 0.2 to 6 mM, and further to the range of 6.5 to 8 mM. The corresponding intercept is increased by 64% and then 476% with increasing the glucose concentration from the range of 0.01 to 0.1 mM to the range of 0.2

to 6 mM, and further to the range of 6.5 to 8 mM. The electrodes manufactured at the deposition potentials of -1.5 and -1.7 V have a similar trend, although the amounts of increase are different.

The electrode manufactured with 1 M  $\text{NH}_4\text{Cl}$  in the electrolyte shows a similar trend as that with 0.5 M  $\text{NH}_4\text{Cl}$ . At a deposition potential of -1.35 V, the slope is decreased by 79% and 89% when the glucose concentration is increased from the range of 0.01 to 0.1 mM to the range of 0.2 to 6.5 mM, and further to the range of 7 to 8 mM. The corresponding intercept is increased by 53% and then 431%. The electrodes manufactured at the deposition potentials of -1.5 have a similar trend, although the amounts of increase are different. However, the sample manufactured at the deposition potential of -1.7 V has four linear ranges. The slope of the current density vs glucose concentration curves is decreased by 67%, 82% and 95% when the glucose concentration is increased from the range of 0.01 to 0.1 mM to the range of 0.2 to 1 mM, 1.5 to 3 mM and then 3.5 to 5 mM. The corresponding intercept is increased by 60%, 175% and 457%, respectively.

The electrode manufactured with 1.5 M  $\text{NH}_4\text{Cl}$  in the electrolyte also shows a similar trend. At a deposition potential of -1.5 V, the slope is decreased by 70% and 81% when the glucose concentration is increased from the range of 0.01 to 0.1 mM to the range of 0.2 to 5 mM, and further to the range of 5.5 to 6.5

mM. The corresponding intercept is increased by 41% and then 261%. At a deposition potential of -1.7 V, the slope is decreased by 65% and 86% when the glucose concentration is increased from the range of 0.01 to 0.4 mM to the range of 0.6 to 3 mM, and further to the range of 3.5 to 5 mM. The corresponding intercept is increased by 105% and then 356%. However, the sample manufactured at the deposition potential of -1.35 V has only two linear ranges. The slope of the current density vs glucose concentration curves is decreased by 81% when the glucose concentration is decreased from the range of 0.01 to 0.1 mM to the range of 0.2 to 8 mM. The corresponding intercept is increased by 55%.

The decreasing slope with increasing glucose concentration is due to increasing gluconolactone produced near the electrode surface in the electrolyte and therefore a sluggish kinetic of glucose electrooxidation reaction, especially in the pores with poor interconnection with other pores inside the electrode. It is difficult for the products to escape from the inter pores, especially in the complex pore structure, which exacerbates the sluggish kinetic reaction. The electrode surface is partially covered by the adsorbed products and therefore, fewer active sites are available for the glucose atoms. In addition, the diffusion of glucose from the bulk solution to the electrode surface is inhibited at a high concentration of reactant and products around the electrode surface.

## 7.5 Comparison with Other Ni Electrodes

Fig. 7.6 shows the variations of anodic peak current density as a function of glucose concentration for the Ni plate, LCS porous Ni and LCS/DHBT porous Ni electrodes. Each current vs concentration curve can be divided into several linear segments. At any given glucose concentration, the LCS/DHBT electrode has the highest current density, up to 2.5 times of that of the plate electrode and 1.62 times of that of the LCS electrode. This is because the LCS/DHBT electrode has a extremely high effective surface area and therefore a large number of active sites for the glucose oxidation reaction. High effective surface area provides a large detection range and a high sensitivity during the electrochemical glucose detection.

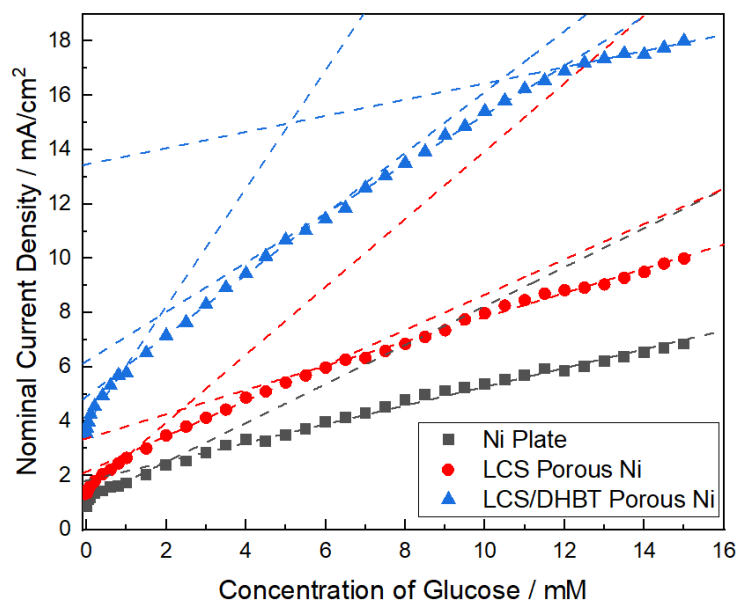


Fig. 7. 6: Anodic peak current density as a function of glucose concentration for the plate, LCS and LCS/DHBT Ni electrodes.

It is shown in Fig. 7.6 that the LCS/DHBT porous Ni electrode the slope of the current density vs glucose concentration curve becomes gentle after increasing glucose concentration to above 12 mM. This decrease in current is due to local exhaustion of glucose. In a porous electrode with large pores, the pores serve as reservoirs, constantly supplying the reactants. The LCS/DHBT electrode contains many very small pores (as shown in Fig. 5.5 G2). The reactants in these pores can be easily exhausted before new reactants are transported to these pores.

The resistance includes the reaction at a high concentration of the electrolyte and the electrodes themselves. In section 7.2, the inner resistance of electrode



is shown as  $R_{\text{LCS/DHBT}} > R_{\text{LCS}} > R_{\text{Ni plate}}$ , by comparing to the width of the anodic peak. Therefore, the LCS/DHBT porous Ni electrode has the largest potential shift at the potential of anodic peak, and then is the LCS porous Ni electrode. The Ni plate electrode has the smallest potential shift among these electrodes in glucose measurement. The anodic peaks move positively with increasing the concentration of glucose. The anodic peak current cannot be distinguished when glucose oxidation's potential overlaps with oxygen evolution at the anode. Hence, the glucose measurement range of the LCS/DHBT porous Ni electrode is not a patch on the LCS porous Ni electrode and Ni plate electrode.

Fig. 7.7 shows the variations of the anodic peak potential as a function of the glucose concentration for the plate, LCS and LCS/DHBT Ni electrodes. The potential shifts of the LCS/DHBT electrodes at a glucose concentration of 15 mM are 0.23, 0.32 and 0.5 V, respectively. The LCS/DHBT electrode has not only the highest potential shift but also the greatest rate of increase with increasing glucose concentration. The anodic peak potential shift is due to the increased concentration of the reaction products in the electrolyte, which increase the resistance of the solution.

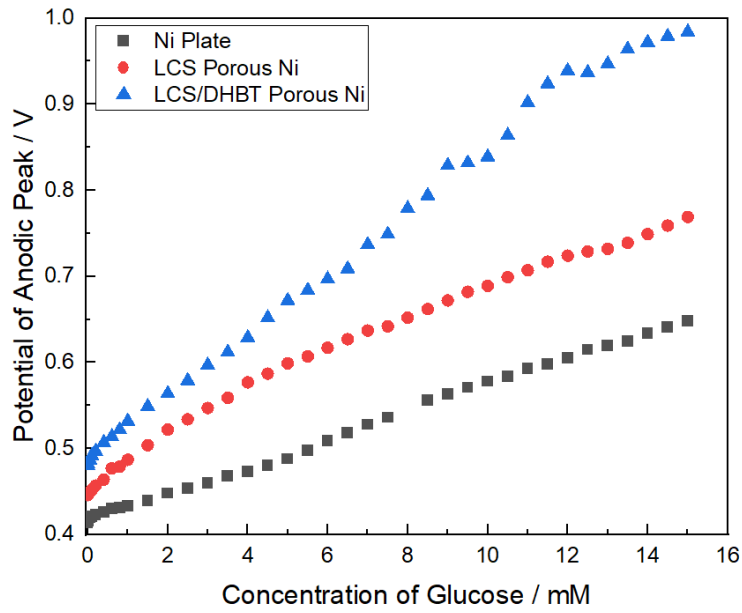


Fig. 7.7: Anodic peak current potential as a function of glucose concentration for the plate, LCS and LCS/DHBT Ni electrodes.

The key parameters to assess the performance of an electrochemical sensor are the Limit of Detection (LOD) and sensitivity. LOD is calculated by (Desimoni and Brunetti 2015):

$$\text{LOD} = \frac{k'\sigma}{b'} \quad 7.2$$

where  $k'$  is the expansion factor (usually = 3),  $\sigma$  is the population standard deviation of the blank signals and  $b'$  is the slope of the signal/concentration functional relationship (the linear part of the current vs concentration curve).

Sensitivity is expressed by:

$$\text{Sensitivity} = \frac{\text{change in the anodic peak current}}{\text{change in the concentration}} \quad 7.3$$

Table 7.3 shows the linear ranges of the current vs concentration curve, anodic peak current, LOD and sensitivity values of the plate, LCS and LCS/DHBT Ni electrodes for electrochemical non-enzymatic glucose measurements. The values of typical Ni electrodes in the literature are listed in Table 7.4 for comparison. It shows that the composite LCS/DHBT and LCS porous Ni electrodes have good linear ranges and high sensitivity as Ni-based non-enzyme electrodes for electrochemical glucose detection.

Table 7. 3 Comparison of electrochemical properties of plate, LCS and LCS/DHBT Ni electrodes for glucose measurement.

Electrode	Linear Range (mM)	Anodic Peak Current ( $\mu\text{A}$ )	LOD ( $\mu\text{M}$ )	Sensitivity ( $\mu\text{A}/\text{cm}^2\text{mM}$ )	Standard Deviation, $\sigma$
Ni Plate	0 - 1	1724	0.49	1724	0.284
	2- 15	4764	7.13	568	1.35
LCS Porous Ni	0 - 1	2651	0.53	2651	0.4695
	1 - 6	4435	2.15	1374	0.989
	4 - 15	7950	4.29	839	1.2
LCS/DHBT Porous Ni	0 - 1	5775	0.43	5775	0.833
	1 - 6	8552	1.83	2781	1.7
	4 - 12	14395	2.91	1686	1.64
	12 - 15	17563	0.66	1297	0.288

Table 7. 4 Comparison of electrochemical properties of Ni-based electrodes  
for electrochemical non-enzymatic glucose measurement

Material	Linear Range (mM)	LOD ( $\mu\text{M}$ )	Sensitivity ( $\mu\text{A}/\text{cm}^2\text{mM}$ )	Reference
Ni nanospheres/RGO	0.001-0.11	N/A	813	Wang et al. 2012
Ordered Ni nanowire arrays	0.0005-7	0.1	1043	Lu et al. 2009
3D porous Ni networks	0.0005-4	0.007	2900	Niu et al. 2013
Ni-MWCNT	3.2-17.5	0.98	67.19	Sun et al. 2012
Ni nanoflake/Ti plate	0.05-0.6	1.2	7320	Yi et al. 2016
NiO microfiber/FTO	0.001-0.27	0.033	1785.41	Cao et al. 2011
Ni nanoparticle/C fiber mixture	Up to 2.55	1	420.4	Liu et al. 2009
Ni nanoparticle	0.001-1	0.05	1438	Nie et al. 2011
Ni foam	0.05-7.35	2.2	N/A	Lu et al.

				2013
Ni nanoparticle on porous GF	0.015-6.45	4.8	207.3	Wang et al. 2017
Ni nanoparticle on porous Si	0.002-5	0.2	N/A	Ensafi et al. 2017
Ni plate	0 - 1	0.49	1724	This work
	2- 15	7.13	568	
LCS porous Ni	0 - 1	0.53	2651	This work
	1 - 6	2.15	1374	
	4 - 15	4.29	839	
LCS/DHBT porous Ni	0 - 1	0.43	5775	This work
	1 - 6	1.83	2781	
	4 - 12	2.91	1686	
	12 - 15	0.66	1297	

Note: RGO - reduced graphene oxide, MWCNT - multiwalled carbon nanotubes, FTO - fluorine tin oxide, GF - graphene foam

The LOD values of the plate, LCS and LCS/DHBT Ni electrodes are in the ranges of 0.49 – 7.13, 0.53 – 4.29 and 0.66 – 2.91  $\mu\text{M}$ , respectively. The sensitivity values are 1724, 2651 and 5775  $\mu\text{A}/\text{cm}^2\text{mM}$ , respectively. The LCS and LCS/DHBT Ni electrodes have excellent electrocatalytic performance for glucose measurement in terms of the LOD and sensitivity, compared to the Ni

plate electrode. This is because the LCS and LCS/DHBT porous Ni electrodes have high effective surface areas and great porous structures in electrochemical measurement (Zhu and Zhao 2017). The composite LCS/DHBT porous Ni electrode, in particular, has nanoscale Ni particles on the surface, which provides superior electrochemical properties compared to those electrodes with smooth surfaces. The macro pores in the structure provide pathways to facilitate the mass transfer of the reactants and products to the surface from the electrolyte.

Compared to the Ni-based sensors reported in the literature, the LCS/DHBT porous Ni has an excellent linear detection range of glucose. As discussed above, the current peak of glucose oxidation is hard to be distinguished if it overlaps with other reactions, e.g., oxygen evolution reaction. The LCS/DHBT porous Ni samples have a large potential difference between the glucose oxidation and oxygen evolution reactions with a slow positive potential shift and the overlapping does not occur until a high glucose concentration. The LCS/DHBT porous Ni samples not only have a large range of LOD comparable to the other Ni-based Ni sensors, but also have a higher sensitivity in glucose detection. The sensitivity of the LCS/DHBT porous electrodes is still high even though the glucose concentration is higher than 10 mM.

## 7.6 Summary

The LCS/DHBT porous Ni electrode shows an excellent performance in electrochemical glucose detection. Compared to the other Ni based sensors in the literature, the LCS/DHBT porous Ni electrode has a large linear detection range and high sensitivity. The effects of scan rate and manufacturing process parameters on current - glucose concentration relationship for the composite LCS/DHBT porous Ni electrode are investigated. The LCS/DHBT electrode has a high sensitivity of 5775  $\mu\text{A}/\text{cm}^2\text{mM}$ , compared to 2651  $\mu\text{A}/\text{cm}^2\text{mM}$  for the LCS porous Ni electrode and 1724  $\mu\text{A}/\text{cm}^2\text{mM}$  for the Ni plate electrode. The peak current densities for the plate, LCS and LCS/DHBT Ni electrodes in the electrolyte with 0.1 M KOH and 0.5 mM glucose at scan rates in the range of 25 – 300 mV/s are in the ranges of 0.314 – 1.85, 1.92 – 5.57 and 3.43 – 13.94  $\text{mA}/\text{cm}^2$ , respectively. The current density decreases with increasing the  $\text{NH}_4\text{Cl}$  concentration during manufacturing, by around 23% and 41% when the  $\text{NH}_4\text{Cl}$  concentration is increased from 0.5 M to 1 M and to 1.5 M, respectively. The current density is increased by around 24% and 58% when the deposition potential is increased from -1.35 to -1.5 and to - 1.7 V. The slope of the current density-glucose concentration curves decreases, and the intercept increases, with increasing glucose concentration.

## **Chapter 8 Conclusions and Future Work**

### **8.1 Conclusions**

#### **8.1.1 Surface Area of LCS Porous Ni**

Both porous structure and surface morphology affect the electroactive and real surface areas of the LCS porous Ni. The surface morphology of the LCS porous Ni samples manufactured with varying process parameters, including pore size, porosity, metal particle size, compaction pressure, sintering temperature and chemical treatment, were characterized and the real and electroactive surface area were measured.

The volumetric and gravimetric real surface areas of the LCS porous Ni samples are in the ranges of 500-1650  $\text{cm}^{-1}$  and 200-650  $\text{cm}^2/\text{g}$ , respectively. The volumetric real surface area increases with increasing fine Ni powder ratio and decreasing pore size and porosity. The gravimetric real surface area increases with increasing fine Ni powder ratio and porosity and decreasing compaction pressure.

The volumetric and gravimetric electroactive surface areas of the LCS porous Ni samples are in the ranges of 60-220  $\text{cm}^{-1}$  and 30-130  $\text{cm}^2/\text{g}$ , respectively. The electroactive surface area increases with increasing porosity and fine Ni



powder contain but decreases with increasing pore size, compaction pressure and sintering temperature. The electroactive surface area also depends on the diffusion layer thickness associated with the electrochemical reaction. In the semi-infinite diffusion controlled regime, the thickness of the diffusion layer mainly depends on the sweep speed. A high sweep speed leads to a relatively thin diffusion layer, which effectively decreases the probe size of measurement. More details on the electrode surface are detected, and therefore a high electroactive surface area is obtained.

### **8.1.2 Surface Area of LCS/DHBT Porous Ni**

The effects of several deposition process parameters on the surface morphology and real surface area of the DHBT porous Ni samples have been investigated. The nominal deposition current density depends on the deposition potential and the concentrations of the  $H^+$  source and Ni salt. The surface morphology is mainly affected by, in order of significance, deposition potential, type of Ni salt, concentration of  $NH_4Cl$ , concentration of Ni precursor and deposition time. The real surface areas of the porous Ni samples manufactured by the DHBT method are in the range of 2.2 – 59  $cm^2$ . In solutions with  $Ni(CH_3COO)_2$ , the real surface area is influenced mainly by deposition potential and deposition time and moderately by the concentrations of  $NH_4Cl$  and  $Ni(CH_3COO)_2$ . In solutions with  $Ni(SO_3NH_2)_2$ , however, decreasing the

concentration of  $\text{Ni}(\text{SO}_3\text{NH}_2)_2$  significantly increases the real surface area. The effect of deposition time is moderate, and the effect of the deposition potential is minor.

### **8.1.3 Mass Transfer Performance of LCS and LCS/DHBT Porous Ni Electrodes**

Porous Ni samples with different surface morphologies were manufactured by using fine Ni powder and applying the DHBT deposition process. The mass transfer performance (product of the mass transfer coefficient and active electrode area) of the LCS porous Ni with different fine Ni powder ratios of 0 – 100% and the LCS/DHBT porous Ni with different potentials of -1.35 – -1.7 V and deposition times of 60 – 300 s at different electrolyte flow rates in the range of 1.32 – 6.6 cm/s were investigated. The mass transfer performance of the LCS porous Ni samples with the fine Ni powder ratio from 0 – 100% is in the range of 0.003 to 0.016  $\text{cm}^3/\text{s}$ , with the peak occurs at 40%. The mass transfer performance of the LCS/DHBT porous Ni is in the range of 0.004 – 0.038  $\text{cm}^3/\text{s}$ . It is increased by 41% and 207% by increasing the deposition potential from 0 to -1.7 V and deposition time from 0 to 300 s, respectively. Increasing the flow velocity causes the mass transfer performance to increase.

### **8.1.4 Relationship between Current and Glucose Concentration**

To obtain high detection accuracy and LOD, the electrodes should possess both high mass transfer performance and high surface area. An LCS/DHBT porous Ni with both large-scale pores (710 -1000  $\mu\text{m}$ ) and small-scale pores (1-25  $\mu\text{m}$ ) has been produced by combining the LCS and DHBT processes. The large-scale pores provide a fast transport of the electrolyte and the small-scale pores provide a large surface area. The as-fabricated porous Ni has an electroactive surface area 1.18 times of that of the LCS porous Ni. The anodic peak current densities for the Ni plate, the LCS porous Ni and the LCS/DHBT porous Ni electrodes, in an electrolyte of 0.1 M KOH containing 0.5 mM glucose at scan rates in the range of 25 – 300 mV/s, are in the ranges of 0.314 – 1.85, 1.92 – 5.57 and 3.43 – 13.94 mA/cm<sup>2</sup>, respectively. Increasing scan rate results in a higher current density and a larger anodic peak potential shift. Current density increases with glucose concentration in several linear segments. The sensitivities of the plate, the LCS and the LCS/DHBT Ni electrodes in the glucose measurement are 1724, 2651 and 5775  $\mu\text{A}/\text{cm}^2\text{mM}$ , respectively. Their respective LOD values are in the ranges of 0.49 – 7.13, 0.53 – 4.29 and 0.66 – 2.91  $\mu\text{M}$ . The LCS/DHBT Ni electrode shows an excellent performance for glucose measurement because of its highly effective surface area.

The current - glucose concentration relationship is also affected by the manufacturing process parameters and scan rate. The peak current density of the LCS/DHBT porous Ni decreases with increasing the  $\text{NH}_4\text{Cl}$  concentration

during manufacturing, by 23% and 41% when the  $\text{NH}_4\text{Cl}$  concentration is increased from 0.5 M to 1 M and to 1.5 M, respectively. The current density is increased by 24% and 58% when the deposition potential is increased from -1.35 V to -1.5 and to -1.7 V. The peak current density increases from 3.43 to 13.94  $\text{mA}/\text{cm}^2$  when the scan rate is increased from 25 to 300  $\text{mV}/\text{s}$ . In comparison, the peak current density for Ni plate and the LCS porous Ni electrodes is in the range of 0.314 – 1.85 and 1.92 – 5.57  $\text{mA}/\text{cm}^2$ , respectively.

## **8.2 Future Work**

### **8.2.1 Surface Area of Porous Metals**

In this study, the surface areas of the LCS and the LCS/DHBT porous Ni samples have been investigated. The manufacturing parameters are shown to have significant effects on the surface area, especially in the LCS/DHBT porous Ni, where different trends were observed when different types of Ni salts were used in the solution. It indicated that changing metal salt and  $\text{H}^+$  source could change the surface morphology of the coating and therefore potentially increase the surface area. The pH value is another important factor in the DHBT process, which could change the kinetics of the metal deposition process and change the surface morphology and surface area. Hence, the effects of various manufacturing parameters on the morphology and surface area of the DHBT porous metals need to be studied further.

The results of this study showed that coating LCS porous Ni with a DHBT film increases the surface area of the composite porous Ni samples dramatically. Hence, composite or hybrid porous structures could be a new pathway to produce porous metals with high surface areas and superior performance. In recent years, a dealloying process was developed for manufacturing porous metals. Alloys with an active metal and a noble metal are etched to eliminate the active component to form porous metals with micropores. Such as-fabricated porous metals have extremely high surface areas. In the future work, the LCS process can be combined with the dealloying process to increase the internal surface area of the LCS porous metals.

### **8.2.2 Mass Transfer Performance**

The mass transfer performance is expressed as the product of mass transfer coefficient and active electrode area. It increases with increasing surface area for the LCS porous Ni samples in the process conditions investigated in this study. Further studies are needed to find out how and to what extent the surface area can influence the mass transfer performance, especially outside the ranges of manufacturing parameters studied in this thesis.

In addition to Ni, other advanced materials with excellent electrocatalytic activity can be combined with the LCS porous structure. The relationship between

electrocatalytic activity and mass transfer performance needs to be investigated.

### **8.2.3 Electrochemical Sensors**

The LCS/DHBT porous Ni has shown to have an excellent sensitivity in non-enzyme electrochemical glucose detection. In the next step, high-activity nanomaterials like Ni(OH)<sub>2</sub>, Cu(OH)<sub>2</sub> and noble metals can be grown on the surface of the LCS/DHBT porous Ni to further enhance the sensitivity for glucose detection.

## References

Adamek, G., Koper, J., & Jakubowicz, J. 2015. Saccharose as a New Space Holder Material for Porous Titanium Implant Formation. *Advanced Materials Research*, 110, 330–335.

Akhtar, N., El-Safty, S., & Khairy, M. 2014. Simple and sensitive electrochemical sensor-based three-dimensional porous Ni-hemoglobin composite electrode. *Chemosensors*, 24, 235-250.

Amatore, C., Szunerits, S., Thouin, L., & Warkocz, J. 2001. The real meaning of Nernst's steady diffusion layer concept under non-forced hydrodynamic conditions. A simple model based on Levich's seminal view of convection. *Journal of Electroanalytical Chemistry*, 500, 62-70.

Arifvianto, B., Leeflang, M., & Zhou, J. 2014. A new technique for the characterization of the water leaching behavior of space holding particles in the preparation of biomedical titanium scaffolds. *Materials Letters*, 120, 204–207.

Armand, D., & Clavilier, J. 1989. Electrochemical behaviour of the 110 orientation of a platinum surface in acid medium: The role of anions. *Journal of Electroanalytical Chemistry and Interfacial Electrochemistry*, 263, 109-126.

Ashby, E. M. F. 2000. *Metal foams: a design guide*. Butterworth-Heinemann.

Ashby, M. F., Evans, A., Fleck, N. A., Gibson, L. J., Hutchinson, J. W., & Wadley, H. N. 2002. *Metal foams: a design guide*. *Materials & Design*, 231, 119.

Ashby, M., Bréchet, Y., Cebon, D., & Salvo, L. 2004. Selection strategies for materials and Processes. *Materials & Design*, 251, 51-67.

Asri, R., Harun, W., Samykano, M., Lah, N., Ghani, S., Tarlochan, F., & Raza, M. 2017. Corrosion and surface modification on biocompatible metals: A review. *Materials Science and Engineering: C*, 77, 1261–1274.

Banerjee, S., & Choudhary, V. R. 2000. A method for increasing the surface area of perovskite-type oxides. *Journal of Chemical Sciences*, 1125, 535-542.

Banhart, J. 2001. Manufacture, characterisation and application of cellular metals and metal foams. *Progress in Materials Science*, 466, 559–632.

Bard, A. J. 2002. *Electrochemical Methods, Student Solutions Manual: Fundamentals and Applications 2nd second edition*. Wiley, 2002.

- Barnes, E. O., Chen, X., Li, P., & Compton, R. G. 2014. Voltammetry at porous electrodes: A theoretical study. *Journal of Electroanalytical Chemistry*, 720, 92–100.
- Baskoro, A. S., Supriadi, S., & Dharmanto. 2019. Review on Plasma Atomizer Technology for Metal Powder. *MATEC Web of Conferences*, 269, 05004.
- Baudrand, D., & Bengston, J. 1995. Electroless plating processes. *Metal Finishing*, 939, 55–57.
- Becerik, I., & Kadirgan, F. 1992. The electrocatalytic properties of palladium electrodes for the oxidation of d-glucose in alkaline medium. *Electrochimica acta*, 37, 2651-2657.
- Beckstead, L. W., & Miller, J. D. 1977. Ammonia, oxidation leaching of chalcopryite — reaction kinetics. *Metallurgical Transactions B*, 81, 19–29.
- Beden, B., Lamy, C., De Tacconi, N., & Arvia, A. 1990. The electrooxidation of CO: A test reaction in electrocatalysis. *Electrochimica Acta*, 354, 691-704.
- Bidault, F., Brett, D., Middleton, P., Abson, N., & Brandon, N. 2009. A new application for Ni foam in alkaline fuel cells. *International Journal of Hydrogen Energy*, 34, 6799-6808.
- Bogdanov, S. V. 2018. Prospects of Production of Granular Composite Materials by Method of the Plasma-Centrifugal Atomization. *Metallurgist*, 61, 1122–1129.
- Boubatra, M., Azizi, A., Schmerber, G., & Dinia, A. 2011. Morphology, structure, and magnetic properties of electrodeposited ni films obtained from different PH solutions. *Journal of Materials Science: Materials in Electronics*, 22, 1804-1809.
- Brewin, P. R., Walker, P. I., & Nurthen, P. D. 1986. Production of High Alloy Powders by Water Atomization. *Powder Metallurgy*, 294, 281–285.
- Brown, C. J., Pletcher, D., Walsh, F. C., Hammond, J. K., & Robinson, D. 1992. Local mass transport effects in the FM01 laboratory electrolyser. *Journal of Applied Electrochemistry*, 227, 613–619.
- Bye, K., & White, E. 1970. Hydrothermal growth of sodalite single crystals. *Journal of Crystal Growth*, 64, 355–356.



Campbell, R., Bakker, M. G., Treiner, C., & Chevalet, J. 2004. Electrodeposition of Mesoporous Ni onto Foamed Metals Using Surfactant and Polymer Templates. *Journal of Porous Materials*, 112, 63–69.

Carpenter, G. J. C., Wronski, Z. S., & Phaneuf, M. W. 2004. TEM study of nanopores and the embrittlement of CVD Ni foam. *Materials Science and Technology*, 201, 1421–1426.

Chakraborty, P., Dhar, S., Deka, N., Debnath, K., & Mondal, S. P. 2020. Non-enzymatic salivary glucose detection using porous CuO nanostructures. *Sensors and Actuators B: Chemical*, 302, 127134.

Chen, G., Tan, P., Zhao, S. Y., He, W. W., & Tang, H. P. 2016. Spherical Ti-6Al-4V Powders Produced by Gas Atomization. *Key Engineering Materials*, 704, 287–292.

Chen, J., Ma, Q., Li, M., Chao, D., Huang, L., Wu, W., Fang, Y., & Dong, S. 2021. Glucose-oxidase like catalytic mechanism of noble metal nanozymes. *Nature Communications*, 121, 3375.

Chen, Q., & Sieradzki, K. 2013. Mechanisms and Morphology Evolution in Dealloying. *Journal of The Electrochemical Society*, 160, C226–C231.

Chen, R., & Zhao, T. 2007. A novel electrode architecture for passive direct methanol fuel cells. *Electrochemistry Communications*, 94, 718–724.

Cherevko, S., & Chung, C. 2010. Impact of key deposition parameters on the morphology of silver foams prepared by dynamic hydrogen template deposition. *Electrochimica Acta*, 552, 6383-6390.

Chierchie, T., & Mayer, C. 1988. Voltammetric study of the underpotential deposition of copper on polycrystalline and Single Crystal Palladium Surfaces. *Electrochimica Acta*, 333, 341-345.

Chung, S. H., & Manthiram, A. 2013. Lithium–sulfur batteries with superior cycle stability by employing porous current collectors. *Electrochimica Acta*, 107, 569–576.

Ci, S., Huang, T., Wen, Z., Cui, S., Mao, S., Steeber, D. A., & Chen, J. 2014. Ni oxide hollow microsphere for non-enzyme glucose detection. *Biosensors and Bioelectronics*, 54, 251-257.

Clark Jr, L. C., & Lyons, C. 1962. Electrode systems for continuous monitoring in cardiovascular surgery. *Annals of the New York Academy of sciences*, 102,

29-45.

Cognet, P., Berlan, J., Lacoste, G., Fabre, P. L., & Jud, J. M. 1995. Application of metallic foams in an electrochemical pulsed flow reactor Part I: Mass transfer performance. *Journal of applied electrochemistry*, 251, 1105-1112.

Compton, R. G., Laborda, E., & Ward, K. R. 2013. *Understanding Voltammetry: Simulation of Electrode Processes*.

Correia, A., Mascaro, L., Machado, S., & Avaca, L. 1997. Active surface area determination of Pd-Si alloys by H-adsorption. *Electrochimica Acta*, 423, 493-495.

Corrigan, D. A., & Bendert, R. M. 1989. Effect of coprecipitated metal ions on the electrochemistry of Ni hydroxide thin films: Cyclic voltammetry in 1M KOH. *Journal of The Electrochemical Society*, 13, 723-728.

Craig, V. S., Ninham, B. W., & Pashley, R. M. 1993. The effect of electrolytes on bubble coalescence in water. *The Journal of Physical Chemistry*, 973, 10192-10197.

Dall'Antonia, L., Tremiliosi-Filho, G., & Jerkiewicz, G. 2001. Influence of temperature on the growth of surface oxides on palladium electrodes. *Journal of Electroanalytical Chemistry*, 502, 72-81.

Deakin, M. R., & Melroy, O. 1988. Underpotential metal deposition on gold, monitored in situ with a quartz microbalance. *Journal of Electroanalytical Chemistry and Interfacial Electrochemistry*, 239, 321-331.

Deckard, C.R. 1986. *Part Generation by Layerwise Selective Sintering*, Master's thesis, University of Texas at Austin.

Delahay, P., & Turner, D. R. 1955. *New Instrumental Methods in Electrochemistry*. *Journal of The Electrochemical Society*, 10, 46C.

Desimoni, E., & Brunetti, B. 2015. About estimating the limit of detection by the signal to noise approach. *Pharmaceutica Analytica Acta*, 6, 2.

Dewidar, M. M., Yoon, H. C., & Lim, J. K. 2006. Mechanical properties of metals for biomedical applications using powder metallurgy process: A review. *Metals and Materials International*, 123, 193–206.

Diao, K., Xiao, Z., & Zhao, Y. 2015. Specific surface areas of porous Cu manufactured by Lost Carbonate Sintering: Measurements by quantitative

stereology and cyclic voltammetry. *Materials Chemistry and Physics*, 162, 571–579.

Drenchev, L., Sobczak, J., Malinov, S. & Sha, W. 2006. Gasars: a class of metallic materials with ordered porosity, *Materials science and technology*, 22, 1135-1147.

Dukhan, N. 2012. *Metal Foams: Fundamentals and Applications*. DEStech Publications.

Đukić, A., Alar, V., Firak, M., & Jakovljević, S. 2013. A significant improvement in material of foam. *Journal of Alloys and Compounds*, 573, 128-132.

Eisenmann, M. 1998. *Metal powder technologies and applications*. ASM Handbook, 7, 1031.

Ensafi, A. A., Ahmadi, N., & Rezaei, B. 2017. Ni nanoparticles supported on porous silicon flour, application as a non-enzymatic electrochemical glucose sensor. *Sensors and Actuators B: Chemical*, 239, 807-815.

Entezarian, M., Allaire, F., Tsantrizos, P., & Drew, R. A. L. 1996. Plasma atomization: A new process for the production of fine, spherical powders. *JOM*, 486, 53–55.

Erlebacher, J., Aziz, M. J., Karma, A., Dimitrov, N., & Sieradzki, K. 2001. Evolution of nanoporosity in dealloying. *Nature*, 410, 450–453.

Ernst, S., Heitbaum, J., & Hamann, C. H. 1979. The electrooxidation of glucose in phosphate buffer solutions: Part I. Reactivity and kinetics below 350 mV/RHE. *Journal of Electroanalytical Chemistry and Interfacial Electrochemistry*, 100, 173-183.

Eugénio, S., Silva, T. M., Carmezim, M. J., Duarte, R. G., & Montemor, M. F. 2013. Electrodeposition and characterization of Ni–copper metallic foams for application as electrodes for supercapacitors. *Journal of Applied Electrochemistry*, 444, 455-465.

Forghani, M., & Donne, S. W. 2019. Complications When Differentiating Charge Transfer Processes in Electrochemical Capacitor Materials: Assessment of Cyclic Voltammetry Data. *Journal of The Electrochemical Society*, 1668, A1370–A1379.

Franklin, T. C., & Franklin, N. F. 1976. The use of underpotential deposition to measure the surface area of metals. *Surface Technology*, 45, 431-440.

Gagnon, E. G. 1976. Determination of the double-layer capacity of porous Ni in KOH in the presence of faradaic current. *Journal of Applied Electrochemistry*, 62, 95–98.

Gamburg, Y.D. and Zangari, G., 2011. *Theory and practice of metal electrodeposition*. Springer Science & Business Media.

Green, C. L., & Kucernak, A. 2002. Determination of the platinum and ruthenium surface areas in platinum–ruthenium alloy electrocatalysts by underpotential deposition of copper. I. Unsupported catalysts. *The Journal of Physical Chemistry B*, 106, 1036-1047.

Griffiths, M., de León, C. P., & Walsh, F. C. 2005. Mass transport in the rectangular channel of a filter - press electrolyzer the FM01 - LC reactor. *AIChE Journal*, 512, 682-687.

Guo, C., Li, H., Zhang, X., Huo, H., & Xu, C. 2015. 3D porous CNT/MnO<sub>2</sub> composite electrode for high-performance enzymeless glucose detection and supercapacitor application. *Sensors and Actuators B: Chemical*, 206, 407–414.

Guo, M. M., Wang, P. S., Zhou, C. H., Xia, Y., Huang, W., & Li, Z. 2014. An ultrasensitive non-enzymatic amperometric glucose sensor based on a Cu-coated nanoporous gold film involving co-mediating. *Sensors and Actuators B: Chemical*, 203, 388-395.

Hammond, R. A. F. 1971. *Electrodeposition from Ni sulphamate solutions*. International Ni limited.

Hanawa, T. 2017. Surface treatment and modification of metals to add biofunction. *Dental Materials Journal*, 365, 533–538.

Hao, M., Charbonneau, V., Fomena, N. N., Gaudet, J., Bruce, D. R., Garbarino, S., Harrington, D. A., & Guay, D. 2019. Hydrogen Bubble Templating of Fractal Ni Catalysts for Water Oxidation in Alkaline Media. *ACS Applied Energy Materials*, 28, 5734–5743.

Hayes, M., & Kuhn, A. 1980. Determination of platinum catalyst surface area with potentiodynamic techniques — effect of experimental parameters. *Applications of Surface Science*, 61, 1-14.

Hernández-Saravia, L. P., Sukeri, A., & Bertotti, M. 2019. Fabrication of nanoporous gold-islands via hydrogen bubble template: An efficient electrocatalyst for oxygen reduction and hydrogen evolution reactions.

International Journal of Hydrogen Energy, 442, 15001-15008.

Herraiz-Cardona, I., Ortega, E., Vázquez-Gómez, L., & Pérez-Herranz, V. 2012. Double-template fabrication of three-dimensional porous Ni electrodes for hydrogen evolution reaction. International Journal of Hydrogen Energy, 373, 2147–2156.

Hsiao, M. W., Adžić, R. R., & Yeager, E. B. 1996. Electrochemical oxidation of glucose on single crystal and polycrystalline gold surfaces in phosphate buffer. Journal of the Electrochemical Society, 143, 759.

Inamdar, A., Kim, Y., Pawar, S., Kim, J., Im, H., & Kim, H. 2011. Chemically grown, porous, Ni oxide thin-film for electrochemical supercapacitors. Journal of Power Sources, 196, 2393-2397.

Ito, Y., Ohmori, T., Nakamatsu, S., & Yoshizawa, S. 1980. A molten salt electrolytic process for recovering chlorine and ammonia from  $\text{NH}_4\text{Cl}$ . I. Journal of Applied Electrochemistry, 104, 419-425.

Jagadeesan, M., Movlaee, K., Krishnakumar, T., Leonardi, S., & Neri, G. 2019. One-step microwave-assisted synthesis and characterization of novel CuO nanodisks for non-enzymatic glucose sensing. Journal of Electroanalytical Chemistry, 835, 161–168.

Jeske, M., Schultze, J., Thönissen, M., & Münder, H. 1995. Electrodeposition of metals into porous silicon. Thin Solid Films, 2551, 63–66.

Jin, C., Sheng, O., Luo, J., Yuan, H., Fang, C., Zhang, W., Huang, H., Gan, Y., Xia, Y., Liang, C., Zhang, J., & Tao, X. 2017. 3D lithium metal embedded within lithiophilic porous matrix for stable lithium metal batteries. Nano Energy, 37, 177–186.

Kalu, E., Nwoga, T., Srinivasan, V., & Weidner, J. 2001. Cyclic voltammetric studies of the effects of time and temperature on the capacitance of electrochemically deposited Ni hydroxide. Journal of Power Sources, 921, 163-167.

Karlsson, R. K., & Cornell, A. 2016. Selectivity between oxygen and chlorine evolution in the chlor-alkali and chlorate processes. Chemical reviews, 116, 2982-3028.

Kessler, T., Castro Luna, A. M., Triaca, W. E., & Arvia, A. J. 1986. The behaviour of platinized platinum electrodes in acid solutions: Correlation

between Voltammetric Data and electrode structure. *Journal of Applied Electrochemistry*, 165, 693-702.

Kieback, B., Stephani, G., Weißgarber, T., Schubert, T., Waag, U., Bohm, A., Anderson, O., Gohler, H., & Reinfried, M. 2003. Powder Metallurgy for Light Weight and Ultra-Light Weight Materials. *Journal of Korean Powder Metallurgy Institute*, 106, 383–389.

Klingenmaier, O. J. 1965. The effect of anode efficiency on the stability of Ni sulfamate solutions. *Plating*, 52, 1138.

Krishnamoorthy, K., Veerasubramani, G. K., Radhakrishnan, S., & Kim, S. J. 2014. One pot hydrothermal growth of hierarchical nanostructured Ni<sub>3</sub>S<sub>2</sub> on Ni foam for supercapacitor application. *Chemical Engineering Journal*, 251, 116–122.

Kruth, J., Mercelis, P., van Vaerenbergh, J., Froyen, L., & Rombouts, M. 2005. Binding mechanisms in selective laser sintering and selective laser melting. *Rapid Prototyping Journal*, 111, 26–36.

Kung, C. W., Cheng, Y. H., & Ho, K. C. 2014. Single layer of Ni hydroxide nanoparticles covered on a porous Ni foam and its application for highly sensitive non-enzymatic glucose sensor. *Sensors and Actuators B: Chemical*, 204, 159–166.

Lamy-Pitara, E., & Barbier, J. 1997. Platinum modified by electrochemical deposition of adatoms. *Applied Catalysis A: General*, 14, 49-87.

Langlois, S., & Coeuret, F. 1989. Flow-through and flow-by porous electrodes of Ni foam. II. Diffusion-convective mass transfer between the electrolyte and the foam. *Journal of applied electrochemistry*, 191, 51-60.

Leitz, F. B., & Marinčić, L. 1977. Enhanced mass transfer in electrochemical cells using turbulence promoters. *Journal of Applied Electrochemistry*, 76, 473–484.

Li, Q., Zhu, S., & Lu, Y. 2017. 3D Porous Cu Current Collector/Li-Metal Composite Anode for Stable Lithium-Metal Batteries. *Advanced Functional Materials*, 27, 1606422.

Li, Y., Song, Y. Y., Yang, C., & Xia, X. H. 2007. Hydrogen bubble dynamic template synthesis of porous gold for nonenzymatic electrochemical detection of glucose. *Electrochemistry Communications*, 95, 981–988.

Liu, P. & Liang, K. 2001 'Review Functional materials of porous metals made by P/M, electroplating and some other techniques', *Journal of materials science*, 36, 5059-5072.

Liu, Y., Teng, H., Hou, H., & You, T. 2009. Nonenzymatic glucose sensor based on renewable electrospun Ni nanoparticle-loaded carbon nanofiber paste electrode. *Biosensors and Bioelectronics*, 24, 3329-3334.

Løvvik, O., & Opalka, S. M. 2008. Reversed surface segregation in palladium-silver alloys due to hydrogen adsorption. *Surface Science*, 602, 2840-2844.

Lu, J., Xiong, T., Zhou, W., Yang, L., Tang, Z., & Chen, S. 2016. Metal Ni foam as an efficient and stable electrode for hydrogen evolution reaction in acidic electrolyte under reasonable overpotentials. *ACS Applied Materials & Interfaces*, 88, 5065-5069.

Lu, L. L., Ge, J., Yang, J. N., Chen, S. M., Yao, H. B., Zhou, F., & Yu, S. H. 2016. Free-Standing Copper Nanowire Network Current Collector for Improving Lithium Anode Performance. *Nano Letters*, 167, 4431–4437.

Lu, L. M., Zhang, L., Qu, F. L., Lu, H. X., Zhang, X. B., Wu, Z. S. & Yu, R. Q. 2009. A nano-Ni based ultrasensitive nonenzymatic electrochemical sensor for glucose: enhancing sensitivity through a nanowire array strategy. *Biosensors and Bioelectronics*, 251, 218-223.

Lu, Q., Lattanzi, M. W., Chen, Y., Kou, X., Li, W., Fan, X., Unruh, K. M., Chen, J. G., & Xiao, J. Q. 2011. Supercapacitor Electrodes with High-Energy and Power Densities Prepared from Monolithic NiO/Ni Nanocomposites. *Angewandte Chemie*, 123, 6979–6982.

Lu, T. J., Stone, H. A., Ashby, M. F. 1998. Heat transfer in open-cell metal foams, *Acta Mater*, 46, 3619–3635.

Lu, W., Qin, X., Asiri, A. M., Al-Youbi, A. O., & Sun, X. 2013. Ni foam: a novel three-dimensional porous sensing platform for sensitive and selective nonenzymatic glucose detection. *Analyst*, 138, 417-420.

Luo, P. F., Kuwana, T., Paul, D. K., & Sherwood, P. M. 1996. Electrochemical and XPS study of the Ni-titanium electrode surface. *Analytical Chemistry*, 68, 3330-3337.

Malinauskas, A. 2001. Chemical deposition of conducting polymers. *Polymer*, 429, 3957–3972.

Mallory, G. O., & Hajdu, J. B. (1991). American Electroplaters and Surface Finishing Society. Electroless plating: fundamentals and applications Orlando, 207.

Marozzi, C., & Chialvo, A. 2000. Development of electrode morphologies of interest in electrocatalysis. Part 1: Electrodeposited porous Ni electrodes. *Electrochimica Acta*, 451, 2111–2120.

Marozzi, C., & Chialvo, A. 2001. Development of electrode morphologies of interest in electrocatalysis. *Electrochimica Acta*, 466, 861–866.

Mattarozzi, L., Cattarin, S., Comisso, N., Gambirasi, A., Guerriero, P., Musiani, M., Verlato, E. 2014. Hydrogen Evolution assisted electrodeposition of porous Cu-Ni alloy electrodes and their use for nitrate reduction in alkali. *Electrochimica Acta*, 140, 337-344.

Mattox, D. M. 1999. Physical vapor deposition PVD processes. *Metal Finishing*, 99, 409–423.

Molina, A., Laborda, E., González, J., & Compton, R. G. 2013. Effects of convergent diffusion and charge transfer kinetics on the diffusion layer thickness of spherical micro- and nanoelectrodes. *Physical Chemistry Chemical Physics*, 15, 7106.

Nie, H., Yao, Z., Zhou, X., Yang, Z., & Huang, S. 2011. Nonenzymatic electrochemical detection of glucose using well-distributed Ni nanoparticles on straight multi-walled carbon nanotubes. *Biosensors and Bioelectronics*, 301, 28-34.

Nikolić, N., Branković, G., Pavlović, M., & Popov, K. 2008. The effect of hydrogen co-deposition on the morphology of copper electrodeposits. II. correlation between the properties of electrolytic solutions and the quantity of evolved hydrogen. *Journal of Electroanalytical Chemistry*, 62, 13-21.

Nikolić, N., Popov, K., Pavlović, L., & Pavlović, M. 2006. The effect of hydrogen codeposition on the morphology of copper electrodeposits. i. the concept of effective overpotential. *Journal of Electroanalytical Chemistry*, 58, 88-98.

Niu, X., Lan, M., Zhao, H., & Chen, C. 2013. Highly Sensitive and Selective Nonenzymatic Detection of Glucose Using Three-Dimensional Porous Ni Nanostructures. *Analytical Chemistry*, 85, 3561–3569.

Nobari, N., Behboudnia, M., & Maleki, R. 2016. Palladium-free electroless deposition of pure copper film on glass substrate using hydrazine as reducing



agent. *Applied Surface Science*, 38, 9-17.

Noelle, D. J., Wang, M., & Qiao, Y. 2018. Improved safety and mechanical characterizations of thick lithium-ion battery electrodes structured with porous metal current collectors. *Journal of Power Sources*, 399, 125–132.

O'hayre, R., Cha, S. W., Colella, W., & Prinz, F. B. 2016. *Fuel cell fundamentals*. John Wiley & Sons.

Oldham, K. B. 2008. A Gouy–Chapman–Stern model of the double layer at a metal/ionic liquid interface. *Journal of Electroanalytical Chemistry*, 61, 131-138.

Pan, Q., Jin, H., Wang, H., & Yin, G. 2007. Flower-like CuO film-electrode for lithium ion batteries and the effect of surface morphology on electrochemical performance. *Electrochimica Acta*, 532, 951-956.

Papantoniou, I., Markopoulos, A., Pantelis, D., & Manolakos, D. 2018. Application of Aluminium Flakes in Fabrication of Open-Cell Aluminium Foams by Space Holder Method. *Materials*, 118, 1420.

Park, J. H., & Sudarshan, T. S. 2001. *Chemical vapor deposition*. The Materials Information Society.

Park, S., Boo, H., & Chung, T. D. 2006. Electrochemical non-enzymatic glucose sensors. *Analytica Chimica Acta*, 556, 46–57.

Paserin, V., Marcuson, S., Shu, J., & Wilkinson, D. 2004. CVD Technique for Inco Ni Foam Production. *Advanced Engineering Materials*, 66, 454–459.

Peigney, A., Laurent, C., Flahaut, E., Bacsa, R., & Rousset, A. 2001. Specific surface area of carbon nanotubes and bundles of carbon nanotubes. *Carbon*, 394, 507–514.

Peissker, E. 1991. Production and handling of electrolytic powders. *Metal Powder Report*, 464, 20–25.

Plowman, B. J., Jones, L. A., & Bhargava, S. K. 2015. Building with bubbles: the formation of high surface area honeycomb-like films via hydrogen bubble templated electrodeposition. *Chemical Communications*, 51, 4331–4346.

Plowman, B. J., Jones, L. A., & Bhargava, S. K. 2015. Building with bubbles: the formation of high surface area honeycomb-like films via hydrogen bubble templated electrodeposition. *Chemical Communications*, 51, 4331-4346.

Podlovchenko, B., & Kolyadko, E. 1987. Effect of the nature of platinum group metals on the formation and properties of Adatom Silver Coatings. *Journal of Electroanalytical Chemistry and Interfacial Electrochemistry*, 224, 225-235.

Popov, K. I., Djokić, S. S., Nikolić, N. D., & Jović, V. D. 2016. Morphology of electrochemically and chemically deposited metals.

Prasad, M., & Sangaranarayanan, M. 2004. Formulation of a simple analytical expression for irreversible electron transfer processes in linear sweep voltammetry and its experimental verification. *Electrochimica Acta*, 49, 2569–2579.

Pu, X., Zhao, D., Fu, C., Chen, Z., Cao, S., Wang, C., & Cao, Y. 2021. Understanding and calibration of charge storage mechanism in cyclic voltammetry curves. *Angewandte Chemie*, 133, 21480-21488.

Qin, J., Chen, Q., Yang, C., & Huang, Y. 2016. Research process on property and application of metal porous materials. *Journal of Alloys and Compounds*, 654, 39–44.

Qiu, H., Xu, H., Liu, L., & Wang, Y. 2015. Correlation of the structure and applications of dealloyed nanoporous metals in catalysis and Energy Conversion/storage. *Nanoscale*, 72, 386-400.

Queheillalt, D. T., Hass, D. D., Sypeck, D. J., & Wadley, H. N. G. 2001. Synthesis of open-cell metal foams by templated directed vapor deposition. *Journal of Materials Research*, 164, 1028–1036.

Rai, G., Lavernia, E., & Grant, N. J. 1985. Powder Size and Distribution in Ultrasonic Gas Atomization. *JOM*, 378, 22–26.

Recio, F. J., Herrasti, P., Vazquez, L., De León, C. P., & Walsh, F. C. 2013. Mass transfer to a nanostructured Ni electrodeposit of high surface area in a rectangular flow channel. *Electrochimica Acta*, 90, 507-513.

Riyanto, R., Othman, M. R., & Salimon, J. 2011. Electrochemical oxidation of ethanol using Ni-Co-PVC composite electrode. *Indonesian Journal of Chemistry*, 111, 75-84.

Rohatgi, P. 2000. STATE OF THE ART IN CASTMETAL, MATRIX COMPOSITES IN THE NEXT MILLENIUM, *The Minerals, Metals & Materials Society*.

Safavi, A., Maleki, N., & Farjami, E. 2009. Fabrication of a glucose sensor

based on a novel nanocomposite electrode. *Biosensors and Bioelectronics*, 246, 1655–1660.

Santos, E. C., Shiomi, M., Osakada, K., & Laoui, T. 2006. Rapid manufacturing of metal components by laser forming. *International Journal of Machine Tools and Manufacture*, 46, 1459–1468.

Scheck, C., Evans, P., Schad, R., Zangari, G., Williams, J. R., & Isaacs-Smith, T. F. 2002. Structure and magnetic properties of electrodeposited ni films on N-gaas001. *Journal of Physics: Condensed Matter*, 14, 12329-12338.

Scholz, F., 2002, *Electroanalytical methods: guide to experiments and applications*, Berlin: Springer, 2002.

Schwarzacher, W. 2006. Electrodeposition: A Technology for the Future. *The Electrochemical Society Interface*, 151, 32–33.

Scortichini, C. L., & Reilley, C. N. 1983. Surface characterization of PT electrodes using underpotential deposition of H and Cu. *Journal of Electroanalytical Chemistry and Interfacial Electrochemistry*, 15, 255-260.

Selcuk, C., Bond, S., & Woollin, P. 2010. Joining processes for powder metallurgy parts: a review. *Powder Metallurgy*, 531, 7–11.

Sengupta, S., Patra, A., Jena, S., Das, K., & Das, S. 2018. A Study on the Effect of Electrodeposition Parameters on the Morphology of Porous Ni Electrodeposits. *Metallurgical and Materials Transactions A*, 493, 920–937.

Shapovalov, V. 2007. Prospective Applications of Gas-Eutectic Porous Materials Gasars in USA. *Materials Science Forum*, 539, 1183–1187.

Sherman, A. 1987. *Chemical Vapor Deposition for Microelectronics: Principles, Technology, and Applications* Materials Science and Process Technology Series. Noyes Publications.

Shin, H. C., Dong, J., & Liu, M. 2003. Nanoporous Structures Prepared by an Electrochemical Deposition Process. *Advanced Materials*, 15, 1610–1614.

Shivkumar, R., Kalaignan, G., & Vasudevan, T. 1998. Studies with porous zinc electrodes with additives for secondary alkaline batteries. *Journal of Power Sources*, 751, 90–100.

Sieradzki, K., Dimitrov, N., Movrin, D., McCall, C., Vasiljevic, N., & Erlebacher, J. 2002. The Dealloying Critical Potential. *Journal of The Electrochemical*

Society, 14, B370.

Simone, A. & Gibson, L. 1997. The compressive behaviour of porous copper made by the GASAR process. *Journal of materials science*, 32, 451-457.

Simone, A.E. & Gibson, L. 1996. The tensile strength of porous copper made by the gasar process. *Acta materialia*, 44, 1437-1447.

Skou, E. 1977. The electrochemical oxidation of glucose on platinum—I. The oxidation in 1 M H<sub>2</sub>SO<sub>4</sub>. *Electrochimica Acta*, 224, 313-318.

Smith, R. E., Davies, T. J., Baynes, N. D. B., & Nichols, R. J. 2015. The electrochemical characterisation of graphite felts. *Journal of Electroanalytical Chemistry*, 747, 29–38.

Smith, R. E., Davies, T. J., Baynes, N. D., & Nichols, R. J. 2015. The electrochemical characterisation of graphite felts. *Journal of Electroanalytical Chemistry*, 747, 29-38.

Sōmiya, S. 1983. Hydrothermal Preparation and Sintering of Fine Ceramic Powders. *MRS Proceedings*, 24, 255-271.

Song, Y. Y., Zhang, D., Gao, W., & Xia, X. H. 2005. Nonenzymatic glucose detection by using a three - dimensionally ordered, macroporous platinum template. *Chemistry—A European Journal*, 117, 2177-2182.

Srinivasan, V., Weidner, J. W. 1997. An Electrochemical Route for Making Porous Ni Oxide Electrochemical Capacitors, *J. Electrochem. Soc.*, 144, L210.

Stefan-van Staden, R. I., & Mitrofan, G. 2018. Molecular enantio recognition of l-glucose and d-glucose in whole blood samples. *Chirality*, 305, 680–685.

Subramanyam, R. B. 1993. Some recent innovations in the Kroll process of titanium sponge production. *Bulletin of Materials Science*, 166, 433–451.

Sun, A., Zheng, J., & Sheng, Q. 2012. A highly sensitive non-enzymatic glucose sensor based on Ni and multi-walled carbon nanotubes nanohybrid films fabricated by one-step co-electrodeposition in ionic liquids. *Electrochimica Acta*, 65, 64-69.

Sun, Q. Q., Wang, M., Bao, S. J., Wang, Y. C., & Gu, S. 2016. Analysis of cobalt phosphide CoP nanorods designed for non-enzyme glucose detection. *Analyst*, 14, 256-260.

Szánto, D. A., Trinidad, P., Whyte, I., & Walsh, F. C. 1996. Electrosynthesis and mass transport measurements in laboratory filter-press reactors. In Proceedings of 4th European Symposium on Electrochemical Engineering: Contemporary Trends in Electrochemical Engineering, Prague, Czech Republic, 273.

Tan, Y. H., Davis, J. A., Fujikawa, K., Ganesh, N.V., Demchenko, A.V., Stine, K.J. 2012. Surface area and pore size characteristics of nanoporous gold subjected to thermal, mechanical, or surface modification studied using gas adsorption isotherms, cyclic voltammetry, thermogravimetric analysis, and scanning electron microscopy, *J. Mater. Chem*, 22, 6733–6745.

Tang, J., Wang, Y., Li, J., Da, P., Geng, J., & Zheng, G. 2014. Sensitive enzymatic glucose detection by TiO<sub>2</sub>nanowire photoelectrochemical biosensors. *J. Mater. Chem. A*, 217, 6153–6157.

Tang, W., Peterson, A. A., Varela, A. S., Jovanov, Z. P., Bech, L., Durand, W. J., Chorkendorff, I. 2012. The importance of surface morphology in controlling the selectivity of polycrystalline copper for CO<sub>2</sub> electroreduction. *Phys. Chem. Chem. Phys.*, 141, 76-81.

Toghill, K., Xiao, L., Stradiotto, N., & Compton, R. 2010. The Determination of Methanol Using an Electrolytically Fabricated Ni Microparticle Modified Boron Doped Diamond Electrode. *Electroanalysis*, 225, 491–500.

Trasatti, S., & Petrii, O. A. 1991. Real surface area measurements in electrochemistry. *Pure and Applied Chemistry*, 635, 711–734.

Trout, W. E. 1938. The metal carbonyls. VII. Industrial significance. *Journal of Chemical Education*, 153, 113

Upadhyaya, A., & Upadhyaya, G. S. 2018. Powder Metallurgy: Science, Technology, and Materials. Universities Press.

Upadhyaya, G. S. 1997. Powder metallurgy technology. Cambridge International Science Publishing.

Van Drunen, J., Pilapil, B. K., Makonnen, Y., Beauchemin, D., Gates, B. D., & Jerkiewicz, G. 2014. Electrochemically active Ni foams as support materials for nanoscopic platinum electrocatalysts. *ACS Applied Materials & Interfaces*, 615, 12046-12061.

Van Drunen, J., Pilapil, B. K., Makonnen, Y., Beauchemin, D., Gates, B. D., & Jerkiewicz, G. 2014. Electrochemically active Ni foams as support materials for

nanoscopic platinum electrocatalysts. *ACS Applied Materials & Interfaces*, 615, 12046-12061.

Vandenbroucke, B., & Kruth, J. 2007. Selective laser melting of biocompatible metals for rapid manufacturing of medical parts. *Rapid Prototyping Journal*, 134, 196–203.

Vesztergom, S., Dutta, A., Rahaman, M., Kiran, K., Zelocualtecatl Montiel, I., & Broekmann, P. 2020. Hydrogen bubble templated metal foams as efficient catalysts of CO<sub>2</sub> electroreduction. *ChemCatChem*, 134, 1039-1058.

Wan, Y., Raman, S., He, F., & Huang, Y. 2007. Surface modification of medical metals by ion implantation of silver and copper. *Vacuum*, 819, 1114–1118.

Wang, H., Pan, Q., Wang, X., Yin, G., & Zhao, J. 2009. Improving electrochemical performance of NiO films by electrodeposition on foam Ni substrates. *Journal of Applied Electrochemistry*, 399, 1597–1602.

Wang, L., Zhang, Y., Yu, J., He, J., Yang, H., Ye, Y., & Song, Y. 2017. A green and simple strategy to prepare graphene foam-like three-dimensional porous carbon/Ni nanoparticles for glucose sensing. *Sensors and Actuators B: Chemical*, 239, 172-179.

Wang, T., Guo, Y., Zhao, B., Yu, S., Yang, H., Lu, D., Wong, C. 2015. NiCO<sub>2</sub>O<sub>4</sub> nanosheets in-situ grown on three dimensional porous Ni film current collectors as integrated electrodes for high-performance supercapacitors. *Journal of Power Sources*, 286, 371-379.

Wang, X. M., & Duo, J. 2011. Effect on Electroless Ni Coating on Magnesium Alloy by Ni Electroless Plating Parameters. *Advanced Materials Research*, 295, 1522–1525.

Wang, Z., Hu, Y., Yang, W., Zhou, M., & Hu, X. 2012. Facile one-step microwave-assisted route towards Ni nanospheres/reduced graphene oxide hybrids for non-enzymatic glucose sensing. *Sensors*, 124, 4860-4869.

Ward, K. R., Gara, M., Lawrence, N. S., Hartshorne, R. S., & Compton, R. G. 2013. Nanoparticle-modified electrodes can show an apparent increase in electrode kinetics due solely to altered surface geometry: The effective electrochemical rate constant for non-flat and non-uniform electrode surfaces. *Journal of Electroanalytical Chemistry*, 695, 1–9.

Wartman, F. S., Baker, D. H., Nettle, J. R., & Homme, V. E. 1954. Some Observations on the Kroll Process for Titanium. *Journal of The Electrochemical*

Society, 101, 507.

Woods, R. 1974. Hydrogen adsorption on platinum, iridium and rhodium electrodes at reduced temperatures and the determination of real surface area. *Journal of Electroanalytical Chemistry and Interfacial Electrochemistry*, 492, 217-226.

Wosch, E., Prikhodovski, A., Feldhaus, S., & Gammal, T. E. 1997. Investigations on the rapid solidification of steel droplets in the plasma-rotating-electrode-process. *Steel Research*, 686, 239–246.

Xia, X. H., Tu, J. P., Zhang, Y. Q., Mai, Y. J., Wang, X. L., Gu, C. D., & Zhao, X. B. 2011. Three-Dimensional Porous Nano-Ni/Co(OH)<sub>2</sub> Nanoflake Composite Film: A Pseudocapacitive Material with Superior Performance. *The Journal of Physical Chemistry C*, 115, 22662–22668.

Xia, Y., Yoshio, M., & Noguchi, H. 2006. Improved electrochemical performance of LiFePO<sub>4</sub> by increasing its specific surface area. *Electrochimica Acta*, 521, 240–245.

Xiao, Q., Wang, X., & Huang, S. 2017. Facile synthesis of Ni(OH)<sub>2</sub> nanowires on Ni foam via one step low-temperature hydrothermal route for non-enzymatic glucose sensor. *Materials Letters*, 198, 19-22.

Xing, W., Qiao, S., Wu, X., Gao, X., Zhou, J., Zhuo, S., Hartono, S. B., & Hulicova-Jurcakova, D. 2011. Exaggerated capacitance using electrochemically active Ni foam as current collector in electrochemical measurement. *Journal of Power Sources*, 19, 4123–4127.

Xu, S., Hartvickson, S., & Zhao, J. X. 2011. Increasing surface area of silica nanoparticles with a rough surface. *ACS Applied Materials & Interfaces*, 36, 1865-1872.

Xu, W., Canfield, N. L., Wang, D., Xiao, J., Nie, Z., Li, X. S., Zhang, J. 2010. An approach to make macroporous metal sheets as current collectors for lithium-ion batteries. *Journal of The Electrochemical Society*, 157, 765-769.

Xue, J., Wu, Q., Wang, Z., & Yi, S. 2006. Function of additives in electrolytic preparation of copper powder. *Hydrometallurgy*, 823, 154–156.

Yang, F., Cheng, K., Xue, X., Yin, J., Wang, G., & Cao, D. 2013. Three-dimensional porous Ni film electrodeposited on Ni foam: High performance and low-cost catalytic electrode for H<sub>2</sub>O<sub>2</sub> electrooxidation in KOH solution. *Electrochimica Acta*, 107, 194–199.

Yang, G. W., Xu, C. L., & Li, H. L. 2008. Electrodeposited Ni hydroxide on Ni foam with ultrahigh capacitance. *Chemical Communications*, 48, 6537.

Yen, T., & Chou, C. 1995. Growth and characterization of carbon nitride thin films prepared by arc - plasma jet chemical vapor deposition. *Applied Physics Letters*, 67, 2801–2803.

Yi, Q., Huang, W., Yu, W., Li, L., & Liu, X. 2008. Hydrothermal synthesis of titanium - supported Ni nanoflakes for electrochemical oxidation of glucose. *Electroanalysis: An International Journal Devoted to Fundamental and Practical Aspects of Electroanalysis*, 201, 2016-2022.

Yoshimura, M. 2006. Soft solution processing: Concept and realization of direct fabrication of shaped ceramics nano-crystals, whiskers, films, and/or patterns in solutions without post-firing. *Journal of Materials Science*, 415, 1299-1306.

Yoshimura, M., & Byrappa, K. 2007. Hydrothermal processing of materials: past, present and future. *Journal of Materials Science*, 437, 2085–2103.

Yoshimura, M., Yoo, S. E., Hayashi, M., & Ishizawa, N. 1989. Preparation of BaTiO<sub>3</sub> thin film by hydrothermal electrochemical method. *Japanese Journal of Applied Physics*, 28, L2007-L2009.

Yu, X., Wang, M., Wang, Z., Gong, X., & Guo, Z. 2016. The structure evolution mechanism of electrodeposited porous ni films on NH<sub>4</sub>Cl concentration. *Applied Surface Science*, 360, 502-509.

Yun, Q., He, Y. B., Lv, W., Zhao, Y., Li, B., Kang, F., & Yang, Q. H. 2016. Chemical Dealloying Derived 3D Porous Current Collector for Li Metal Anodes. *Advanced Materials*, 283, 6932–6939.

Yur'ev, B. P., & Golubkov, L. A. 1967. Electrolytic method of preparation of composite cobalt-Ni powder. *Soviet Powder Metallurgy and Metal Ceramics*, 67, 525–531.

Yur'ev, B. P., & Sviridova, S. A. 1969. Electrolytic method of continuous production of multicomponent metal powders. *Soviet Powder Metallurgy and Metal Ceramics*, 87, 519–522.

Zankowski, S. P., & Vereecken, P. M. 2019. Electrochemical Determination of Porosity and Surface Area of Thin Films of Interconnected Nickel Nanowires. *Journal Of The Electrochemical Society*, 166, D227-D235.



Zhang, H., Ye, Y., Shen, R., Ru, C., & Hu, Y. 2013. Effect of bubble behavior on the morphology of foamed porous copper prepared via electrodeposition. *Journal of The Electrochemical Society*, 160, 441-445.

Zhang, L. P., & Zhao, Y. Y. 2008. Fabrication of high melting-point porous metals by lost carbonate sintering process via decomposition route. *Proceedings of the Institution of Mechanical Engineers, Part B: Journal of Engineering Manufacture*, 222, 267–271.

Zhang, L., Zhang, J., Jiang, Z., Xie, S., Jin, M., Han, X., Kuang, Q., Xie, Z., & Zheng, L. 2011. Facile syntheses and electrocatalytic properties of porous Pd and its alloy nanospheres. *Journal of Materials Chemistry*, 21, 9620-9625.

Zhang, Y., Huang, L., Arunagiri, T. N., Ojeda, O., Flores, S., Chyan, O., & Wallace, R. M. 2004. Underpotential deposition of copper on electrochemically prepared conductive ruthenium oxide surface. *Electrochemical and Solid-State Letters*, 7, 107-110.

Zhao, Y. 2013. Porous metallic materials produced by P/M Methods. *Journal of Powder Metallurgy & Mining*, 2, 2-3.

Zhao, Y., & Sun, D. 2001. A novel sintering-dissolution process for manufacturing al foams. *Scripta Materialia*, 441, 105-110.

Zhao, Y., Fung, T., Zhang, L., & Zhang, F. 2005. Lost carbonate sintering process for manufacturing metal foams. *Scripta Materialia*, 524, 295–298.

Zheng, Y., Ding, H., & Zhang, M. 2009. Preparation and electrochemical properties of Ni oxide as a supercapacitor electrode material. *Materials Research Bulletin*, 442, 403-407.

Zhou, W., Wang, Q., Qiu, Q., Tang, Y., Tu, J., Hui, K., & Hui, K. 2015. Heat and mass transfer characterization of porous copper fiber sintered felt as catalyst support for methanol steam reforming. *Fuel*, 145, 136–142.

Zhu, H., Tong, H., Yang, F., & Cheng, C. 2018. Plasma-assisted preparation and characterization of spherical stainless steel powders. *Journal of Materials Processing Technology*, 252, 559–566.

Zhu, J., Yin, H., Gong, J., Al-Furjan, M., & Nie, Q. 2018. Easy one pot synthesis of NiO/Nitrogen doped carbon spheres for highly sensitive enzyme free amperometric glucose sensors. *Applied Surface Science*, 444, 56–64.

Zhu, N., Gu, L., Wang, J., Li, X., Liang, G., Zhou, J., & Zhang, Z. 2019. Novel

and Sensitive Chemiluminescence Sensors Based on 2D-MOF Nanosheets for One-Step Detection of Glucose in Human Urine. *The Journal of Physical Chemistry C*, 123, 9388–9393.

Zhu, P., & Zhao, Y. 2017. Effects of electrochemical reaction and surface morphology on electroactive surface area of porous copper manufactured by Lost Carbonate Sintering. *RSC Advances*, 742, 26392-26400.

Zhu, P., & Zhao, Y. 2019. Cyclic voltammetry measurements of electroactive surface area of porous Ni: Peak current and peak charge methods and diffusion layer effect. *Materials Chemistry and Physics*, 233, 60–67.

Zhuo, K., Jeong, M., & Chung, C. 2013. Highly porous dendritic ni–SN anodes for lithium-ion batteries. *Journal of Power Sources*, 244, 601-605.

Žlvčák, J., Šarik, M., & Hudák, R. 2016. FEA simulation of thermal processes during the direct metal laser sintering of Ti64 titanium powder. *Measurement*, 94, 893–901.

Zolfaghari, A., Villiard, F., Chayer, M., & Jerkiewicz, G. 1997. Hydrogen adsorption on Pt and rh electrodes and blocking of adsorption sites by chemisorbed sulfur. *Journal of Alloys and Compounds*, 253, 481-487.

## Appendixes

A. Raw data of electroactive and real surface areas for the LCS porous Ni samples presented in Chapter 4.

Table A1: Electroactive surface areas of the Ni plate for calibration.

Geometric surface area of sample (cm <sup>2</sup> )	Scan rate (V/s)	Peak current (mA)	Calculated Area (cm <sup>2</sup> )
0.342	0.005	0.0165	0.343
	0.01	0.023	0.338
	0.05	0.051	0.335
	0.1	0.072	0.334
	0.2	0.103	0.338
	0.3	0.127	0.341
0.479	0.005	0.024	0.499
	0.01	0.033	0.485
	0.05	0.073	0.480
	0.1	0.103	0.478
	0.2	0.147	0.483
	0.3	0.183	0.491
0.636	0.005	0.031	0.644
	0.01	0.044	0.647
	0.05	0.096	0.631
	0.1	0.134	0.623
	0.2	0.192	0.631
	0.3	0.236	0.633

0.823	0.005	0.04	0.831
	0.01	0.056	0.823
	0.05	0.122	0.802
	0.1	0.175	0.813
	0.2	0.249	0.818
	0.3	0.309	0.829
0.981	0.005	0.048	0.998
	0.01	0.067	0.985
	0.05	0.148	0.973
	0.1	0.213	0.990
	0.2	0.3	0.986
	0.3	0.364	0.977

Table A2: Variation of volumetric real surface area with level of parameter.

Parameter / Level of parameter	Volumetric real surface area (cm <sup>-1</sup> )			
	Level 1	Level 2	Level 3	Level 4
Pore size	1124.87	1088.52	1068.83	998.51
Porosity	1260.01	1147.33	989.58	875.34
Fine Ni powder ratio	540.96	829.42	1349.25	1553.62
Compaction pressure	1112.17	1071.85	1052.10	1044.28
Sintering temperature	1101.46	1109.79	1063.89	994.50

Note: Values of level 1-4. Pore size: 250-425, 425-710, 710-1000 and 1000-1500  $\mu\text{m}$ ; Porosity: 65%, 70%, 75% and 80%; Fine Ni powder ratio: 0%, 20%, 40% and 60%; Compaction pressure: 0, 50, 100 and 200 MPa; Sintering temperature: 700, 750, 800 and 850  $^{\circ}\text{C}$ .

Table A3: Variation of gravimetric real surface area with level of parameter.

Parameter / Level of parameter	Gravimetric real surface area (cm <sup>2</sup> /g)			
	Level 1	Level 2	Level 3	Level 4
Pore size	460.14	435.66	429.72	429.37
Porosity	400.10	434.27	438.11	479.72
Fine Ni powder ratio	212.24	348.25	561.89	640.56
Compaction pressure	493.36	460.14	401.75	394.41
Sintering temperature	459.79	438.11	430.42	424.83

Table A4: Variation of volumetric electroactive surface area with level of parameter.

Parameter / Level of parameter	Volumetric real surface area (cm <sup>-1</sup> )			
	Level 1	Level 2	Level 3	Level 4
Pore size	112.26	90.58	89.05	86.95
Porosity	95.03	95.06	102.59	105.98
Fine Ni powder ratio	80.15	90.02	99.05	110.30
Compaction pressure	102.99	98.81	90.46	86.07
Sintering temperature	107.44	101.13	90.15	81.77

Table A5: Variation of gravimetric electroactive surface area with level of parameter.

Parameter / Level of parameter	Gravimetric real surface area (cm <sup>2</sup> /g)			
	Level 1	Level 2	Level 3	Level 4
Pore size	49.32	40.27	39.13	39.44
Porosity	31.69	36.56	47.92	52.08
Fine Ni powder ratio	34.23	40.01	44.98	48.94
Compaction pressure	46.71	42.81	40.82	37.69
Sintering temperature	47.21	43.65	41.03	36.26

Table A6: Variation of volumetric real surface area with fine Ni powder ratio at different porosities (first column). Other parameters: pore size 425 – 710  $\mu\text{m}$ , compaction pressure 200 MP and sintering temperature 850  $^{\circ}\text{C}$ .

Porosity / Fine Ni content	Volumetric real surface area ( $\text{cm}^{-1}$ )					
	0%	20%	40%	60%	80%	100%
60%	922.08	1168.02	1361.20	1574.68	1228.90	1133.93
70%	701.22	905.03	1026.79	1215.91	967.53	866.88
80%	501.62	539.77	635.55	728.08	646.10	573.05

Table A7: Variation of gravimetric real surface area with fine Ni powder ratio at different porosities (first column). Other parameters: pore size 425 – 710  $\mu\text{m}$ , compaction pressure 200 MP and sintering temperature 850  $^{\circ}\text{C}$ .

Porosity / Fine Ni content	Gravimetric real surface area ( $\text{cm}^2/\text{g}$ )					
	0%	20%	40%	60%	80%	100%
60%	269.69	339.90	394.37	458.57	357.16	326.73
70%	283.50	341.30	384.91	453.84	367.90	328.77
80%	280.43	304.73	352.43	406.78	357.03	317.26

Table A8: Variation of volumetric electroactive surface area with fine Ni powder ratio at selected scan rates (first row). Other parameters: pore size 425 – 710  $\mu\text{m}$ , porosity 60%, compaction pressure 200 MP and sintering temperature 850°C.

Fine Ni content / Scan rate	Volumetric electroactive surface area ( $\text{cm}^{-1}$ )					
	0.005 (V/s)	0.01 (V/s)	0.02 (V/s)	0.05 (V/s)	0.1 (V/s)	0.4 (V/s)
0%	65.04	82.07	101.39	123.82	124.91	131.19
20%	75.45	92.06	107.26	131.47	148.87	169.22
40%	80.40	92.10	121.41	140.86	160.38	180.69
60%	82.38	98.67	121.05	148.33	173.31	195.67
80%	84.33	99.38	128.71	159.07	179.64	208.42
100%	78.41	98.34	127.97	170.77	199.16	218.18

Table A9: Variation of gravimetric electroactive surface area with fine Ni powder ratio at selected scan rates (first row). Other parameters: pore size 425 – 710  $\mu\text{m}$ , porosity 60%, compaction pressure 200 MP and sintering temperature 850°C.

Fine Ni content / Scan rate	Gravimetric electroactive surface area ( $\text{cm}^2/\text{g}$ )					
	0.005 (V/s)	0.01 (V/s)	0.005 (V/s)	0.05 (V/s)	0.005 (V/s)	0.4 (V/s)
0%	36.54	46.10	56.96	69.56	70.17	73.70
20%	42.39	51.72	60.26	73.85	83.63	95.06
40%	45.17	51.74	68.21	79.13	90.10	101.51
60%	46.28	55.43	68.01	83.33	97.36	109.93
80%	47.37	55.83	72.31	89.36	100.92	117.09
100%	44.05	55.24	71.89	95.93	111.88	122.57



Table A10: Variation of peak current density with scan rate for different fine Ni powder ratios (first row). Other parameters: pore size 425 – 710  $\mu\text{m}$ , porosity 60%, compaction pressure 200 MP and sintering temperature 850 $^{\circ}\text{C}$ .

Scan rate (V/s) / Fine Ni content	Current density (mA/g)					
	0%	20%	40%	60%	80%	100%
0.005	1.75	2.04	2.17	2.22	2.28	2.12
0.01	3.13	3.52	3.52	3.77	3.8	3.76
0.02	5.48	5.8	6.56	6.54	6.96	6.92
0.03	7.79	7.8	8.73	8.81	9	9.68
0.04	9.24	9.72	10.65	10.68	10.96	12.52
0.05	10.58	11.24	12.04	12.68	13.6	14.6
0.06	11.51	12.84	13.95	14.59	15.28	16.68
0.07	12.55	14.6	15.08	16.13	16.84	19.12
0.08	13.41	15.4	17.60	17.68	19.16	20.36
0.09	14.55	16.24	17.91	19.5	20.56	22.12
0.1	15.10	18	19.39	20.95	21.72	24.08
0.11	16.20	18.68	21.56	22.5	22.96	25.72
0.125	17.13	20.24	22.95	24.13	25.16	27.64
0.15	19.06	22.84	25.56	26.86	27.76	30.6
0.175	20.86	25.32	28.21	29.36	31.52	33.44
0.2	22.41	27.08	31.21	31.86	34.44	36.28
0.225	23.82	28.88	32.13	34.09	36.84	38.92
0.25	24.82	31.28	34.60	36.45	39.48	41.12
0.275	26.17	33.04	36.391	38.95	41.24	43.36
0.3	27.62	34.44	38	40.63	43.6	45.48
0.35	29.79	37.92	41.95	43.86	46.8	49.2
0.4	31.72	40.92	43.69	47.31	50.4	52.76

B. Raw data of real surface areas for the DHBT porous Ni samples presented in Chapter 5.

Table B1: Real surface area of the DHBT porous Ni samples at different parameter levels

Parameter / Level of parameter	Real surface area (cm <sup>2</sup> )		
	Level 1	Level 2	Level 3
Concentration of Ni(CH <sub>3</sub> COO) <sub>2</sub>	7.48	7.23	4.36
Concentration of NH <sub>4</sub> Cl	8.99	7.33	7.23
Deposition potential	7.23	16.17	26.19
Deposition time	2.21	7.23	8.03

Note: Values of level 1-3. Concentration of Ni(CH<sub>3</sub>COO)<sub>2</sub>: 0.1, 0.2 and 0.4 M; Concentration of NH<sub>4</sub>Cl: 0.5, 1 and 1.5 M; Deposition potential: -1.35, -1.5 and -1.7 V; Deposition time: 60, 150 and 300 s. The reference parameter: 0.2 M Ni(CH<sub>3</sub>COO)<sub>2</sub>, 1.5 M NH<sub>4</sub>Cl, -1.5 V deposition potential and 150 s deposition time.

Table B2: Real surface area of the DHBT porous Ni samples at different parameter levels.

Parameter / Level of parameter	Real surface area (cm <sup>2</sup> )		
	Level 1	Level 2	Level 3
Concentration of Ni(SO <sub>3</sub> NH <sub>2</sub> ) <sub>2</sub>	58.99	38.49	49.19
Deposition potential	38.49	49.26	40.44
Deposition time	28.92	38.49	35.85

Note: Values of level 1-3. Concentration of Ni(SO<sub>3</sub>NH<sub>2</sub>)<sub>2</sub>: 0.1, 0.2 and 0.4 M; Deposition potential: -1.7, -1.9 and -2.1 V; Deposition time: 100, 150 and 200 s. The reference parameter: 0.2 M Ni(SO<sub>3</sub>NH<sub>2</sub>)<sub>2</sub>, -1.7 V deposition potential and 150 s deposition time.

C. Raw data of mass transfer performance for the LCS and LCS/DHBT porous Ni samples presented in Chapter 6.

Table C1: Mass transfer performance of the LCS porous Ni samples manufactured with different fine Ni powder ratios (first column) measured at different electrolyte flow rates (first row).

Fine Ni content / Flow rate	Mass transfer performance (cm <sup>3</sup> /s)			
	1.32 (cm/s)	2.22 (cm/s)	4.38 (cm/s)	6.6 (cm/s)
0%	0.00424	0.00648	0.0112	0.0159
20%	0.00498	0.00681	0.01	0.0125
40%	0.00577	0.00756	0.01104	0.0141
60%	0.00372	0.00528	0.0088	0.012
80%	0.00342	0.005	0.00852	0.0116
100%	0.00311	0.00472	0.00773	0.0109

Table C2: Mass transfer performance of the composite LCS/DHBT porous Ni samples manufactured with different deposition time (first column) under a deposition potential of -1.35 V measured at different electrolyte flow rates (first row).

Deposition time (s) / Flow rate	Mass transfer performance (cm <sup>3</sup> /s)			
	1.32 (cm/s)	2.22 (cm/s)	4.38 (cm/s)	6.6 (cm/s)
0	0.00424	0.00648	0.0112	0.0159
60	0.00836	0.0116	0.0185	0.0247
150	0.00911	0.0129	0.0203	0.0267
300	0.0095	0.0136	0.022	0.0296

Table C3: Mass transfer performance of the composite LCS/DHBT porous Ni samples manufactured with different deposition time (first column) under a deposition potential of -1.5 V measured at different electrolyte flow rates (first row).

Deposition time (s) / Flow rate	Mass transfer performance (cm <sup>3</sup> /s)			
	1.32 (cm/s)	2.22 (cm/s)	4.38 (cm/s)	6.6 (cm/s)
0	0.00424	0.00648	0.0112	0.0159
60	0.00948	0.0131	0.0205	0.0272
150	0.0104	0.0149	0.0239	0.0316
300	0.01073	0.0154	0.0251	0.0336

Table C4: Mass transfer performance of the composite LCS/DHBT porous Ni samples manufactured with different deposition time (first column) under a deposition potential of -1.7 V measured at different electrolyte flow rates (first row).

Deposition time (s) / Flow rate	Mass transfer performance (cm <sup>3</sup> /s)			
	1.32 (cm/s)	2.22 (cm/s)	4.38 (cm/s)	6.6 (cm/s)
0	0.00424	0.0064	0.0112	0.0159
60	0.0118	0.0156	0.0221	0.0282
150	0.0125	0.0175	0.0267	0.0347
300	0.0130	0.0183	0.0281	0.0377

D. Raw data of potential shift and peak current at different glucose concentrations for the Ni plate, LCS porous Ni and the LCS/DHBT porous Ni samples presented in Chapter 7.

Table D1: Peak current corresponding to potential shift for Ni plate, LCS porous Ni and LCS/DHBT porous Ni electrodes.

Ni Plate		LCS porous Ni		LCS/DHBT porous Ni	
Potential Shift (mV)	Peak current (mA)	Potential Shift (mV)	Peak current (mA)	Potential Shift (mV)	Peak current (mA)
0	0.314	0	1.92	0	3.43
9	0.546	18	2.47	40	5.09
21	0.885	38	3.36	110	7.6
32	1.18	56	4.01	165	9.45
42	1.44	75	4.76	215	11.2
49	1.64	85	5.09	260	12.8
58	1.85	97	5.57	295	13.9

Table D2: Peak current at different scan rates for the Ni plate, LCS porous Ni and LCS/DHBT porous Ni electrodes

Scan rate (V/s)	Peak current (mA)		
	Ni Plate	LCS Porous Ni	LCS/DHBT Porous Ni
0.025	0.31	1.92	3.43
0.05	0.55	2.47	5.09
0.1	0.89	3.36	7.60
0.15	1.18	4.01	9.45
0.2	1.44	4.76	11.22
0.25	1.64	5.09	12.84
0.3	1.85	5.57	13.94

Table D3: Peak current at different glucose concentrations offer the LCS/DHBT porous Ni samples manufactured with a deposition potential of - 1.35 V in solutions with Ni(CH<sub>3</sub>COO)<sub>2</sub> concentrations of 0.5, 1 and 1.5 M.

Glucose concentration (mM) / Ni(CH <sub>3</sub> COO) <sub>2</sub> concentration	Peak current (mA)		
	0.5 (M)	1 (M)	1.5 (M)
0	9.2	8.6	7.9
0.01	10	9.3	8.8
0.05	13.5	11	10.2
0.1	15.9	13.4	12.4
0.2	18.4	15.7	14.6
0.4	20.4	17.46	16.03
0.6	22.4	19.78	18.9
0.8	25.2	21.05	19.8
1	27.5	23.8	21
1.5	33.5	28.2	24.5
2	38.3	32.7	28.3
2.5	43.9	38.1	32.3
3	50.1	43.5	36.5
3.5	56.1	47.2	39.9
4	62.2	53.4	44
4.5	68	59	48.6
5	74.7	65.2	53.6
5.5	80.5	69	57.9
6	86.2	74.8	62.4
6.5	89.9	77.5	66.8
7	93.4	82.7	71.2
7.5	96.16	85.1	73.5
8	98.2	87.9	77.4

Table D4: Peak current at different glucose concentrations offer the LCS/DHBT porous Ni samples manufactured with a deposition potential of - 1.5 V in solutions with Ni(CH<sub>3</sub>COO)<sub>2</sub> concentrations of 0.5, 1 and 1.5 M.

Glucose concentration (mM) / Ni(CH <sub>3</sub> COO) <sub>2</sub> concentration	Peak current (mA)		
	0.5 (M)	1 (M)	1.5 (M)
0	11.5	10.7	9.37
0.01	13.1	12.1	10.6
0.05	15.7	13.4	11.5
0.1	17.86	16.1	13.4
0.2	20.62	18.7	16
0.4	23.97	20.9	18.3
0.6	27.56	23.3	20.5
0.8	31.83	26.7	22.2
1	34.89	29.5	24.6
1.5	41.18	35.7	29.2
2	47.68	42.3	35.7
2.5	54.89	49.8	40.2
3	60.54	56.4	46.8
3.5	66.58	61.2	51.4
4	73.41	65.1	56.9
4.5	78.28	72.9	62.1
5	85.45	79.5	67.8
5.5	89.06	83.9	73.2
6	92.37	87.6	76.5
6.5	94.45	89.3	80.1



Table D5: Peak current at different glucose concentrations offer the LCS/DHBT porous Ni samples manufactured with a deposition potential of - 1.7 V in solutions with Ni(CH<sub>3</sub>COO)<sub>2</sub> concentrations of 0.5, 1 and 1.5 M.

Glucose concentration (mM) / Ni(CH <sub>3</sub> COO) <sub>2</sub> concentration	Peak current (mA)		
	0.5 (M)	1 (M)	1.5 (M)
0	17.1	15.2	13.3
0.01	20.5	17.3	14.8
0.05	24.39	20.8	17.9
0.1	29.83	25.7	24.1
0.2	35.23	31.5	30.5
0.4	43.83	38.6	36.7
0.6	48.31	45.3	42.3
0.8	58.4	51.7	48.1
1	65.65	58.2	52.2
1.5	78.9	70.3	63
2	90.6	79.4	75.3
2.5	99.1	88.7	82.7
3	107.03	97.34	91.6
3.5	110.62	104	98.21
4	114.3	108	102.4
4.5	117.1	110	107
5	117.8	111.5	110

Table D6: Peak current at different glucose concentrations for the Ni plate, LCS porous Ni and composite LCS/DHBT porous Ni electrodes.

Glucose concentration (mM) / Ni samples	Peak current (mA)		
	Ni plate	LCS porous Ni	LCS/DHBT porous Ni
0	0.86	1.32	3.55
0.01	1.07	1.43	3.75
0.05	1.13	1.52	3.97
0.1	1.19	1.64	4.25
0.2	1.33	1.79	4.55
0.4	1.43	2.05	4.94
0.6	1.57	2.21	5.32
0.8	1.61	2.45	5.7
1	1.72	2.65	5.78
1.5	2.04	3	6.52
2	2.37	3.48	7.15
2.5	2.53	3.81	7.64
3	2.84	4.13	8.3
3.5	3.11	4.43	8.92
4	3.32	4.87	9.44
4.5	3.27	5.1	10.08
5	3.48	5.43	10.68
5.5	3.72	5.69	11.02
6	3.96	5.98	11.45
6.5	4.13	6.27	11.85
7	4.29	6.33	12.6
7.5	4.51	6.59	13.04
8	4.77	6.85	13.51
8.5	4.97	7.11	13.93

9	5.12	7.35	14.53
9.5	5.24	7.75	14.87
10	5.37	7.98	15.42
10.5	5.52	8.26	15.81
11	5.7	8.46	16.24
11.5	5.93	8.7	16.55
12	5.86	8.83	16.89
12.5	6.01	8.92	17.2
13	6.21	9.04	17.36
13.5	6.36	9.28	17.54
14	6.54	9.5	17.51
14.5	6.7	9.81	17.76
15	6.84	10	18.01

Table D7: Peak potential at different glucose concentrations for the Ni plate, LCS porous Ni and composite LCS/DHBT porous Ni electrodes.

Glucose concentration (mM) / Ni sample	Potential (mV)		
	Ni plate	LCS porous Ni	LCS/DHBT porous Ni
0	414	446	480
0.01	416	447	482
0.05	420	449	487
0.1	421	452	492
0.2	423	457	497
0.4	426	464	507
0.6	430	477	514
0.8	431	479	522
1	433	487	532
1.5	439	504	549

2	448	522	564
2.5	454	534	579
3	460	547	597
3.5	468	559	612
4	473	577	629
4.5	480	587	652
5	488	599	672
5.5	498	607	684
6	509	617	697
6.5	518	627	709
7	528	637	737
7.5	536	642	749
8	543	652	779
8.5	556	662	794
9	563	672	829
9.5	571	682	832
10	578	689	839
10.5	584	699	864
11	593	707	902
11.5	598	717	924
12	605	724	939
12.5	615	729	937
13	620	732	947
13.5	625	739	964
14	634	749	972
14.5	641	759	979
15	648	769	984

Table D8: Slope and intercept of the current density - glucose concentration curves for the composite LCS/DHBT porous Ni samples manufactured at different  $\text{NH}_4\text{Cl}$  concentrations (first column) and different deposition potentials (first row).

Concentration of $\text{NH}_4\text{Cl}$ / Deposition potential	-1.35 V		-1.5 V		-1.7 V	
	Slope	Intercept	Slope	Intercept	Slope	Intercept
0.5 M	67.90	9.43	60.58	12.12	118.50	18.22
	11.73	15.50	13.33	20.12	28.02	33.48
	5.53	54.31	6.06	55.48	5.60	90.95
1 M	46.94	8.70	49.84	11.08	100.48	15.73
	10.09	13.27	12.66	16.55	33.25	25.11
	5.20	46.23	6.62	47.01	18.08	43.25
					4.90	87.55
1.5 M	42.90	8.11	36.48	9.76	58.81	15.43
	8.17	12.59	10.78	13.78	20.55	31.57
			6.90	35.20	7.99	70.43